Theses and Dissertations

Spring 2010

A sharp interface Cartesian grid hydrocode

Shiv Kumar Sambasivan
University of Iowa

Recommended Citation
Sambasivan, Shiv Kumar. "A sharp interface Cartesian grid hydrocode." PhD (Doctor of Philosophy) thesis, University of Iowa, 2010.
https://doi.org/10.17077/etd.b55egfyg

A SHARP INTERFACE CARTESIAN GRID HYDROCODE

by

Shiv Kumar Sambasivan

<u>An Abstract</u>

Of a thesis submitted in partial fulfillment of the
requirements for the Doctor of Philosophy
degree in Mechanical Engineering
in the Graduate College of
The University of Iowa

May 2010

Thesis Supervisor: Professor H.S. Udaykumar

ABSTRACT

Dynamic response of materials to high-speed and high-intensity loading conditions is important in several applications including high-speed flows with droplets, bubbles and particles, and hyper-velocity impact and penetration processes. In such high-pressure physics problems, simulations encounter challenges associated with the treatment of material interfaces, particularly when strong nonlinear waves like shock and detonation waves impinge upon them. To simulate such complicated interfacial dynamics problems, a fixed Cartesian grid approach in conjunction with levelset interface tracking is attractive. In this regard, a sharp interface Cartesian grid-based, Ghost Fluid Method (GFM) is developed for resolving embedded fluid, elasto-plastic solid and rigid (solid) objects in hyper-velocity impact and high-intensity shock loaded environment. The embedded boundaries are tracked and represented by virtue of the level set interface tracking technique. The evolving multi-material interface and the flow are coupled by meticulously enforcing the boundary conditions and jump relations at the interface. In addition, a tree-based Local Mesh Refinement scheme is employed to efficiently resolve the desired physics. The framework developed is generic and is applicable to interfaces separating a wide range of materials and for a broad spectrum of speeds of interaction (O(km/s)). The wide repertoire of problems solved in this work demonstrates the flexibility, stability and robustness of the method in accurately capturing the dynamics of the embedded interface. Shocks interacting with large ensembles of particles are also computed.

Abstract Approved: _____

Thesis Supervisor

_____

Title and Department

_____

Date

A SHARP INTERFACE CARTESIAN GRID HYDROCODE

by

Shiv Kumar Sambasivan

A thesis submitted in partial fulfillment of the
requirements for the Doctor of Philosophy
degree in Mechanical Engineering
in the Graduate College of
The University of Iowa

May 2010

Thesis Supervisor: Professor H.S. Udaykumar

Graduate College
The University of Iowa
Iowa City, Iowa

CERTIFICATE OF APPROVAL

_____

PH.D. THESIS

_____

This is to certify that the Ph.D. thesis of

Shiv Kumar Sambasivan

has been approved by the Examining Committee for the thesis re-
quirement for the Doctor of Philosophy degree in Mechanical Engi-
neering at the May 2010 graduation.

Thesis Committee: _____

H. S. Udaykumar, Thesis Supervisor

_____

P. Barry Butler

_____

Christoph Beckermann

_____

James Buchholz

_____

Pablo M. Carrica

_____

George Constantinescu

ACKNOWLEDGEMENTS

It is my pleasure to thank those who made this thesis possible. First and foremost, I owe my deepest and sincere gratitude to my thesis supervisor, Prof. H.S. Udaykumar, without whose guidance and constant encouragement this work would have been entirely impossible. His endless patience and professional acumen are undeniably the reason for instilling inspiration and reinforcing confidence in me. I have interacted with him both at personal and professional levels, and I am grateful for the invaluable lessons that I have learned from these interactions. I consider myself extremely fortunate to have him as my thesis supervisor and I undeniably attribute the success of this thesis to his guidance.

I would also like to extend my sincere gratitude to all the members of my thesis committee. Their painstaking effort in reading my thesis, the insightful suggestions and the noteworthy advice are greatly and immensely appreciated.

Special thanks to my friend Haribalan Kumar for helping me compiling the figures and movies presented in this thesis, and not to mention his excellent culinary skills that made my stay supremely comfortable. I should also thank all the past and the present members of my lab and friends who have made this journey a pleasant and an enjoyable one. I would also like to thank the staff members of the Department of Mechanical Engineering, for their timely help and support that kept me on track with the official responsibilities with least encumbrance.

Finally words are not enough to thank my family, to whom this thesis is dedicated, for their unconditional support that made this thesis feasible. Their continuous encourage-

ment bolstered my confidence in overcoming every obstacle that I came across during the course of this thesis.

iii

TABLE OF CONTENTS

vi

LIST OF TABLES

LIST OF FIGURES

Figure

xix

CHAPTER 1
INTRODUCTION

The dynamic response of materials to high speed flows and/or high intensity loading conditions due to shock and detonation waves is important in several applications including high-speed flows with droplets [78], bubbles and particles [139, 147], hypervelocity impact and penetration [190], and detonation diffraction [158, 204]. In such high pressure physics problems, there are computational challenges associated with the treatment of material interfaces, particularly when the interface interacts with strong nonlinear waves like shock and detonation waves. The result of such shock-interface interactions may be partial reflection, refraction or transmission of the impinging waves and rapid and severe distortion of the material interfaces under the influence of the shocked fields [73]. To simulate such complicated interfacial dynamics problems, a fixed Cartesian grid approach in conjunction with level set interface tracking is attractive. In this Eulerian framework, the grid remains indifferent to the fate of the interfaces, with the level sets carrying the onus of tracking the interfaces through the likely topological changes. However, accurate treatment and representation of these phenomena by retaining the interface as a sharp entity is a key challenge, and this is addressed in this thesis.

1.1 Specific Objectives

In this work, a general framework is developed to solve multi-material interaction problems with interfaces separating a wide range of materials (liquids, elasto-plastic solids and rigid solids) and for a broad spectrum of speeds of interaction (for high Mach num-

bers). Based on the material-strength/material-stiffness of the constituent media, materials can range from negligible strength (fluid) to moderate strength (solids that undergo elastic deformation followed by plastic flow) and infinite strength (i.e. rigid solids). These categories of materials cover a plethora of applications ranging from shock-droplet interactions at the small scale to geophysical impact at the large scale. In particular, the class of problems that can be solved can be categorized as follows:

1. Resolution of Fluid Objects:

   The framework can be applied to resolve fluid objects such as droplets and bubbles immersed in high speed compressible flows. Fluids, by definition, are characterized as materials with negligible strength as they offer no resistance to external shear or torsional loads. Fluid objects, such as droplets and bubbles, embedded in the flow interact with shock and detonation waves that may lead to reflection, refraction or transmission of the impinging waves. Capturing the interface conditions in such situations are important in applications such as shock wave lithotripsy [92], high speed coating technologies [40, 78], under-water detonation/explosions [73] etc. For instance, see Figures 1.1 & 1.2.

2. Resolution of Elasto-Plastic Solids:

   The framework can be employed to study the deformation of elasto-plastic solids. Elasto-plastic solids are materials with moderate to large material-strength. These materials undergo very severe deformation when subject to intense shock and impact loads. Elasto-plastic solids, unlike fluids, behave like a shape-memory material for loads within the elastic regime [183]. When the applied load increases in strength

and beyond the elastic limit, the material tends to flow (plastic deformation). Because of the high speeds involved in the interaction process, these problems are characterized by nonlinear wave propagation phenomena in the material. The elasto-plastic response of materials typically consist of a precursor elastic wave followed by a plastic wave. These phenomena are common in high speed multi-material dynamics problems such as munition-target interactions [17, 212], geological impact dynamics [8, 150], shock-processing of powders [21, 22], vehicular collision crashworthiness [23, 214], formation of shaped charges [195, 199] etc..Some of these applications are displayed in Figures 1.3 & 1.4.

3. Resolution of Rigid (Solid) Objects:

Materials with infinite material-strength are classified as rigid (solid) objects. With infinite material-strength, rigid objects (embedded in high speed flows) do not deform to external loads. Shock waves interacting with stationary or moving rigid solid objects give rise to complex diffraction patterns that are important in applications such as supersonic aerodynamics (Figures 1.5 & 1.6) of projectiles [96, 97], explosive/shock dispersal of particles [114, 154], shock waves traversing through dusty gas layers [56] etc.. Thus, the framework developed in this work can be applied to study and capture such shock diffraction patterns arising from shock-interface interactions.

1.2 Highlights of the Thesis

The unifying feature in the high-speed/high-strain rate phenomena is the hyperbolic character of the system of conservation laws that govern the dynamics and the large mo-

tions/deformations of the embedded interface in such systems. Furthermore, despite the fact that the response of materials to such high speed multi-material interaction phenomena has similar signature in different media, the numerical techniques developed thus far are either directed towards specific applications [56, 78, 114, 129] or limited to resolve particular material enclosed within the interface [58, 136, 180, 190, 192]. The reason for this dearth in generality can be attributed to the modeling complexities and intricacies that one has to pay close attention while solving such high speed interaction problems. In contrast, the framework developed in this thesis is generic and has the simulation capabilities designed to handle the modeling issues such as:

- Representation of nonlinear wave propagation phenomena in the material:

  The response of materials to high speed and high intensity loading conditions are dictated by the propagation of nonlinear stress waves in the interacting media. The nature of the waves propagating in the material could be a combination of (longitudinal) dilatational and (shear or transverse) distortional waves, which depend on the material being subjected to the loading conditions. For instance, if the interacting materials are made of fluids, then the waves generated are primarily dilatational (longitudinal pressure waves) in nature. On the other hand, if the constituent materials are elastic or elasto-plastic, then the material can sustain elastic wave or elastic wave followed by a slower, but intense plastic (distortional) wave. For very high speeds of interaction, the nonlinear waves steepen to form much stronger (compressive shock or tensile rarefaction) waves in the material. Thus the physical characteristics that are common to these problems are dictated by the nature of stress waves propagating

in the material. For instance, the interaction of these stress waves with the embedded interface often lead to spallation, fracture or complete failure of the interacting materials. Hence, special care must be exercised in developing numerical techniques for solving such problems, so that the nonlinear wave propagation phenomena and the associated material response are captured accurately. It will be shown later that the methodology developed in this work is robust in resolving the wave-patterns and wave-interactions for a wide class of materials.

- Resolution of the embedded interface undergoing large deformation:

Because of the very high speeds involved in the interaction process, the embedded interface is often subject to very large deformations occurring at high strain-rate conditions. Traditionally, numerical techniques developed to handle high speed multi-material interaction phenomena treat the moving material boundaries by either allowing the boundaries to flow through a fixed mesh while computing the flow field on the fixed mesh (Eulerian framework), or by allowing the mesh to follow the material points in the deforming materials (Lagrangian framework) [192]. An intermediate approach, ALE (Arbitrary Lagrangian Eulerian), allows the mesh to move so as to conform to the contours of the deforming object, but the mesh is not necessarily attached to the material points [192]. In the Lagrangian moving mesh methods, considerable complexity is enjoined by the need for mesh management, to accommodate the large distortion of the embedded boundary. Therefore in such methods, periodical re-meshing operations are required, so that an adequately refined mesh with good mesh quality is maintained. In some cases, it is advantageous to use meshless

methods such as the Smooth-Particle Hydrodynamics (SPH) to cope with severe deformations [214]. However such methods are not suitable for Eulerian-based flow calculations. For very severe deformations, the use of embedded boundary methods wherein a fixed global mesh with embedded boundary tracking (sharp interface treatment) and local mesh enrichment have emerged as promising alternatives.

In recent years, the use of Cartesian grid-based sharp interface approaches have become immensely popular because such methods do not suffer from the complex grid generation and grid management requirements inherent to other methods. In addition, Cartesian grid methods come with numerous advantages including simpler flux construction and formulation, simplifications of the data structure, incidental cancellation of truncation errors etc [198,207]. Cartesian grid methods retain the simplicity associated with discretization of governing equations while shifting the onus to the numerical treatment at the embedded interface. Hence in this thesis, a Cartesian grid based Eulerian framework is developed for resolving and capturing the interface conditions for embedded multi-material interface.

- Capturing interface conditions involving collision, fragmentation, and merging of the multi-material interface:

  The high speed interaction problems are often characterized by complex phenomena such as collision, fragmentation, and merging of multi-material interfaces. Capturing interface conditions in such situations pose significant modelling challenges particularly when the mesh does not conform and adhere to the shape of the embedded interface. To relieve this shortcoming, in the present framework, level sets are used

to track and represent the arbitrarily oriented interface [137]. With the level set technique, collision, fragmentation and merging of embedded interfaces can be naturally incorporated in the interface tracking procedure.

- Sharp treatment of the multi-material interface:

Since the zero level set contour implicitly determines the boundary that separates different media, mixing of materials inherent in techniques that smear the material interface [5, 25, 98, 102] is prohibited. Hence, the exact location of the interface and the materials enclosed by the interface are known at all times [190]. Thus, the boundary conditions and the jump relations can be directly imposed on the interface by suitably communicating with the flow and the tracked interface. In the present framework, this task is accomplished via the Ghost fluid Method (GFM) developed in [58].

The pivotal theme in the GFM approach lies in the definition of a band of ghost points corresponding to each phase of the interacting media. The ghost band when supplied with appropriate flow conditions, together with the respective real fluid, constitutes a single flow field. Hence higher-order numerical schemes such as ENO [163] and WENO [74] developed for single component flows, can be readily employed at the interface. The success of the GFM approach largely depends on the accuracy with which the ghost states are predicted. The ghost states in turn are derived based on the material enclosed by the embedded object. Thus in the GFM framework, the treatment of embedded interfaces essentially boils down to suitably defining the ghost states such that the material properties and the interface conditions are depicted ac-

curately.

- Resolution of disparate lengths:

  While the GFM-based Cartesian grid approach significantly alleviates the complexity associated with mesh management, the method lacks flexibility in effective and automatic grid point placement in regions with rich structures in the flow field. This is particularly crucial for problems involving disparate length scales and steep gradients in the flow field, and large deformations of the embedded interface [108, 191]. Typically in compressible flows, such regions are concentrated spatially, near shock waves, contact discontinuities, rarefactions waves, detonation waves or in the regions of baroclinic vorticity concentration, that occupy a small fraction of the computational domain. To adequately capture such intricate flow features arising from the diffraction patterns of shock or detonation waves, one must resort to numerical schemes of inherently higher-order with extremely fine mesh resolution throughout the computational domain [146]. An alternative approach is to supplement the solution with adaptive grid technology that automatically refines and follows discontinuities with the evolution of the flow field. Hence, the GFM approach developed in this work, is augmented with the quadtree- (octree- in three dimensions) based Local Mesh Refinement (LMR) technique developed in [108] to efficiently resolve the desired physics.

In this thesis, the framework has been applied to capture the interface conditions for embedded fluid, elasto-plastic solids and rigid solid objects in high speed multi-material impact and shock loaded environment. The broad range of results presented in this work

demonstrates the flexibility and robustness of the current approach. Shocks interacting with stationary and moving boundaries have been computed.

1.3 Constitutive Relations and Governing Equations

The constitutive relations and the governing equations solved in this work have been discussed in [190, 192]. For the sake of completeness, a brief review of the equations are presented here.

1.3.1 Constitutive Relations

The response of materials to high intensity (shock/impact) loading conditions are modeled by assuming the additive decomposition of strain rule,

$$D_{ij} = D_{ij}^E + D_{ij}^P \tag{1.1}$$

where D_{ij} is the total strain-rate tensor given as,

$$D_{ij} = \frac{1}{2} \left(\frac{\partial u_i}{\partial x_j} + \frac{\partial u_j}{\partial x_i} \right) \tag{1.2}$$

and D_{ij}^E & D_{ij}^P are the elastic and plastic strain-rate components respectively, and u_i is the velocity component. The validity of additive strain rule can be justified for the relatively small elastic strain-rate experienced in the high speeds considered in this work. Assuming incompressibility (isochoric) of the plastic flow ($tr\left(D_{ij}^P\right) = 0$), the volumetric or dilatational response is governed by an equation of state while the deviatoric response obeys a conventional flow theory of plasticity [190]. Hence, the total stress in the material can be expressed as

$$\sigma_{ij} = S_{ij} - P\delta_{ij} \tag{1.3}$$

where σ_{ij} is the Cauchy stress tensor, S_{ij} is the deviatoric component and P is the hydrostatic pressure taken to be positive in compression. Using Eq 1.1, the rate of change of deviatoric stress component can be modeled using the hypo-elastic stress-strain relation (Hooke's law):

$$\overset{\triangledown}{S}_{ij} = 2G(\bar{D}_{ij} - D^P_{ij}) \tag{1.4}$$

where G is the shear or rigidity modulus, $\overset{\triangledown}{S}_{ij}$ is the Jaumann derivative [201]

$$\overset{\triangledown}{S}_{ij} = \dot{S}_{ij} + S_{ik}\Omega_{kj} - \Omega_{ik}S_{kj} \tag{1.5}$$

and Ω_{ij} is the spin tensor. The Jaumann derivative is used to ensure objectivity of the stress tensor with respect to rotation. The spin tensor used in Eq 1.5 is given by:

$$\Omega_{ij} = \frac{1}{2}\left(\frac{\partial u_i}{\partial x_j} - \frac{\partial u_j}{\partial x_i}\right) \tag{1.6}$$

The deviatoric strain-rate component, $\bar{D}_{ij}$, in Eq 1.4 is given by:

$$\bar{D}_{ij} = D_{ij} - \frac{1}{3}D_{kk}\delta_{ij} \tag{1.7}$$

The isochoric plastic strain-rate component ($D^P_{ij} = \bar{D}^P_{ij}$) in Eq 1.2 is modeled assuming a coaxial flow theory (Druckers' postulate) for strain hardening materials [105]:

$$D^p_{ij} = \Lambda N_{ij} \tag{1.8}$$

where $N_{ij} = \frac{S_{ij}}{\sqrt{S_{kl}S_{kl}}}$ is the unit outward normal to the yield surface and Λ is a proportional positive scalar factor called the consistency parameter [190]. The consistency parameter Λ is determined using J_2 Von Mises yield condition. The effective plastic stress (S_e) and the

effective plastic strain-rate ($\dot{\bar{\epsilon}}_p$) are given by:

$$S_e^2 = \frac{3}{2} tr\left(S_{ij} S_{ji}\right) = 3\left(S_{xx}^2 + S_{yy}^2 + S_{zz}^2\right) \qquad (1.9)$$

$$(\dot{\bar{\epsilon}}_p)^2 = \frac{2}{3} tr\left(D_{ij}^p D_{ji}^p\right) = \frac{2}{3}\Lambda^2 \qquad (1.10)$$

The evolution of temperature due to heat conduction and thermal energy produced by work done during elasto-plastic deformation is written as

$$\rho C \dot{T} = k \nabla^2 T - \alpha \left(3\lambda + 2\mu\right) T_o \dot{\epsilon}_{kk}^e + \beta \dot{W}_p \qquad (1.11)$$

where T is the temperature, C the specific heat, k thermal conductivity, α thermal expansion coefficient, λ & μ are the Lamé constants, $\dot{W}_p$ is the stress power due to plastic work and β is the Taylor-Quinney parameter [186]. The Taylor-Quinney parameter implies the fraction of mechanical power converted to thermal power and is taken as 0.9. The stress power due to plastic work is given by

$$\dot{W}_p = \dot{\bar{\epsilon}}_P S_e \qquad (1.12)$$

where S_e is the Von-Mises effective stress (Eq 1.9). For the applications considered in this work, the conduction and elastic work terms are small in comparison with the plastic stress power term $\dot{W}_p$.

1.3.2 Governing Equations

To solve high strain-rate deformation of materials, the traditional operator splitting algorithm is employed [164]. The integration of the mass, momentum and energy balance laws are performed assuming pure elastic deformation (with $D_{ij}^P = 0$) to obtain the elastic

predictor step, followed by a radial return mapping to bring the predicted stress back to the

yield surface (Kuhn-Tucker consistency conditions) [165].

Because of the high speeds involved in the interaction process, the governing equations comprise a set of hyperbolic conservation laws. Cast in Cartesian coordinates, the governing equations take the following form:

$$\frac{\partial \vec{U}}{\partial t} + \frac{\partial \vec{F}}{\partial x} + \frac{\partial \vec{G}}{\partial y} + \Phi_{3D}\frac{\partial \vec{H}}{\partial z} = \vec{S} \tag{1.13}$$

For the elastic predictor step, in addition to the mass, momentum and energy equations, the constitutive models for deviatoric stress terms are evolved. Thus the conservative variable and the fluxes in Eq 1.13 take the form given below:

$$\vec{U} = \begin{pmatrix} \rho \\ \rho u \\ \rho v \\ \rho w \\ \rho E \\ \rho \bar{\epsilon}_p \\ \rho T \\ \rho S_{xx} \\ \rho S_{xy} \\ \rho S_{yy} \\ \rho S_{xz} \\ \rho S_{yz} \end{pmatrix}, \vec{F} = \begin{pmatrix} \rho u \\ \rho u^2 + p \\ \rho uv \\ \rho uw \\ u(\rho E + p) \\ \rho u\bar{\epsilon}_p \\ \rho uT \\ \rho u S_{xx} \\ \rho u S_{xy} \\ \rho u S_{yy} \\ \rho u S_{xz} \\ \rho u S_{yz} \end{pmatrix}, \vec{G} = \begin{pmatrix} \rho v \\ \rho uv \\ \rho v^2 + p \\ \rho vw \\ v(\rho E + p) \\ \rho v\bar{\epsilon}_p \\ \rho vT \\ \rho v S_{xx} \\ \rho v S_{xy} \\ \rho v S_{yy} \\ \rho v S_{xz} \\ \rho v S_{yz} \end{pmatrix}, \vec{H} = \begin{pmatrix} \rho w \\ \rho uw \\ \rho vw \\ \rho w^2 + p \\ w(\rho E + p) \\ \rho w\bar{\epsilon}_p \\ \rho wT \\ \rho w S_{xx} \\ \rho w S_{xy} \\ \rho w S_{yy} \\ \rho w S_{xz} \\ \rho w S_{yz} \end{pmatrix}.$$

The source term in Eq 1.13 is given as:

$$\vec{S} = \begin{pmatrix} -\Phi_A \frac{\rho u}{x} \\[2ex] \frac{\partial S_{xx}}{\partial x} + \frac{\partial S_{xy}}{\partial y} + \Phi_{3D} \frac{\partial S_{xz}}{\partial z} - \Phi_A \left(\frac{\rho u^2}{x} - S_{xx} + S_{zz} \right) \\[2ex] \frac{\partial S_{xy}}{\partial x} + \frac{\partial S_{yy}}{\partial y} + \Phi_{3D} \frac{\partial S_{yz}}{\partial z} - \Phi_A \left(\frac{\rho uv}{x} - \frac{S_{xy}}{x} \right) \\[2ex] \Phi_{3D} \left(\frac{\partial S_{xz}}{\partial x} + \frac{\partial S_{yz}}{\partial y} + \frac{\partial S_{zz}}{\partial z} \right) \\[2ex] S_E \\[2ex] -\Phi_A \frac{\rho u \bar{\epsilon}_p}{x} \\[2ex] -\Phi_A \frac{\rho u T}{x} \\[2ex] S_{S_{xx}} \\[2ex] S_{S_{xy}} \\[2ex] S_{S_{yy}} \\[2ex] S_{S_{xz}} \\[2ex] S_{S_{yz}} \end{pmatrix}.$$

where

$$S_E = \begin{cases} \frac{\partial}{\partial x} \left(u S_{xx} + v S_{xy} + \Phi_{3D} w S_{xz} \right) + \\[2ex] \frac{\partial}{\partial y} \left(u S_{xy} + v S_{yy} + \Phi_{3D} w S_{yz} \right) + \\[2ex] \Phi_{3D} \frac{\partial}{\partial z} \left(u S_{xz} + v S_{yz} + w S_{zz} \right) - \\[2ex] \Phi_A \left(\frac{u(\rho E + P)}{x} - \frac{u S_{xx} + v S_{xy}}{x} \right) \end{cases} \tag{1.14}$$

$$S_{S_{xx}} = \begin{cases} 2\rho \Omega_{xy} S_{xy} + \Phi_{3D} 2\rho \Omega_{xz} S_{xz} + \\[2ex] 2\rho G \bar{D}_{xx} - \Phi_A \frac{\rho u S_{xx}}{x} \end{cases} \tag{1.15}$$

$$S_{S_{xy}} = \begin{cases} \rho\Omega_{xy}\left(S_{yy} - S_{xx}\right) + \\ \Phi_{3D}\left(\rho\Omega_{xz}S_{zy} - \Omega_{zy}S_{xz}\right) + \\ 2\rho G\bar{D}_{xy} - \Phi_A \frac{\rho u S_{xy}}{x} \end{cases} \tag{1.16}$$

$$S_{S_{yy}} = \begin{cases} 2\rho\Omega_{yx}S_{xy} + \Phi_{3D}2\rho\Omega_{yz}S_{yz} + \\ 2\rho G\bar{D}_{yy} - \Phi_A \frac{\rho u S_{yy}}{x} \end{cases} \tag{1.17}$$

$$S_{S_{xz}} = \Phi_{3D} \begin{cases} \rho\Omega_{xz}\left(S_{zz} - S_{xx}\right) + \\ \left(\rho\Omega_{xy}S_{yz} - \Omega_{yz}S_{xy}\right) + 2\rho G\bar{D}_{xz} \end{cases} \tag{1.18}$$

$$S_{S_{yz}} = \Phi_{3D} \begin{cases} \rho\Omega_{yz}\left(S_{zz} - S_{yy}\right) + \\ \left(\rho\Omega_{yx}S_{xz} - \Omega_{xz}S_{xy}\right) + 2\rho G\bar{D}_{yz} \end{cases} \tag{1.19}$$

where the switch functions Φ_{3D} & Φ_A take the value 1 for three-dimensional and axisymmetric problems respectively. For the two-dimensional problems of interest in this work, the switch function Φ_{3D} is set to zero. The deviatoric strain-rate components used in Eqs 1.15 - 1.19 are given as follows:

$$\bar{D}_{xx} = \frac{\partial u}{\partial x} - \frac{1}{3}\left(\frac{\partial u}{\partial x} + \frac{\partial v}{\partial y} + \Phi_{3D}\frac{\partial w}{\partial z}\right) - \Phi_A\left(\frac{u}{x}\right) \tag{1.20}$$

$$\bar{D}_{yy} = \frac{\partial v}{\partial y} - \frac{1}{3}\left(\frac{\partial u}{\partial x} + \frac{\partial v}{\partial y} + \Phi_{3D}\frac{\partial w}{\partial z}\right) - \Phi_A\left(\frac{u}{x}\right) \tag{1.21}$$

$$\bar{D}_{xy} = \bar{D}_{yx} = D_{xy} = \frac{1}{2}\left(\frac{\partial u}{\partial y} + \frac{\partial v}{\partial x}\right) \tag{1.22}$$

$$\bar{D}_{xz} = \bar{D}_{zx} = D_{xz} = \frac{1}{2}\left(\frac{\partial u}{\partial z} + \frac{\partial w}{\partial x}\right) \tag{1.23}$$

$$\bar{D}_{yz} = \bar{D}_{zy} = D_{yz} = \frac{1}{2}\left(\frac{\partial v}{\partial z} + \frac{\partial w}{\partial y}\right) \tag{1.24}$$

The evolution of effective plastic strain ($\bar{\epsilon}_p$) and temperature (T) (in conservative form)

included in the governing equations are given by:

$$\frac{\partial \rho \bar{\epsilon}_p}{\partial t} + \vec{\nabla} \bullet (\rho \vec{u} \bar{\epsilon}_p) = -\Phi_A \frac{\rho u \bar{\epsilon}_p}{x} \tag{1.25}$$

$$\frac{\partial \rho T}{\partial t} + \vec{\nabla} \bullet (\rho \vec{u} T) = \frac{k}{c} \left(\nabla^2 T - \alpha \left(3\lambda + 2\mu \right) T_o \dot{\epsilon}_{kk}^e + \beta \dot{W}_p \right) - \Phi_A \frac{\rho u T}{x} \tag{1.26}$$

where in Eq 1.25 the plastic deformation (D_{ij}^P) is neglected in the elastic predictor step. Eigenvalue analysis for the (one-dimensional) system of equations conducted in [194], reveal that the Eigenvalues are real for the problems of interest in this work. In the one dimensional set up, the Eigenvalues of the system of equations are $\lambda_1 = \lambda_2 = \lambda_3 = u, \lambda_4 = u + c$ & $\lambda_5 = u - c$, where c is the speed of sound.

1.3.3 Equation of State (E.O.S)

Closure for the set of governing equations is obtained by modelling the dilatational (pressure) response of the material using a suitable equation of state. For this purpose, the pressure P, specific internal energy e and specific volume ($V = \frac{1}{\rho}$) are related through a relation of the form:

$$P(e, V) \approx \Gamma(V) \frac{(e - e_c(V))}{V} + P_c(V) = \Gamma \frac{e}{V} + f(V) \tag{1.27}$$

where e_c and P_c denote the reference specific internal energy and pressure at 0 K. The E.O.S shown in Eq 1.27 is the incomplete Mie-Grüneisen formulation [190]. Eq 1.27 can also be viewed as the first-order approximation of the state surface in the neighborhood of the measured Hugoniot curve along an isochoric path [83]. $\Gamma(V)$ in Eq 1.27 is the Grüneisen parameter defined as

$$\Gamma(V) = V \left(\frac{\partial P}{\partial e}\right)|_v = \frac{\Gamma_0 \rho_0}{\rho} \tag{1.28}$$

where ρ_0 is the density of the unstressed material. As pointed out in [83], it is important to note that the Mie-Grüneisen formulation is not applicable for problems with phase change.

The overall pressure is expressed as the sum of thermal excitation and attractive/repulsive forces in the lattice atoms [190]. Accommodating for negative pressure (tension) and preserving the positivity of sound speed-squared, the function $f(V)$ in Eq 1.27 is written as

$$f(V) = \begin{cases} \frac{\rho_0 c_0^2 \Phi}{(1 - s\Phi^2)^2}[1 - \frac{\Gamma}{2V}(V_0 - V)] \text{ if } V \leq V_0 \\ \\ c_0^2(\frac{1}{V} - \frac{1}{V_0}) \text{ if } V > V_0 \end{cases} \tag{1.29}$$

In the above expression, the constants c_0 is the bulk sound speed and s is related to the isentropic pressure derivative of the isentropic bulk modulus [190]. The c_0 & s coefficients relate the shock speed U_s and the particle velocity U_p. Experiments on solids provide a relation between U_s and U_p. A first approximation consists of a linear relation given as

$$U_s = c_o + sU_p \tag{1.30}$$

The expression for the speed of sound in the material is then given by

$$c^2 = \frac{\partial P}{\partial \rho}|_e + \frac{P}{\rho^2}(\frac{\partial P}{\partial e})|_\rho = \Gamma e + f'(V) + \Gamma \frac{P}{\rho} \tag{1.31}$$

The parameters for the Mie-Grüneisen E.O.S. for some of the commonly used materials are given in Table 1.1. For additional details regarding the equation of state the reader may refer to [12, 190] and the references cited therein.

1.3.4 Radial Return Mapping Algorithm

The plastic deformation of material is governed by the yield function that constrains the stress to remain on or within the elastic domain [143]:

$$f\left(S_{ij}, \alpha_k\right) \leq 0 \Rightarrow \text{admissible stress state} \tag{1.32}$$

$$f\left(S_{ij}, \alpha_k\right) > 0 \Rightarrow \text{inadmissible stress state} \tag{1.33}$$

where f is a generic yield function and α_k is the scalar or tensor hardening parameter [105]. In the traditional operator splitting algorithms, if the predicted "trial" elastic state (determined by freezing the plastic flow) falls within the yield surface, i.e. $f < 0$, then the deformation is purely elastic and the final stress state is indeed the predicted trial state. The yield and the subsequent plastic flow is said to occur when $f = 0$. The inadmissible trial state for $f > 0$ is corrected by bringing the stress back to the yield surface, i.e. by enforcing the consistency condition $f = 0$, along a direction normal to the yield surface ($\frac{\partial f}{\partial \sigma_{ij}}$, Figure 1.7). Conventionally, the return mapping to obtain the final corrected stress state is effected by classical radial return algorithms [130, 142, 143, 164, 165]. In this work, the algorithm due to Ponthot et al [142, 143] is adopted and is explained below.

The radial return algorithm due to Ponthot et al [142, 143] is based on the J_2 Von-Mises flow theory which assumes the existence of a yield function (for isotropic materials) of the form

$$f(S_{ij}, \sigma_Y) = S_e - \sigma_Y = 0 \tag{1.34}$$

with linear hardening law given by:

$$\dot{\sigma}_Y = \sqrt{\frac{2}{3}} h \Lambda \tag{1.35}$$

where σ_Y is the current yield stress (determined from material models discussed in section 1.3.5) and h (also called plastic modulus) is the slope of the effective stress versus effective plastic strain curve under uniaxial loading. Using Eq 1.10, the yield stress can be written as

$$\dot{\sigma}_Y = h\bar{\dot{\epsilon}}_{ij}^P \tag{1.36}$$

When elastic deformation occurs, $f < 0$ and $\Lambda = 0$. Plastic deformation is said to occur when the consistency condition holds true, $\dot{f}(S_{ij}, \sigma_Y) = 0$. Thus, for elastic and plastic deformation, f and Λ can be obtained from the Kuhn-Tucker conditions of optimization theory [143, 164, 165]:

$$\Lambda f = 0, \Lambda \geq 0, f \leq 0 \tag{1.37}$$

In conjunction with the operator splitting algorithm, deviatoric stress update

$$\dot{S}_{ij} + S_{ik}\Omega_{kj} - \Omega_{ik}S_{kj} = 2G\left(\bar{D}_{ij} - \bar{D}_{ij}^P\right) \tag{1.38}$$

is split into two parts - predictor and corrector steps. The predicted trial elastic state "tr" is obtained by freezing the plastic flow ($\bar{D}_{ij}^P = 0$),

$$\dot{S}_{ij,tr} + S_{ik,tr}\Omega_{kj} - \Omega_{ik}S_{kj,tr} = 2G\bar{D}_{ij} \tag{1.39}$$

where $S_{ij,tr}$ is the trial elastic stress tensor. The trial elastic state is determined by numerically integrating the governing equations (Eq 1.13). The plastic corrector step is enforced to bring the computed trial stress back to the yield surface:

$$\dot{S}_{ij,cor} = -2GD_{ij}^P = -2G\Lambda N_{ij} \tag{1.40}$$

where $S_{ij,cor}$ is the corrected stress update and N_{ij} is the normal direction in which the return mapping is effected:

$$N_{ij} = \frac{S_{ij,tr}}{\sqrt{S_{kl,tr}S_{kl,tr}}} \tag{1.41}$$

In discrete form, the plastic corrector step can be obtained by integrating Eq 1.40 (by holding the global configuration fixed) to obtain

$$S_{ij,cor} = S_{ij,tr} - 2GN_{ij,tr}\zeta \tag{1.42}$$

where $\zeta = \int_{t_0}^{t_1} \Lambda dt$, with t_0 and t_1 denoting the beginning and end of the time interval of integration. The parameter ζ is determined by enforcing the generalized consistency condition, $f = 0$, at time t $= t_1$.

$$f = \sqrt{\frac{3}{2}\left[(S_{ij,tr} - 2GN_{ij,tr}\zeta)(S_{ij,tr} - 2GN_{ij,tr}\zeta)\right]} = 0 \tag{1.43}$$

Integrating Eqs 1.10 & 1.36 in time, we get

$$\bar{\epsilon}_1^P = \bar{\epsilon}_0^P + \sqrt{\frac{2}{3}}\zeta \tag{1.44}$$

$$\sigma_Y^1 = \sigma_Y^0 + \sqrt{\frac{2}{3}}h\zeta \tag{1.45}$$

where "0" and "1" denote the values at t_0 and t_1, respectively. Substituting for σ_Y^1, Eq 1.43 is simplified

$$\left(4G^2 - \frac{4}{9}\right)\zeta^2 - \left(4G\sqrt{S_{ij,tr}S_{ij,tr}} + \frac{4}{3}\sqrt{\frac{2}{3}}h\right)\zeta + \left(S_{ij,tr}S_{ij,tr} - \frac{2}{3}\sigma_Y^{0^2}\right) = 0 \quad \tag{1.46}$$

to obtain

$$\zeta = \frac{\sqrt{S_{ij,tr}S_{ij,tr}} - \frac{2}{3}\sigma_Y^0}{2G\left(1 + \frac{h}{3G}\right)} \tag{1.47}$$

Thus, once ζ is obtained, the correction of the predicted deviatoric stresses is performed using Eq 1.40 and the consistency condition is enforced.

1.3.5   Material Models

Material models are required to determine the flow (yield) stress to enforce the consistency conditions in the return mapping algorithm. The two main models used in this work for strain hardening materials are the rate independent Prandtl-Ruess material model [105] (Eq 1.48) and thermal softening based Johnson-Cook material model [99] (Eq 1.49), given as:

$$\sigma_Y = A + B(\bar{\epsilon}^P)^n \tag{1.48}$$

$$\sigma_Y = \left(A + B(\bar{\epsilon}^P)^n\right)\left(1 + Cln\left(\frac{\dot{\bar{\epsilon}}^P}{\dot{\bar{\epsilon}}_0^P}\right)\right)(1 - \theta^m) \tag{1.49}$$

where A, B, C, n, m, $\dot{\bar{\epsilon}}_0^P$ are model constants and $\theta = \frac{T-T_0}{T_m-T_0}$, where T_m and T_0 are material melting and the reference room temperatures respectively. The specific values of the parameters used in the Johnson-Cook model are given in Table 1.2. In the Johnson-Cook material model (Eq 1.49), the flow stress σ_Y, increases with an increase in effective plastic strain and effective plastic strain-rate and decreases with an increase in temperature [190]. The yield stress in fact approaches zero as the temperature approaches the melting temperature of the material.

1.4   Local Mesh Refinement

A crucial aspect of this thesis is the resolution of dominant structures and disparate length scales present in the computational domain. As mentioned before, a tree-based Local Mesh Refinement (LMR) scheme is used for grid adaptation. In contrast to traditional grid adaptation approaches [26, 82, 196], the LMR scheme sub-divides each cell that is tagged for refinement to form four (quadtree in two dimension) or eight (octree in three

dimensions) child cells resulting in highly unstructured mesh. Since each cell is created and destroyed individually, the LMR scheme does not require constant re-meshing and update of the global mesh. As the resulting mesh is unstructured, the hierarchical data structure associated with LMR scheme contains neighbor and parent-child connectivity information stored in the cell structure. With hierarchical data structure the grid refinement and coarsening operations are trivial to accomplish. Furthermore, as the LMR scheme does not require optimized rectangular patches of mesh, fewer mesh points are used in the computation resulting in significant savings in computational memory and on a Cartesian mesh, features that are misaligned with the mesh can be captured by mesh refinement tangent to the feature. Unlike the AMR approach, the flow field is evolved only on the finest (undivided) cells (termed leaf cells in LMR terminology). Thus the solution for every time step is achieved in a single sweep of solution step making the LMR scheme more attractive than its counterpart. Since the flow field is evolved only on the leafcells, no special treatment is required for points near the embedded interface and the numerical scheme can be uniformly integrated throughout the computational domain. The coupling algorithm, refinement criterion to trigger refinement and coarsening operations, along with the effectiveness of the LMR approach are discussed at length in chapter 2.

1.5   Tracking of Embedded Interface

1.5.1   Implicit Interface Representation Using Level sets

Sharp interface treatment requires tracking and representation of material interfaces as the underlying global mesh does not conform to the shape of the interface. In this

work, level sets introduced by Osher and Sethian [137] are used to represent the embedded interface. The value of the level set field, ϕ_l, at any point is the signed normal distance from the lth embedded interface with $\phi_l \leq 0$ inside the immersed boundary and $\phi_l > 0$ outside. The interface is implicitly determined by the zero level set field, i.e., the $\phi_l = 0$ contours represent the lth immersed boundary. The levelset field is defined only in a small neighborhood of the interface ($\phi_l = 0$ contours) called the *narrow band*. For interfaces representing bubbles, droplets and elasto-plastic solids that undergo large deformations, the level set field is advected using the traditional level set advection equation [161, 162].

$$\frac{\partial \phi_l}{\partial t} + \vec{V}_l \cdot \vec{\nabla} \phi_l = 0, \tag{1.50}$$

where $\vec{V}_l$ denotes the level set velocity field for the lth embedded surface. A fourth-order ENO scheme for spatial discretization and a fourth-order Runge-Kutta time integration are used in solving the level set advection equation. The velocity of the levelset field $\vec{V}_l$, is defined only on the embedded interface (the zero-levelset contours). The value of velocity field at the grid points that lie in the narrow band around the zero-levelset is determined by solving the extension equation [15] to steady state as given below:

$$\frac{\partial \Psi}{\partial \tau} + H(\phi_l)\vec{n} \cdot \vec{\nabla} \Psi = 0 \tag{1.51}$$

where Ψ is the variable extended across the interface, τ is the pseudo-time and $H(\phi_l)$ is the unit Heaviside function defined as

$$H(\phi_l) = \begin{cases} 0 \text{ if } \phi_l \leq 0.0, \\ 1 \text{ if } \phi_l > 0.0. \end{cases}$$

A reinitialization procedure [179] is initiated at regular intervals to enforce the condition $|\vec{\nabla}\phi_l| = 1$. The reinitialization of the levelset field is effected by solving the following equation to steady state:

$$\frac{\partial \phi_l}{\partial \tau} + \vec{w} \cdot \nabla \phi_l = sign(\phi_l) \tag{1.52}$$

where

$$\vec{w} = sign((\phi_l)_0)\frac{\nabla(\phi_l)_0}{|\nabla(\phi_l)_0|}$$

$$sign((\phi_l)_0) = \frac{(\phi_l)_0}{\sqrt{(\phi_l)_0^2 + \Delta x^2}}$$

with initial condition $\phi_l(\vec{x}, 0) = (\phi_l)_0(\vec{x})$ For the case of embedded (rigid) solid objects considered in this work, the level set field is reconstructed by advancing the center of mass based on the net (pressure) force acting on the body:

$$\rho_s \forall_s \frac{d^2\vec{x}_{cm}}{dt^2} = \int_s P\hat{n}_l da \tag{1.53}$$

where $\rho_s, \forall_s$ & $\vec{x}_{cm}$ are the density, volume and the coordinates of the center of mass of the embedded rigid object. The normal vector ($\hat{n}_l$) in equation (1.53) and the curvature (κ_l) at the interface can be computed from the level set field according to

$$\hat{n}_l = \frac{\vec{\nabla}\phi_l}{\|\vec{\nabla}\phi_l\|}, \tag{1.54}$$

$$\kappa_l = -\vec{\nabla} \cdot \hat{n}_l, \tag{1.55}$$

For other relevant details regarding the implementation of level set methods, the reader is referred to the literature [137, 160].

1.5.2   Classification of Grid Points

The grid points on the Cartesian mesh can be classified as *bulk points* and *interfacial points*. The points which lie immediately adjacent to the interface are tagged as interfacial points as shown in Figure 1.8. Identification of interfacial points is straightforward with the level set field. If $\phi_{curr}\phi_{nbr} \leq 0$, where the subscript $curr$ denotes the current point and nbr denotes the neighboring point, then the current and the neighboring point are tagged as interfacial points. All the other points are classified as bulk points. A band of ghost points are defined for each phase of the interacting media as shown in Figure 1.8. The ghost point band typically extends up to 4 max(Δx,Δy) distance from the interface. Again, the level set field can be used to define the band of ghost points. The set of ghost points which are immediately adjacent to the interface are tagged as *interfacial ghost points* similar to the regular interfacial points.

1.6   Ghost Fluid Method (GFM)

One of the main highlights of this thesis is the development a general framework for treating embedded interfaces subject to intense loading conditions. For this purpose, the Ghost Fluid Method (GFM) due to Fedkiw et al [58] is employed to capture the interface conditions. The Ghost Fluid Method was first proposed by Glimm et al [67], later adopted by Fedkiw et al [58], and is frequently employed to treat compressible flow problems with embedded interfaces. The GFM formulated by Fedkiw and co-workers provides a simple framework to inject the boundary conditions for sharp representation of discontinuities [133]. The central idea is the definition of a band of ghost points corresponding

to each phase of the interacting materials. For instance, consider the case of two materials separated by an interface as shown in Figure 1.9. Once the set of ghost field is identified and defined with flow conditions, the two-material problem can be converted to two, single-material problem consisting of the respective real field and the corresponding ghost field. Thus, effective communication with the flow solver can be achieved by suitably populating these ghost points with flow properties such that the real field together with the corresponding ghost field depict the interface properties and conditions precisely.

1.6.1 The Basic Mechanism of the GFM

The first step in the GFM approach is to identify the band of ghost points corresponding to each phase of the interacting materials. The band of ghost points can be easily identified based on the sign of the level set field. For instance, in the one-dimensional setup shown in Figure 1.10, the ghost points for the two interacting fluids can be identified based on the change in sign of the level set field across the interface. Once the band of ghost points are determined, the next step is to infuse these band of ghost points with appropriate flow conditions. For the case of the interface that separates two-fluids (Figure 1.10), the following approach was adopted in [58]. In [58], the ghost cells were populated based on the fact that the pressure and velocity are continuous across the contact discontinuity. This enables the pressure and velocity to be directly copied from the real field onto the ghost fluid. Since the entropy advects with material velocity (corresponding to the characteristic wave traveling with fluid/particle velocity), there is no entropy exchange between the two fluids. This allows the entropy to be extended to the ghost points (isobaric fix) which can

then be used to compute the density for the ghost points (Figure 1.10). Thus with the in-fused ghost-field and the corresponding real field the two-fluid problem can now be solved as two single-fluid problem.

1.6.2 Defining the Ghost States

In the original GFM approach [58] described in the previous section, a methodology was formulated to populate ghost points that apply particularly for interfaces separating fluid media. In this work, the GFM approach is extended to resolve interfaces separating materials with varied stiffness. In general, for any surface of discontinuity (nonlinear shock wave or linear contact discontinuity), such as Ω_0 in Figure 1.11, the following jump relations in mass, momentum and energy (Eqs 1.56 - 1.58) hold true (for any point on Ω_0):

$$[\rho(\vec{u} - \vec{u}_I)\bullet\hat{n}] = 0 \tag{1.56}$$

$$[\rho\vec{u}(\vec{u} - \vec{u}_I)\bullet\hat{n} - \hat{n}\bullet\sigma] = 0 \tag{1.57}$$

$$[\rho E(\vec{u} - \vec{u}_I)\bullet\hat{n} - \hat{n}\bullet\sigma\bullet(\vec{u} - \vec{u}_I) + q_n] = 0 \tag{1.58}$$

where $\vec{u}$ and $\vec{u}_I$ are the flow velocity and the velocity of the discontinuity and q_n is the heat flux crossing the interface. Denoting the values immediately ahead of and behind the discontinuity as (R) and (L), the jump relation for any quantity Ψ, is given as

$$[\Psi] = \Psi^R - \Psi^L \tag{1.59}$$

When $[\Psi] = 0$, the quantity Ψ is conserved (continuous), otherwise the quantity is discontinuous. It is desirable to populate the ghost points by solving the mass, momentum and energy jump relations across the embedded material interface. As noted in [58], due to

the linear degeneracy associated with material interface, the solution for the jump relations (Eqs 1.56 - 1.58) is not straightforward. In fact for a material interface the jump relations are trivially satisfied [58]. However, depending on the type and strength of the materials enclosed/separated by the interface, the jump relations can be simplified such that the resulting set of equations can be solved to define the ghost states.

1.6.2.1 Conditions Enforced at the Interface Separating Fluid Media

By definition, fluids are materials that offer negligible resistance to external shear or torsional loading. Neglecting the material-strength associated with shear/torsional loading, the conservative variables and fluxes in the governing equations (Eq 1.13) reduce to

$$\vec{U} = \begin{pmatrix} \rho \\ \rho u \\ \rho v \\ \rho w \\ \rho E \end{pmatrix}, \vec{F} = \begin{pmatrix} \rho u \\ \rho u^2 + p \\ \rho uv \\ \rho uw \\ u\left(\rho E + p\right) \end{pmatrix}, \vec{G} = \begin{pmatrix} \rho v \\ \rho uv \\ \rho v^2 + p \\ \rho vw \\ v\left(\rho E + p\right) \end{pmatrix}, \vec{H} = \begin{pmatrix} \rho w \\ \rho uw \\ \rho vw \\ \rho w^2 + p \\ w\left(\rho E + p\right) \end{pmatrix}.$$

In the above equations, the terms corresponding to the constitutive equations for modelling the deviatoric response of the material are neglected. However, the dilatational response of the material is retained and is governed by an E.O.S. of the form given in Eq 1.27. Simplifying Eq 1.27, we get

$$P = \rho e(\gamma - 1) - \gamma P_\infty, \tag{1.60}$$

where $\gamma = \Gamma + 1$ is the specific heat ratio and P_∞ is a material dependent constant [43]. For the case of ideal gas we have $\gamma = \frac{c_p}{c_v}$ and $P_\infty = 0$. For fluids like water, the Grüneisen exponent and the material dependent constant take the values of 4.5 and 0.613 GPa respectively.

From the definition of sound speed,

$$c = \sqrt{\frac{\gamma(P + P_\infty)}{\rho}}. \tag{1.61}$$

For embedded fluid objects such as droplets, bubbles etc. immersed in strongly shocked flows, it has been well established that the original approach due to Fedkiw et al [58] for the definition of ghost states failed to maintain a non-oscillatory pressure field, particularly when strong shock and detonation waves reside in close proximity to the interface [118]. During the few time steps when the shock and the interface are coincident, the interface treatment technique should temporarily reduce to a shock tracking method. Therefore, in this regard, the Rankine-Hugoniot (R-H) jump conditions must be solved across the interface to define the ghost states. Thus, with the modified governing equations and the E.O.S., the jump relations (Eqs 1.56 - 1.58) are simplified to obtain:

$$[\rho\tilde{u}] = 0 \Rightarrow \rho_L\tilde{u}_L = \rho_R\tilde{u}_R \tag{1.62}$$

$$[\rho\tilde{u}^2 + P] = 0 \Rightarrow \rho_L\tilde{u}_L^2 + P_L = \rho_R\tilde{u}_R^2 + P_R \tag{1.63}$$

$$[\tilde{u}(\rho E + P)] = 0 \Rightarrow \tilde{u}_L(\rho_L E_L + P_L) = \tilde{u}_R(\rho_R E_R + P_R) \tag{1.64}$$

$$\tilde{u}_{L|R} = \vec{u}_{L|R}\cdot\hat{n} - U_s \tag{1.65}$$

The R-H jump equations given in Eqs 1.62 - 1.64, are cast in a reference frame attached to the material discontinuity, and the jump relations are solved assuming that the shock and the material discontinuity are coincident. The nature of the reflected and the refracted waves could be shock waves or rarefaction waves or both, and can be determined from the solution of the R-H jump conditions at the interface. The existence and the uniqueness of the solution for the set of (hydrodynamic) jump relations are well established [189].

Exact and approximate solutions (Riemann solvers) for the system of algebraic equations are available and have been well documented [189]. The ghost states defined with the solution obtained from such Riemann solvers satisfy the jumps in mass, momentum and energy conservation laws and also respect the nature of the wave interactions occurring at the material interface. The approach developed to construct the Riemann problem at the interface is discussed in detail in chapter 3 of this thesis.

1.6.2.2 Conditions Enforced at the Interface Separating Elasto-Plastic Material from other media

For materials with moderate to large material-strength, such as elasto-plastic solids, the governing equations (Eq 1.13) along with the constitutive relations are solved in its entirety. Hence, unlike the case of embedded fluid objects, a Riemann solver based solution is not readily available for the jump relations (Eqs 1.56 - 1.58). Obtaining an exact solution for the system of equations (Eqs 1.56 - 1.58) is far fetched particularly for the complex E.O.S such as the Mie-Grüneisen E.O.S. employed in the present work.

Alternatively, since the high speed multi-material interaction phenomena are dictated by the propagation of nonlinear waves and their interaction with the material interface, the ghost states can be defined such that they are in line with the wave-interface interaction phenomena. For instance, a compressive wave incident on a free surface is reflected as a tensile wave and vice-versa. In the hydrodynamic case, the wave interaction phenomena are resolved by solving the R-H jump conditions at the interface. For elasto-plastic material, the wave-reflection and refraction phenomena are captured by enforcing one or more

of the following conditions at the material interface:

- Continuity of normal velocity component:

$$[\vec{u} \cdot \hat{n}] = 0 \tag{1.66}$$

- Discontinuity in density and tangential velocity components:

$$[\rho] \neq 0 \tag{1.67}$$

$$[\vec{u} \cdot \hat{t}_1] \neq 0 \tag{1.68}$$

$$[\vec{u} \cdot \hat{t}_2] \neq 0 \tag{1.69}$$

- Discontinuity in tangential stress components:

$$[\tilde{\sigma}_{t_1 t_1}] \neq 0 \tag{1.70}$$

$$[\tilde{\sigma}_{t_1 t_2}] \neq 0 \tag{1.71}$$

$$[\tilde{\sigma}_{t_2 t_2}] \neq 0 \tag{1.72}$$

- Traction-based condition for normal stress components:

  1. For material-void interface i.e. for interfaces that separate elasto-plastic materials from voids (free-surfaces), zero-traction condition (or alternatively wave reflection condition) is enforced at the interface:

$$\tilde{\sigma}_{nn} = 0 \tag{1.73}$$

$$\tilde{\sigma}_{nt_1} = 0 \tag{1.74}$$

$$\tilde{\sigma}_{nt_2} = 0 \tag{1.75}$$

$$[P] \neq 0 \tag{1.76}$$

2. For (elasto-plastic) material - (elasto-plastic) material interface, continuity of normal stress is enforced:

$$[\tilde{\sigma}_{nn}] = 0 \tag{1.77}$$

$$[\tilde{\sigma}_{nt_1}] = 0 \tag{1.78}$$

$$[\tilde{\sigma}_{nt_2}] = 0 \tag{1.79}$$

$$[P] = 0 \tag{1.80}$$

3. For FSI coupling i.e. for interfaces separating elasto-plastic solids from fluids, continuity of normal stress is enforced in the following manner:

$$\tilde{\sigma}_{nn}^{EP} + P^{EP} = P^L \tag{1.81}$$

$$\tilde{\sigma}_{nt_1}^{EP} = 0 \tag{1.82}$$

$$\tilde{\sigma}_{nt_2}^{EP} = 0 \tag{1.83}$$

$$[P] \neq 0 \tag{1.84}$$

where the subscripts EP and L denote the elasto-plastic and the liquid material respectively.

4. For interfaces separating elasto-plastic material and rigid solids, the discontinuity in normal stress components are enforced:

$$[\tilde{\sigma}_{nn}] \neq 0 \tag{1.85}$$

$$[\tilde{\sigma}_{nt_1}] \neq 0 \tag{1.86}$$

$$[\tilde{\sigma}_{nt_2}] \neq 0 \tag{1.87}$$

$$[P] \neq 0 \tag{1.88}$$

In addition to the above conditions, the normal velocity at the interface is modified as

$$\vec{u} \cdot \hat{n} = U_n \tag{1.89}$$

where U_n is the normal velocity of the rigid solid object.

The total stress tensor in the normal and tangential coordinates ($\tilde{\sigma}$) is given by

$$\tilde{\sigma} = \mathbb{J} \sigma \mathbb{J}^T \tag{1.90}$$

where

$$\mathbb{J} = \begin{pmatrix} n_x & n_y & n_z \\ t_{1x} & t_{1y} & t_{1z} \\ t_{2x} & t_{2y} & t_{2z} \end{pmatrix} \tag{1.91}$$

is the Jacobian matrix, and $\hat{n}$, $\hat{t}_1$ & $\hat{t}_2$ are the local normal and tangential vectors defined at the interface. The ghost points are populated with flow properties such that the conditions hold true exactly at the embedded interface. The approach developed to enforce the aforementioned conditions at the interface is discussed in detail in chapter 4 of this thesis.

1.6.2.3 Conditions Enforced at the Interface Separating Rigid Objects

Solids with infinite material-strength, that register negligible deformation under intense loading conditions, are classified as rigid objects. There are significant differences between the treatment of fluid/elasto-plastic materials and rigid solid objects in the ghost fluid framework. For instance, in the case of elasto-plastic materials the flow variables such as velocity and pressure that are continuous across the interface are directly injected into

the ghost field. In the latter case, due to the absence of flow fields on one side of the interface (the solid side), it is not immediately clear how to populate the ghost cells with the virtual flow properties. At the interface of a solid body, the following boundary conditions are to be applied for velocity, temperature and pressure fields

   i. No-penetration condition for the normal velocity :

$$v_n = U_n, \tag{1.92}$$

where U_n is the velocity of the center of mass.

   ii. Slip condition for the tangential velocity:

$$\frac{\partial v_{t_1}}{\partial n} = 0, \tag{1.93}$$

$$\frac{\partial v_{t_2}}{\partial n} = 0, \tag{1.94}$$

   iii. Adiabatic condition for temperature :

$$\frac{\partial T}{\partial n} = 0, \tag{1.95}$$

   iv. Normal force balance on pressure :

$$\frac{\partial p}{\partial n} = \frac{\rho_s v_{t_1}{}^2}{R} - \rho_s a_n, \tag{1.96}$$

where,

$$v_n = \vec{V} \bullet \hat{n}, \tag{1.97}$$

$$v_{t_1} = \vec{V} \bullet \hat{t_1}, \tag{1.98}$$

$$v_{t_2} = \vec{V} \bullet \hat{t}_2 \qquad\qquad (1.99)$$

are the normal and (contravariant) tangential velocities in the body fitted curvilinear coordinate, $\vec{V}$ is the velocity vector in the global Cartesian coordinate, $\hat{n}, \hat{t}_1, \hat{t}_2$ are the normal and tangential vectors, R is the radius of curvature and a_n is the acceleration of the interface. The set of boundary conditions given in Eqs (1.92) - (1.96) govern the behavior of the flow near the embedded solid body and must be enforced on the real fluid by suitably populating the corresponding ghost cells. There are several ways in which this task can be accomplished which is the subject of discussion in chapter 5 of this thesis.

1.7   Numerical Examples

The illustrative numerical examples presented in this work were simulated by solving the governing equations using a third-order TVD-based Runge-Kutta scheme for time integration and third-order convex ENO scheme [120] for spatial discretization. Since the numerical schemes implemented in this work are well established, the implementation details are not presented here. Interested readers may refer to the original articles [120, 163] for details. The purely inviscid Euler equations were non-dimensionalized based on free stream density ρ_∞, pressure p_∞ and the sonic velocity $a_\infty = \sqrt{\frac{p_\infty}{\rho_\infty}}$. Unless stated to the contrary, the standard atmospheric conditions are chosen to non-dimensionalize the governing equations. A suitable length scale is chosen depending on the dimensions of the immersed object. The CFL number was set to 0.6 for all of the simulations presented in this work unless stated to the contrary. Numerical Schlieren images shown in this work

were generated using the method outlined in [147]:

$$\upsilon = e^{-\kappa \frac{\|\nabla \rho\|}{\|\nabla \rho\|_{max}}} \tag{1.100}$$

where κ is a problem-dependent coloring constant and υ is the shade function.

Material	ρ_0	ν	c $\frac{W}{m-K}$	K $\frac{J}{kg-K}$	Γ_0	$c_0 \frac{m}{s}$	S
Copper	8930	0.35	383.5	401	2.0	3940	1.49
Tungsten heavy alloy	17600	0.29	477	38	1.43	4030	1.24
High-hard steel	7850	0.30	134	75	1.16	4570	1.49
Aluminum	2700	0.30	896	166.9	1.99	5386	1.339
HMX	1891	-	1000	0.4	1.1	2058	2.38
Polymer Binder	1100	-	1.00	5.1	1.55	2350	1.7

Table 1.1: Parameters for the Mie-Grüneisen E.O.S. for commonly used materials

Material	Y_0 (GPa)	B (GPa)	N	C	m	G (GPa)	$T_m(K)$
Copper	0.4	0.177	1.0	0.025	1.09	43.33	1358
Tungsten	1.51	0.177	0.12	0.016	1.0	124.0	1777
High-hard steel	1.50	0.569	0.22	0.003	1.17	77.3	1723
Aluminum	0.324	0.114	0.42	0.002	1.34	26.0	925.0
HMX	0.26	NA	NA	NA	NA	NA	NA
Polymer Binder	89.0	NA	NA	NA	NA	NA	NA

Table 1.2: Johnson-Cook material model parameters: A = Y_0, $T_0 = 294K$ and $\dot{\epsilon}_0^P = 1.0s^{-1}$
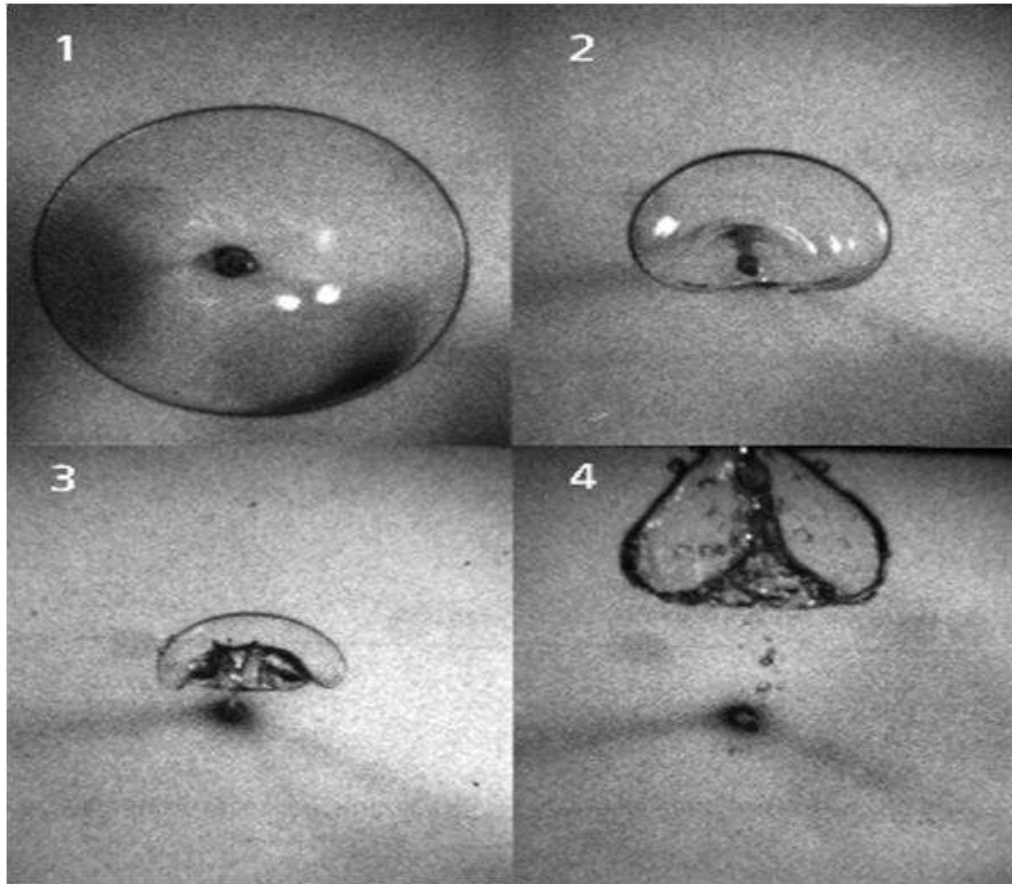
Figure 1.1: Spark-generated bubbles for modeling underwater explosion bubble dynamics. This allows clear observation of re-entrant jet formation inside the bubble, because the explosive detonation products generally occlude the view of the interior of the bubble; Courtesy - Georges L. CHAHINE, Dynaflow, Fulton, MD. Proc. 66th Shock and Vibration Symp., Biloxi, MS (1995). SAVIAC, Arlington, VA (1995), vol. 2, p. 265
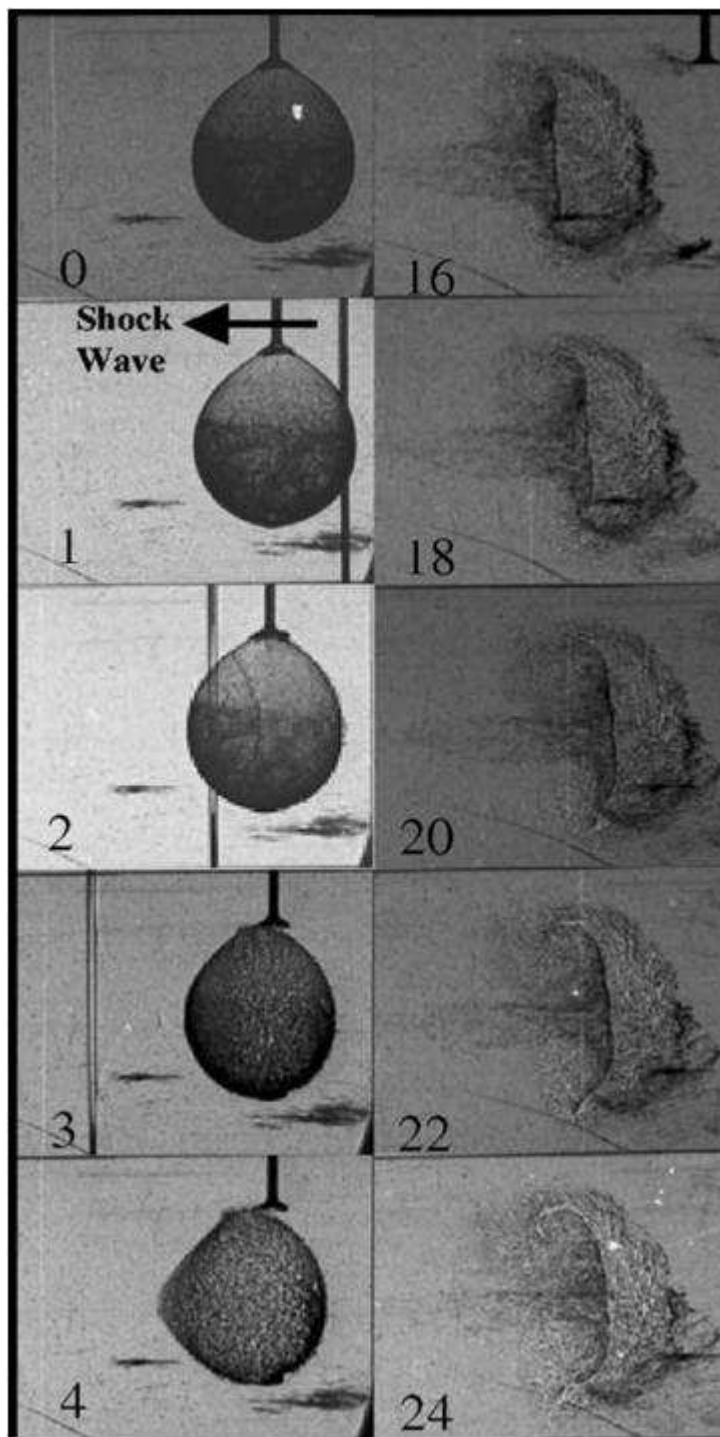
Figure 1.2: Snapshots of deformation of a bubble subject to a planar shock wave.
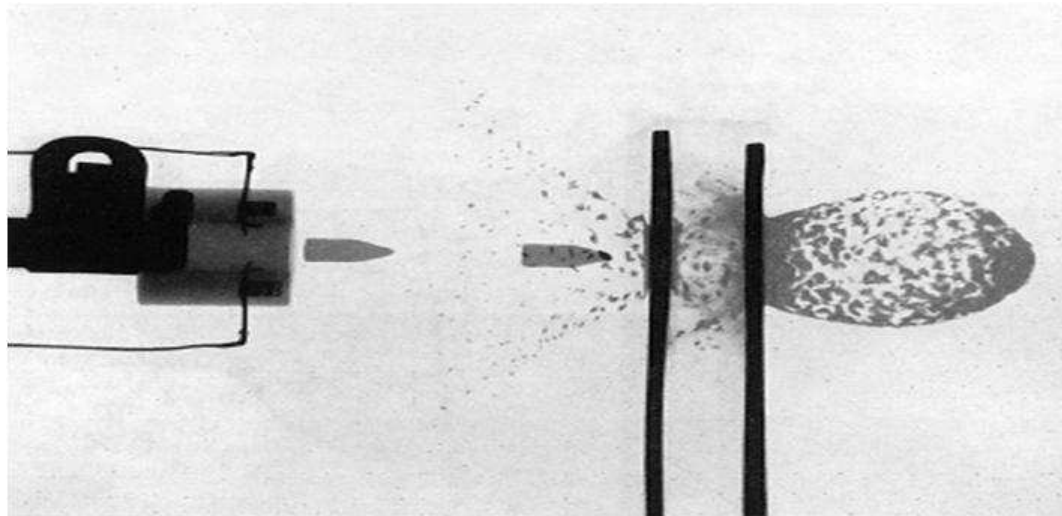
Figure 1.3: Superposition of three flash radiographs showing a sequence of a 30-06 bullet in air penetrating a so-called Whipple shield - a configuration invented in 1946 by the astronomer Fred L. WHIPPLE. It is based on the principle that small meteoroids and orbital debris explode when they strike a solid surface. Courtesy - John P. BARBOUR and associates at Field Emission Corporation in McMinnville, OR. See Proc. 7th Int. Congr. on High-Speed Photography, Zurich (1965). Helwich, Darmstadt (1967), p. 292

Figure 1.4: Crater formation details: Aerial view of Meteor Crater which is 1.2 km in diameter and 200 m deep, officially called "Barringer Crater" that is about 50,000 years old. Photo by David J. RODDY and Karl ZELLER, courtesy USGS

Figure 1.5: Snapshot of shock condensation effect around the jet fighter Boeing F-18 (Hornet) at transonic flight in humid air. It arises during acceleration when the air flow at some parts of the fuselage reaches supersonic speeds. When the resulting shock wave detaches, it builds up a sudden rarefaction that, lowering the temperature, causes condensation of the ambient water vapor.[Courtesy: J. GAY, U.S. Navy] A similar picture was recently taken from an F-4 (Phantom II) during an air show at Point Magu Naval Air Station, CA. (The MilitaryAircraft Archive, http://www.milair.simplenet.com/)

Figure 1.6: Snapshot of the bow shock wave formed due to the supersonic flight of the NASAs new Ares -1X rocket
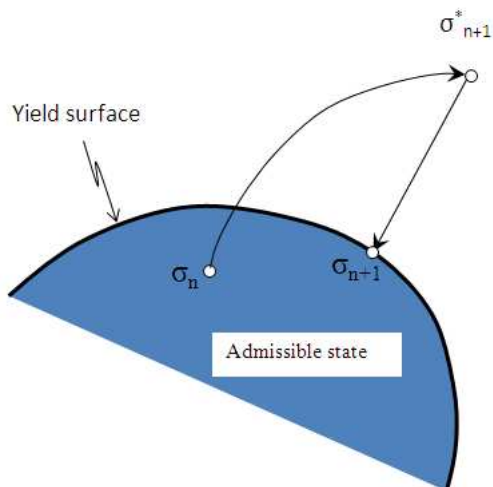
Figure 1.7: Radial Return Algorithm: The predicted stress σ_{n+1}^* lies outside the yield surface. The predicted stress is brought back to the yield surface to obtain the final corrected stress σ_{n+1}, using a return mapping algorithm, along a direction normal to the yield surface $\frac{\partial f}{\partial \sigma_{ij}}$.
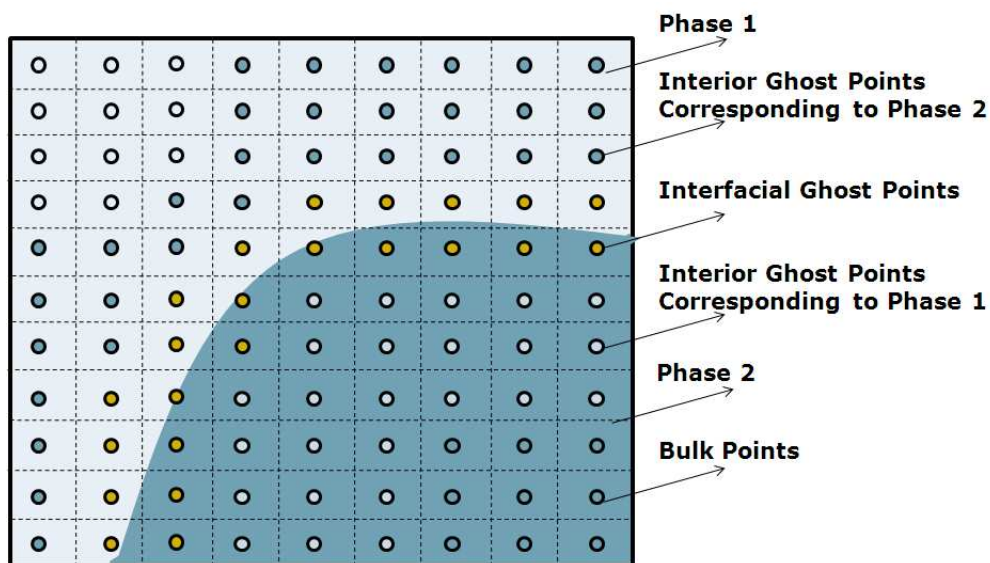
Figure 1.8: Classification of grid points - bulk points, interfacial ghost points and interior ghost points.
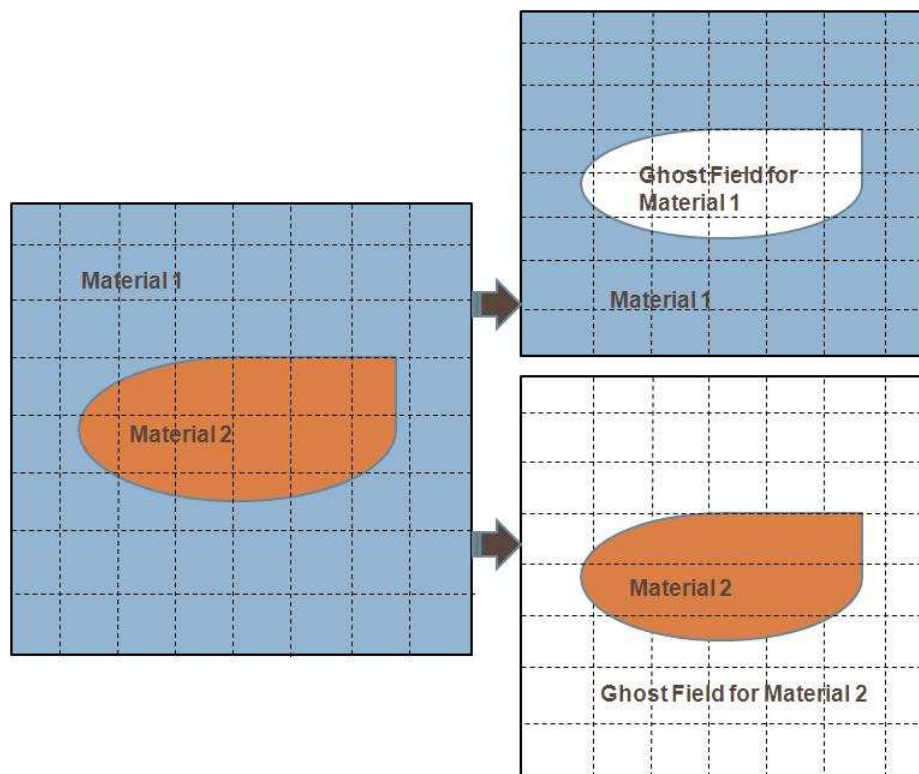
Figure 1.9: The GFM approach converts a two-material problem to two single-material problem
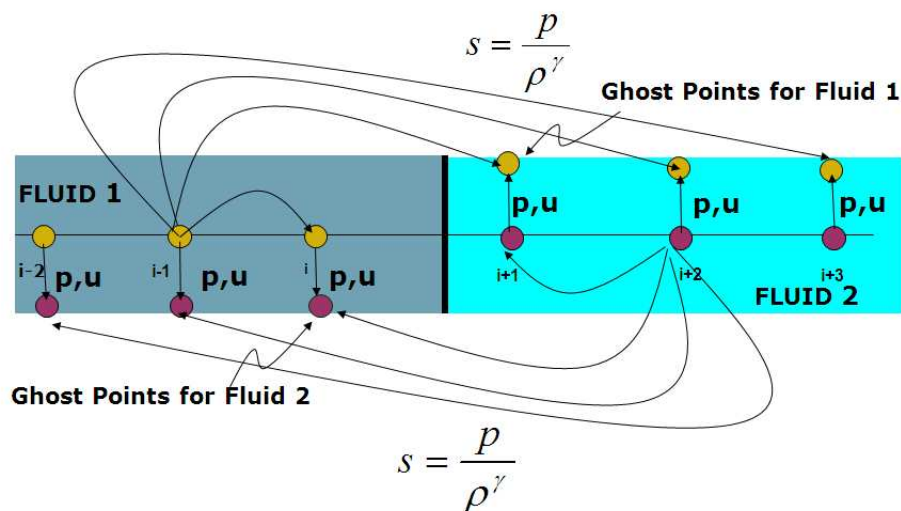
Figure 1.10: The basic mechanism of the Ghost Fluid Method.
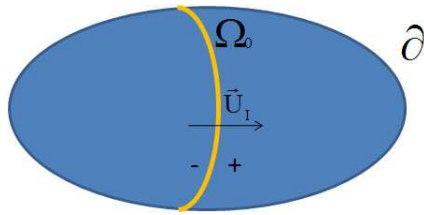
Figure 1.11: Discontinuity Ω_0 (shock or material discontinuity) traveling inside a material bounded by ∂.

CHAPTER 2
LOCAL MESH REFINEMENT

2.1   Introduction

Grid adaptation has gained renewed interest in the last decade since the pioneering work by Berger and co-workers [26, 27]. Adaptivity requires automatic and optimized grid point placement in the domain of interest such that the resulting grid topology significantly reduces computational time and effort. There are several approaches that have been used to accomplish grid adaptation both in compressible [19, 26, 82, 136, 146, 196] and incompressible flows [72, 108, 121, 122, 178]. All of these methods have the same underlying principle of operation. In general, the process of grid adaptation can be described as follows: A fixed base mesh that is fine enough to capture the global flow features is employed as a starting point. Then a suitable refinement criteria (usually first or second gradient gradient-based [108, 191] or in some instances, wavelet-based [32]) is invoked to identify flow structures (such as shock waves, strong rarefaction waves, vorticity, etc.) and embedded objects that are under-resolved. Once such regions are identified, either individual cells encompassing the regions (LMR [108, 191]) or patches of rectangular mesh (AMR [26, 136, 146]) are recursively subdivided until the desired level of refinement is achieved. In essence, the grid adaptation technique judiciously identifies and quarantines fine mesh cells to those regions with active structures and enables the use of coarse grid elsewhere. This results in dramatic savings in memory and processor time.

In this chapter, the GFM-based approach is augmented with the quadtree- (octree-

in three dimensions) based Local Mesh Refinement (LMR) technique developed in [191], for computationally efficient calculations involving strong shock interactions with embedded solid and fluid objects(s) in high speed compressible multiphase flows. It was demonstrated by Berger et al [26], and later by Jameson [93], that a combination of a higher-order scheme and adaptive grid refinement technique is the best strategy, if a solution of reasonable accuracy with least computational overhead is sought [146]. The tree-based mesh adaptation schemes for compressible flows developed in the past used lower-order linear reconstruction technique such as the minimum energy [45] or linear Green-Gauss [45, 207] flux reconstruction technique. In this work, the higher-order aspect for temporal and spatial resolutions are retained by means of a third order TVD-based Runge-Kutta scheme [163] and third order convex ENO scheme [120] respectively. Higher-order schemes such as ENO use wider support cells that demand a conservative approach to compute numerical fluxes at mesh interfaces. Application of third and higher-order ENO/WENO schemes have been proven computationally effective only for uniform and smoothly varying curvilinear meshes [159]. Particularly, limited progress has been made in this direction to couple higher-order schemes with tree-based grid adaptive schemes. Recently, Cecil et al [36] have developed generalized ENO schemes on octree-based unstructured non uniform meshes. However, the applications reported in their work are limited to one-dimensional weak shocks traversing in single fluid medium. The current work focuses on extending such an approach for strong shock applications and to shock-interface interactions. In essence, the following efforts are reported in this chapter:

i. A simple, conservative formulation for accurate computation of ENO-based numer-

ical fluxes at the fine-coarse mesh boundaries in tree-based LMR schemes. The methodology adopted in this work provides a general framework to uniformly integrate the solution throughout the computational domain. Thus, the GFM approach and other interface treatment techniques can be directly employed in the current framerwork.

ii. A refinement criteria is developed for identifying and tagging cells for refinement. Obtaining suitable criteria that simultaneously track strong and weak shocks, rarefaction waves, sliplines and contact discontinuities (material interfaces) is a tricky proposition. The criteria proposed in this work is simple and effective in identifying under-resolved regions.

The broad range of results presented in this work demonstrates the flexibility and robustness of the current method in efficiently resolving dominant features and disparate length scales for a wide spectrum of Mach numbers. Shocks interacting with multiple moving boundaries are also computed.

2.2   Automatic Grid Adaptation Schemes

Among the various mesh enrichment techniques that have been used in the past [26, 82, 121, 196], Adaptive Mesh Refinement (AMR) schemes due to Berger et al [26, 27] have been extensively used for compressible [26, 136, 138, 145], incompressible [72, 126, 151, 178] and astrophysical [30, 41, 104] flow computations. AMR generates blocks of structured, non-overlapping, Cartesian mesh patches over the underlying coarse mesh, and the flow field is evolved on all mesh patches. The two main operations involved in the AMR

technique are the *prolongation* and *restriction* operations [30]. The flow field corresponding to the newly formed mesh at the finer levels are interpolated from the corresponding mesh at coarser levels based on the flow solution from the preceding time step (prolongation operation). Thus in the prolongation operation, information propagates from coarse mesh to fine mesh patches. On the other hand, the evolution of the flow field follows from the finest to the coarsest level (restriction operation); i.e. the flow field is first evolved on the fine mesh patch, and this solution from the fine mesh patch is projected on the coarse mesh patch before computing the flow field on the coarse mesh patch. Thus the AMR scheme requires repeated interpolation back and forth between different grid levels at each time step [191]. As rectangular blocks of structured mesh are formed at every level, the implementation of AMR scheme is less complicated and more straightforward than other methods, and demands no major changes in the data structure. As the flow field is evolved on all grid levels, different time steps could be used for grids at different levels. Hence the smallest time steps are local to the finest levels and is not enforced for the grids at coarser levels.

Although the AMR scheme is attractive and has been proven to be effective for a wide gamut of problems, their applicability for sharp interface calculations involving fluids with high impedance mismatch is not straightforward. The problem lies with the restriction operation which requires interpolation from fine mesh to the coarse mesh patch, and a conservative interpolation at the interface results in mixing of fields and numerical fluxes across the interface in a manner that is detrimental to the overall numerical computation. Nourgaliev et al [136], have identified and demonstrated this potential pitfall of the AMR

approach for interfaces separating fluids of high impedance mismatch. To extend its applicability to sharp interface multiphase flow computations, the AMR approach described in [136] uses a non-conservative Natural Neighbor Interpolation (NNI) [29, 173] method. The NNI approach carefully avoids interpolation across the interface of the embedded object, but results in complications in the implementation that detract from the inherently simple AMR scheme. Alternatively, one could use a generic grid adaptation technique such as the hierarchical tree-based Local Mesh Refinement (LMR) [191] scheme, that does not require the evolution of the flow field on all grid levels. This latter approach is the one elaborated in the present work.

In contrast to the AMR approach, the LMR scheme sub-divides each cell that is tagged for refinement to form four (quadtree in two dimension) or eight (octree in three dimensions) child cells resulting in highly unstructured mesh rather than blocks of rectangular grid patches. Since each cell is created and destroyed individually, the LMR scheme does not require constant re-meshing and update of the global mesh. As the mesh is now unstructured, the hierarchical data structure associated with LMR scheme contains neighbor and parent-child connectivity information stored in the cell structure. With hierarchical data structure the grid refinement and coarsening operations are trivial to accomplish. Furthermore, as the LMR scheme does not require optimized rectangular patches of mesh, fewer mesh points are used in the computation resulting in significant savings in computational memory and on a Cartesian mesh, features that are misaligned with the mesh can be captured by mesh refinement tangent to the feature. Unlike the AMR approach, the flow field is evolved only on the finest (undivided) cells (termed leaf cells in LMR terminology).

Thus the solution for every time step is achieved in a single sweep of solution step making the LMR scheme more attractive than its counterpart. Since the flow field is evolved only on the leafcells, no special treatment is required for points near the embedded interface and the numerical scheme can be uniformly integrated throughout the computational domain.

2.3 Local Mesh Refinement (LMR)

As stated in the previous section, the octree-based mesh refinement schemes are more general but come with an added price of complexity associated with the data structure, and pose significant challenges for algorithmic implementation [121, 122]. However the implementational intricacies associated with octree and quadtree-based LMR schemes have been clearly identified and outlined by Greaves et al [68–71]. The application of octree-/quadtree-based LMR schemes for compressible flows dates back to the work of Zeeuw et al [205–207]. Although LMR-based adaptive schemes have found limited applications for compressible flow computations [36, 44, 45, 50], one may find a multitude of applications pertaining to incompressible flow simulations [7, 108, 121, 122, 128, 144, 169–172, 198]. For compressible flow simulations, AMR schemes have been preferred over LMR approach despite of the potential savings in computational resources. Although the reason for this trend is not apparent, it was pointed out in [121, 122] that spurious and artificial reflected waves were generated with the use of LMR schemes, when waves of large magnitude were allowed to pass through the fine-coarse mesh boundaries [41]. One possible reason for the generation of such spurious waves could be the fact that the low frequency errors on a given fine grid becomes high frequency errors when passed on to coarse grids [207]. As will be

evident from the current work, LMR schemes can be employed effectively by judiciously enforcing refinement criteria that prohibit waves of large magnitude from passing the fine-coarse mesh boundaries. The impact of the wave passage through the fine-coarse mesh interfaces have been carefully examined and further discussion on this topic is deferred to section 2.4.1.1

2.3.1 LMR Terminologies and Hierarchical Data Structure

Since computational cells are created and destroyed locally and individually, implementation of LMR scheme requires compatible data structures for easy cell addition, cell removal, access of neighbor cells and mesh traversal [191]. To facilitate such operations, the most obvious choice is to use a hierarchical (quadtree in two dimensions and octree in three dimensions) data structure that stores cell-connectivity and cell-hierarchy information. When a cell is marked for refinement, it is divided to form four cells in two dimensions or eight cells in three dimensions. The four (eight) new cells formed during the refinement operation are called child cells and the cell which is refined to form these child cells is called the parent cell. The undivided cells at the bottom of the hierarchy/tree level (that has no children) are called the leafcells. It is in these undivided leaf cells in which the flow calculations are evolved. A parent cell can also be coarsened by aggregating its child cells and pruning their branches.

Whenever a cell is coarsened, the child cells are destroyed and the parent cell becomes an undivided leaf cell. Typical representation of the tree structure is displayed in Figure 2.1(a). The data structure used to describe the cell is displayed in Figure 2.1(b).

As shown in Figure 2.1(b), in addition to the the regular cell attributes pertaining to the flow variables, the data structure for individual cell stores pointer information pointing to its parent cell, child cells and to its neighbors. The pointer information for each cell can be updated independently, every time a cell is refined or coarsened. Thus, with the use of a hierarchical data structure, each time a cell is refined or coarsened no global re-meshing is required and the grid adaptation operations are local. Since the flow field is evolved only on the undivided cells, the attributes corresponding to the flow variables need to be stored only on the leaf cells resulting in savings in memory. The hierarchical data structure makes it feasible for easy traversal through the tree to access the parent and child cell information. For ease of computation and to obtain balanced tree distribution, the refined grid is smoothed to ensure that no two neighboring cells have more than one grid-level difference. As pointed out in [167], balancing enables easy navigation through the tree structure to efficiently access neighbor cell information, besides providing equal load distribution [36] and a gradually varying mesh distribution. For additional details pertaining to the implementation of the tree-based LMR scheme in the current context, the reader may refer to [192].

2.3.2   Coarsening and Refinement Operations

Cells are refined and coarsened based on the presence of structures and dominant features in the flow field. As the refinement process is solution adaptive, a base mesh that is fine enough to capture the global flow structure is selected, and the initial level set field is constructed on this base mesh. Once the base mesh is defined, all those cells that

exceed a preset threshold limit of the refinement criteria are tagged, and the refinement operation is carried out on these cells until the desired level of refinement is achieved. The computational cells straddling the interface of the embedded object(s), that lie within the narrow band of the level set field are refined to the maximum level. This eliminates interpolation errors and associated instabilities from being introduced at the interface [167]. Thus initial discontinuities (such as shock and detonation waves) and the cells in the narrow band of the level set field are uniformly refined to the finest level, and are maintained at the finest level throughout the computation. Other flow structures that develop with evolution of the flow field are refined by repeated application of the refinement criteria at regular intervals in time (the interval at which LMR is invoked is determined by the fastest traveling (characteristic) wave in the domain (CFL condition)). In addition, adequate number of buffer cells are provided in refinement zones around strong shock and rarefaction waves. As a band of fine (buffer) cells always surround these flow structures, any new structure formed with the evolution of the flow field will remain within these band of fine cells. This further ensures that interpolations are not performed near discontinuities in the flow field.

Since each time a cell is divided four (eight) new child cells are formed, a constant refinement factor of 2 is maintained i.e. a cell which is recursively refined k times (for $k > 1$) forms 2^k child cells. Therefore, a (child) cell at k^{th} level formed by $k - 1$ recursive divisions of a parent cell will have sides of length $\Delta x = \frac{1}{2^{k-1}} \Delta x_g$, where Δx_g is the size of the base mesh with level 1 denoting the global base mesh (Figure 2.1(a)).

Divided cells that are not tagged for refinement are coarsened. Whenever a cell is coarsened, the flow properties for the parent cell are determined from aggregating the flow

properties from its child cells.

$$\vec{U} = \frac{1}{N_{child}} \sum_{ich=1}^{N_{child}} \vec{U}_{ich} \tag{2.1}$$

where $\vec{U}$ corresponds to the primitive variables and $N_{child} = 4$ for quadtree and $N_{child} = 8$ for octree data structures. The flow attributes for the newly formed child cells are derived from interpolating on the leafcells in the preceding time step. One of the most commonly used approach for child cell interpolation in both LMR and AMR framework is the MUSCL-based interpolation scheme [145, 146]. Cecil et al [36] have used higher-order ENO-based interpolations for defining the flow attributes for the newly created child cells. The ENO-based interpolations for child cells were carried out by choosing stencils along the diagonal and grid directions. In this work, a simple conservative bilinear interpolation due to Berger et al [26] is used to define the flow attributes for the newly created child cells. Noting that the child cells are created and destroyed only at the edges of the buffer cells that surrounds the fine mesh cells encompassing dominant flow features, a simple bilinear interpolation scheme appears to be an obvious choice.

2.3.3   Refinement Criteria

As mentioned before, the refinement criteria identify and tag cells in the regions with distinct structures and steep gradients in the flow field. The refinement criteria is critical for tree-based mesh adaptive schemes particularly when applied to compressible flow calculations, as interpolations between grid levels near discontinuities are not permissible. Such interpolations can be averted if the fine-coarse mesh interface is sufficiently far away from discontinuities and the flow field varies smoothly across the mesh interface.

Berger et al [26,27] employed Richardson extrapolation based estimate of the local trunca-
tion error of the solution, to identify regions with discontinuities. A similar approach was
used in [104] for astrophysical flow computations. In [45,198,207] a statistical description
based on the cell-size-weighted curl and divergence of the velocity field were employed
to identify regions that are excessively compressed and sheared. Flow field gradient-based
(density, velocity and speed of sound) estimates were used in [211] for refining and coars-
ening grid patches. Recently, Karni et al [103] developed a smoothness indicator (SI)
based on weak local truncation error estimate to identify roughness and discontinuities in
the solution. The approach, appears promising, may not be computationally efficient as
wider support stencil and time history (up to three consecutive time levels) are required to
compute the SI.

An ideal refinement criteria must not only tag cells that straddle the discontinuity,
but also tag cells in the vicinity of the discontinuity. This is required to ensure that enough
(buffer) cells are provided to confine discontinuities within the fine grid For any differen-
tiable, Lipschitz continuous function $f(x)$, there exists a unique derivative at the point x_i;
i.e

$$\lim_{x \to x_i^-} \frac{df(x)}{dx} = \frac{df(x)}{dx}\big|_{x_i} = \lim_{x \to x_i^+} \frac{df(x)}{dx} \tag{2.2}$$

In such regions where the function is continuously differentiable, a second order central-
difference estimate will converge with the corresponding second-order one-sided estimates
for the first derivative. On the contrary, for those regions where the function $f(x)$ is dis-
continuous, the central difference scheme based estimate will significantly deviate from
the corresponding one sided estimates of the first derivative. Thus cells enclosing smooth

regions can be effectively segregated from those cells straddling discontinuities by comparing the first derivative estimates. In essence the following steps are performed to identify potential cells for refinement:

- At each cell center, second order one sided and second order central difference based derivatives are evaluated as follows:

$$\frac{df(x)^-}{dx} = \frac{f(x_{i-2}) - 4f(x_{i-1}) + 3f(x_i)}{2\Delta x} + \frac{1}{3}\Delta x^2 \frac{d^3 f(x)}{dx^3}; \ \forall x \le x_i \tag{2.3}$$

$$\frac{df(x)^+}{dx} = \frac{-3f(x_i) + 4f(x_{i+1}) - f(x_{i+2})}{2\Delta x} + \frac{1}{3}\Delta x^2 \frac{d^3 f(x)}{dx^3}; \ \forall x \ge x_i \tag{2.4}$$

$$\frac{df(x)}{dx} = \frac{f(x_{i+1}) - f(x_{i-1})}{2\Delta x} - \frac{1}{6}\Delta x^2 \frac{d^3 f(x)}{dx^3} \tag{2.5}$$

- Since in smooth regions, the one sided estimates approach the central difference scheme based value, the one sided derivatives are compared with the central difference scheme based estimate to obtain

$$\xi_1 = |\frac{df(x)}{dx} - \frac{df(x)^-}{dx}| \tag{2.6}$$

$$\xi_2 = |\frac{df(x)}{dx} - \frac{df(x)^+}{dx}| \tag{2.7}$$

$$\xi_3 = MAX(|\frac{df(x)^-}{dx}|, |\frac{df(x)}{dx}|, |\frac{df(x)^+}{dx}|) \tag{2.8}$$

where ξ_1, ξ_2 & ξ_3 are the estimates of error.

- As the derivatives $\frac{df(x)^-}{dx}$, $\frac{df(x)}{dx}$ & $\frac{df(x)^+}{dx}$ are comparable in smooth regions, the error estimates ξ_1 & ξ_2 are of O(Δx^2). For those regions with discontinuities, the error estimates $max(\xi_1, \xi_2) \ge \delta_1$ or $\xi_3 \ge \delta_2$, where $\delta_1 > 0$ & $\delta_2 > 0$ are user-defined tolerance limits. The criterion δ_1 is primarily used to identify dominant flow structures such as shocks and contact discontinuities, while δ_2 is used for resolving weak

shocks and other weak structures such as expansion waves and sliplines, that may evolve in the flow field. Since shocks and contact discontinuities are O(1) discontinuities, the threshold for the criterion $\delta_1 \approx O(\Delta x)$. As will be shown in the results section, based on the numerical experiments conducted in this work, δ_1 is set in the range $\delta_1 \Delta x_g \approx (\Delta x_g - 1.0)$ where Δx_g is the size of the base mesh. The value of the δ_2 depends on the features and gradients that the user desires to resolve.

The above procedure is repeated along all grid directions. Since the refinement criteria for a point x_i uses points $\{x_{i-2}, x_{i-1}, x_i, x_{i+i}, x_{i+2}\}$ in the neighborhood of x_i, the procedure is highly effective in flagging cells that fall in the vicinity of the discontinuity. Furthermore, in addition to the above refinement criteria, three layers of buffer cells are provided at the fine-coarse mesh boundary to ensure that the discontinuities are confined well within the fine mesh level. Thus, in contrast to the refinement criteria developed in [26, 27], the criterion adopted in this work neither requires data storage at different time levels nor involves complex interpolation at different grid patches/levels. The function f chosen in the current work correspond to the density, pressure and entropy fields that reside at the centers of the computational cells.

2.3.4 Computing ENO Based Numerical Flux at the Mesh Interface

One of the crucial aspects of this work concerns the extension of the higher-order ENO-based flux discretization schemes developed for uniform meshes, to the fine-coarse mesh boundary of the unstructured, adaptive, tree-based mesh refinement schemes. Several unstructured mesh-based ENO schemes have been developed in the past [4, 34] but such

schemes vary in complexity depending on the grid structure [36]. Cecil et al [36] have developed an efficient scheme to construct ENO-based fluxes by identifying ghost points at the mesh interface. The ghost points in turn derived their flow properties from higher-order ENO-based interpolation. The success of this approach is largely dependent on a stringent restriction imposed on the the grid level difference between neighbor cells. In their approach, the neighbor cells and the neighbor of neighbor cells, both in the grid and in the diagonal directions, were prohibited from having more than one level difference. One may have to extend the restriction to many cells for higher-order schemes. In contrast, in the current approach only the neighbor cells along the grid directions are not allowed to have more than one level difference in grid level, and thereby provides easy extension to any desirable order of accuracy. The approach adopted in this work also uses ghost points to construct fluxes at the mesh interface. As mentioned before, since the fine-coarse mesh transitions are designed to lie away from significant gradients in the flow and occupy a lower-dimensional space in the computational domain, a (conservative) bilinear interpolation scheme is found to be adequate to obtain the values at these ghost points. Moreover, with bilinear interpolation, extension to three-dimensions is straightforward. Details pertaining to the ENO-based flux construction approach for a uniform mesh distribution are discussed in [190, 192]; the generic procedure for constructing the ENO-based numerical fluxes at the fine-coarse mesh interface is outlined below.

2.3.4.1   Flux Construction for a Cell that is finer than its Neighbor

Consider the typical case of the coarse-fine mesh boundary as shown in Figure 2.2(a). In Figure 2.2(a), cell P is at a level higher than its immediate neighbor cells W and N. In this section, the flux construction approach for the west face of cell P is illustrated:

i. The ghost points required for completing the ENO stencils are identified. The ghost points can be identified by simply comparing the status (divided or undivided) and refinement level of the neighboring cells. For cell P, three ghost points (GW_1, GW_2, GW_3) on the west side, and two ghost points (GE_2, GE_3) on the east side are required to complete the support stencil.

ii. Once the ghost points are identified, the next step is to derive the fluxes and the flow properties for these ghost points. As mentioned before, several interpolation schemes such as the ENO-based [36] or MUSCL-based [145, 146] schemes have been used in the past. Berger et al [26] employed a conservative bilinear interpolation procedure to determine the fluxes and the flow field at the ghost points. Quirk [145, 146] used a MUSCL-based interpolation procedure to define the ghost points. Losasso et al [122] used a direct injection method. In their approach, the flow properties and fluxes from the nearest undivided leafcell were directly injected to the ghost points. Recently, Choi et al [41] proposed a quadratic ghost point filling technique. Recognizing that a linear interpolation procedure at the ghost points results in spurious reflected waves, a quadratic interpolation procedure along with explicit gradient continuity were enforced at the mesh interface for determining the flow properties at the ghost points. The method was shown to be effective in suppressing the spurious os-

cillations arising at the mesh interface, but was found to be complicated for two- and three-dimensional applications. Cecil et al [36] modified their linear interpolation based ghost point filling approach [35] with an efficient and higher-order ENO based interpolation procedure.

In this work, a simple conservative bilinear interpolation approach is adopted, as the bilinear interpolation procedure is used to determine the flow properties for the newly formed child and parent cells. Moreover, the refinement criteria developed in this work ensures that the flow field spanning the fine-coarse boundary is smooth and that the discontinuities are contained well within the fine mesh cells. Hence a conservative, bilinear interpolation approach, is the most straightforward choice.

In order to construct the attributes for the ghost point GW_1, a non-conservative interpolation technique can either use points P, W, NW and N or points P, PS, W and NW for interpolation as shown in Figure 2.2(a). Here the choice for interpolation points is not unique. On the other hand, a conservative interpolation scheme uses a unique set of points for interpolation such as points W, NW, PI and N (Figure 2.2(a)). The point PI corresponds to the parent of cell P, and the flow attributes for point PI can be obtained by aggregating from its child cells i.e from cells P, PE, PS and PSE. Essentially, a conservative interpolation scheme uses points on the same level for interpolation. To clarify this procedure, a complex scenario involving cells at different levels of refinement is presented in Figure 2.2(b). As shown in Figure 2.2(b), the fine-coarse grid interface involves grids with more than one level difference (along the diagonal direction). In such cases, points NWI, NI, PI and WI on the same level

are used for interpolation. Figure 2.2(b) shows how the flow properties and fluxes are aggregated from child cells to determine the flow properties at point NI. A similar procedure can be adopted to determine the flow properties and fluxes at points PI and WI. Identification of points of interpolation on the same grid level is straightforward. The procedure described above is applied repeatedly to define the flow attributes and fluxes for the remaining ghost points.

iii. Once the attributes for the ghost points are determined, the construction of flux f_{p_W} follows from the uniform mesh approach. Thus the method outlined in this section does not deviate much from the uniform mesh-based flux construction approach, and retains the simplicity of the ENO scheme flux construction for uniform meshes. The approach for constructing fluxes for other faces of cell P follow directly the procedure described above.

2.3.4.2 Flux Construction at the Fine-Coarse Interface for Cells Abutting Divided Neighbors

If the cell under consideration is at a level lower than its immediate neighbor, the numerical flux corresponding to that face is not explicitly computed. With reference to Figure 2.2(b), cell W that abuts the fine mesh cells (P and PS) is at a level lower than its potential neighbors P and PS. Hence the flux crossing the mesh interface at the east face of cell W is not explicitly computed. Instead, the west fluxes for cells P and PS are summed to determine the net flux crossing the east face of cell W. Thus for the flux crossing the east

face of cell W:

$$f_E = f_{P_W} + f_{PS_W}$$

where f_{P_W} and f_{PS_W} correspond to the fluxes crossing the west face of cells P and PS respectively. The fluxes f_{P_W} and f_{PS_W} are computed based on the procedure outlined above. Thus, explicit conservation of numerical fluxes particularly at the interface of fine-coarse boundaries is achieved.

2.3.4.3   Flux Construction Near the Embedded Interface

Since all cells in the narrow band of the level set field corresponding to the embedded interface are refined uniformly to the same level, no special treatment is required for constructing the fluxes near the interface of the embedded object(s). Therefore, the Riemann solver based GFM technique developed for uniform mesh can be directly applied near the interface of the embedded object(s).

2.4   Numerical Examples

As a representative measure of the computational memory usage, the percentage Occupancy Ratio (OR) (Eq (2.9)) is computed. The OR is defined as the ratio of the maximum number of cells used in the solution adaptive LMR calculation with the number of cells if a uniform fine mesh (corresponding to size of the finest mesh in the LMR calculation) was used.

$$OR = \frac{MAX(NCELLS_{LMR}(t))}{NCELLS_{UNIFORM\ FINE\ MESH}} \times 100 \qquad (2.9)$$

For problems involving moderate to strong shocks interacting with gas-gas or gas-

solid interfaces, the threshold for the refinement criteria were set in the range $\delta_1 = 1.0 - 100.0$ and $\delta_2 = 1.0 - 100000.0$ (arbitrarily large value). The threshhold limit for δ_2 is set to arbitrarily large value if the resultant shock diffraction pattern does not contain weak structures and gradients that are under-resolved. For gas-water interface problems, due to very large difference in the stiffness of the material strength (impedance mismatch ρa), the threshhold limits were set in the range $\delta_1 = 100.0 - 10000.0$ and δ_2 to an arbitrarily large value.

2.4.1 One-Dimensional Example

For the one-dimensional test case considered in this section, a computational domain corresponding to a shock tube of unit length and unit height was chosen. A base mesh of size $\Delta x_g = 0.02$ was used for the simulations and the solutions were evolved with three different (3, 4 and 5 levels of mesh refinement corresponding to fine mesh size $\Delta x_f = \frac{1}{200}, \Delta x_f = \frac{1}{400}$ & $\Delta x_f = \frac{1}{800}$ respectively) levels of mesh refinement.

2.4.1.1 Sod's Shock Tube Problem

A simple, canonical, Sod's shock tube problem is considered first. The initial conditions for the problem are as follows:

$$(\rho, P, u, \gamma) = \begin{cases} (1.0, 10.0, 0.0, 1.4) \text{ for x} < 0.5, \\ \\ (0.125, 1.0, 0.0, 1.4) \text{ for x} \geq 0.5. \end{cases}$$

Pressure ratio across the discontinuity is fairly low, $\frac{P_2}{P_1} = 10$. The initial discontinuity results in a rightward moving shock wave and contact discontinuity, and a leftward moving rarefaction wave. In this example no interface treatment technique was employed to resolve

the contact discontinuity. The simulations were evolved to time T = 0.167 units. Since the strengths of the shock wave and the expansion wave are low, the threshold for the refinement criteria were set at $\delta_1 = 1.0$ and $\delta_2 = 100000.0$. The solution obtained from the current simulations along with the exact solution are displayed in Figure 2.3. As can be seen from the plots, the numerical solutions from the current calculations closely follow the exact solution.

In order to investigate the impact of the interpolation procedures at the fine-coarse mesh boundary, the mesh refinement was frozen after the first time step, prohibiting the mesh from adapting to the solution. This allows the shock wave, the contact discontinuity and the rarefaction wave to pass through the fine-coarse mesh boundary and hence the interpolation errors generated at the fine-coarse mesh interface can be examined. The motivation for this analysis comes from the fact that spurious reflected waves were observed in [41] when waves were made to pass through coarse-fine mesh interface. Although the refinement criteria developed in this work prohibits the passage of strong discontinuities across mesh interface, the intent of this analysis is to examine the errors generated in the limiting case of a shock wave passing through the mesh interface.

The density and the entropy plots for the frozen mesh condition are displayed in Figure 2.4. Once the shock and the contact discontinuity move into the coarse base mesh region, they assume a more diffusive profile (corresponding to the size of the coarse base mesh Δx_g). The plots are synchronous with the uniform mesh solutions. The spatial variation of the absolute errors ($\epsilon = |\rho_{Numerical} - \rho_{Exact}|$) and the $L_2(\rho)$ errors (also computed with respected to the exact solution), for different levels of mesh refinement are plotted in

Figure 2.5. As can be seen from Figure 2.5(a), no spurious reflected waves from the mesh interface are observed. The errors near the region occupied by the shock and the contact discontinuity are consistent with the prediction made by the uniform base mesh solution. But the errors near the head and the tail of the rarefaction waves are significantly smaller than the errors generated by the uniform base mesh solution. This is because of the presence of the frozen patch of fine mesh around the initial discontinuity (i.e. at x = 0.5) that partly spans the region occupied by the tail of the rarefaction wave. Furthermore, in the region occupied by the shock and the contact discontinuity, the error distribution decreases with increase in mesh refinement level. This is counter-intuitive, particularly for higher levels of mesh refinement which involve interpolations across different grid levels. The reason for this can be attributed to the nature with which the solution is evolved in the LMR framework. As mentioned before, unlike AMR schemes, the flow field is evolved in a single sweep for any given time step. As a result, the smallest time step determined by the size of the fine mesh cell is enforced for the global time update. With the increase in mesh refinement levels, smaller and smaller time steps are enforced globally and hence make the interpolation errors more benign. The $L_2(\rho)$ errors computed for both the frozen mesh condition and the LMR solution are plotted in Figure 2.5(b) clearly confirm this fact (the errors decrease with increase in mesh refinement levels).

Next a stronger shock was simulated with pressure ratio $\frac{P_2}{P_1} = 1000$. The solution obtained from the current simulations for different levels of mesh refinement are displayed in Figure 2.6. The threshold for the refinement criteria are the same as in the previous case, and the solutions are evolved to time T = 0.021 units. The numerical solutions tend towards

the analytical solutions with increase in mesh refinement level. Similar to the previous case, the mesh evolution was frozen after the first time step, and L_2 errors computed with respect to the exact solution are displayed in Table 2.1. The errors incurred, although very large for some variables, are comparable for different levels of mesh refinement. The difference in the L_2 errors computed for the uniform base mesh solution and the LMR solution with frozen mesh condition, are plotted in Figure 2.7. In contrast to the previous case, the L_2 errors increase with mesh refinement level. Thus, as one would expect, it can be inferred from the above two examples that the errors incurred due to interpolation across shock waves increase with shock strength. Such errors can be averted if shocks and other strong discontinuities are contained well within the fine mesh level, by inhibiting their movement across fine-coarse mesh boundaries.

2.4.2   Two-Dimensional Example

2.4.2.1   Two-Dimensional Riemann Problem (TDRP)

The two-dimensional Riemann problems (TDRP) consist of a combination of one-dimensional wave patterns, giving rise to 19 different configurations [110]. As one can construct numerous elementary wave patterns, it is not possible to derive an analytical solution for the TDRPs. However, the solution for each configuration of the TDRP is well established and has been widely used to test several high resolution numerical schemes [103, 110]. In this work, three different configurations (6,8 & 19) of the TDRP are considered, to test the accuracy and performance of the LMR scheme in the two-dimensional set up. The initial conditions for each configuration correspond to a constant state in each quadrant of a

computational domain of unit length and unit height. The boundaries of the computational domain are imposed with Neumann conditions. The initial conditions corresponding to each configuration are listed in Table 2.3.

Simulations were performed with the traditional shock capturing approach (ENO scheme) with no explicit interface treatment technique. Shown in the figure are the density contours and the mesh topology for 5 levels of mesh refinement, on a base mesh of size $\Delta x_g = 0.02$. The details of the numerical solutions are displayed in Table 2.2. The L_2 errors displayed in the table are computed by comparing the solution with the corresponding uniform fine mesh calculations (with $\Delta x = \frac{\Delta x_g}{2^{k-1}}; k = 3, 4 \& 5$.). The L_2 errors remain almost constant for different levels of mesh refinement, indicating that the solutions obtained from the LMR calculations are consistent, and concur with the corresponding fine mesh calculations. In addition, the OR shown in Table 2.2, decreases with increase in mesh refinement level. In particular, the OR for configuration 19 is 5 % (only 5 % of the computational domain is occupied by fine mesh cells). Thus with the current formulation of the tree-based LMR scheme, substantial savings in computational memory can be attained. Plots obtained from the current simulations are presented in Figure 2.8. The mesh topology shown in the figure indicate that the refinement critetion developed in this work is effective in identifying and following the important features such as shocks and entropy layers.

Refinement Level	$L_2(\rho)$	$L_2(P)$	$L_2(u)$	$L_2(S)$	
$\frac{P_2}{P_1} = 10$					
1	4.07569×10^{-3}	4.241×10^{-3}	1.0865×10^{-2}	1.2559×10^{-2}	
3	3.36566×10^{-3}	3.503×10^{-3}	1.049×10^{-2}	1.08668×10^{-2}	
4	3.061×10^{-3}	3.401×10^{-3}	1.036×10^{-2}	1.049×10^{-2}	
5	3.24515×10^{-3}	3.379×10^{-3}	1.031×10^{-2}	1.038×10^{-2}	
$\frac{P_2}{P_1} = 1000$					
1	4.567×10^{-2}	557.8874	0.958	1478.400	
3	4.61×10^{-2}	557.9053	0.9774	1478.465	
4	4.613×10^{-2}	557.9093	0.9808	1478.475	
5	4.619×10^{-2}	557.9098	0.9819	1478.484	

Table 2.1: L_2 errors computed with respect to the exact solution for frozen mesh condition, for Sod's shock tube problem.

Configurations	Time	Levels	δ_1	δ_2	L_2	OR
6	0.3	3	25.0	1000.0	5.79×10^{-5}	26.42 %
		4	25.0	1000.0	5.33×10^{-5}	13.03 %
		5	25.0	1000.0	3.87×10^{-5}	9.1 %
8	0.25	3	1.0	1000.0	9.077×10^{-6}	31.58 %
		4	1.0	1000.0	8.204×10^{-6}	19.74 %
		5	1.0	1000.0	6.278×10^{-6}	11.78 %
19	0.3	3	20.0	1000.0	7.19×10^{-5}	29.9 %
		4	20.0	1000.0	4.13×10^{-5}	16.1 %
		5	20.0	1000.0	2.37×10^{-5}	5.71 %

Table 2.2: $L_2(\rho)$ and OR for the two-dimensional Riemann problem

Configurations	Initial Conditions	
	$x < 0.5; y > 0.5$	$x > 0.5; y > 0.5$
	$\rho_2 = 2.0\ P_2 = 1.0$	$\rho_1 = 1.0\ P_1 = 1.0$
	$u_2 = 0.75\ v_2 = 0.5$	$u_1 = 0.75\ v_1 = -0.5$
6	$x < 0.5; y < 0.5$	$x < 0.5; y < 0.5$
	$\rho_3 = 1.0\ P_3 = 1.0$	$\rho_4 = 3.0\ P_4 = 1.0$
	$u_3 = -0.75\ v_3 = 0.5$	$u_4 = -0.75\ v_4 = -0.5$
	$x < 0.5; y > 0.5$	$x > 0.5; y > 0.5$
	$\rho_2 = 1.0\ P_2 = 1.0$	$\rho_1 = 0.5197\ P_1 = 0.4$
	$u_2 = -0.6259\ v_2 = 0.1$	$u_1 = 0.1\ v_1 = 0.1$
8	$x < 0.5; y < 0.5$	$x < 0.5; y < 0.5$
	$\rho_3 = 0.8\ P_3 = 1.0$	$\rho_4 = 1.0\ P_4 = 1.0$
	$u_3 = 0.1\ v_3 = 0.1$	$u_4 = 0.1\ v_4 = -0.6259$
	$x < 0.5; y > 0.5$	$x > 0.5; y > 0.5$
	$\rho_2 = 1.0\ P_2 = 1.0$	$\rho_1 = 0.5197\ P_1 = 0.4$
	$u_2 = -0.6259\ v_2 = 0.1$	$u_1 = 0.1\ v_1 = 0.1$
19	$x < 0.5; y < 0.5$	$x < 0.5; y < 0.5$
	$\rho_3 = 0.8\ P_3 = 1.0$	$\rho_4 = 1.0\ P_4 = 1.0$
	$u_3 = 0.1\ v_3 = 0.1$	$u_4 = 0.1\ v_4 = -0.6259$

Table 2.3: Initial conditions for the two-dimensional Riemann problem

(a) Hierarchical tree structure   (b) Hierarchical data structure
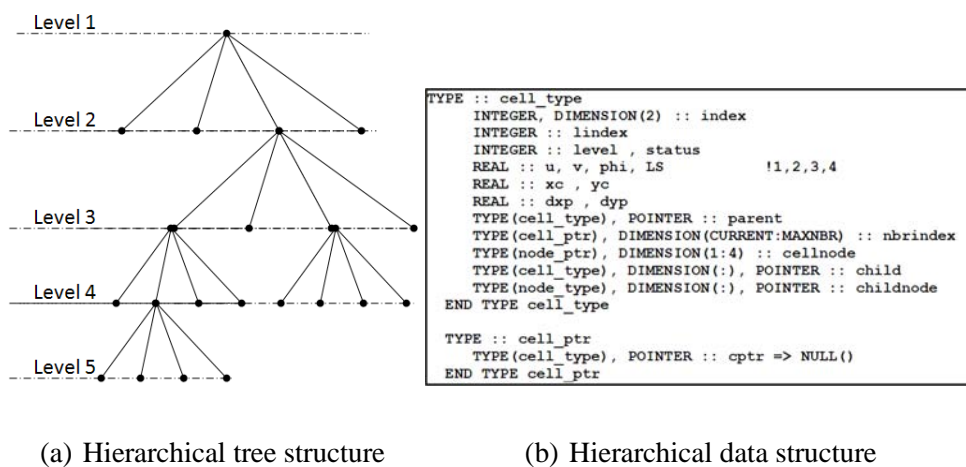
Figure 2.1: Data Structures used in LMR: (a) Hierarchical (quad)tree structure; (b) hierarchical data structure
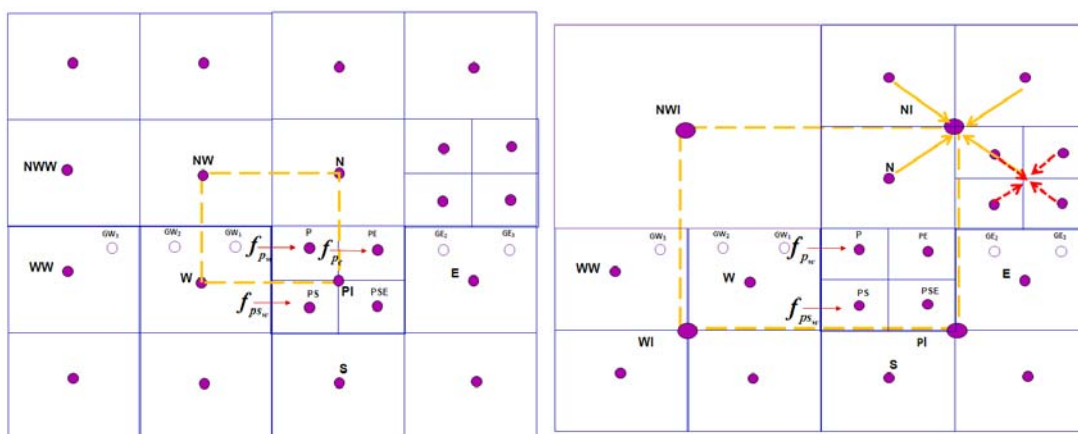
(a) Adjoining cells with one level difference (b) Adjoining cells with more than one level difference

Figure 2.2: ENO-based flux construction at the fine-coarse mesh boundary: (a) adjoining cells having one level difference along the diagonal direction (b) adjoining cells having more than one level difference along the diagonal direction
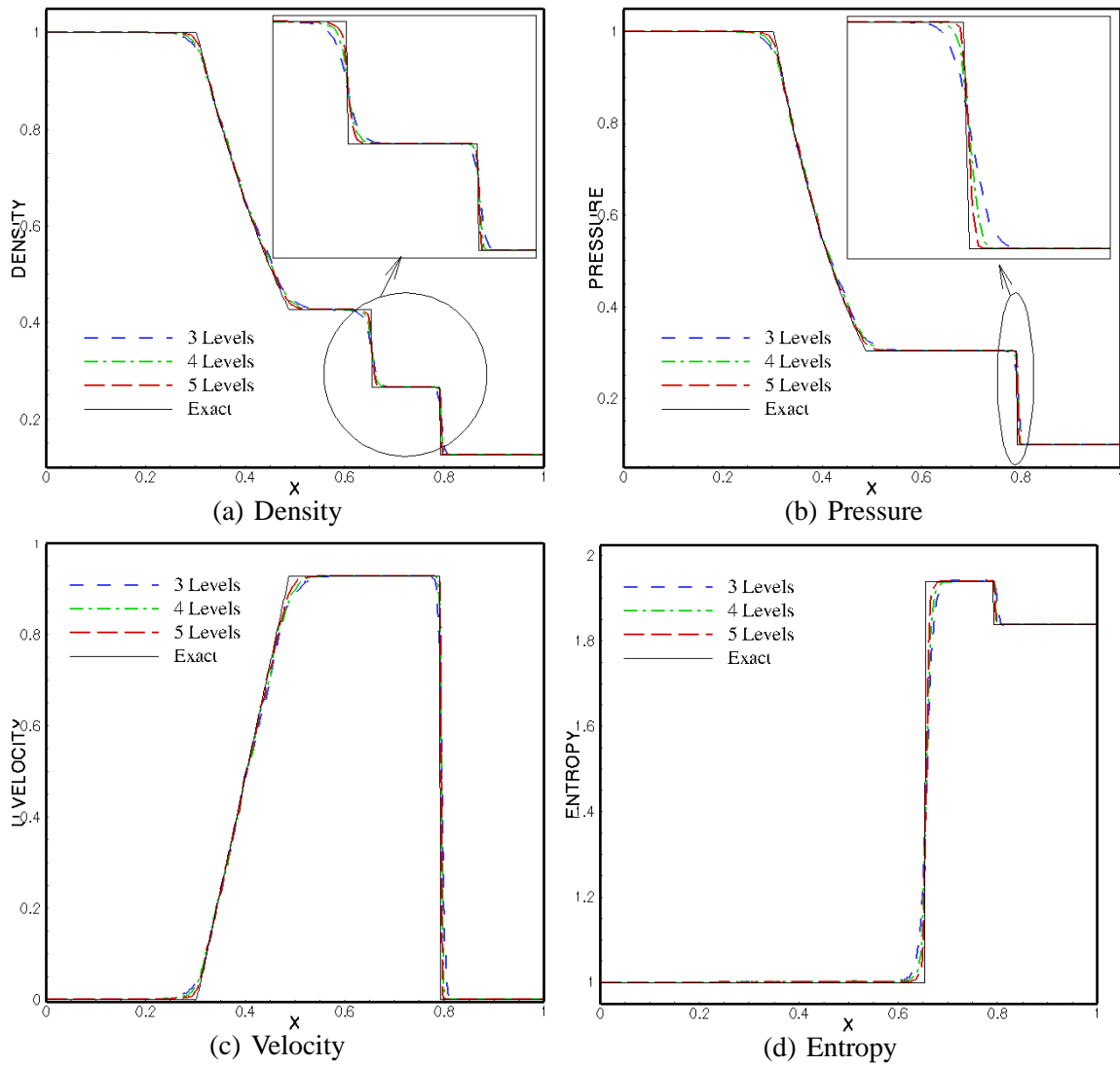
Figure 2.3: Sod's shock tube problem with pressure ratio $\frac{P_2}{P_1} = 10$: Plots of (a) density, (b) pressure, (c) velocity (d) entropy.
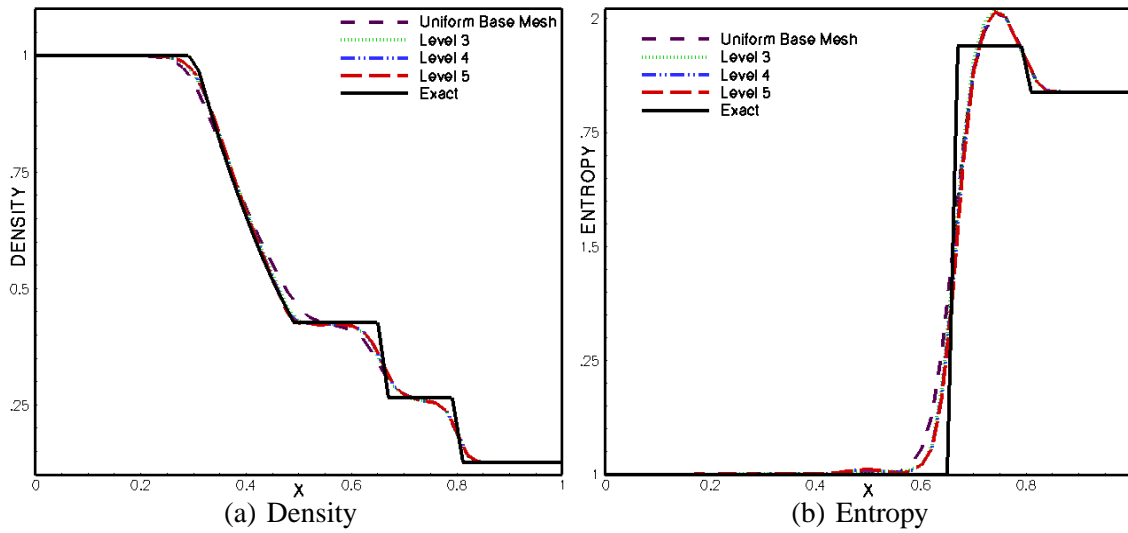
(a) Density   (b) Entropy

Figure 2.4: for Sod's shock tube problem with pressure ratio $\frac{P_2}{P_1} = 10$: Plots of (a) Density and (b) entropy for different levels of mesh refinement, for frozen mesh condition.

(a) Spatial variation of the absolute errors ($\|\rho - \rho_{EXACT}\|$)
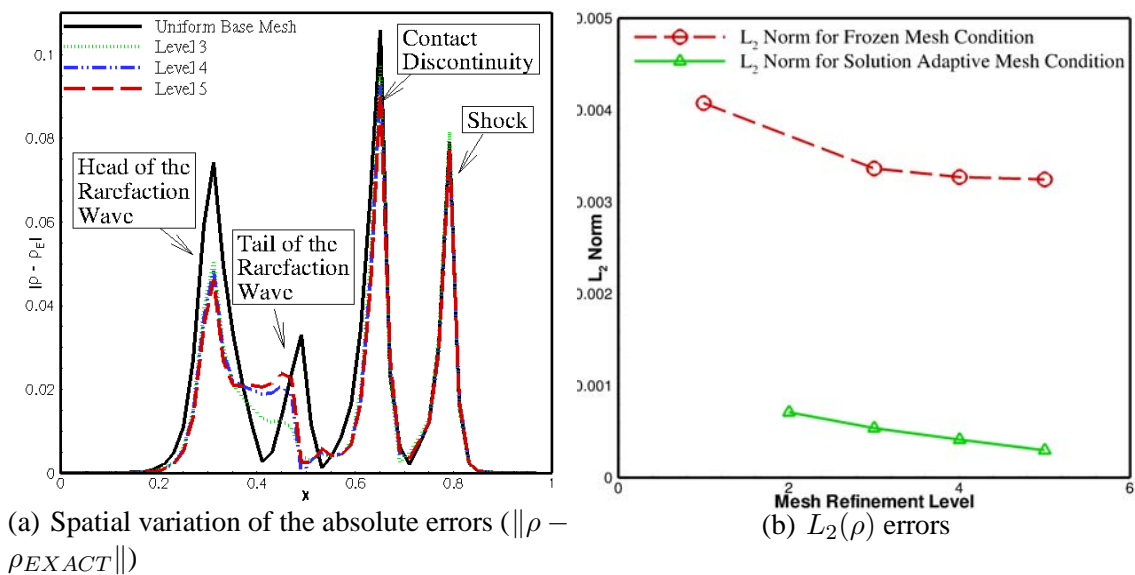
(b) $L_2(\rho)$ errors

Figure 2.5: Plots of errors: (a) Spatial variation of the absolute errors ($\|\rho - \rho_{EXACT}\|$) computed with respect to the exact solution for different refinement levels, for frozen mesh condition (b) $L_2(\rho)$ errors computed with respect to the exact solution, for different refinement levels, for solution adaptive and frozen grid conditions.
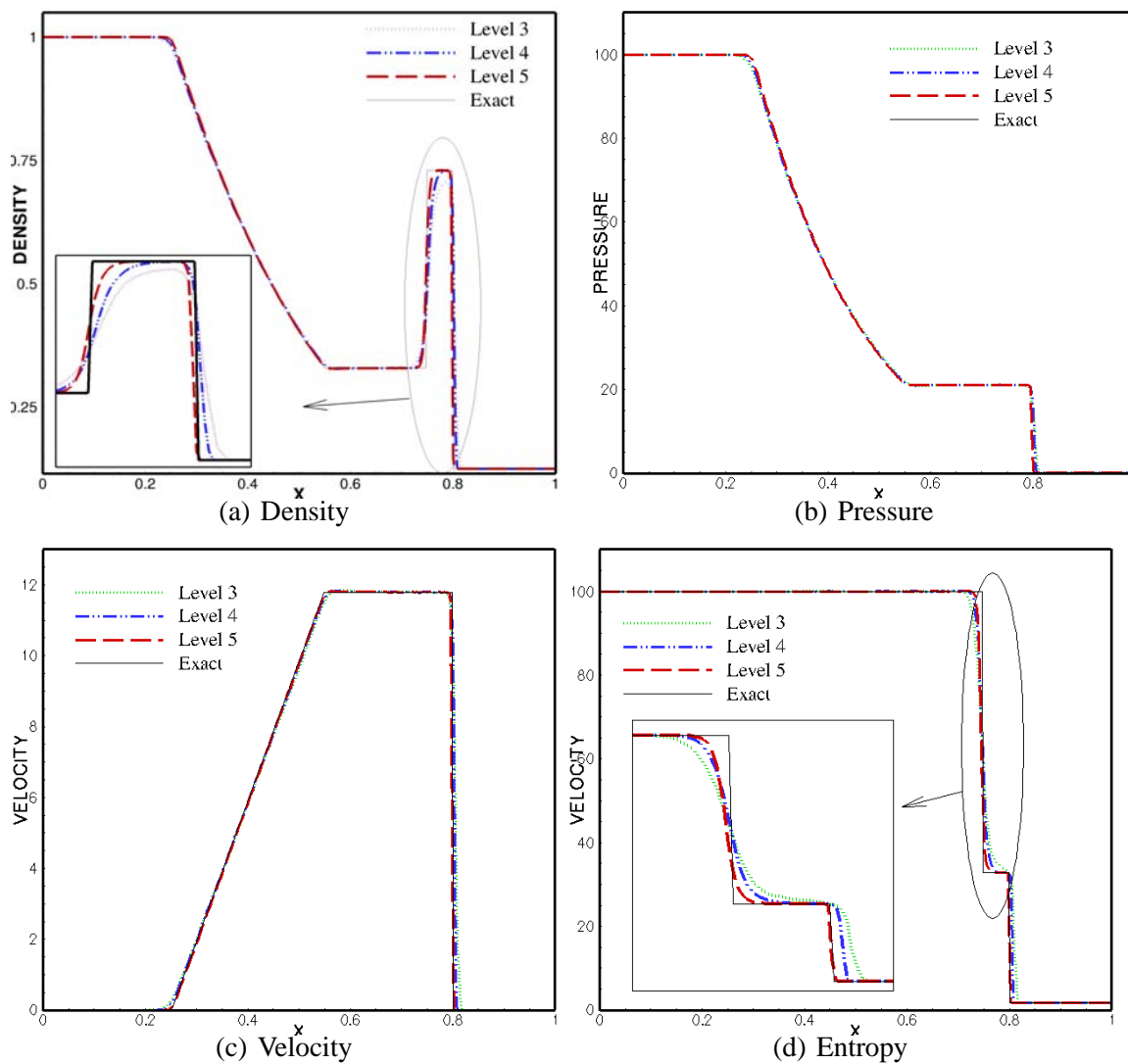
Figure 2.6: Sod's shock tube problem with pressure ratio $\frac{P_2}{P_1} = 1000$: Plots of contours of (a) density, (b) pressure, (c) velocity and (d) entropy.
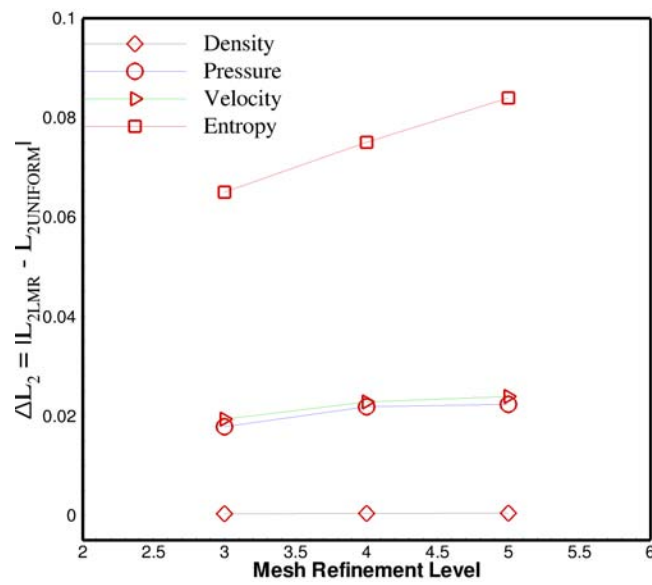
Figure 2.7: Variation of $|L_{2_{LMR}} - L_{2_{Uniform}}|$ for different levels of mesh refinement for the frozen mesh condition.

(a) Configuration-6: Entropy Contours

(b) Configuration-6: Mesh Topology

(c) Configuration-8: Density Contours

(d) Configuration-8: Mesh Topology

(e) Configuration-19: Entropy Contours

(f) Configuration-19: Mesh Topology
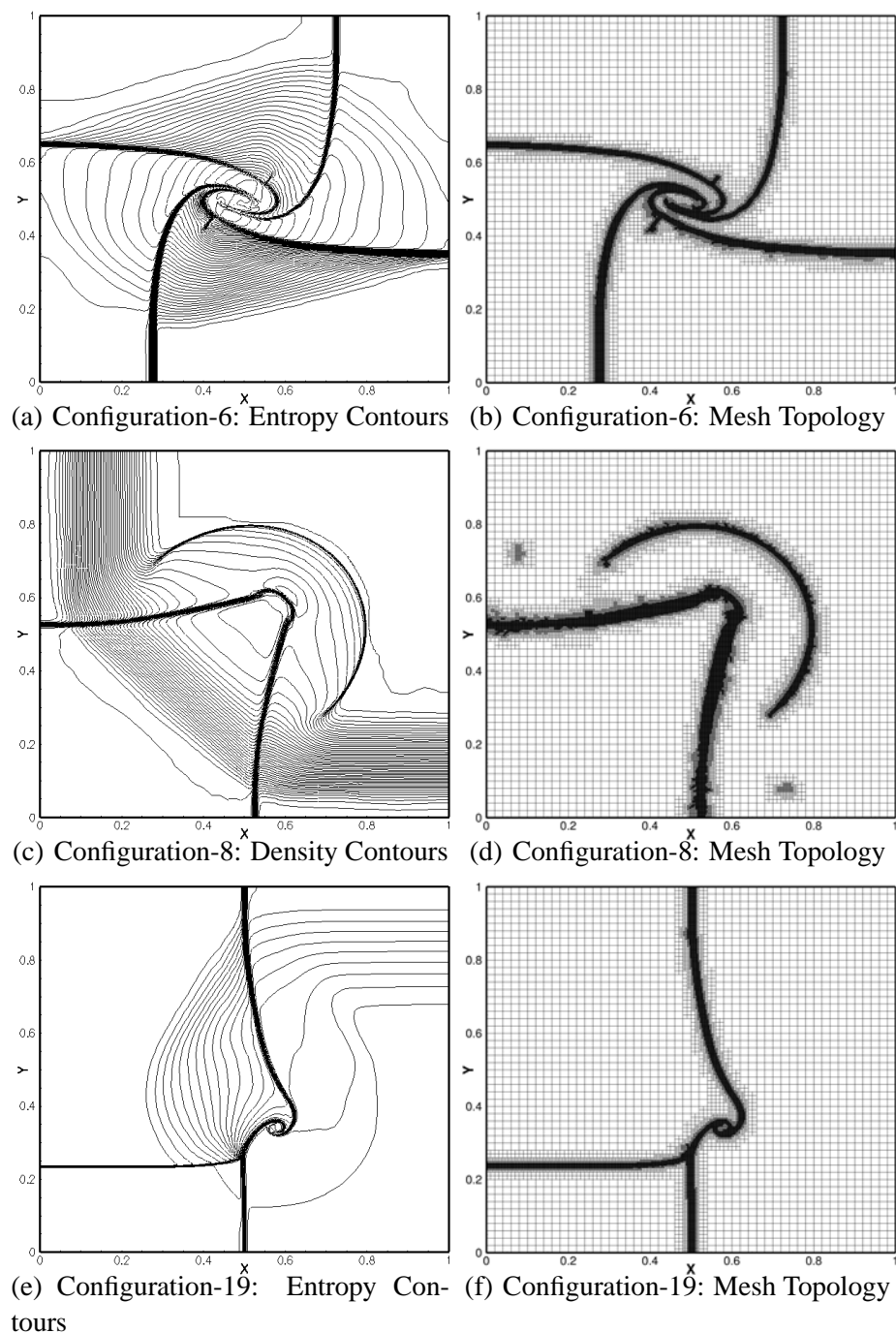
Figure 2.8: The two-dimensional Riemann Problem computed on a base mesh of size $\Delta x_g = 0.02$ with 5 levels of mesh refinement: Entropy contours (Figures (a) and (e)), density contours (Figure(c)) and Mesh Topology (Figures (b), (d) and (f)).

CHAPTER 3
SHARP INTERFACE TREATMENT FOR FLUID OBJECTS

3.1   Introduction

High-resolution and higher-order schemes such as ENO [163] and WENO [74] perform very well for single fluid media with discontinuities [116]. However, when such schemes are employed directly to solve multi-component flows, undesirable oscillations in the form of pressure waves are prevalent near the material interface [98]. The difficulty resides in maintaining pressure equilibrium between the fluid components at the material interface, which results in computational inaccuracies and spurious oscillations [102]. Discontinuities such as shocks are nonlinear phenomena with converging characteristics and so the numerical errors generated are confined within the (smeared) discontinuity [66]. On the other hand, for contact discontinuities the characteristics run parallel to each other and hence there is no steepening mechanism to counter the numerical dissipation of the errors generated near the discontinuity [49]. Thus, errors in treating the presence of embedded interfaces can permeate the solution away from the interface. To prevent these spurious oscillations when dealing with material discontinuities, care must be exercised when treating the embedded interfaces in a sharp manner.

Several methods have been proposed in the past to extend the numerical schemes developed for single component flows to multi-component flows [5, 6, 94, 98, 102]. These methods are based on the fact that a strictly conservative scheme will not be able to maintain pressure equilibrium across the material interface [6]. In Abgrall et al [5,6], a separate non-

conservative transport equation was solved to update the specific function ($\Gamma(\gamma) = \frac{1}{(\gamma-1)}$) for the mixture. In Karni et al [102], a non-conservative pressure evolution equation was used to compute the pressure near the material interface. In Jenny et al [94], a thermo-dynamically consistent correction algorithm for the total energy was proposed. All of these methods fall under the category of front-capturing methods. A good review of such methods can be found in Abgrall et al [6]. Although these methods are at least quasi-conservative, smearing of the interface is an inherent feature. Treating materials that are separated by distinct sharp interfaces (as in droplet/bubble dynamics) by reformulating the problem using a mixture model (with diffuse interfaces) and therefore as a single-component inhomogeneous medium, casts the onus on the continuum formulation, while relieving the numerical techniques. However, treatment of interfaces as non-sharp or dif-fuse zones within a mixture formulation is not devoid of numerical problems. For example, across the interface of multiphase compressible flow (say containing gas-liquid interfaces) there are jumps in material properties. There are also sharp changes in material behavior and constitutive laws, for example in the equation of the state. When a shock is transmitted across an interface, failure to capture this discontinuous response of the contiguous ma-terials results in severe numerical instabilities or unphysical flow fields. For example, if the interface is not treated as a sharp entity, due to the presence of numerical diffusion at the interface, a non-physical zone with artificially diffused density field will result [42]. In such situations, it becomes necessary to use an *ad-hoc* equation of state (representing some non-physical averaged material) to obtain a continuous pressure field [43]. This results in inaccurate wave interactions and boundary conditions corresponding to this non-physical

zone being enforced at the interface [118]. Nevertheless, it is important to point out that despite these shortcomings, in some instances (like the shattering of droplets/bubble under the impact of strong shocks [38, 125]), the diffuse interface approach may still be the most judicious choice.

Alternatively, front tracking methods which preserve interfaces as sharp discontinuities retain the two fluid regions as separate entities but must contend with the numerical challenges of discretizing the governing equations to apply relevant boundary conditions on the interface. In recent times the use of sharp interface methods for the representation of solid and fluid boundaries in incompressible [86, 124, 148, 177] and compressible [57, 58, 118, 133, 135, 190] flows have become popular. These methods are particularly attractive for the treatment of moving boundaries in the flow domain since grid generation and management are dispensed with. In this regard, the Ghost Fluid Method (GFM) originally formulated by Fedkiw et al [58] provides a simple framework to implicitly transmit the presence of an interface to the flow field. The GFM requires the definition of a band of ghost fluid points corresponding to each phase of the interacting media. The band of ghost fluid points (when populated with suitable flow properties) together with its respective real fluid constitutes in effect a single flow field. Thus, discretization schemes with uniform order of accuracy can be applied throughout the computational domain without requiring any special treatment near the interface. Hence, the implementation of the numerical scheme and the interface treatment are decoupled, and the onus is shifted to populating the ghost points with the appropriate flow properties.

GFM has been widely used to treat the presence of embedded fluid-fluid and solid-

fluid interfaces [57,58,60,118,133,135,190]. However, these variants in GFM differ in the way in which the ghost points are populated. In Fekdiw et al [59], GFM was used in the context of shock and detonation tracking. The Rankine-Hugoniot (R-H) jump conditions were solved across the discontinuity to populate the ghost points. In a subsequent work, Fedkiw et al [33, 57] extended the GFM approach for coupling stiff and non-stiff fluids (gas-water interfaces). In this case, the ghost fluid states were defined by extrapolating the velocity at the interface in the water medium and the pressure from the air medium [57]. This approach, although attractive for gas-water interfaces, was not suitable to represent gas-gas interfaces. Aslam [13, 14] proposed to construct a Riemann problem across discontinuities (shocks and contacts) and populate the ghost points by solving a Riemann problem normal to the interface. Liu et al [118], clearly demonstrating the failure of the original GFM, proposed the Modified GFM (MGFM). Attributing the failure of original GFM to inaccurate treatment of the wave interactions occurring at the interface, Liu and co-workers solved the local Riemann problem by carrying out characteristic analysis on the waves arriving at the interface. Later Hu et al [87], extended this approach by solving two separate Riemann problems - one for the real fluids and second for the real and corresponding ghost fluid. By enforcing the condition that the two Riemann problems work in conjunction such that the pressure and the velocity obtained from the real-ghost interactions correspond to the real interactions [87], they were able to employ the isobaric fix to compute the density field for the ghost points. This approach was called Interface Interaction GFM (IGFM). Both IGFM and MGFM were successfully applied to solve a multitude of problems involving strong shocks interacting with gas-gas and gas-water interfaces.

In this work, a simple but efficient method to construct the Riemann problem has been developed. The method developed provides a uniform formulation to treat both fluid-fluid and solid-fluid interfaces. In the case of solid objects embedded in a compressible flow, it is well known that numerical schemes suffer from acute over-/under-heating errors [127, 132]. Several corrective measures have been developed to suppress the growth of such errors. A unified methodology should be able to suppress these over-/under-heating errors, and also accurately capture the wave interactions occurring at the interface. Hence, the focus of this work is on designing a simple yet robust method that can handle strong shock interactions with gas-gas, gas-water and solid-fluid interfaces.

The approach adopted in this work has a multi-dimensional characteristic intrinsic to the construction procedure making it attractive for three-dimensional applications. Briefly, a local Riemann problem is constructed at the interface which is then solved using an exact Riemann solver. The resulting Riemann states obtained from solving the Riemann problem are used to populate the respective ghost points. In chapter 5, this method is extended to treat embedded solid objects in compressible flows, and has been shown to be effective in suppressing the over-/under-heating errors. As demonstrated in section 3.2, the results obtained from the current simulations clearly indicate that the proposed method is consistent in generating satisfactory solutions for several complex configurations and shocks interacting with interfaces; shocks interacting with droplets, bubbles and free surface have been computed. The method is currently being applied to study the dynamics of dense particulate compressible flows.

3.1.1   Survey of the Ghost Fluid Method (GFM) for Resolving Fluid-Fluid Interfaces

In Fedkiw et al [58], the ghost points were populated based on the fact that the pressure and velocity are continuous across the contact discontinuity. This enables the pressure and velocity to be directly copied from the real fluid onto the ghost field. Since the entropy advects with material velocity (corresponding to the characteristic wave traveling with fluid/particle velocity), there is no entropy exchange between the two fluids. This allows the entropy to be extended to the ghost points (a procedure called isobaric fix in Fedkiw et al [58]) which can then be used to compute the density for the ghost points (Figure 1.10).

This simple approach was found to be robust for weak shocks interacting with the interface. However, when the shock strength and the material stiffness of the interacting fluids were increased considerably, it was found that this method failed to maintain a non-oscillatory pressure field. The reason for this failure is intuitive and is largely attributed to the definition of the ghost states. When strong shocks reside on/near the interface, the density, pressure and velocity fields cease to be continuous and hence cannot be directly copied onto the ghost points. The problem is more severe with stiff fluids, as the pressure and density fields are coupled with a highly sensitive stiffened equation of state. As a result, a small perturbation in density acutely amplifies the oscillations in the pressure field, resulting in stalling of the computation. During the few time steps when the shock and the interface are coincident, the interface treatment technique should temporarily reduce to a shock tracking method. Therefore, in this regard, the Rankine-Hugoniot (R-H) jump conditions must be solved across the interface to define the ghost states. Liu et al [118] pointed

out the inability of the original GFM to accurately resolve the wave interactions at the interface. According to them, GFM essentially solves two separate single medium Riemann problems (real-ghost interaction Riemann problem) across the interface. The resolution of the waves from the real-ghost interaction does not always concur with the Riemann states generated from real fluid interactions [118]. Hence, with strong shocks impinging on interfaces with high impedance mismatch, this discrepancy in wave representation results in inaccurate shock and interface locations that result in unphysical oscillations in the flow field [118].

3.1.2 Riemann Problem at the Interface

Carefully developed interface treatments can avoid the shortcomings of the original GFM by decomposing the singularities in the flow field and material properties [118]. Interfacial states satisfying such conditions can be obtained by locally solving a Riemann problem normal to the interface. Davis [49] solved an approximate Riemann problem across the interface using the method of characteristics approach. The solution from this approximate Riemann solver was then used to construct the second-order Godunov fluxes. Cocchil et al [42] employed an exact Riemann solver to correct the numerical errors afflicting the interfacial points. The interfacial points suffering from numerical diffusion were treated using a combination of the solution obtained from the numerical scheme and Riemann solution. The method was found to be promising for one-dimensional problems, but was complicated when applied for multi-dimensional problems. A modified version of this approach was incorporated in the GFM framework by Takahira et al [181]. This version

of GFM was successfully used to simulate shocks interacting with gas bubbles and water droplets. However, their method involves an iterative process in the correction procedure. Fedkiw et al [59] obtained the numerical fluxes for the ghost points by directly solving the R-H jump conditions across shocks and detonation fronts. Aslam [13,14] modified this approach by solving a local Riemann problem at the discontinuity to define the ghost states. Liu et al [118] developed the Modified Ghost Fluid Method (MGFM); As shown in Figure 3.1(a) the Riemann problem formulated locally, in the normal direction to the interface, was solved by carrying out a characteristic analysis of the nonlinear waves arriving at the interface. Later Hu et al [87], extended this approach by solving two separate Riemann problems - one for the real fluids and second for the real and corresponding ghost fluid. By enforcing the condition that the two Riemann problems work in conjunction such that the pressure and the velocity obtained from the real-ghost interactions correspond to the real interactions [87], they were able to employ the isobaric fix to compute the density for the ghost fluids. It is worth noting that, although explicit enforcement of isobaric fix [58] (which is a simple extension of entropy from the real field to define the ghost field) substantially reduced the over-/under-heating errors, such errors were not totally removed from the solution.

Thus it is clear that the methods discussed above differed in the way in which the Riemann problem was incorporated and solved at the interface. Along the same lines, the methodology developed in this work focuses on designing a simple yet robust method for constructing the Riemann problem along the local normal to the interface. The method has multi-dimensional characteristics inbuilt in the construction procedure and is easy to

implement. The method is an extension of Aslam [13, 14] and has been shown here to successfully simulate strong shocks interacting with both gas-gas and gas-water interfaces. It is worth noting that a similar method was independently developed by Wang et al [197]. As will be shown in section 3.2.1.2, the approach adopted in this work has been shown to minimize and confine the associated conservation errors near the interface. In chapter 5, this method is extended to mitigate over-/under-heating errors effectively and also to work consistently for a wide range of problems involving strong and weak shock interactions with embedded solid boundaries.

3.1.3 Constructing the Local Riemann Problem at the Interface

The aforementioned (GFM and non-GFM) sharp interface methods, require the construction of a local Riemann problem normal to the interface. In this section, a simple method is presented to accomplish this task. From each interfacial point, such as point P in Figure 3.1(b), a probe is inserted in the normal direction to the interface. The coordinates of the point of intersection of the probe (from point P) and the interface, i.e. point IP on the interface in Figure 3.1(b), can be determined as follows:

$$\vec{X}_{\text{IP}} = \vec{X}_P + \mid \phi_P \mid \vec{N}_P. \tag{3.1}$$

The left and the right states required for assembling the Riemann problem are obtained by advancing a distance of 1.5 Δx on either side of the interface from IP. The length of the probe (1.5 Δx) is chosen so that the interfacial point P, for which the Riemann problem is being constructed, bears no or minimal weight in the interpolation procedure involved in defining the Riemann problem. This enables the Riemann problem to be constructed

with points which are not infused with the errors generated at the interface. In order to maintain consistency, the point which lies inside the levelset is always denoted as the left state and the point which lies outside the levelset is always denoted as the right state. Thus the coordinates of the points corresponding to the left and right states can be computed as follows:

$$\vec{X}_L = \vec{X}_{\text{IP}} - 1.5\Delta x \vec{N}_P, \tag{3.2}$$

$$\vec{X}_R = \vec{X}_{\text{IP}} + 1.5\Delta x \vec{N}_P. \tag{3.3}$$

The flow properties ($\vec{W}_{L|R}$) corresponding to the left ($\vec{X}_L$) and the right ($\vec{X}_R$) states can then be obtained using a simple bilinear interpolation procedure as shown in Figure 3.1(b).

3.1.3.1   Generalized Riemann Solver for Gas - Water Interface

For the sake of completeness, the analytical solution for the Riemann problem is briefly described here. Once the Riemann problem is constructed, the solution for the initial value problem can be obtained using a suitable Riemann solver. In this case the Riemann problem was solved exactly. A good discussion on standard procedures to solve the Riemann problem can be found in the book by Torro [189]. Haller et al [78] and Cocchil et al [43] have outlined the procedure to solve the Riemann problem for a gas-water interface (based on stiffened equation of state). The solution for the Riemann problem consists of four states separated by three waves as shown in Figure 3.1(c). The nonlinear characteristic waves (with wavespeeds u + a and u - a) can be either a shock wave or a rarefaction wave. The linear characteristic wave (which travels at the particle velocity u) represents the interface separating the interacting materials. The solution for the Riemann problem

determines the intermediate ("$\star$") states sandwiching the interface (contact discontinuity), across which pressure and normal velocity are continuous but the density is discontinuous. Leaving the details pertaining to the steps for constructing the functions required to solve the Riemann problem to Toro et al [189], the functions and the algebraic equation are listed below:

$$f(p, \vec{W}_L, \vec{W}_R) = f_L(p, \vec{W}_L) + f_R(p, \vec{W}_R) + \Delta u^n = 0 \text{ where },\tag{3.4}$$

$$\Delta u^n = u_L^n + u_R^n, \text{ where } u_{L|R}^n \text{ are the normal velocity components},$$

$$\vec{W}_{L|R} = \left(\rho_{L|R}, u_{L|R}^n, p_{L|R}\right)^T, \text{ and}$$

$$f_{L|R}(p, \vec{W}_{L|R}) = \begin{cases} f_{L|R}^{rarefaction} &= \frac{2a_{L|R}}{\gamma_{L|R}-1}\{1 - \left(\frac{p^\star + p_\infty^{L|R}}{p^\star + p_\infty^{L|R}}\right)^{\frac{\gamma_{L|R}-1}{2\gamma_{L|R}}}\} \text{ if } \frac{p^\star + p_\infty^{L|R}}{p^\star + p_\infty^{L|R}} < 1.0 \\[2ex] f_{L|R}^{shock} &= \sqrt{\frac{A_{L|R}}{B_{L|R} + \left(p^\star + p_\infty^{L|R}\right)}} \left(p^\star - p_\infty^{L|R}\right) \text{ if } \frac{p^\star + p_\infty^{L|R}}{p^\star + p_\infty^{L|R}} \geq 1.0 \\[2ex] A_{L|R} &= \frac{2}{(\gamma_{L|R}+1)\rho_{L|R}} \\[2ex] B_{L|R} &= \left(\frac{\gamma_{L|R}-1}{\gamma_{L|R}+1}\right)\left(p_{L|R} + p_\infty^{L|R}\right) \end{cases}$$

The nonlinear algebraic equation (3.4) can be solved *via* Newton iterations to determine the intermediate states $\vec{W}_{L|R}^\star$. The intermediate states ($\vec{W}_{L|R}^\star$) obtained from solving the Riemann problem are then used to correct the flow properties of the real fluid at the interfacial points. For instance, as shown in Figure 3.2(b), the Riemann state $\vec{W}_L^\star$ obtained from solving the Riemann problem constructed at the interfacial point P, is used to correct the flow properties of the real fluid at point P.

This will ensure that a constant entropy field is maintained throughout the interacting materials (except across shocks). This in turn prevents the diffusion of the entropy field across the interface and hence prohibits entropy exchange between the interacting (real) flu-

ids. It was pointed out earlier in section 3.1.1, that a simple extension of the entropy field to correct the real fluid properties at the interfacial points does not comply with the nature of the characteristic waves arriving/leaving the interface. On the contrary, the correction procedure enforced in the current approach account for the wave systems interacting with the interface.

3.1.3.2 Populating the Ghost Points

Once the flow properties at the interfacial points are corrected, the flow properties are extended along the normal direction to the interface to populate the respective interior ghost points. To carry out the multi-dimensional extrapolation procedure, the partial differential equation given in equation (3.5) is solved to steady state.

$$\frac{\partial \Psi}{\partial \tau} + H(\phi_l)\vec{n}\cdot\vec{\nabla}\Psi = 0 \tag{3.5}$$

where Ψ is the variable extended across the interface, τ is the pseudo-time and $H(\phi_l)$ is the unit Heaviside function defined as

$$H(\phi_l) = \begin{cases} 0 \text{ if } \phi_l \leq 0.0, \\ \\ 1 \text{ if } \phi_l > 0.0. \end{cases}$$

In the current work, the variable Ψ extended across the interface correspond to the flow properties at the intermediate state ($\vec{W}^{\star}_{L|R}$) obtained from solving the Riemann problem. As given in equation (3.5) a constant extrapolation method is used for populating the ghost points, although higher-order extrapolation procedures are possible [15]. Figure 3.2(b) shows the multi-dimensional correction and extension procedure carried out along the normal direction to the interface. The point P in Figure 3.2(b) is inside the object i.e. $\phi_l \leq 0$

and corresponds to the left state of the Riemann problem. Hence, as mentioned before, the Riemann state corresponding to $\vec{W}_L^\star$ obtained from solving the Riemann problem is used to correct the flow properties at point P. Then the flow field corresponding to $\vec{W}_L^\star$ is extended along the normal direction to populate the interior ghost points (Figure 3.2(b)). The one-dimensional version of the correction and the extension procedure is shown in Figure 3.2(a).

It is important to note that the velocity obtained from the Riemann solver corresponds to the normal velocity component computed in the local curvilinear coordinate. In order to reconstruct the velocity vector in the global Cartesian coordinates, the slip condition at the interface is enforced. Thus, the tangential velocities computed for the Riemann problem (the left and the right states) are extrapolated across the interface. Accordingly, the velocity vector can be reconstructed as

$$\vec{u}_L^\star = u^{n\star}\hat{n} + \vec{u}_L^t \tag{3.6}$$

$$\vec{u}_R^\star = u^{n\star}\hat{n} + \vec{u}_R^t \tag{3.7}$$

where $\hat{n}$ is the normal vector defined in Eq (1.54), $u^{n\star}$ is the normal velocity obtained from the Riemann solver and $\vec{u}_{L|R}^t$ are the tangential velocities (corresponding to the left and right states of the Riemann problem) computed as follows:

$$\vec{u}_L^t = \vec{u}_L - (\vec{u}_L\bullet\hat{n})\hat{n} \tag{3.8}$$

$$\vec{u}_R^t = \vec{u}_R - (\vec{u}_R\bullet\hat{n})\hat{n} \tag{3.9}$$

The velocity vector can then be decomposed into its corresponding components (u, v, w) in the Cartesian coordinates.

3.1.3.3   Freshly Cleared Cells

As the interface sweeps through the computational domain, a computational point which was previously inside the object (i.e. belonging to say phase 1) may now lie outside the object (i.e. belonging to phase 2) and vice versa. Identification of these points is straightforward once the levelset field is updated. Explicitly, points for which $\phi_i^n \phi_i^{n+1} < 0$ are tagged as "freshly cleared cells". Although the values with which the freshly cleared cells are populated are temporary (as they are overwritten in the correction procedure), depending on the location of these points, they may or may not participate in the interpolation procedure involved in constructing the Riemann problem. Hence it is required to update the flow and material properties belonging to these points at the beginning of each time step. There are several ways to update the properties of the freshly cleared cells. The easiest and the most direct method in the GFM framework adopted in this work is to copy the properties of ghost fluid variables at that point onto the real fluid properties.

3.2   Numerical Examples

3.2.1   One-Dimensional Examples

In this section a series of one-dimensional shock tube (of unit length) problems are presented. The initial condition corresponds to a singularity in flow variables that resolves into a transmitted and a reflected shock or expansion wave or both (depending on the impedance mismatch between the interacting fluids), and a contact discontinuity. The resulting contact discontinuity is tracked and represented as a sharp interface using the GFM approach.

For the one-dimensional test cases considered in this section, a computational domain corresponding to a shock tube of unit length and unit height was chosen. The grid spacing for one-dimensional simulations was set at $\Delta x = 1/200$ unless stated to the contrary. For LMR calculations, a base mesh of size $\Delta x_g = 0.02$ was used for the simulations and the solutions were evolved with three different (3, 4 and 5 levels of mesh refinement corresponding to fine mesh size $\Delta x_f = \frac{1}{200}, \Delta x_f = \frac{1}{400}$ & $\Delta x_f = \frac{1}{800}$ respectively) levels of mesh refinement.

3.2.1.1 Example 1 - Single Fluid Test Case

In this example, a set of one-dimensional test cases in a single fluid medium are considered.

CASE(A) : Sod's Shock Tube Problem

The initial conditions for this problem are given below:

$$(\rho, P, u, \gamma) = \begin{cases} (1.0, 10.0, 0.0, 1.4) \text{ for x} < 0.6, \\ \\ (0.125, 1.0, 0.0, 1.4) \text{ for x} \geq 0.6. \end{cases}$$

A fairly low pressure ratio, $\frac{P_2}{P_1} = 10$ was simulated. The typical solutions after 100 time steps are shown in Figure 3.3. The figure shows the comparison between Riemann GFM (henceforth R-GFM) and original GFM with isobaric fix. The solution obtained from traditional shock-capturing schemes (without explicit interface treatment) for the contact discontinuity is also shown in the figure. As is evident from the plots, the methods seem to produce results that conform to the exact solution. From the entropy plots both original GFM and R-GFM were found to suffer from slight over-heating errors at the interface. The

R-GFM yields a lower level of over-heating than the original GFM approach.

Next, the pressure ratio ($\frac{P_2}{P_1}$) was increased to 1000. Figure 3.4 shows that the original GFM severely over-predicts the density field near the contact discontinuity. The solution obtained from the R-GFM approach shows slight over-heating errors but over-all the shock, rarefaction and the contact align with the exact solution. As was pointed out in section 3.1.1, the initial large discontinuity in flow variables (density and pressure field in this case) results in a strong shock wave and a contact discontinuity traveling to the right, and an expansion wave traveling to the left. The initial velocity of the interface/contact discontinuity is very high, so that the interface stays in close proximity to the shock. Hence, during these few instances, the pressure and velocity field across the interface register jumps, which when copied directly onto the ghost points results in inaccurate representation of the Riemann states generated at the interface. On the other hand, the R-GFM approach resolves the wave patterns accurately and hence predicts shock and interface locations which agree well with the exact solution, as indicated by the enlarged view near the interface in Figure 3.4. Figure 3.4 also shows that the traditional shock-capturing approach results in smearing of the interface over a few grid cells, as opposed to the GFM approach which retains the interface as a sharp entity.

Comparing the over-heating errors incurred by the R-GFM and the original GFM approach, the R-GFM approach is found to incur lower over-heating errors as seen from Figures 3.3(b) & 3.4(b). In particular, Figure 3.4(a) shows that the over-heating errors incurred by the original GFM approach result in catastrophic oscillations in the density field and inaccurate predictions of the shock and interface locations. Thus it is clear that

even for a single fluid problem with strong discontinuity considered here, the original GFM approach fails to maintain a non-oscillatory flow field.

CASE(B) : Woodward Colella "Bang Bang" Problem

This problem was formulated by Woodward et al [200]. Unlike the previous case, this example involves strong shock reflections and collisions. The initial conditions for the problem are

$$(\rho, P, u, \gamma) = \begin{cases} (1.0, 1000.0, 0.0, 1.4) \text{ if x} < 0.1, \\\\ (1.0, 0.01, 0.0, 1.4) \text{ if } 0.1 \leq \text{x} \geq 0.9, \\\\ (1.0, 100.0, 0.0, 1.4) \text{ if } 0.9 < \text{x} \leq 1.0. \end{cases}$$

Reflective boundary conditions were applied at the two ends of the domain to enforce the presence of enclosing surfaces. The initial conditions set off strong shock waves that interact with each other. The solution obtained from the current simulation at T = 0.038 is compared with the reference solution. The reference solution corresponds to a fine grid calculation obtained without employing GFM. Only the solution obtained using R-GFM method is presented in Figure 3.5. The plots show that with increase in mesh resolution the R-GFM solution approaches the reference solution. The peak pressure and the maximum velocity matches well with the reference solution, especially with finer mesh resolution. The slight over-/under-heating errors found in the entropy plots displayed in Figure 3.5(d) are mitigated with improved mesh resolution.

The conservation errors (plotted in Figure 3.6) were minimal and localized to the instant when the shock impinged on the interface. As pointed out by Liu et. al [118] it

takes very few timesteps for the normal motion of the interface to resume after the impact of the shock.

3.2.1.2 Example 2

An example of a multi-material shock tube problem is the one-dimensional air-helium shock tube with the initial conditions given below:

$$(\rho, P, u, \gamma) = \begin{cases} (1.0, 1.0, 0.0, 1.4) \text{ for x} < 0.5, \\ \\ (0.125, 0.1, 0.0, 1.667) \text{ for x} \geq 0.5. \end{cases}$$

The plots of density, pressure, velocity and entropy after 100 time steps are displayed in Figure 3.7. As in the previous case, both versions of GFM under-predict the density near the interface. The insert shows the zoomed-in view of the density profile close to the interface. The interface position predicted by original GFM is shifted by two/three grid points relative to the exact solution. In contrast, the interface location predicted by the R-GFM approach is in line with the exact solution. The pressure and the velocity plots also show good agreement with the exact solution. The entropy plots show modest over-heating errors at the interface.

A Note on Conservation Error

A conservation error analysis was carried out for this problem. The total mass, momentum and energy conservation errors computed using the approach outlined by Wang et al [197], are presented in Figure 3.8. It was found that the conservation errors were noticeable only during the initial 4 - 5 time steps, when the shock wave was in the vicinity of the interface. This is consistent with the trend observed by Liu et al [118] and Hu et

al [87]. The conservation errors observed in this case are mainly due to the errors which are inherent in the GFM approach. These errors arise from the numerical flux computed based on the ghost field. The numerical flux computed at the interface does not ensure strict conservation. As shown in Figure 3.9, for all the bulk points explicit numerical flux conservation can be achieved easily. On the other hand, due to the ghost fluid treatment from each side of the interface and the construction of fluxes using the ghost field, it is not possible to compute a unique numerical flux crossing the cell boundary for the interfacial points. The errors generated due to the non-uniqueness in the numerical flux computed at the interface becomes significant when strong shocks or detonation waves impinge on the interface.

It was pointed out by Abgrall et al [6] that a non-oscillatory pressure field can be produced by methods that are not strictly conservative at the interface. Due to the intrinsic nature of the ghost fluid treatment, where the ghost field is populated via extension from the real fluid, it is not straightforward to devise a scheme in the ghost fluid framework that would completely annihilate these conservation errors. However, Glimm et al [66] have attempted to construct conservative fluxes by locally rearranging the cells cut by the interface and explicitly enforcing appropriate jump conditions to guarantee equality of the numerical fluxes at the cell interface. This procedure of dynamically removing the conservation errors at the interface is appealing and feasible for one-dimensional problems, but becomes extremely complicated when extended to multi-dimensional problems. A relatively simpler approach was proposed by Nguyen et. al [47]. In this approach, the conservation errors were alleviated by redistributing these errors to the numerical fluxes computed at the in-

terface, at the end of each RK sub-step. As pointed out by Hu et al [87], it is not readily apparent that such a post-processing measure to correct the conservation errors is effective, particularly when conservation errors have already been incurred in the previous RK time step. In this work, no such additional measures were enforced to conserve the numerical fluxes at the interface. Furthermore, the conservation error analysis carried out in this work points out that these errors are confined to very few time steps when the shock resides on/near the interface and were found to be benign from the viewpoint of stable computation over the overall time of calculation. As shown in the insert in the density plots, both the interface and the shock locations are captured to a good degree of accuracy, indicating that the conservation errors involved are spatially and temporally localized (close to the interface and to the duration of shock-interface coincidence), and do not pollute the bulk of the solution or the long term evolution of the flow field.

3.2.1.3 Example 3

The next example considered in this section is a gas-water shock tube problem. The initial conditions shown above is analogous to the one-dimensional version of an underwater explosion. Unlike the previous examples, the initial conditions are normalized with respect to the properties of water at ambient conditions and unit (1m) length scale. This example is taken from Tang et al [184]. The problem was also solved by Hu et al [87].

$$(\rho, P, u, \gamma) = \begin{cases} (0.01, 1000.0, 0.0, 1.4) \text{ for x} < 0.5, \\ \\ (1.0, 1.0, 0.0, 4.4) \text{ for x} \geq 0.5 \end{cases}$$

The configuration corresponds to a fast-slow interface as the shock wave is incident in a material with higher acoustic impedance. Due to high pressure ratio, a relatively strong shock wave is transmitted into the water medium and a weaker reflected shock wave in the air medium. The comparison between the numerical simulation obtained after 200 time steps with the corresponding exact solution are shown in Figure 3.10. The numerical solution closely follows the exact solution.

3.2.1.4   Example 4

The second in the series of the gas-water shock tube problem considered in this work is taken from Hu et al [87,88]. In comparison with the previous example, the pressure ratio for this problem is further increased by a factor of 10. The initial conditions are modified as

$$(\rho, P, u, \gamma) = \begin{cases} (0.5, 20000.0, 100.0, 2.5) \text{ for } x < 0.5, \\ \\ (1.0, 1.0, 0.0, 4.4) \text{ for } x \geq 0.5. \end{cases}$$

In this case, a much stronger shock is both reflected and transmitted. Figure 3.11 shows the plots obtained after 200 time steps. As in the previous case, both the reflected and transmitted shocks are captured precisely. The position of the contact discontinuity matches very well with that of the exact solution. These features indicate that the conservation errors generated, even in the case of stiff fluids, are negligible. Because of very large entropy disparities between the interacting media, the entropy plots do not reveal any significant over-/under-prediction of the flow properties.

3.2.1.5   Example 5

The next example considered is a water-air shock tube problem. The water medium is on the high pressure side and the air is maintained at ambient condition. The initial conditions normalized with respect to the ambient conditions of water are given below:

$$(\rho, P, u, \gamma) = \begin{cases} (1.3, 10000.0, 0.0, 4.4) \text{ for x} < 0.5, \\ \\ (0.001, 1.0, 0.0, 1.4) \text{ for x} \geq 0.5. \end{cases}$$

In this example the shock wave travels from the water side into the air side and hence can be categorized as a fast-slow interface [81]. Due to high impedance mismatch, a strong rarefaction wave is reflected in the water medium and a weak shock wave is transmitted in the air medium. The transmitted shock is extremely weak (the pressure ratio across the reflected rarefaction wave is much larger than the pressure ratio across the transmitted shock wave) and hence not readily visible from the density or pressure plots (Figures 3.12(a) & 3.12(b)). However, the entropy plots shown in Figure 3.12(d) show the jump across the transmitted shock in air. Also revealed by the entropy plots are the over-heating errors. Although the over-heating errors observed in this case are relatively large in magnitude, they are not significant enough to afflict the global solution. The computed position of the transmitted shock wave and the reflected expansion wave match well with the exact solution.

It is clear from the examples shown above that the R-GFM approach developed in this work is able to accurately resolve strong shock interactions with both gas-gas as well as gas-water interfaces. On the other hand, the original GFM approach generated unphysical oscillations in the flow field, and in some cases, resulted in complete break-down of the so-

lution (gas-water interfaces). In order for the original GFM approach to apply to gas-water interfaces, Fedkiw et al [33, 57] modified the GFM approach by extrapolating the velocity at the interface in the water medium and the pressure from the air medium to define the ghost states. However, such modifications would render the original GFM approach unsuitable for resolving gas-gas interfaces. In contrast, the methodology developed in this work is found to be robust and accurate in resolving multi-material interfaces without requiring special treatments at the interface. Furthermore, the plots shown in Figure 3.8 clearly indicate the the conservation errors and the resulting under-/over-heating errors incurred are localized close to the interface.

In the next few examples, shock tube problems involving multi-fluids are solved using dynamic mesh adaptation techqniue described in chapter 2.

3.2.1.6 Example 6

The next one-dimensional example considered in this work is taken from Hu et al [87]. The problem involves interaction between a relatively stiff fluid and helium. The pressure and density ratio for this problem are also higher than considered before. The initial conditions for this problem are given below :

$$(\rho, P, u, \gamma) = \begin{cases} (0.384, 100.0, 27.077, 1.667) \text{ for x} < 0.6, \\ \\ (100.0, 1.0, 0.0, 3.0) \text{ for x} \geq 0.6. \end{cases}$$

The simulation was carried out up to a time T = 0.03 units. The values selected for the refinement criteria are $\delta_1 = 5.0$ and $\delta_2 = 100000.0$ (arbitrary large value). The variation of typical flow variables are compared with the exact solution in Figure 3.13. The agreement

between the two solutions is good. The contact discontinuity is resolved sharply within a mesh cell without oscillations in the pressure field. The width of the shock wave is confined to 2-3 mesh cells (for 5 levels of refinement). In addition, the locations of the shock, contact discontinuity and the rarefaction waves match very well with the exact solution. The L_2 errors for the flow variables are displayed in Table 3.1. As can be verified from the table, the L_2 errors and the difference in L_2 errors (ΔL_2, computed with respect to the corresponding fine mesh calculations) decrease with increase in the levels of mesh refinement.

3.2.1.7   Example 7

A shock-tube problem involving air and water is solved. The problem is taken from Wang et al [196]. The initial conditions for the problem are given below:

$$(\rho, P, u, \gamma) = \begin{cases} (1.27, 8000.0, 0.0, 1.4) \text{ for x} < 0.5, \\ (1.0, 1.0, 0.0, 5.5) \text{ otherwise.} \end{cases}$$

The solution is evolved to time T = 0.0015 units. The values selected for the refinement criteria are $\delta_1 = 100.0$ and $\delta_2 = 100000.0$ (arbitrarily large value). The results from the calculations are displayed in Figure 3.14. As can be seen from the figure, the transmitted shock wave and contact discontinuity along with the reflected rarefaction wave are captured accurately. The entropy plot (Figure 3.14(d)) reveals modest over-heating errors generated at the interface. As expected, the over-heating errors decrease with increase in the levels of mesh refinement. In addition, the over-heating errors are concentrated close to the interface and are not visible in the density plots. The L_2 errors displayed in Table 3.1 show that the errors incurred in density field are 3 orders of magnitude lower than the errors incurred in

the entropy field. Furthermore, it can be verified that the errors decrease with increase in mesh refinement levels. The over-/under-heating errors generated in the current approach are consistent and problem independent, and have been well documented in previous examples.

3.2.1.8 Example 8

The gas-water shock tube problem considered in this section is taken from Hu et al [87, 88]. The initial conditions are modified as

$$(\rho, P, u, \gamma) = \begin{cases} (0.5, 20000.0, 100.0, 2.5) \text{ for x} < 0.5, \\ \\ (1.0, 1.0, 0.0, 4.4) \text{ for x} \geq 0.5. \end{cases}$$

The initial configuration resolves itself into a strong shock wave transmitted into air and a strong shock wave reflected into water. Figure 3.15 shows the plots obtained after time T = 0.001 units. The values selected for the refinement criteria are $\delta_1 = 100.0$ and $\delta_2 = 100000.0$ (arbitrary large value). Both the reflected and transmitted shocks are captured accurately. The entropy and the density plots do not reveal any significant over-/under-heating errors. The position of the contact discontinuity and the location of the shock wave matches very well with that of the exact solution. This indicates that the conservation errors incurred, even for interfaces separating fluids with high impedance mismatch, is negligible. As pointed out in section 3.2.1.2, the conservation errors incurred are intrinsic to the GFM approach [47, 66, 87, 88, 197], and hence cannot be entirely annulled.

3.2.2 Two-Dimensional Examples

3.2.2.1 Spherical Riemann problem

First in the multi-dimensional test cases presented in this work is the single phase spherical Riemann problem. The initial conditions for this problem are given below:

$$(\rho, P, u, v, \gamma) = \begin{cases} (1.0, 5.0, 0.0, 0.0, 1.4) \text{ for} \sqrt{x^2 + (y - 0.5)^2} \leq 0.2, \\ \\ (1.0, 1.0, 0.0, 0.0, 1.4) \text{ otherwise.} \end{cases}$$

The one-dimensional problem in spherical coordinates is reconstructed in cylindrical coordinates (axisymmetric form) as shown in Figure 3.16. The center of the spherical discontinuity is located at (0.0,0.6) and a pair of reflecting walls (also modeled as embedded objects) are located at y = 0.1 and y = 1.1. Reflective Boundary Condition (RBC) augmented with a Riemann solver was employed to model the reflecting walls and the R-GFM was used to model the initially spherical contact discontinuity. Euler equations in axisymmetric form were solved in a 1.5 × 1.2 domain with 600 × 450 points. The simulations were carried out both with (R-GFM) and without explicit interface treatment (i.e. using ENO shock-capturing) for the contact discontinuity. The simulations were carried out till T = 0.8. The initial condition corresponds to a jump in pressure in the radial direction. This results in an inward moving expansion wave, an outward moving shock wave and a contact discontinuity. Figure 3.17 shows that the R-GFM is able to resolve the contact discontinuity accurately without modifying the overall wave structure and their relative positions. The solution obtained from the R-GFM follows closely the trend observed by the shock-capturing schemes with no explicit interface treatment. Moreover, the enforcement of the sharp interface treatment accentuates weak features that are lost in the single-field

simulation. As pointed out by Langseth et al [111], the non-physical zone developed due to wave focusing is visible at the center in both solutions. For a quantitative comparison, the variation of density and pressure along the centerline (at y = 0.6) at T = 0.5 are shown in Figure 3.18. The plots are in close agreement with each other.

3.2.2.2 Shock Interacting with Cylindrical Helium Bubble in Air

CASE A : Mach 1.22 Shock interacting with Helium Bubble in Air

The interaction of shock waves with gas bubbles have applications ranging from astrophysics [37, 140] to cavitation damage of human tissue (shock wave lithotripsy) [92]. The example considered in this section corresponds to the interaction of a Mach 1.22 shock with a cylindrical Helium bubble in air. The configuration of this multi-component system provides a weak shock interacting with fluids of varied stiffness. Haas et al [75] considered shock waves interacting with R-22 refrigerant and Helium bubbles. They provided a series of experimental observations which were later verified numerically by Quirk et al [147] and several others [16, 58, 87, 98, 125]. The initial conditions for this problem are such that a Helium bubble of 50 mm radius resides in thermal equilibrium with surrounding air at ambient conditions. The initial conditions normalized based on the property of air at 1 atm and length scale 1 mm are

$$(\rho, P, u, v, \gamma) = \begin{cases} (1.3764, 1.5698, -0.394, 0.0, 1.4) \text{ for post-shocked air i.e.} x \geq 225, \\ (1.0, 1.0, 0.0, 0.0, 1.4) \text{ for pre-shocked air}, \\ (0.138, 1.0, 0.0, 0.0, 1.667) \text{ for} \sqrt{(x-150)^2 + y^2} \leq 25 \end{cases}$$

The computational domain (325×89) is similar that used by Fedkiw et al [58]. The top and bottom of the domain are prescribed with reflective boundary conditions. The right end of the domain is prescribed with a Dirichlet inflow condition corresponding to post-shocked air and the left end with Neumann outflow condition. The grid spacing $\Delta x = 0.25$.

As the speed of sound in Helium is faster than in the surrounding air, the system can be classified as a slow-fast interface. [3]. Hence, the impinging shock results in a refracted shock wave and a reflected rarefaction wave. As mentioned in Johnsen et al [98], the refracted shock, upon reaching the other end of the bubble, further degenerates into a weaker reflected shock wave and a transmitted shock in air. This process of reflection continues until the resulting wave system degenerates into a weaker wave system [98]. The numerical Schlieren image and density contours generated from the current simulation are shown in Figures 3.20 & 3.21 respectively. Figures 3.20(a) & 3.21(a) show the transmitted shock wave and the reflected expansion. It is clear from the figure that the refracted shock inside the Helium bubble travels faster than the incident shock. Figures 3.20(b) & 3.21(b) show the transmitted wave from the Helium bubble and the incident shock in air. The multiply reflected weak wave system inside the Helium bubble is also clearly visible. A closer examination of the figure depicts the initial stage of jet formation at the center of the bubble. The jet becomes more clearly visible in Figures 3.20(c) & 3.21(c). The bubble has now taken the familiar kidney bean shape. Not so readily visible features in Figures 3.20(c) & 3.21(c) are the Kelvin-Helmholtz instability [125] reported on the surface of the bubble. These features may become evident with increase in mesh resolution. Finally, in Figures 3.20(d) & 3.21(d), the bubble is shattered into fragments due to the impact of the jet. It is worth

noting that the giant vortical structures reported by Marquina et al [125] are not readily visible in the current simulation. The reason is that Marquina et al have used an extremely fine mesh (8000 X 600) and a front capturing technique which adds sufficient amount of numerical diffusion at the interface to capture these vortical structures and the associated Kelvin-Helmholtz instability. The plots of density and pressure along the horizontal line of symmetry, along with the pressure history registered at a distance 3 mm downstream of the initial bubble location are displayed in Figure 3.22.

CASE B : Mach 6 Shock interacting with Helium Bubble in Air

In this example, the Mach number of the impinging shock wave is increased to M = 6. The configuration of the system, including the domain boundary conditions and the grid resolution, are the same as in the previous case. The initial conditions are modified as :

$$(\rho, P, u, v, \gamma) = \begin{cases} (5.268, 41.83, -5.752, 0.0, 1.4) \text{ for post-shocked air i.e.} x \geq 225, \\ (1.0, 1.0, 0.0, 0.0, 1.4) \text{ for pre-shocked air}, \\ (0.138, 1.0, 0.0, 0.0, 1.667) \text{ for} \sqrt{(x-150)^2 + y^2} \leq 25 \end{cases}$$

Bagabir et al [16] have analyzed the response of a gas bubble to shocks of different strengths. In their work, the computations were carried out for a single component flow (with $\gamma = 1.4$) system. Hu et al [88] carried out the corresponding multi-component flow simulation with a helium bubble and air.

The snapshots of the numerical Schlieren image from the current simulations are displayed in Figure 3.24. Since the refracted shock wave travels faster inside the bubble, it reaches the rear end of the bubble before the incident shock wave. The shock wave is then

transmitted to the air medium which is at rest. In the previous case, this transmitted shock wave coalesces with the incident shock wave to form a single planar shock wave that travels in the air medium. In this case, because of the time lag developed due to greater celerity of shock wave inside the bubble, the incident shock wave cannot coalesce with the transmitted shock wave, leaving behind a curved shock front from the transmitted shock attached to the planar incident shock wave. The strength of the incident shock is high enough to impart sufficient momentum to the helium bubble to drag the bubble along with it. As a result of this, the location of the shock and the interface are always in close proximity to each other. Moreover, the resultant changes on the topology of the interface are so intricate that the bubble shatters into tiny fragments due to the impact of the jet. The topology of the interface at different instants in time are displayed in Figure 3.25. At time T = 15.3 μs, the transmitted shock deforms the front portion of the bubble leaving the leeward side unaffected. At T = 38.25 μs, the shock has traversed most part of the bubble and at time t = 61.2 μs the bubble starts to deform. At T = 78 μs, the bubble has deformed completely and starts to form fragments. Once such fragments are formed, it is not possible to continue the simulation without employing special mesh enrichment techniques. Hu et al [88] have carried out their simulation by explicitly deleting small pockets of mass. No such additional measures were taken in this work; given the limitations of a uniform non-adaptive mesh, the results obtained are in close agreement with that of Hu et al [88].

3.2.2.3 Underwater Explosion Near a Free Surface

Numerical simulation of an under-water detonation of gaseous products near a free surface is considered in this section. Analysis for this application have been carried out in the past by several authors [38, 73, 117, 136]. The initial configuration of the system as outlined in Liu et al [117] is shown in Figure 3.26. A cylindrical gaseous explosive core of unit radius is located 3 units below the free surface, at the center of a 12 X 12 domain. The initial conditions are normalized with properties of water at 1 atm and with length scale 0.1m (the initial radius of the core). The time sequence of the configuration of the system is shown in Figure 3.27. The explosion sets off a cylindrical shock front advancing away from the core. Due to large impedance mismatch between the air - water interface at the free surface, a relatively weak shock wave is transmitted into the air medium and a "relief" wave in the form of strong rarefaction wave propagates towards core in the water medium [38, 117]. The flow features resulting from this explosion are symmetrical until $T = 0.00892$. It is at this instant that the reflected rarefaction wave interacts with the explosive core. At $T = 0.024$, the free surface is deformed due to the impact of the incident shock wave. The expansion wave generated in the water has interacted with the bubble and produces a reflected compression wave (which eventually turns into a shock wave) and an expansion wave inside the bubble [38]. Due to the interaction of the relief wave with the bubble, the top portion of the bubble accelerates towards the free surface distorting it from its initial shape to an elongated 'egg-like' shape. Also visible at this instant is reflected shock wave at the bottom of the domain due to the impact of the initial shock wave from the explosion. At $T = 0.045$, this reflected wave interacts with the bottom of the bubble

further distorting the shape of the bubble.

3.2.2.4   Shock Loading on a Submerged Structure due to an Underwater Explosion

The next problem considered in this section is the evolution of an underwater explosion and its impact on a submerged structure. A square structure submerged in water is impacted by a circular shock wave generated by an explosion. The shock wave imparts severe loading on the structure which could potentially damage the structure. This is a multi-material flow problem consisting of multiple interfaces: air-water, gas-water and solid-water interface. For the fluid-fluid interfaces, the methodology discussed in the previous sections was adopted to define the ghost states. For the solid-fluid interface, the Reflective Boundary Condition (RBC) augmented with a Riemann solver was used to construct the ghost field. This problem is discussed at length in Liu et al [119]. The explosive core of 0.1 m radius is located at (1.5,2.0) in a 6m $\times$ 6m domain. The free surface separating water from air is located at Y = 5.0. The square structure with length = 1.0m is located at the center of the domain. The flow conditions, normalized with properties of water at ambient conditions, are

$$(\rho, P, u, v, \gamma) = \begin{cases} (1.27, 9000.74, 0.0, 0.0, 1.4) \text{ for the core}, \sqrt{(x - 1.5)^2 + (y - 2.0)^2} \leq 0.1, \\ \\ (1.0, 1.0, 0.0, 0.0, 5.5) \text{ for quiescent water}, y < 5.0, \\ \\ (0.001, 1.0, 0.0, 0.0, 1.4) \text{ for ambient air}, y \geq 5.0. \end{cases}$$

The bottom of the domain is prescribed with reflective boundary condition and the top, right and the left boundaries are prescribed with Neumann conditions. The explosion sets off a circular shock wave that interacts with the structure and later with the free surface.

The incident shock impacts first on the bottom and the left face of the square structure resulting in a complex shock diffraction pattern as shown in Figure 3.29. Figures 3.29(a) & 3.29(b) shows the shock diffracting of the structure along with the vortices produced at the top left and the bottom right corner. At this stage, the shock has not impacted the free surface. The inward traveling expansion wave and the contact discontinuity separating the explosive core from water are also clearly visible. The shock wave reflected off the bottom wall of the domain can be seen advancing towards the explosive core. Figures 3.29(c) & 3.29(d) show the plots at a later instant in time. The shock wave has impacted the free surface and the reflected expansion wave traveling in the water medium and the transmitted shock wave in air are clearly visible. The reflected shock wave from the bottom wall of the domain has now reached the explosive core, deforming its shape.

The net horizontal and vertical force components were computed by integrating the pressure force acting on the structure. The force components exerted on the square structure are plotted are shown in Figure 3.30. The horizontal and the vertical force components have the same form and they overlap with each other until $T = 0.017$. This is expected because the wave structure resulting from the initial shock impact (on the bottom and the left wall) is symmetric with respect to the structure. Later in time, the vertical force is considerably modified due to the strong reflected rarefaction wave from the free surface and hence begins to depart from the horizontal component. The moment exerted on the structure due to these forces was also computed and plotted in Figure 3.30. For a quantitative comparison, the force components computed from the current simulation are compared with those obtained by Liu et al [119]. Liu et al [119] have used MGFM to resolve the fluid-fluid interface and

symmetry based RBC (developed by Forrer et. al [62]) for the solid-fluid interface. As shown in Figure 3.31, the results from the present simulation compare very well with those of Liu et al [119].

3.2.2.5   Richtmyer-Meshkov Instability (RMI)

The next example presented in this work is the evolution of the single mode Richtmyer-Meshkov instability (RMI). The problem consists of an embedded fluid-fluid interface impacted by a shock. The R-GFM approach outlined in chapter 3 is used to capture the interface conditions. The problem set up is the same as that of Nourgaliev et al [136]. A computational domain of length 4 units and height 1 unit is chosen. The top and the bottom portions of the domain are prescribed with reflective boundary conditions, depicting the presence of walls of the shocktube. The right and the left sides are imposed with Neumann conditions. The unperturbed interface separating SF_6 and air is initially located at $x_I = 2.9$. A perturbation with maximum magnitude $\epsilon = 0.1$ and wavelength $\lambda = 1$ is imposed over the interface as given below:

$$\phi(x) = x_I - x - \epsilon SIN(2\pi(\frac{y}{\lambda} + \frac{1}{4}))$$

A planar shock corresponding to Mach 1.24 is initially located at $x_s = 3.2$ with the conditions as follows:

$$(\rho, P, u, v, \gamma) = \begin{cases} (1.628, 1.411, -0.39, 0.0, 1.4)\,\text{x} \geq 3.2, \\\\ (1.0, 1.0, 0.0, 0.0, 1.4)\,\phi(x_I) \geq \text{x} < 3.2 \\\\ (5.04, 1.0, 0.0, 0.0, 1.093)\,\text{x} < \phi(x_I) \end{cases}$$

The problem was simulated with a base mesh of size $\Delta x_g = 0.02$ with 3 levels of mesh refinement. The threshold limit for the refinement criteria (δ_1 & δ_2) were set to 10.0 and 10000.0 (arbitrary large value) respectively. The fine mesh size corresponds to 200 points per unit wavelength of the perturbation. In Figure 3.32(a), the density contours obtained from the current LMR calculations are juxtaposed over the corresponding uniform fine mesh calculation. Except for minor discrepancies observed in the coarse mesh regions, the global flow structure along with the shock and the interface locations are captured to a good degree of accuracy. The $L_2(\rho)$ error computed at the instant shown in the figure (Figure 3.32(a)) for this simulation is 3.923×10^{-4}. The evolution of the interface at different instants in time is displayed in Figure 3.32. As reported in [136], the barotropic generation of vorticity and the eventual rollups are evident. The contours of density and the mesh evolution are displayed in Figure 3.33. As can be seen from the figure, the mesh adaptation follows the interface and the shock maintaining high precision around discontinuities, with coarse base mesh elsewhere. The OR for this calculation is only 5%, resulting in savings in computational memory.

3.2.2.6 Mach 1.22 Shock Interacting with Cylindrical (R_{22}) Gas Bubble

High resolution computation of a weak shock (Mach 1.22) interacting with a cylindrical R_{22} bubble in air is considered. The initial planar shock is located at x = 155 mm in a computational domain of size 200 mm $\times$ 44.5 mm. The cylindrical bubble of diameter 50 mm is initially located at x = 125 mm. Due to the symmetry of the problem only one half of the bubble was modeled. The initial conditions for the shocked and un-shocked air

along with the conditions inside the bubble are given below:

$$(\rho, P, u, v, \gamma) = \begin{cases} (1.3764, 1.5698, -0.394, 0.0, 1.4) \text{ x} \geq 155.0, \\ (1.0, 1.0, 0.0, 0.0, 1.4) \text{ x} < 155.0 \\ (3.15385, 1.0, 0.0, 0.0, 1.249) \sqrt{(x-125)^2 + (y)^2} \leq 50 \end{cases}$$

The right end of the domain is prescribed with the Dirichlet condition corresponding to the post-shocked air. The left end of the domain is prescribed with Neumann conditions, the top and bottom portions of the domain with reflective conditions. The simulations were evolved with a base mesh $\Delta x_g = 1.0$, with 4 levels of mesh refinement (corresponding to 800 points per diameter). Due to the weak strength of the shock, the threshold for the refinement criteria were set at $\delta_1 = 0.01$ & $\delta_2 = 0.01$.

Since the impedance offered by the R_{22} bubble is comparable to that of post-shocked air ($(\rho c)_{R_{22}} - (\rho c)_{air} \approx 0.09$), the shock-interface interaction resolves into a transmitted shock wave and a reflected shock wave. As the speed of sound is greater in the air medium, the incident shock wave travels faster than the weak refracted wave system (Figures 3.34(a) & 3.34(b)). Furthermore, the velocity of air behind the incident shock wave is greater than the velocity behind the transmitted shock wave inside the bubble. As pointed out in [2], this velocity difference introduces a counter-clockwise torque on the interface of the bubble which later develops into Kelvin-Helmholtz (KH) instability at the interface. In addition, the interface is also subjected to Richtmyer-Meshkov instability (RM) due to the interaction of the shock system with the curved front of the bubble. The unstable interface eventually rolls up to form vortices and fragments of vortices on the interface (Figures 3.34(c) & 3.34(d)). To accurately resolve these vortical structures generated on

the interface, extremely fine grid resolution is required as the sharp interface calculations are devoid of numerical diffusion phenomena that are common with approaches such as the diffuse interface approaches [38, 125]. As shown in Figure 3.34(d) & 3.35(b), with the current LMR scheme the vortical patterns and the shock systems are captured. Also seen in the figure is the R_{22} jet formed in the trailing edge of the bubble. As pointed out in [2], due to the formation of the compression wave inside the bubble and the focussing effect of the incident shock wave, there is a steep rise in the pressure at the trailing edge of the bubble. This steep rise in pressure causes the onset of a jet at the trailing edge of the bubble. In Figure 3.35, the topology of the interface at different instants in time are plotted. The figure clearly shows the instabilities and the R_{22} jet formed on the interface. The dynamic adaptation of the mesh is apparent from Figure 3.34. The occupancy ratio computed for this simulation is 17.3 %.

3.2.2.7 Shock Interacting with Spherical Water Droplet

Shock-droplet interaction is a typical multi-material problem with wide range of applications such as corrosion effects on turbine blades, fuel-coolant interaction in nuclear reactors, ablation of space vehicles during re-entry etc. [39]. Effect of planar shock waves interacting with *cylindrical* water column(s) have been investigated and well documented in the past [38, 39, 89, 136]. Here the interaction of planar shock waves with a *spherical* water droplet suspended in ambient air is investigated. Three different shock strengths, Mach 1.47, 3.0 and 6.0 are considered. The spherical liquid mass of radius 0.105 mm is located at (0.0,0.5) in a 0.5 mm × 1.0 mm domain. Euler equations in the axisymmetric

form are solved for this problem. The simulations are carried out on a base mesh of size $\Delta x_g = \frac{1}{200}$ with 3, 4 and 5 levels of mesh refinement (corresponding to 5.12 million grid points for the finest level).

The shock systems observed for the interaction of planar shock wave with spherical and cylindrical droplets are identical, except for the strengths of the reflected and refracted shock systems. The configuration forms a curved gas-liquid slow-fast interface [136]. As pointed out in [39], the shock wave upon impacting the water column transmits only a small fraction of the energy into the water medium due to large acoustic impedance. As a result of this impedance mismatch, a reflected and a refracted shock systems are generated. The refracted weak shock wave on the water side travels faster than the incident shock wave and is reflected back as a "relief wave" by the curved interface. As pointed out by Chang et al [38], due to the curvature of the interface these rarefaction waves later coalesce to form a shock wave. Thus the refracted shock wave gets trapped inside the water column by undergoing multiple reflections off the curved interface and hence does not affect the surrounding air. In what follows, the shock diffraction patterns generated for different shock strengths are briefly examined.

Effect of Mach 1.47 Shock Interacting with Spherical Water Droplet:

The threshold for the refinement criteria were set at $\delta_1 = 1.0$ and $\delta_2 = 75.0$. The results from the current calculations with 5 levels of mesh refinement are displayed in Figure 3.36. The reflected, refracted and the incident shock systems along with the "peeling off" effect on the bubble (reported in [136]) are clearly visible. In Figure 3.36(d), the pres-

sure distribution along the axis of symmetry are plotted for both the cylindrical and the spherical bubble. In comparison with the cylindrical water column, the strengths (pressure ratio) of the reflected and the transmitted shock waves are significantly lower for the spherical droplet (three-dimensional effect). Figure 3.36(d) also confirms the mesh independence of the solution. The OR for this calculation is 10.0 %.

To validate the current approach, a comparison of the unsteady drag coefcient computed on the surface of a cylindrical droplet is presented in Figure 3.37. The drag coefficient is compared with that of Igra et al [89], Chen [39] and Terashima et al [187]. The drag coefficient distribution predicted with the current method is in good agreement with available solution.

Effect of Mach 3 Shock Interacting with Spherical Water Droplet:

For the Mach 3 shock wave, the threshold for the refinement criteria were increased to $\delta_1 = 10.0$ and $\delta_2 = 150.0$. The results from the present calculations with 4 levels of mesh refinement are shown in Figure 3.38. The reflected shock wave in the air side forms a "bow shock", similar to that of the shock negotiating a solid obstacle, which travels upstream to transform to a Mach reflection. Figure 3.38 verifies the features of this peculiar type of anomalous refraction [136]. During the initial stages of shock interaction, a striking similarity was observed with the wave patterns generated by the shock wave diffracting a solid cylinder (results for shock negotiating cylindrical obstacle are presented in section 5.3.2.3). The initial Regular Refraction transforms to Mach Reflection forming a Mach stem (Figure 3.38(a)). In Figure 3.38(d), the shock systems for the cylindrical and the spherical

droplet are compared. The enlarged view shown in the insert confirms the formation of the Mach stem and the roll up of the slipline emanating from the Mach stem. The OR for this calculation is 11.3 %.

Effect of Mach 6 Shock Interacting with Spherical Water Droplet:

The threshold for the refinement criteria were set at $\delta_1 = 10.0$ and $\delta_2 = 150.0$. The shock diffraction patterns for this case are displayed in Figure 3.39. A double Mach reflection system, as opposed to a single Mach system, is formed. The double Mach stem is not visible in Figure 3.39(a), but is visible in Figure 3.39(c) with additional mesh resolution (with $\Delta x_f = \frac{1}{3200}$). The pressure distribution along the line of symmetry displayed in Figure 3.39(d) confirms convergence of solution with mesh refinement. The increase in refinement level only accentuates fine structures that are otherwise not visible. The strengths of the reflected and refracted shock systems are comparable. The OR for this calculation is 13.3 %.

3.2.2.8 Collapse of Cylindrical Air Cavity in Water

In this example, numerical computation of the experimental work carried out by Bourne et al [28] is presented. Numerical analysis for this problem has been performed and reported in the past [18, 73, 80, 87]. The initial configuration of the system is given

below:

$$(\rho, P, u, v, \gamma) = \begin{cases} (1.31, 19000, 67.32, 0.0, 5.5) \text{ for post-shocked water i.e.} x \leq 2.6, \\[2mm] (1.0, 1.0, 0.0, 0.0, 5.5) \text{ for pre shocked water i.e.} x > 2.6, \\[2mm] (0.0012, 1.0, 0.0, 0.0, 1.4) \text{ for } \sqrt{(x-6)^2 + (y-6)^2} \leq 3 \end{cases}$$

A cylindrical air cavity of 6 mm diameter, which is located at the center of the computational domain, is impacted by a strong shock corresponding to a pressure ratio of 19000. The shock wave impacting the cylindrical cavity resolves to form a strong reflected "relief" wave and refracted shock wave. In Figure 3.40, the numerical Schlieren image at the time of break-up (t = 0.0316) is displayed. The reflected rarefaction wave generates a high velocity jet which impacts the air cavity, which in turn generates an intense blast wave that splits the air cavity. The numerical Schlieren image reveals oscillations in the density field close to the interface. These oscillations are present only close to the interface which indicates that these are numerical artifacts arising from the interface treatment technique and are not physical phenomena. In order to investigate the underlying cause for these oscillations, the one-dimensional version of the problem is analyzed. The initial conditions for the one-dimensional case are as follows:

$$(\rho, P, u, v, \gamma) = \begin{cases} (1.31, 19000, 67.32, 0.0, 5.5) \text{ for post-shocked water i.e. } x \leq 0.5, \\[2mm] (0.0012, 1.0, 0.0, 0.0, 1.4) \text{ for un-shocked air i.e } x > 0.5 \end{cases}$$

A strong shock corresponding to a pressure ratio of 19000 resides on the interface separating water and air. The initial conditions correspond to a water-air shock tube problem which resolves into a weak shock wave traveling in air and a strong rarefaction wave into the water medium, similar to the two-dimensional version considered above.

Figure 3.41 shows the density and the pressure variation for this case. As can be seen from the insert in the figure, both density and pressure fields are under-predicted. It was shown in section 3.2.1, that the approach adopted in this work results in (like other GFM approaches) consistent over-/under-heating errors that were found not to be problem dependent. However, in this case, due to the sensitivity of the stiffened equation of state employed for water, a small perturbation in the density field (and in the internal energy field) may result in a negative pressure field. As the material properties of water are such that it can sustain tensile stresses provided the pressure field remains above a certain critical limit, the computed sound speed is well within the realistic regime and hence does not cause the break-down of the simulation. Moreover, the negative pressure is observed close to the interface indicating that these undershoots are truly due to numerical errors introduced by the interface treatment technique. Furthermore, these under-predictions in the flow variables were found to decrease with grid refinement demonstrating a strong dependence on the mesh resolution. Thus it is believed that the oscillations revealed by the two-dimensional simulation and the corresponding under-shoots in the pressure and density fields in the one-dimensional version, are due to the numerical errors generated at the interface by the interface treatment technique employed.

The problem is now repeated here with dynamic mesh adaptation. In this simulations, a base mesh of size $\Delta x_g = 0.16$ was chosen with 4 levels of mesh refinement (with effective grid resolution of about 1.44 million points). The threshold for the refinement criteria were set at $\delta_1 = 1000.0$ and $\delta_2 = 1000000.0$ (arbitrarily large value). The reflected relief or expansion wave in the water medium, and the transmitted shock wave in the cavity

are visible in Figure 3.42(a). The pressure ratio across the transmitted shock wave is 33.28 which is 570 times smaller than the pressure ratio across the incident shock wave. Since a strong expansion wave is reflected off the cavity surface, in addition to capturing the wave patterns near the air cavity, attention is also paid in capturing the large gradients across the reflected expansion waves. Figures 3.42(a) & 3.42(d) show that the mesh evolution follows the head and tail of the rarefaction wave in addition to the transmitted and the incident shock waves. The formation of water jet at the center of the bubble is clearly visible in Figure 3.42(b). The high speed jet of water results in splitting the air cavity which in turn sends out a blast wave (Figure 3.42(c)). The enlarged view of the numerical Schlieren image and the Mach contours at the instant at which the splitting occurs are displayed in Figures 3.43(a) & 3.43(b) respectively. Figure 3.43(d) shows the velocity of the tail (rear end) of the cavity as a function of time. The velocity of the water jet at the instant of collapse is about 2.82 km/s which agrees with the values 2.8 km/s and 2.85 km/s reported by Hu et al [87] and Nourgaliev et al [136] respectively. The topology of the interface at different instants in time are plotted in Figure 3.43(d). The plots are in good agreement with that of Hu et al [87]. Since emphasis was made in capturing weak - strong gradients occurring near the head and tail of the strong reflected wave, the OR computed for this simulation is 46.6 %.

3.2.2.9 High Speed Impact of a Liquid Droplet

In this example, high speed impact of a liquid droplet over a flat substrate is considered. Impact of high speed droplets and the resultant wave mechanisms are important

in thermal spray and coating technologies [40, 78]. A 200μm diameter liquid droplet is injected with a high velocity of 500 m/s, towards a rigid flat substrate located at the bottom. The initial conditions, normalized with respect to the properties of surrounding air are given below:

$$(\rho, P, u, v, \gamma) = \begin{cases} (1000.0, 1.0, 0.0, -1.571, 5.5) \text{ for the liquid droplet,} \\ \\ (1.0, 1.0, 0.0, -1.571, 1.4) \text{ for the surrounding air.} \end{cases}$$

Figure 3.44 shows the geometrical setup for this problem. The left boundary is prescribed with a symmetry condition and the bottom boundary with reflective wall boundary condition. The top and the right boundaries are prescribed with a Neumann condition. Euler equations in the axisymmetric form are solved. Haller et al [76–79] have provided a detailed survey of this problem. They have provided theoretical predictions for the jetting time that matched well with their corresponding numerical model. However, it is not clear from their analysis how the surrounding air was modeled. In this example the flow inside the droplet as well as in the surrounding air is considered; i.e. both the droplet and the surrounding air are injected with the same velocity towards the wall. The snapshots of the numerical Schlieren image from the current simulation are shown in Figure 3.45. The fluid droplet, after impacting the rigid substrate, moves off the surface at right angles to its approach path. This tangential movement of the droplet is due to the momentum transfer from the droplet to the impacted surface [212]. The jetting of the droplet continues until all of its kinetic energy is lost in the process. This is in direct contrast to the impact of an elastic object, such as an elastic ball, which rebounds after transferring its momentum to the impacted surface [212]. The figures indicate that most of the key features such as

lateral jetting of the liquid droplet along the contact edge, the shock wave traveling in the droplet and in the surrounding air, the reflected rarefaction wave and focusing of the rarefaction wave at the top end of the droplet are captured well. It is worth mentioning that the fine mesh calculation shown in this example were carried out with roughly million points (935000 grid points) which is half the number of mesh points used by Haller et al (2 million grid points) who used a front tracking solution procedure (FronTier) due to Glimm et al [64, 65].

The above calculations are repeated with mesh adaptation. The solution is evolved with 4 levels of refinement on a base mesh of size $\Delta x = 1.75 \mu m$ (an effective resolution of 1.13 million grid points). The snapshots of the numerical Schlieren image from the current simulation are shown in Figure 3.46. The mesh adaptation to the shock diffraction features is evident in the figure. The solution also agrees well with the non-LMR calculation presented in Figure 3.46

3.3 Conclusions

The interaction of strong shock waves with embedded fluid-fluid interfaces in compressible flows was studied. The interface is retained as a sharp entity by virtue of the Ghost Fluid Method (GFM). The failure of the original GFM, particularly with strong shock interactions was demonstrated. It was shown earlier that solving a local Riemann problem at the interface alleviated the pitfalls encountered by the original GFM approach. Hence in this work, a simple procedure to incorporate the Riemann problem at the interface was developed. The method was found to be robust in handling shocks of varied magnitude

interacting with both gas-gas and gas-liquid interfaces. The (mass, momentum and energy) conservation error analysis carried out for this method reveal that these errors are significantly attenuated and localized close to the interface. Under-/Over-heating errors are mitigated but not entirely eliminated by the present approach. This is due to the intrinsic non-conservative nature of the ghost fluid approach in treating sharp interfaces. The proposed method was shown to generate satisfactory solutions for several complex configurations and shocks interacting with single and multiple interface(s); shocks interacting with droplets, bubbles and free surface have been computed.

L_2	$\Delta x_{fine} = \frac{1}{200}$ (3 Levels)			$\Delta x_{fine} = \frac{1}{400}$ (4 Levels)			$\Delta x_{fine} = \frac{1}{800}$ (5 Levels)		
	LMR	U-Mesh	ΔL_2	LMR	U-Mesh	ΔL_2	LMR	U-Mesh	ΔL_2
Example 6									
$L_2(\rho)$	0.3655	0.3654	0.0001	0.2427	0.2427	-	0.1217	0.1217	-
$L_2(P)$	2.236	2.233	0.003	1.576	1.573	0.003	0.8256	0.8239	0.0017
$L_2(u)$	0.1146	0.1144	0.0002	0.074	0.074	-	0.0392	0.039	-
$L_2(S)$	0.732	0.732	-	0.425	0.425	-	0.2203	0.22	0.0003
Example 7									
$L_2(\rho)$ E-2	8.291	8.296	147.6	3.476	3.473	32.9	1.943	1.940	28.544
$L_2(P)$	23.07	23.076	0.0014	10.52	10.542	0.0265	7.384	7.384	-
$L_2(u)$ E-2	0.1162	0.1162	-	0.0522	0.0522	0.0265	3.457	3.457	-
$L_2(S)$	2.254	2.257	0.0004	0.979	0.9814	0.001	0.4774	0.4778	0.0004

Table 3.1: L_2 errors for the Gas-Gas Shocktube Problem and Air-Water Shocktube Problem I.

(a) MGFM approach

(b) Procedure to construct the Riemann problem

(c) Characteristic waves

Figure 3.1: The Riemann problem: (a) Approximate Riemann solver employed in MGFM; (b) Procedure to construct the Riemann problem at the interface; (c) Typical characteristic wave structure for Riemann problem.
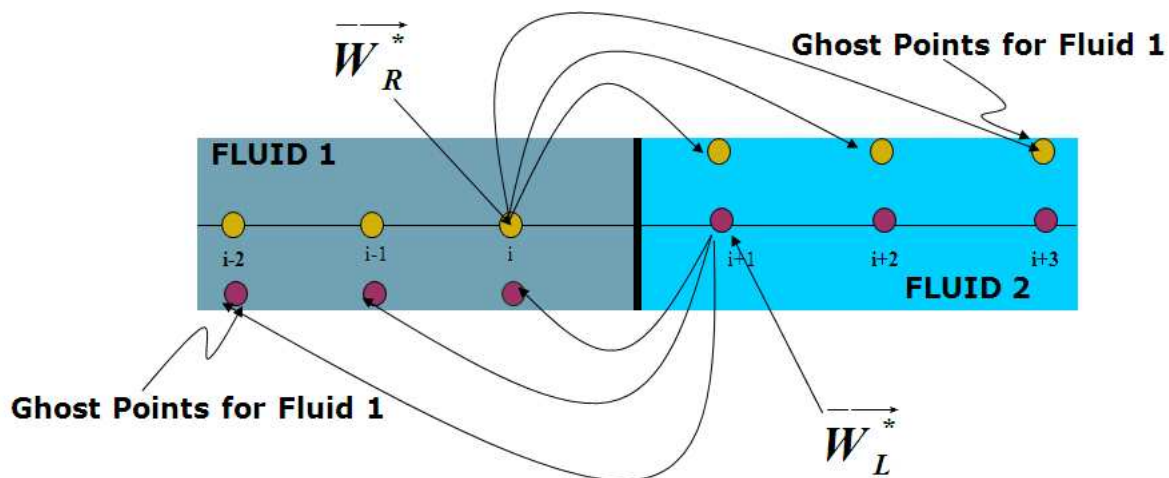
(a) One-dimensional correction procedure
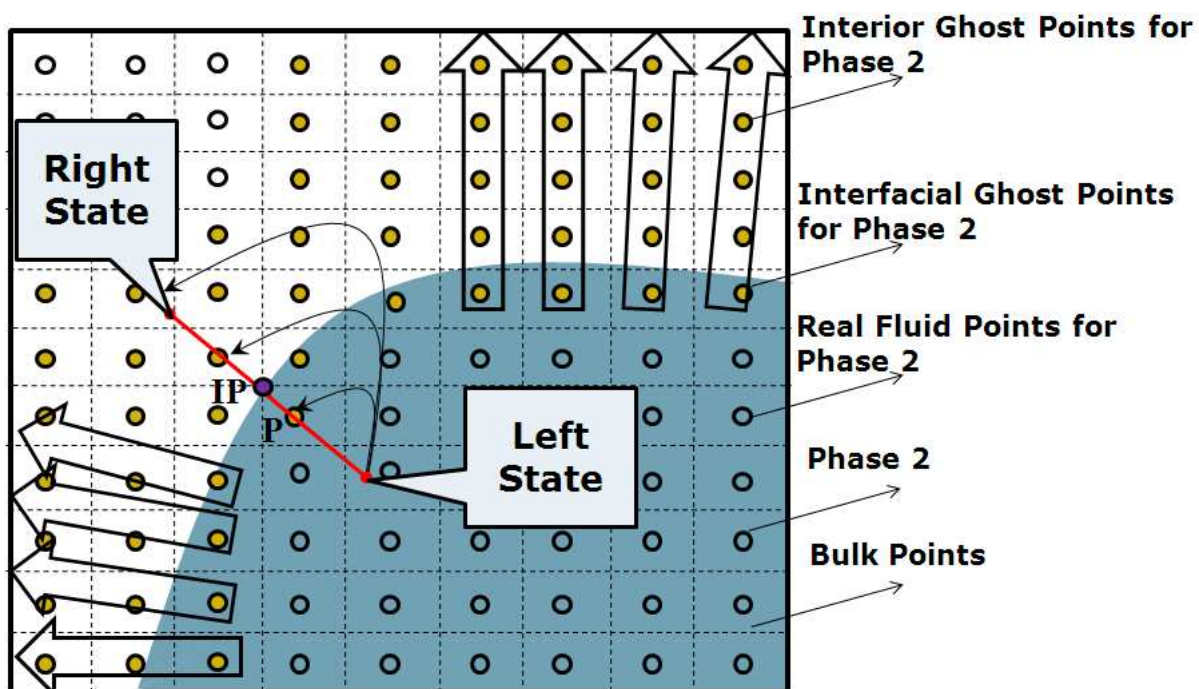
(b) Multi-dimensional correction procedure

Figure 3.2: Extension procedures: (a) One-dimensional version of the correction and extension procedure (b) Multi-dimensional correction and extension procedure.
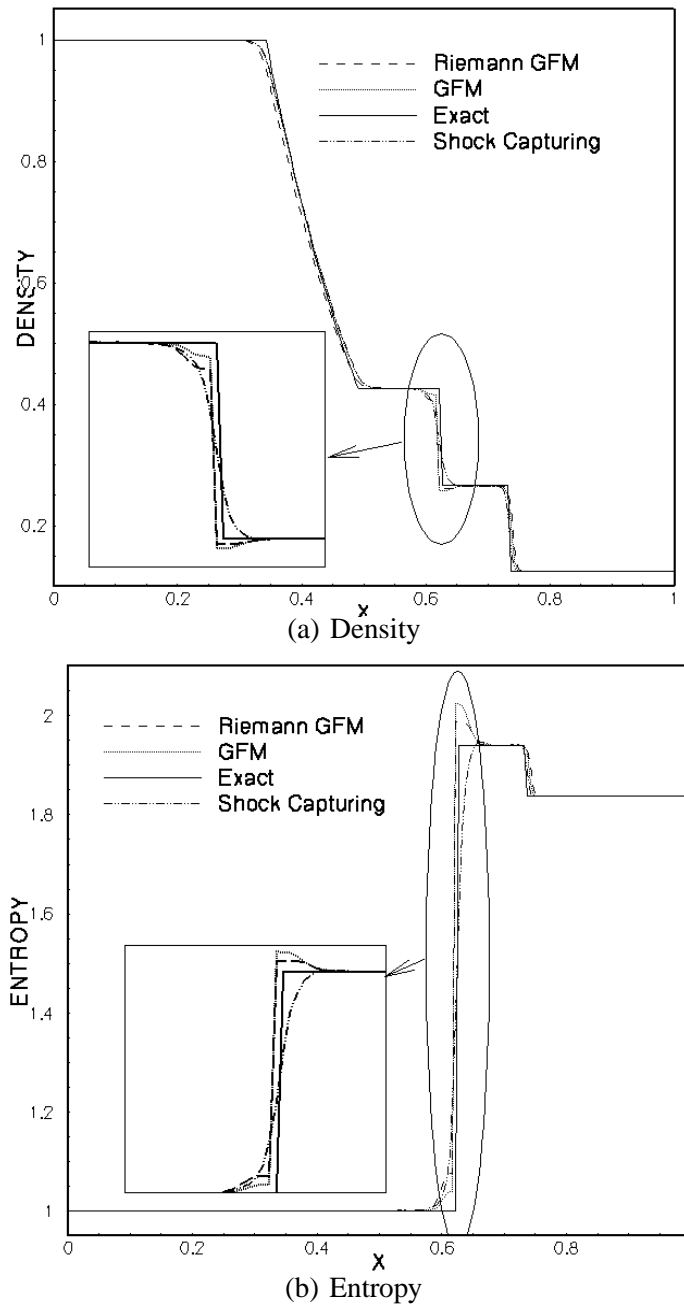
(a) Density

(b) Entropy

Figure 3.3: Example 1 - CASE(A): Plots of (a) density and (b) entropy for single fluid Sod's shock tube problem with pressure ratio $\frac{P_2}{P_1} = 10$.
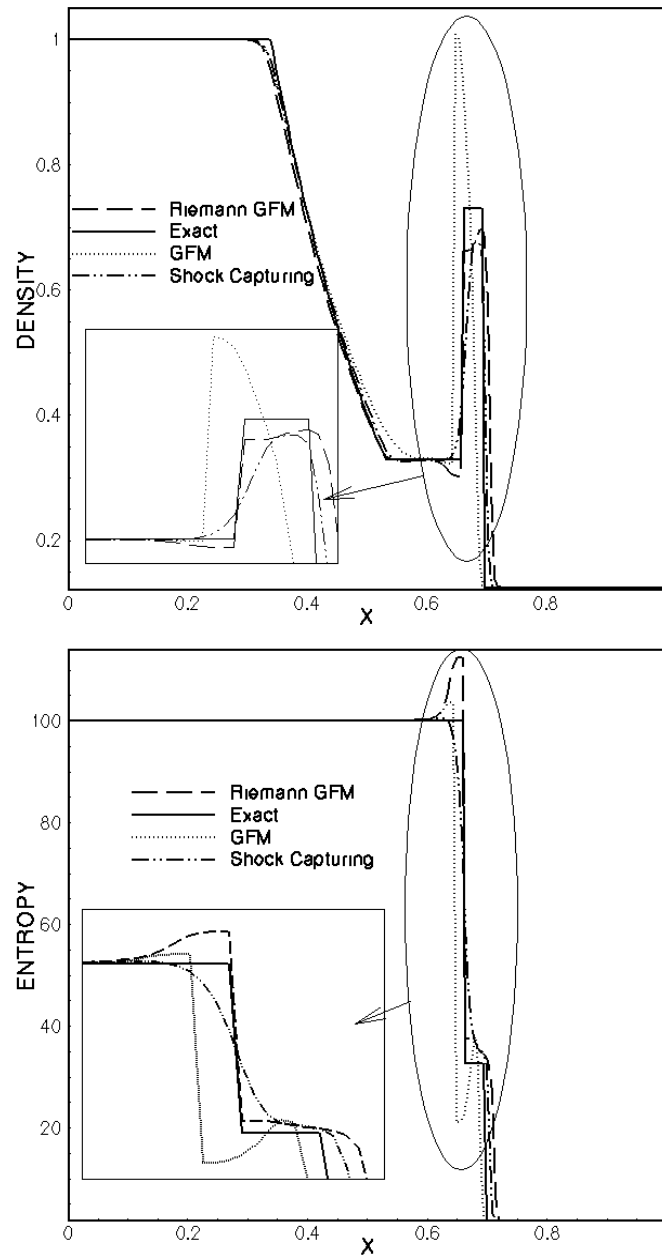
Figure 3.4: Example 1 - CASE(A): Plots of (a) density and (b) entropy for single fluid Sod's shock tube problem with pressure ratio $\frac{P_2}{P_1} = 1000$.

(a) Density

(b) Pressure

(c) Velocity

(d) Entropy

Figure 3.5: Example 1 - CASE(B): Plots of (a) density, (b) pressure, (c) velocity and (d) entropy for Woodward Colella Bang Bang problem.
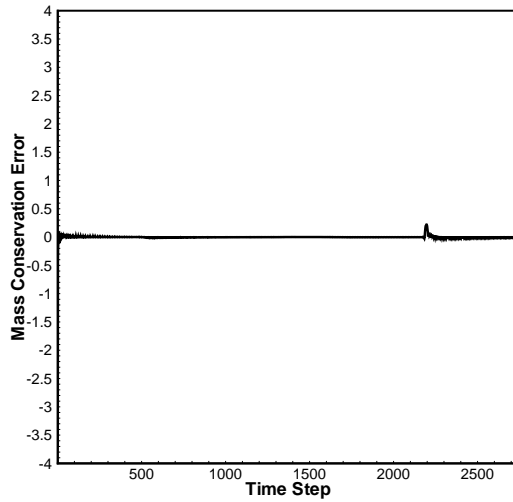
(a) Total Mass Conservation Error
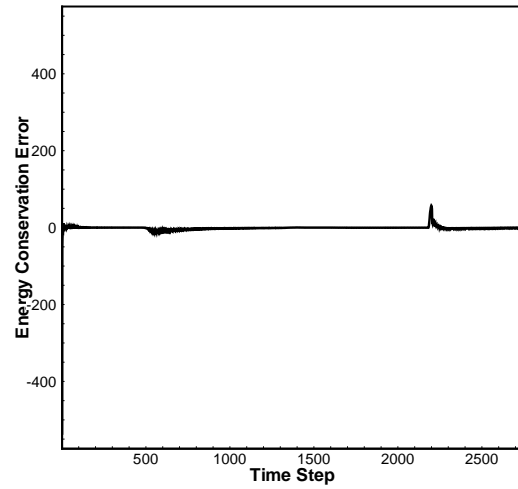
(b) Total Energy Conservation Error
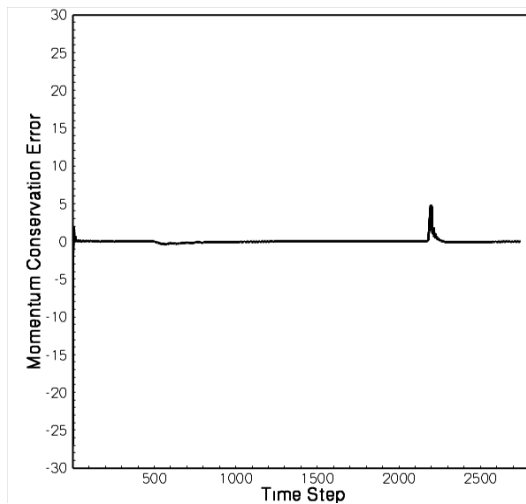
(c) Total Momentum Conservation Error

Figure 3.6: Example 1 - CASE(B): Plots of total (a) mass, (b)energy and (c) momentum conservation errors for Woodward Colella Bang Bang problem.

(a) Density

(b) Pressure

(c) Velocity
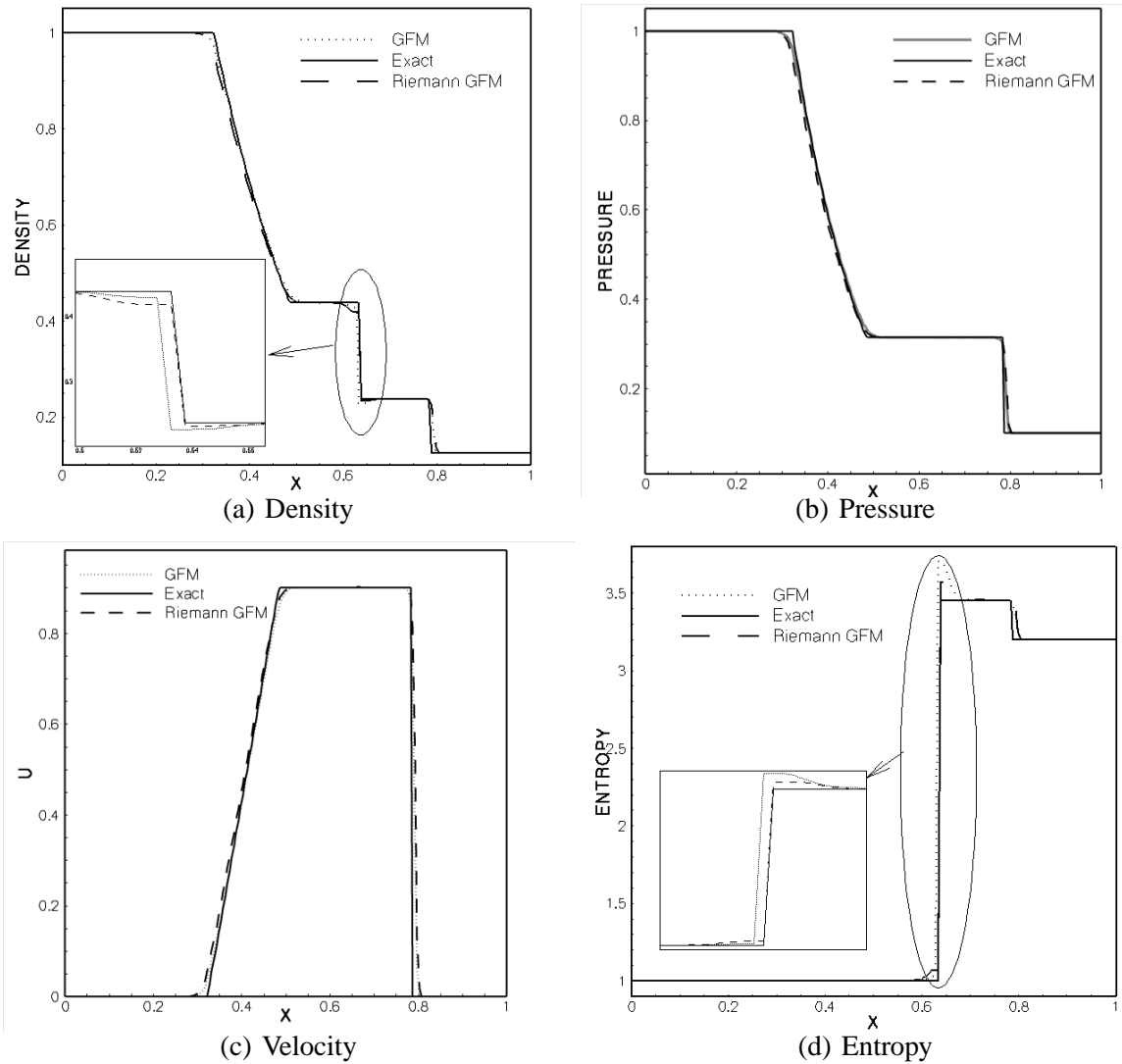
(d) Entropy

Figure 3.7: Example 2 - Plots of (a) density, (b) pressure, (c) velocity and (d) entropy for air-helium shock tube problem. The inserts correspond to the zoomed in view of the variation close to the interface.

(a) Total Mass Conservation Error

(b) Total Energy conservation Error

(c) Total Momentum Conservation Error
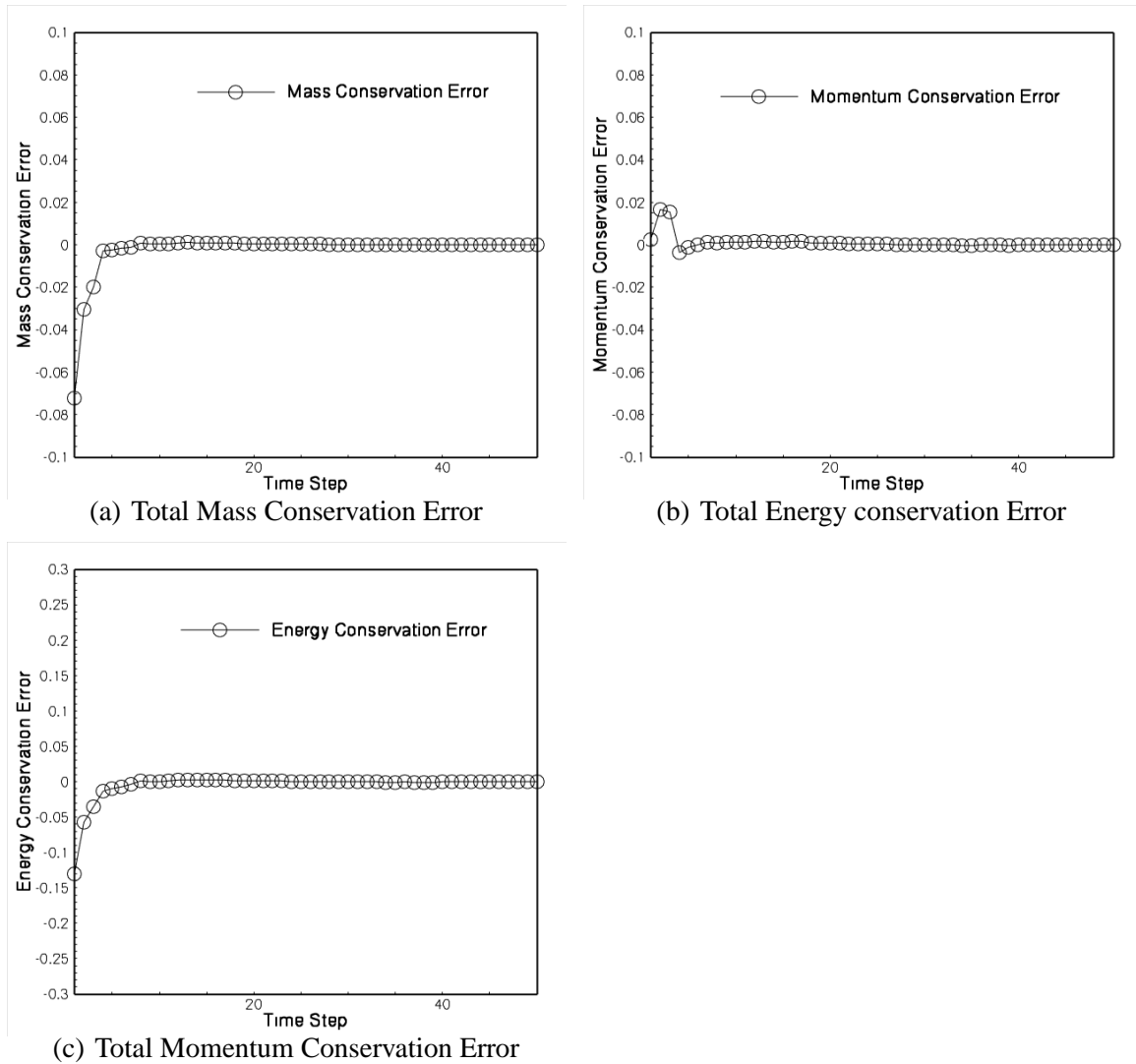
Figure 3.8: Example 2 - Plots of total (a) mass, (b) energy and (c) momentum conservation errors for air-helium shock tube problem.
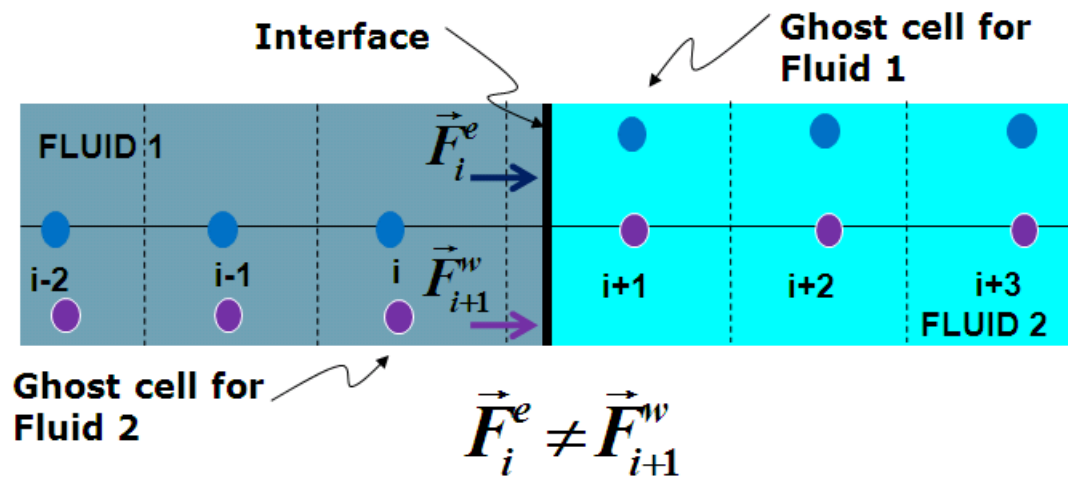
Figure 3.9: Non-uniqueness in the numerical flux computed at the interface; Figure reproduced from "Abgrall, R. and Karni, S., *Computations of Compressible Multi-Fluids*, Journal of Computational Physics, 169, 594-623(30), 20 May 2001".

(a) Density

(b) Pressure

(c) Velocity
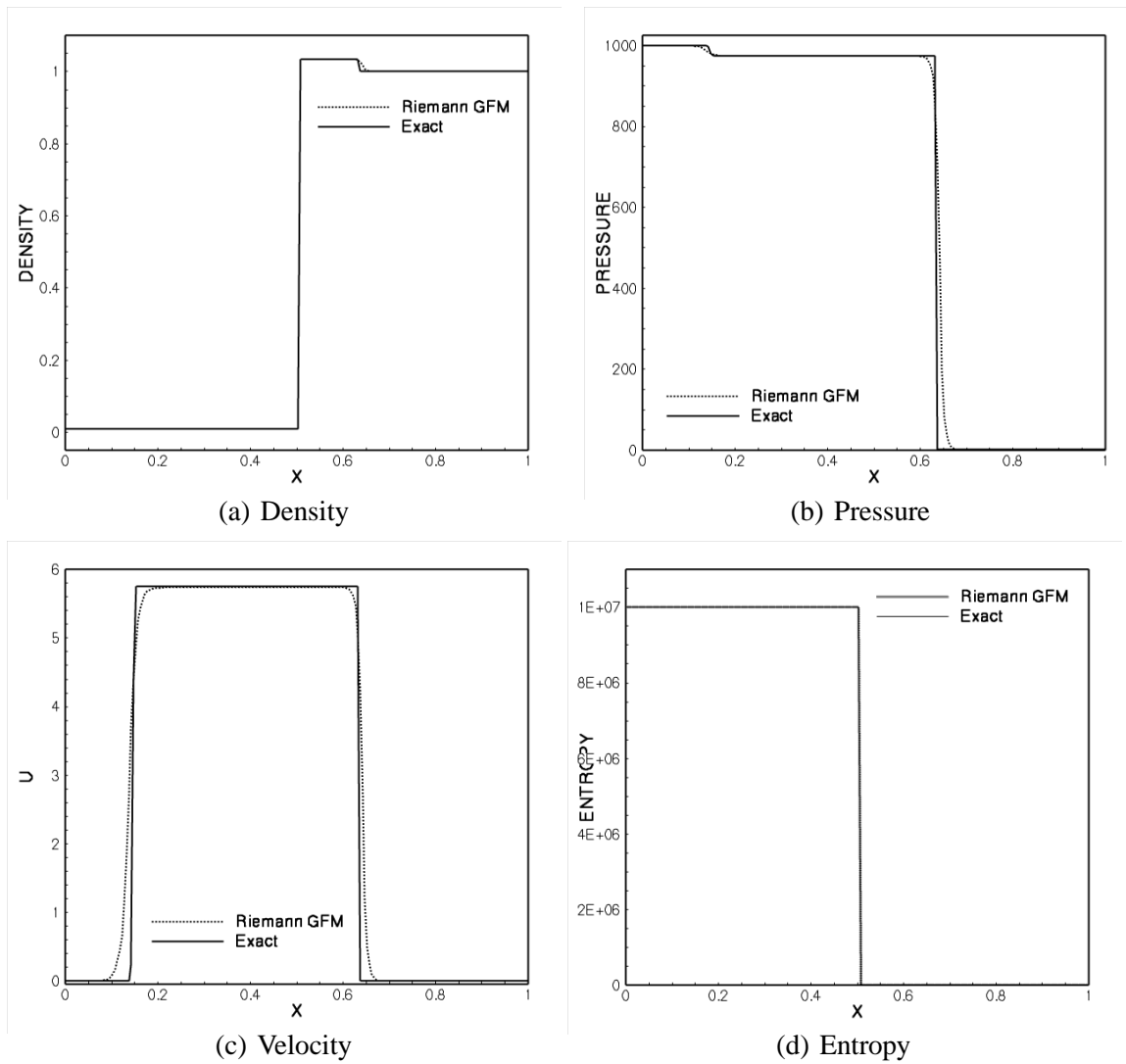
(d) Entropy

Figure 3.10: Example 3 - Plots of (a) density, (b) pressure, (c) velocity and (d) entropy for gas-water shock tube problem.

(a) Density

(b) Pressure

(c) Velocity
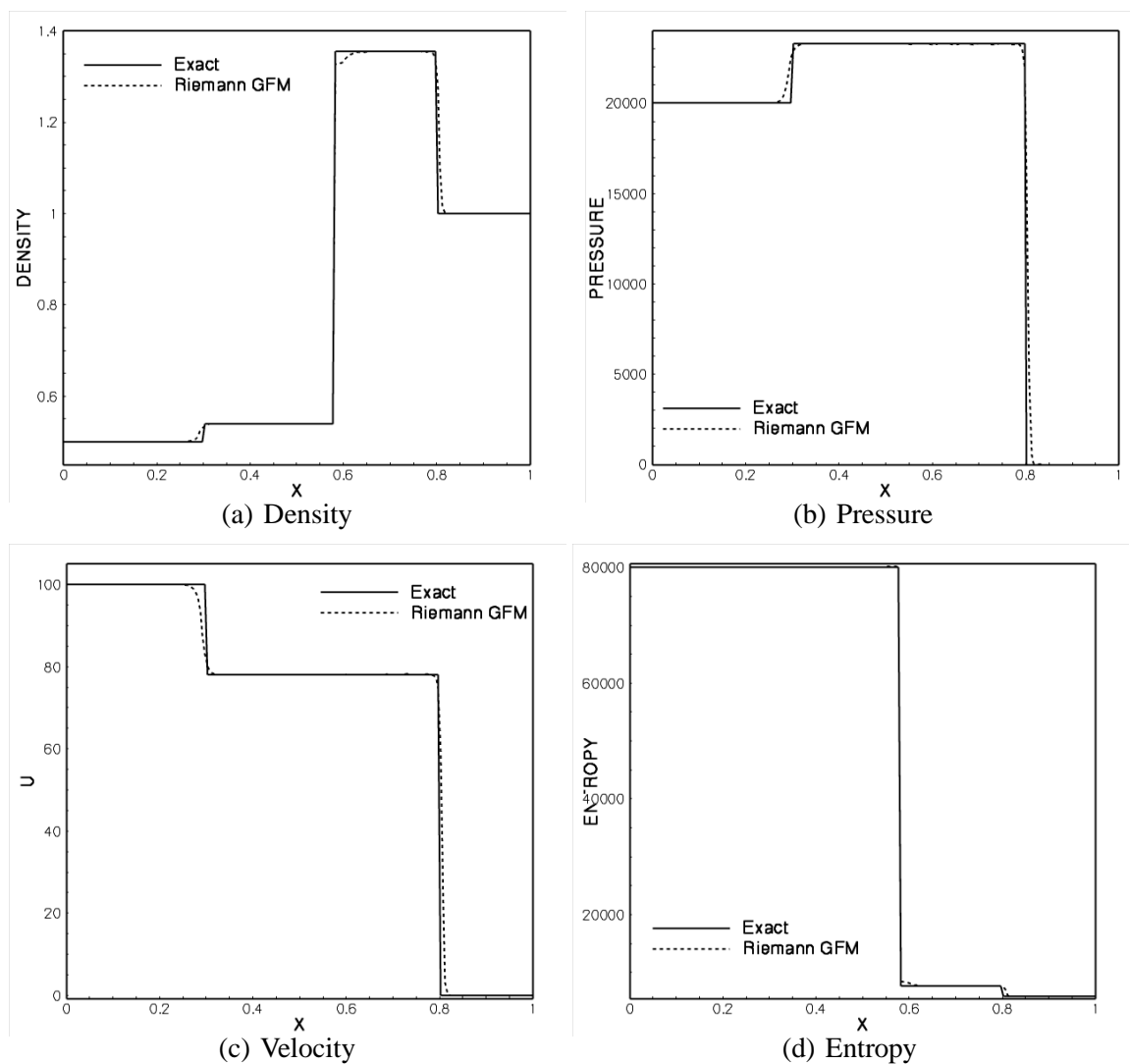
(d) Entropy

Figure 3.11: Example 4 - Plots of (a) density, (b) pressure, (c) velocity and (d) entropy for gas-water shock tube problem.
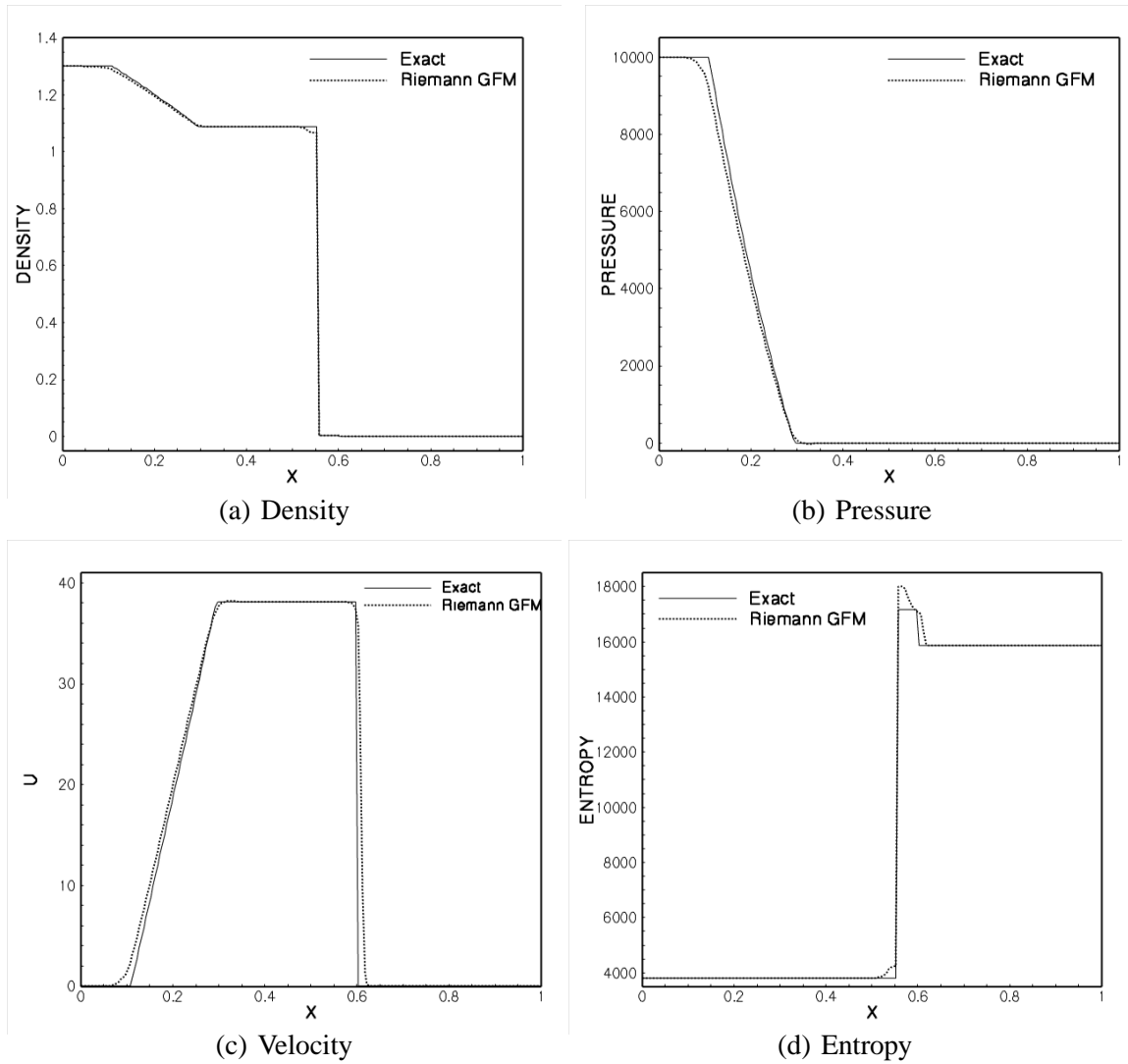
Figure 3.12: Example 5 - Plots of (a) density, (b) pressure, (c) velocity and (d) entropy for water-air shock tube problem.
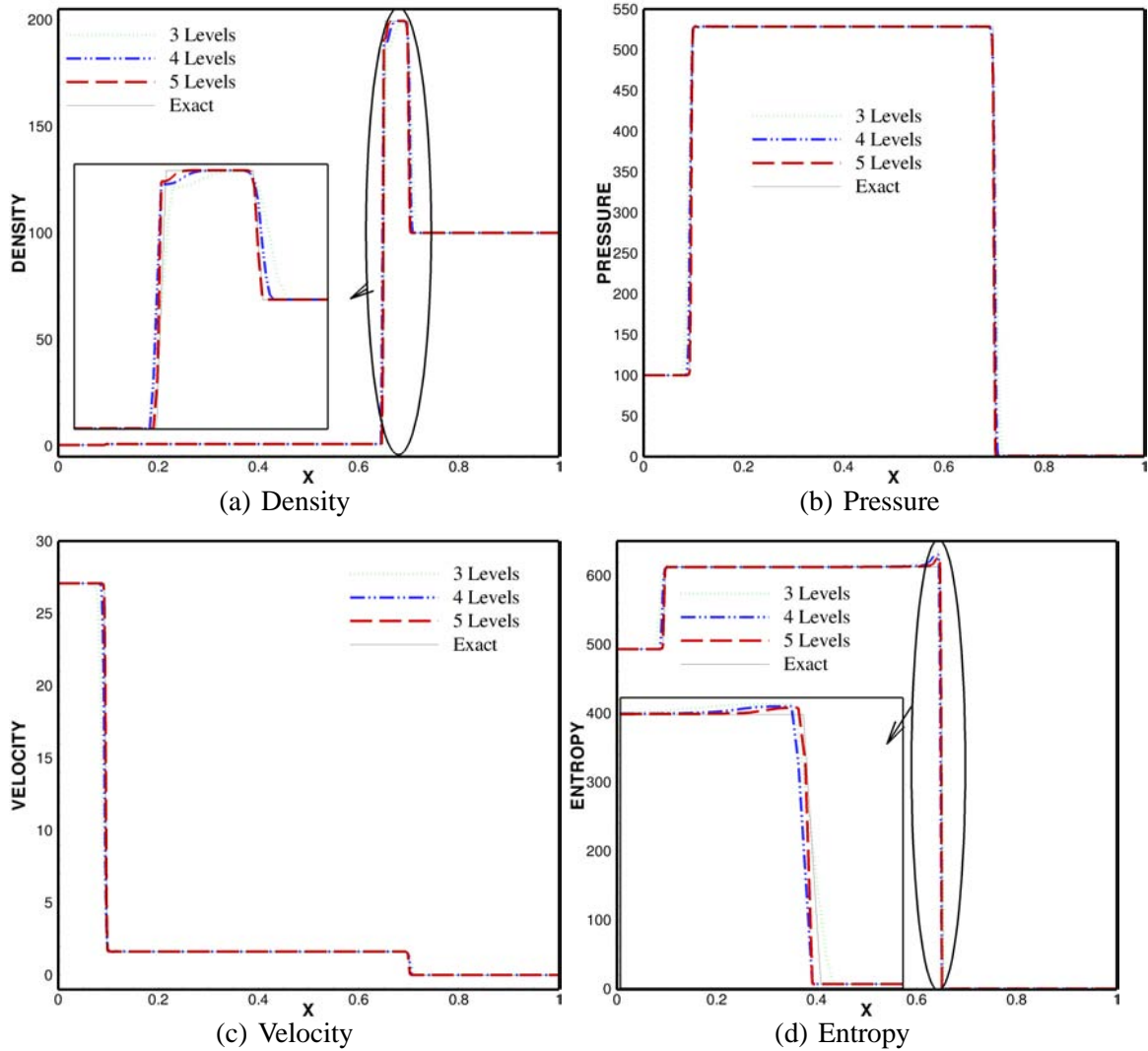
Figure 3.13: Example 6 - Plots of (a) density, (b) pressure, (c) velocity and (d) entropy for gas-gas shock tube problem at time T = 0.03 units.
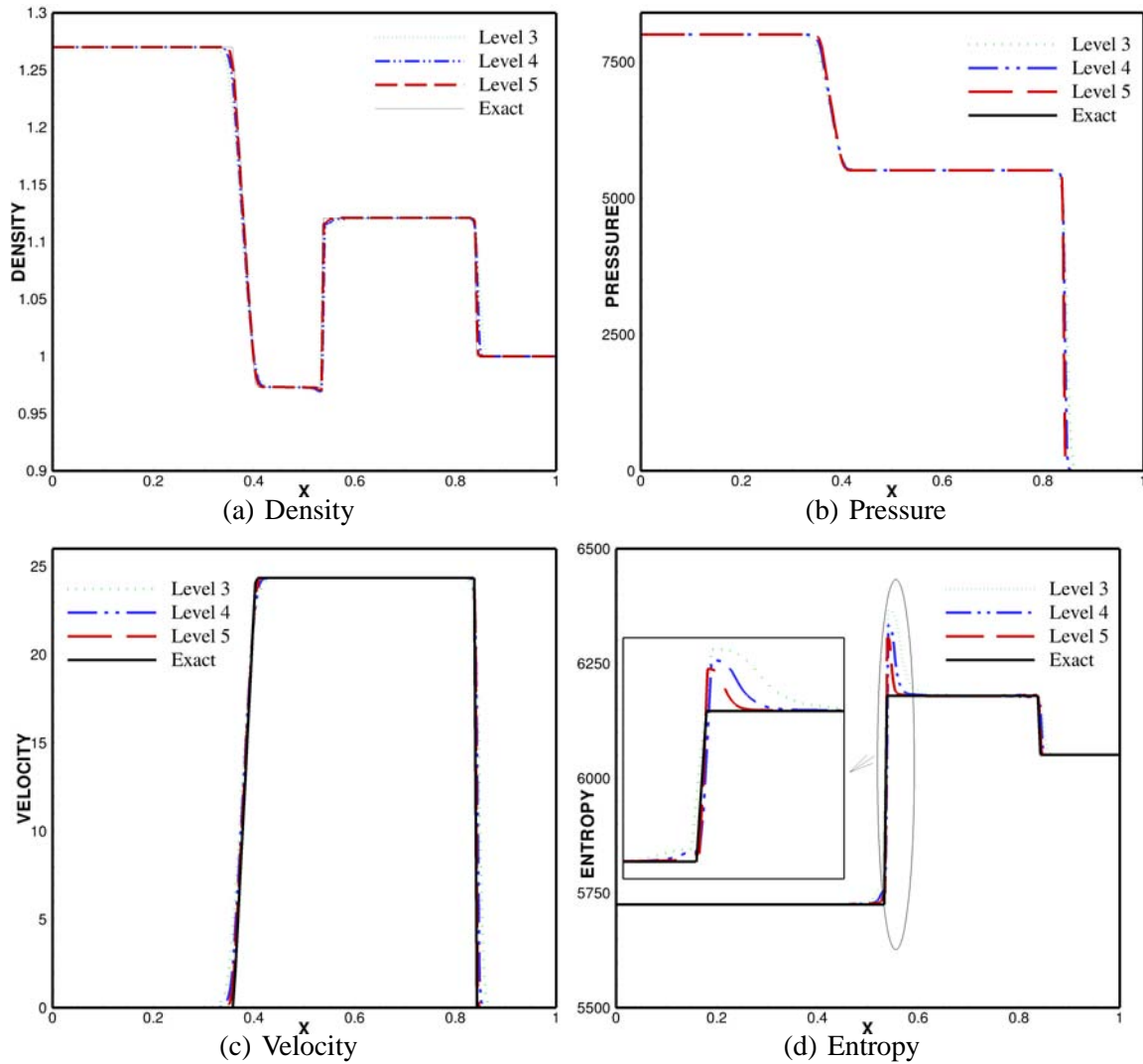
Figure 3.14: Example 7 - Plots of (a) density, (b) pressure, (c) velocity and (d) entropy for air-water shock tube problem (I) at time T = 0.0015 units.

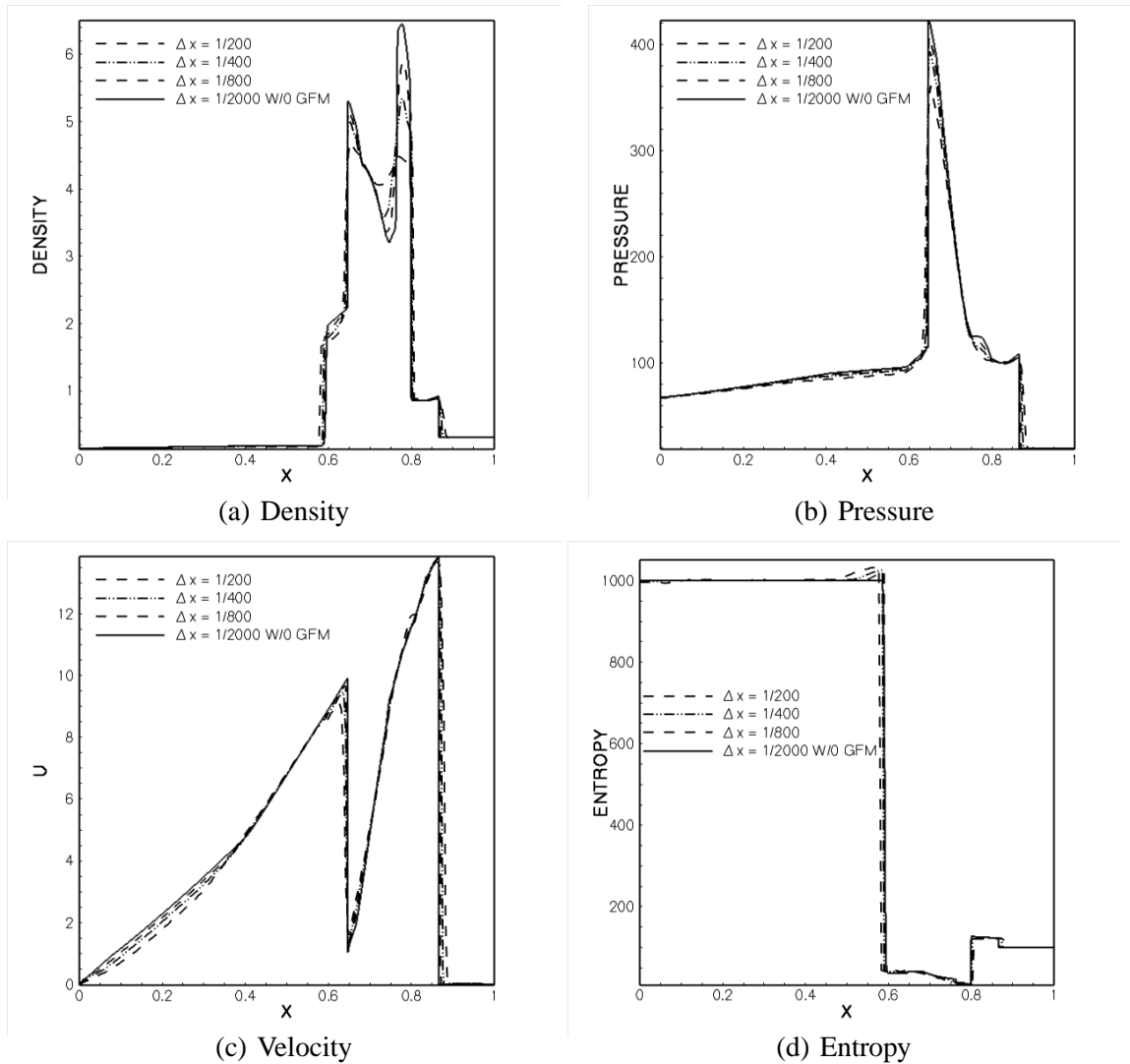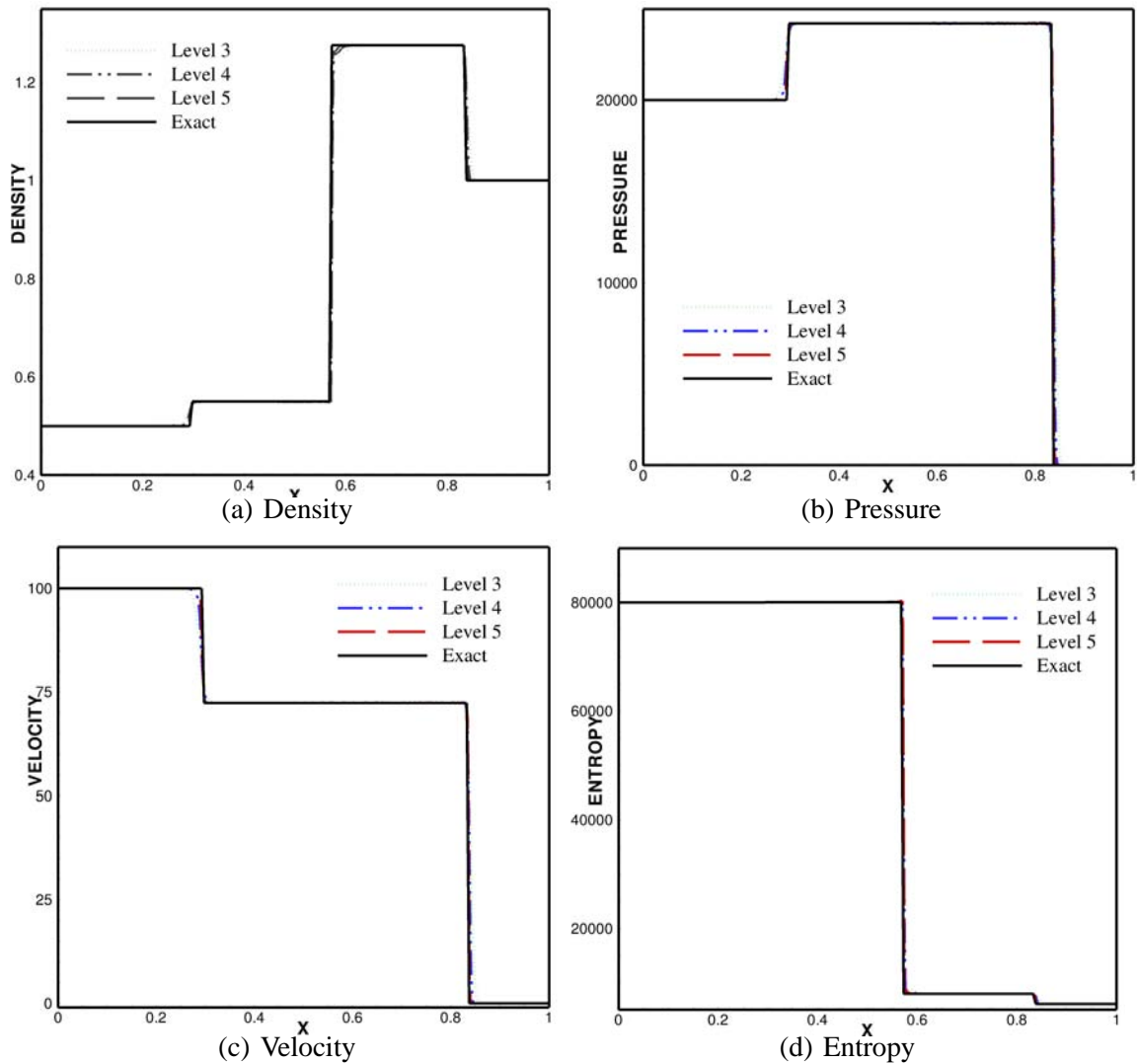Figure 3.15: Example 8 - Plots of (a) density, (b) pressure, (c) velocity and (d) entropy for gas-water shock tube problem (II) at time T = 0.001 units.
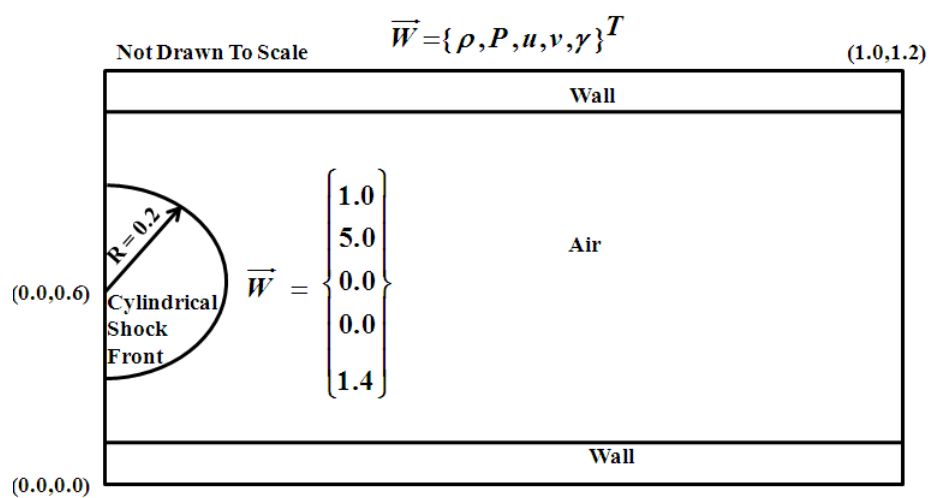
Figure 3.16: Initial configuration for single phase spherical Riemann problem.
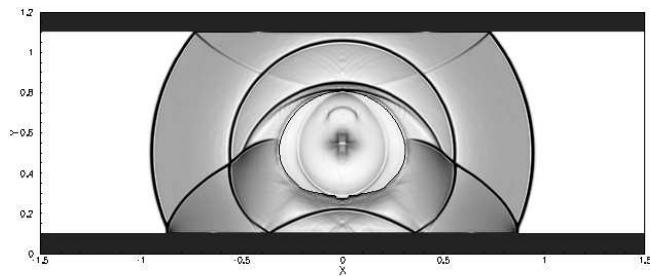
(a) t = 0.5, R-GFM
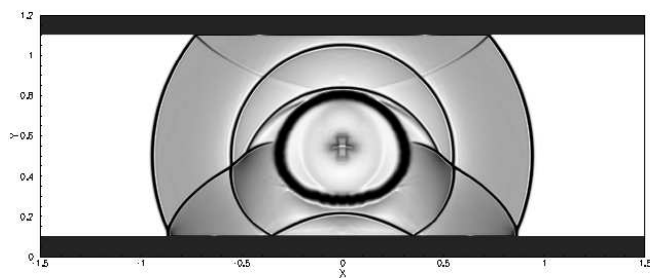
(b) t = 0.5, Shock-Capturing Scheme (without GFM)
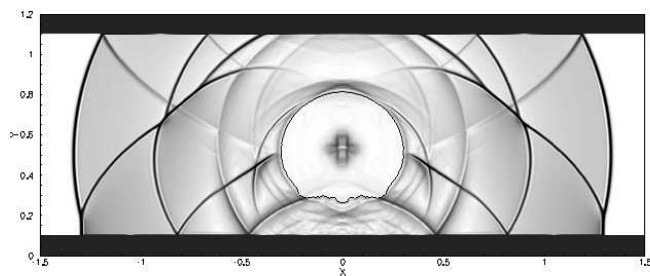
(c) t = 0.8, R-GFM
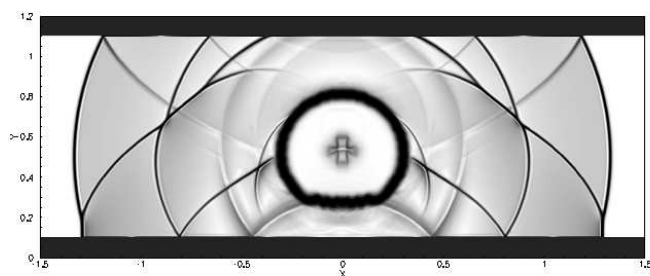
(d) t = 0.8, Shock-Capturing Scheme (without GFM)

Figure 3.17: Snapshots of numerical Schlieren image obtained with and without GFM treatment for the initially spherical contact discontinuity.
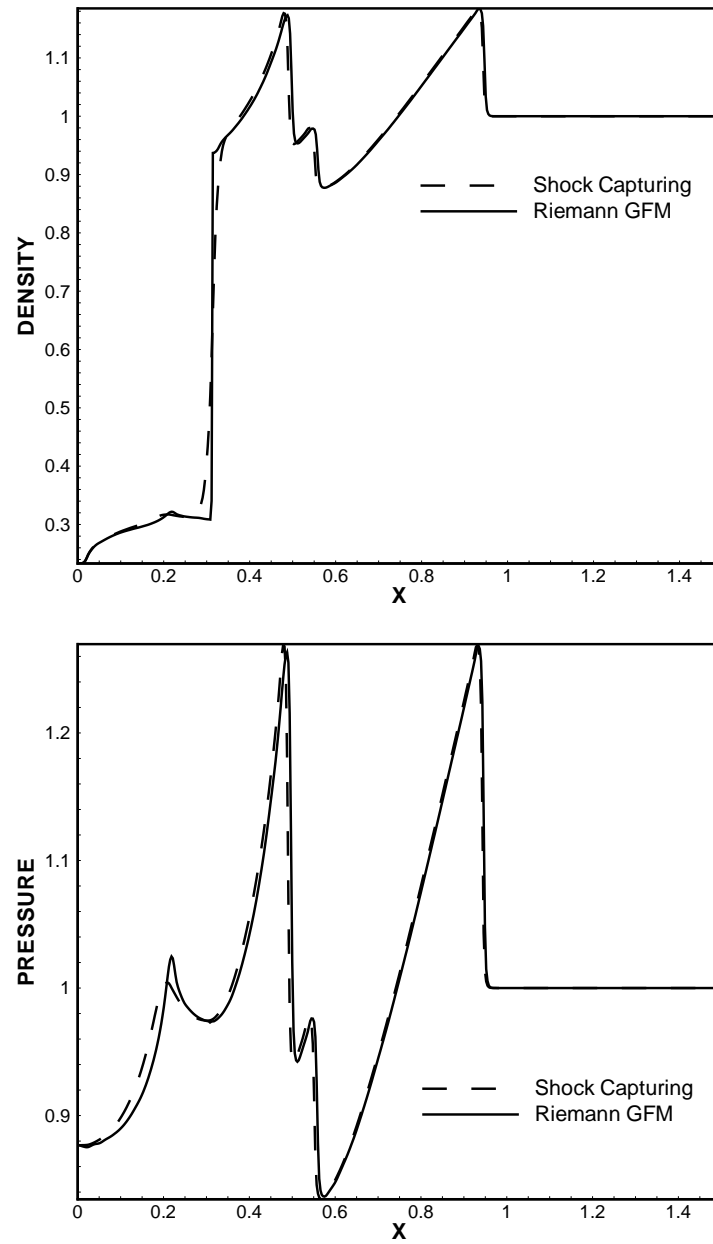
Figure 3.18: Spherical Riemann problem: Comparison of (a) density and (b) pressure variation at y = 0.6 at T = 0.5.
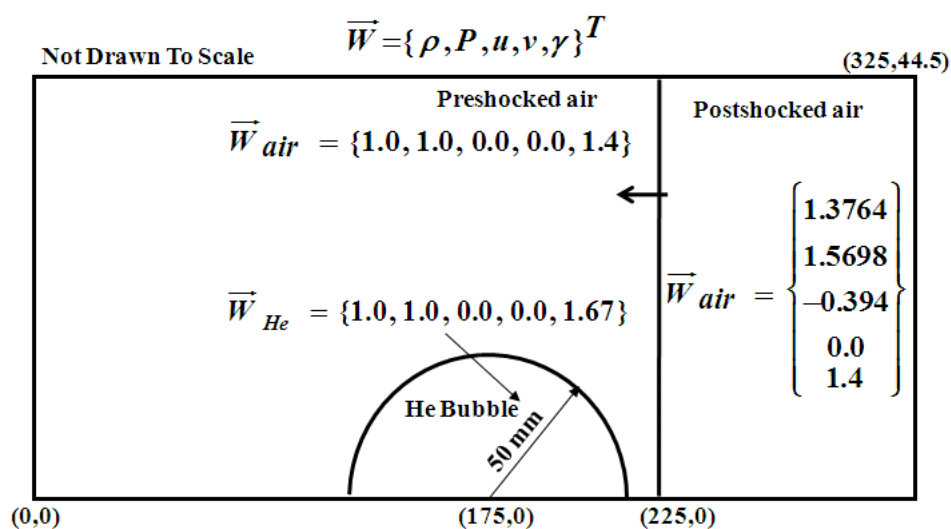
Figure 3.19: Initial configuration for a Mach 1.22 shock impinging on a cylindrical helium bubble.
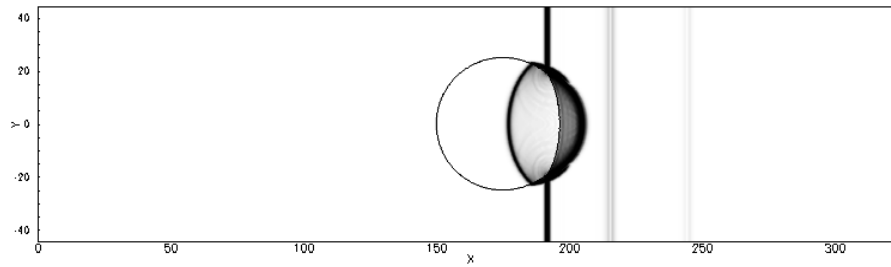
(a) Numerical Schlieren Image at T = 85 μs
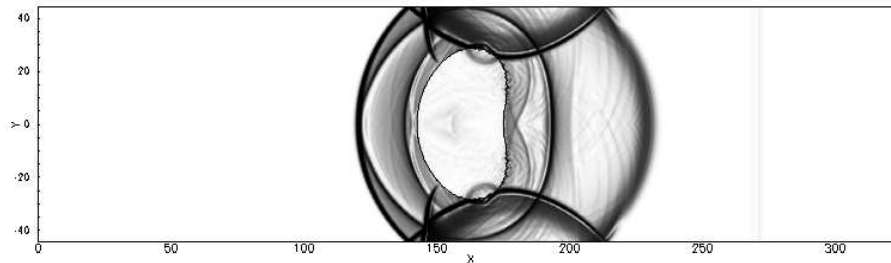
(b) Numerical Schlieren Image at T = 188 μs
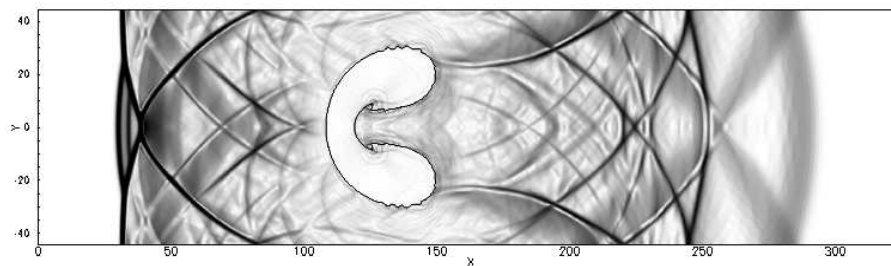
(c) Numerical Schlieren Image at T = 427 μs
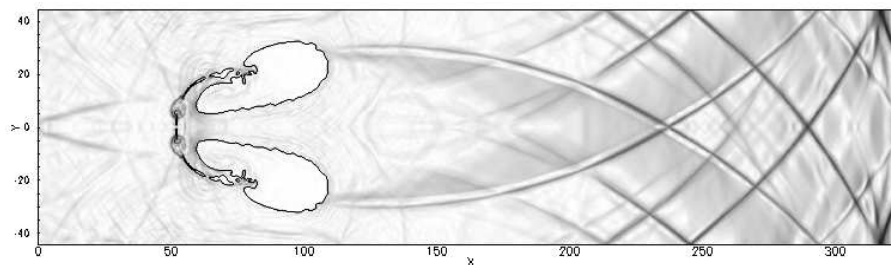
(d) Numerical Schlieren Image at T = 803 μs

Figure 3.20: Snapshots of numerical Schlieren image at different instants in time for a Mach 1.22 shock impinging on a cylindrical He bubble: (a) T = 85 μs, (b) T = 188 μs, (c) T = 427 μs, and (d) T = 803 μs.
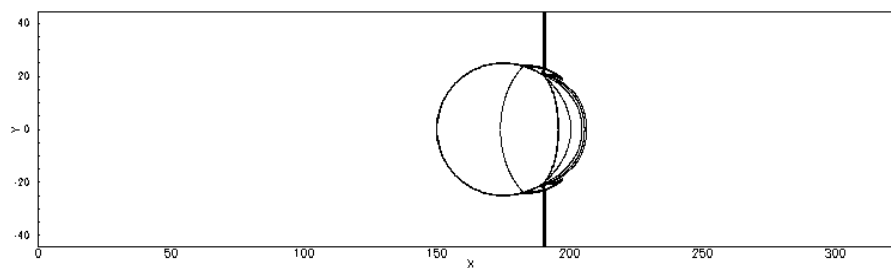
(a) Density Contours at T = 85 μs
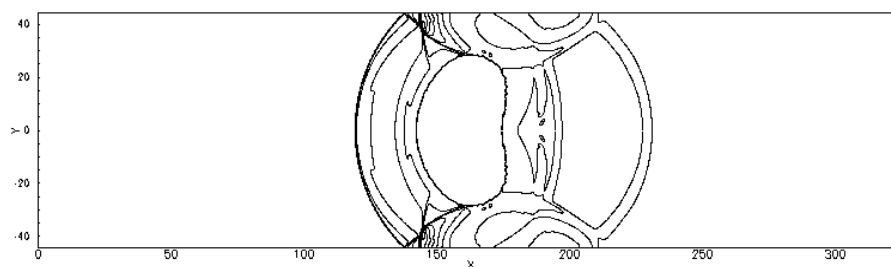
(b) Density Contours at T = 188 μs
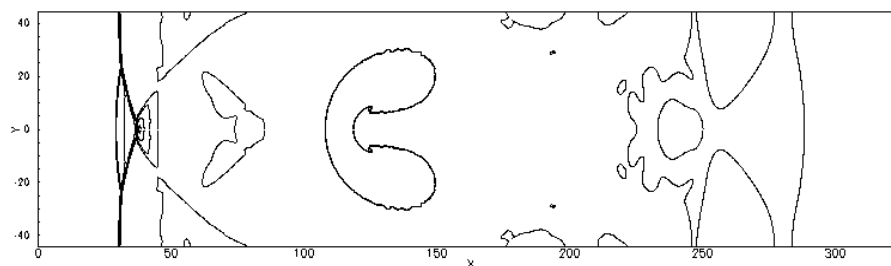
(c) Density Contours at T = 427 μs
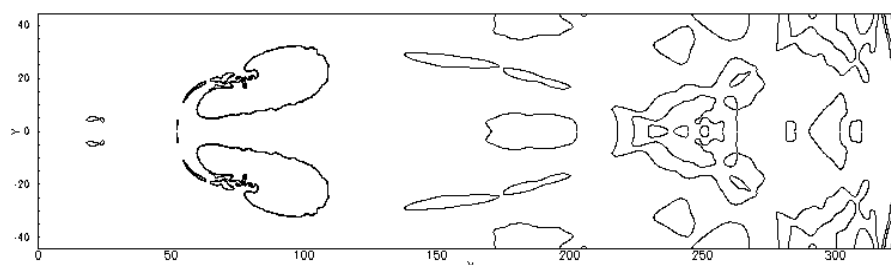
(d) Density Contours at T = 803 μs

Figure 3.21: Snapshots of density contours at different instants in time for a Mach 1.22 shock impinging on a cylindrical He bubble: (a) T = 85 μs, (b) T = 188 μs, (c) T = 427 μs, and (d) T = 803 μs.
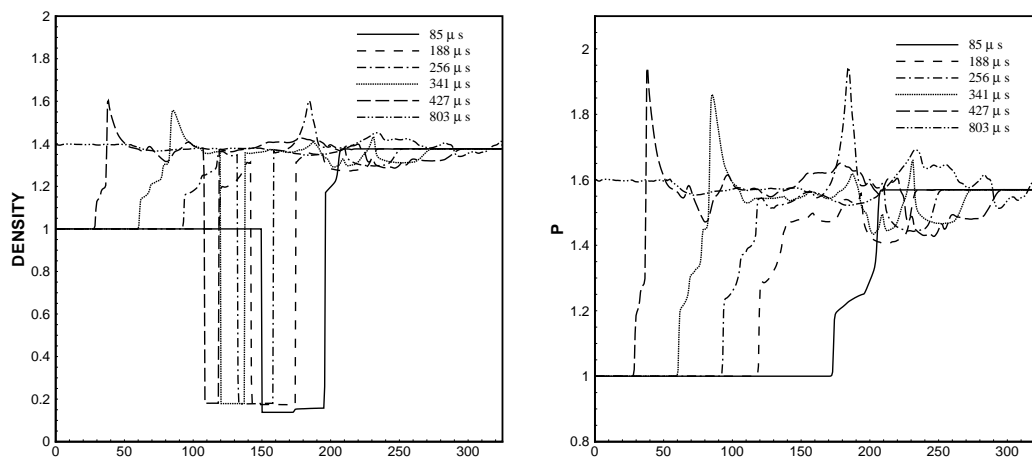
(a) Density Variation along Horizontal Symmetry Line

(b) Pressure Variation along Horizontal Symmetry Line
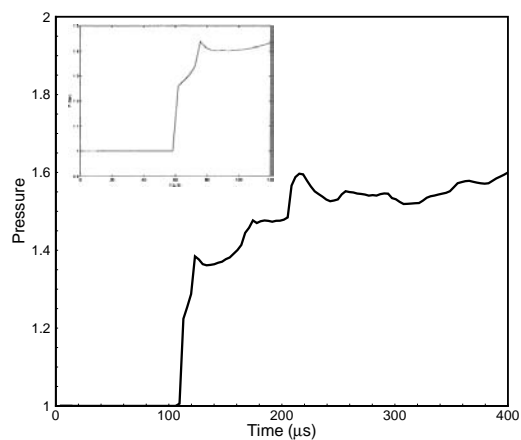
(c) Pressure History at 3mm Downstream of the Initial Bubble Location

Figure 3.22: Plots of density (Figure 3.22(a)) and pressure (Figure 3.22(b)) along the horizontal line of symmetry, and pressure as a function of time at 3mm downstream of the initial bubble location (Figure 3.22(c)). The insert displayed in Figure 3.22(c) corresponds to the plot obtained by Marquina et al[2003].
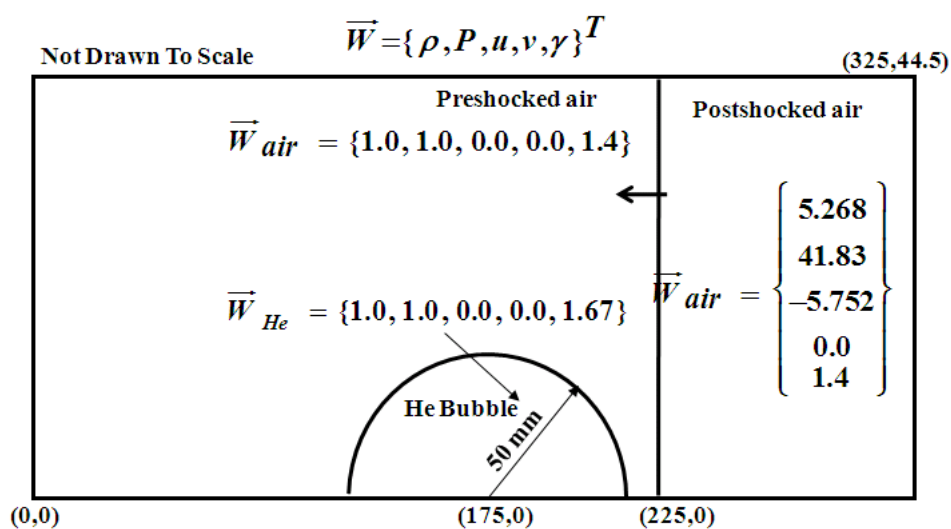
Figure 3.23: Initial configuration for a Mach 6 shock interacting with a cylindrical helium bubble.
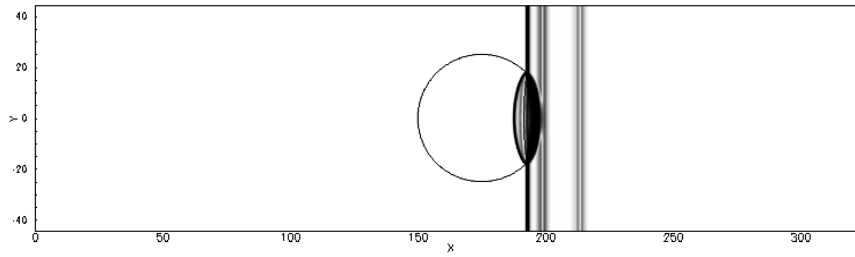
(a) Numerical Schlieren Image at T = 15.3 μs
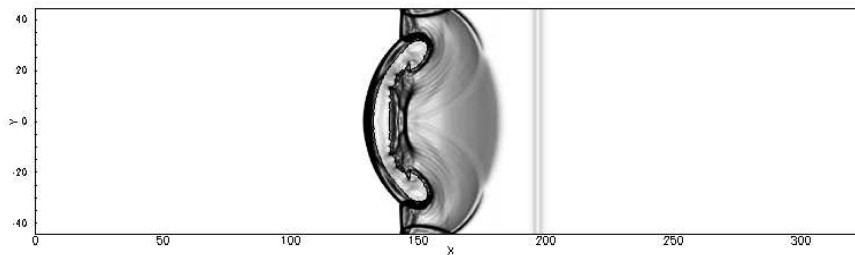
(b) Numerical Schlieren Image at T = 38.25 μs
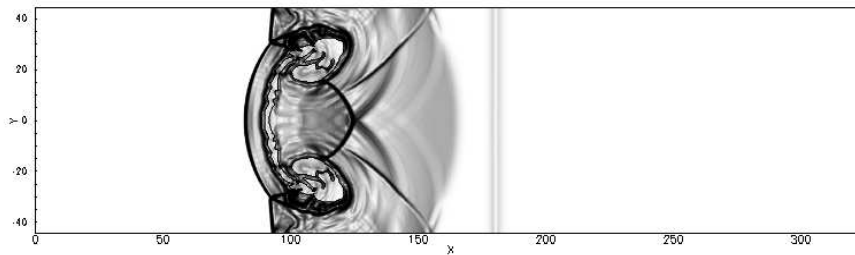
(c) Numerical Schlieren Image at T = 61.2 μs
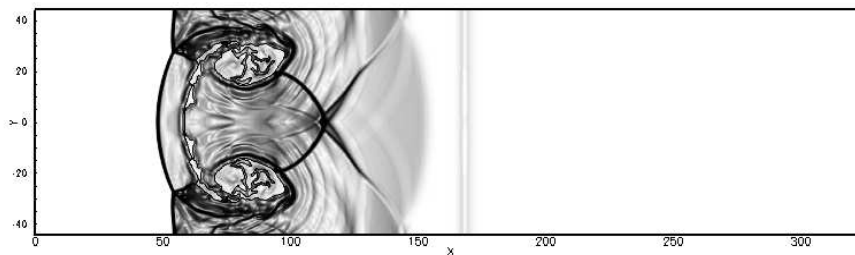
(d) Numerical Schlieren Image at T = 78 μs

Figure 3.24: Snapshots of numerical Schlieren image for a Mach 6 shock interaction with a cylindrical He bubble at different instants in time.
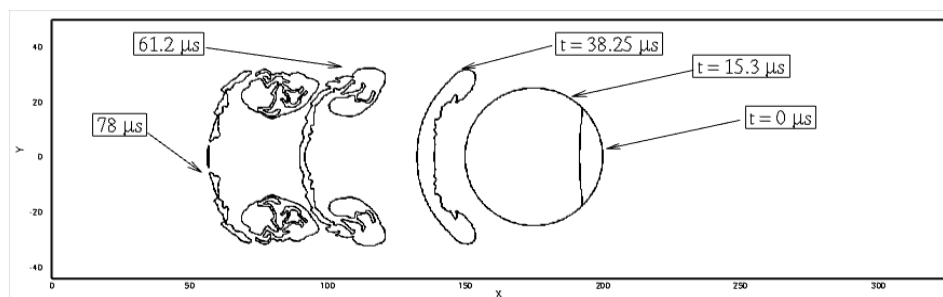
Figure 3.25: Topology of the interface (zero level set field) at different instants in time.

$$\vec{W} = \{\rho, P, u, v, \gamma\}^T$$

Not Drawn To Scale (12,12)

Air $\quad \vec{W}_{air} = \{1.0, 1.0, 0.0, 0.0, 1.4\}^T$

Water

R = 1m

Explosive Core

$$\vec{W}_{exp} = \left\{ \begin{array}{c} 1.27 \\ 8290.0 \\ 0.0 \\ 0.0 \\ 1.4 \end{array} \right\}$$

H = 9 m

$$\vec{W}_{water} = \{1000.0, 1.0, 0.0, 0.0, 5.5\}^T$$

(0,0)
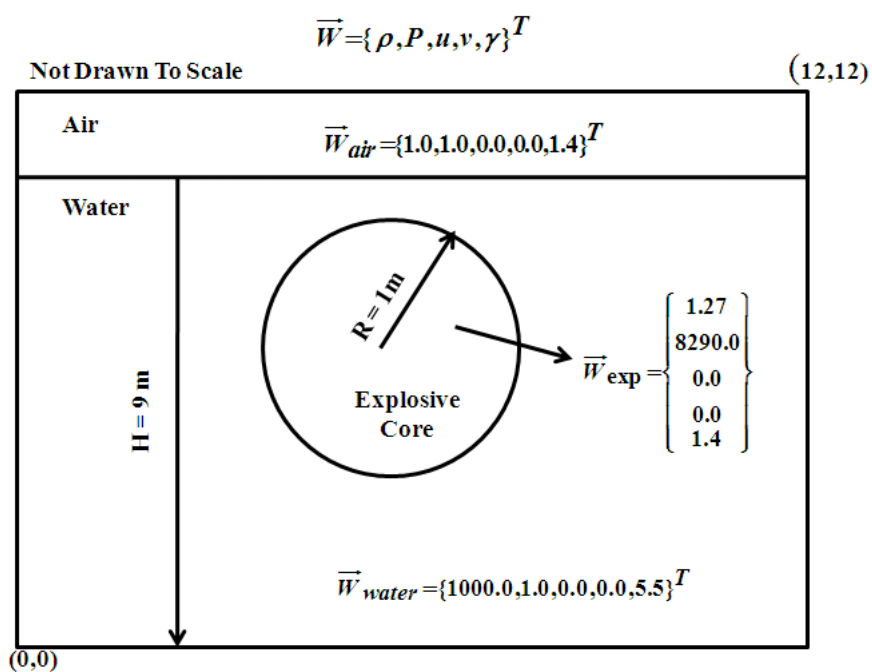
Figure 3.26: Initial configuration for underwater explosion near a free surface.
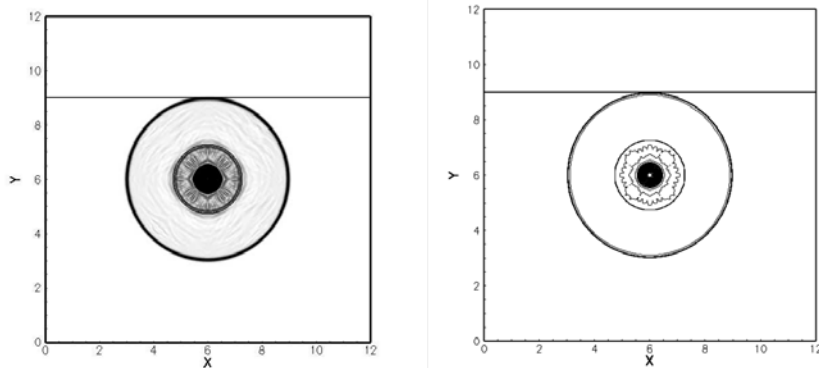
(a) T = 0.00892
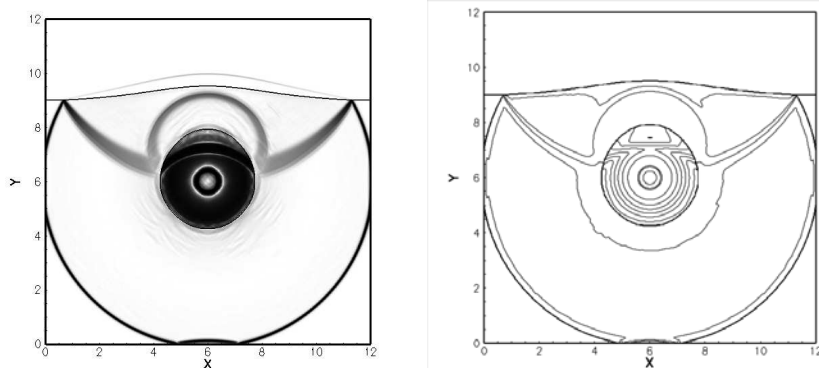
(b) T = 0.024
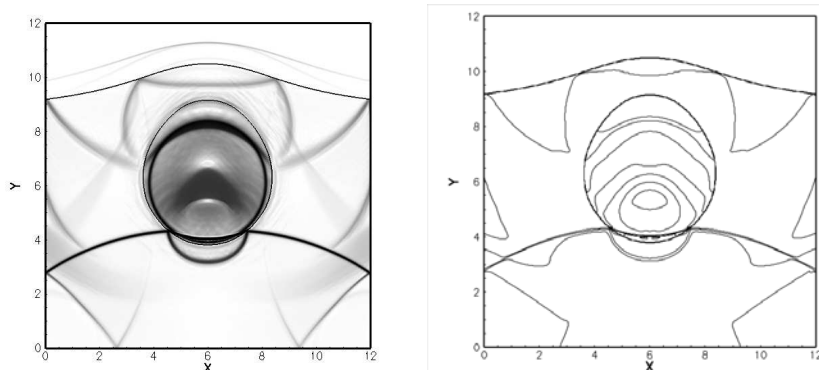
(c) T = 0.045

Figure 3.27: Snapshots of numerical Schlieren image and the corresponding density contours at different instants in time.

$$\vec{W} = \{\rho, P, u, v, \gamma\}^T \qquad (6,6)$$

Not Drawn To Scale

Air

$$\vec{W}_{air} = \{1.0, 1.0, 0.0, 0.0, 1.4\}^T$$

Water

Square Cylinder

(3.0,3.5)

H = 5m

R = 1m

(1.5,2.0)

Explosive Core

$$\vec{W}_{exp} = \{1.27, 8290.0, 0.0, 0.0, 1.4\}^T$$

$$\vec{W}_{water} = \{1000.0, 1.0, 0.0, 0.0, 5.5\}^T$$

(0,0)
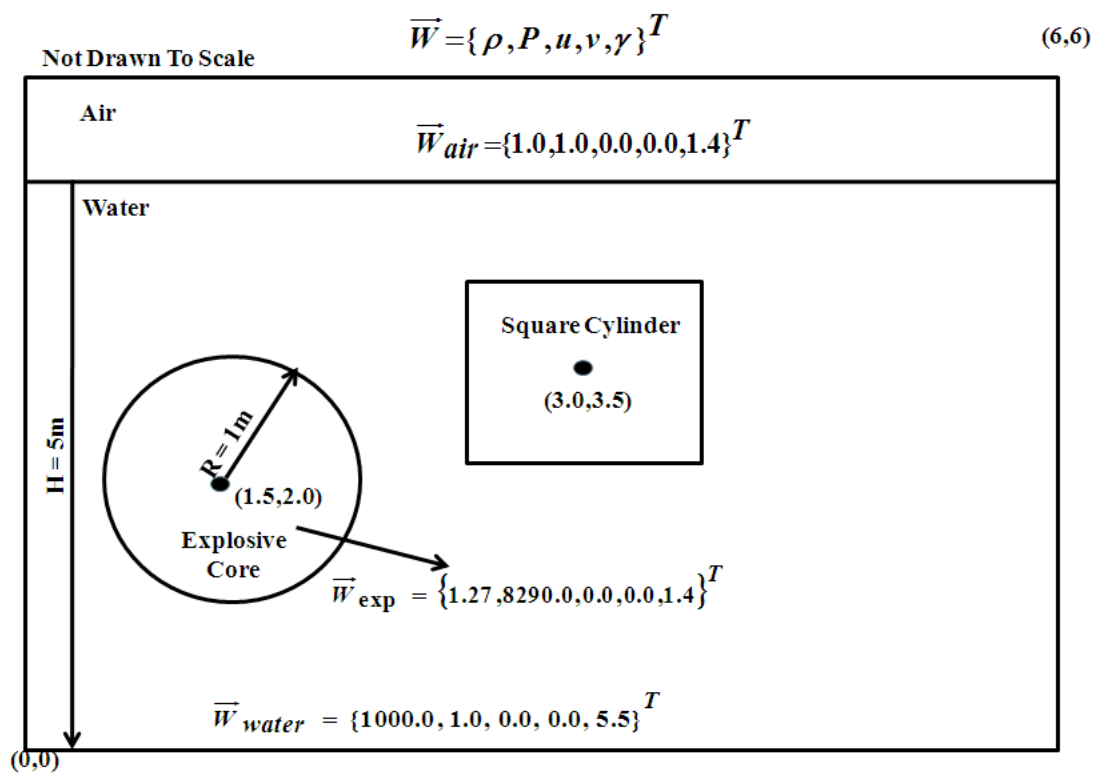
Figure 3.28: Initial configuration for underwater explosion near a free surface with immersed structure.

(a) Numerical Schlieren Image at T = 0.01

(b) Pressure Contours at T = 0.01

(c) Numerical Schlieren Image at T = 0.0197

(d) Pressure Contours at T = 0.0197
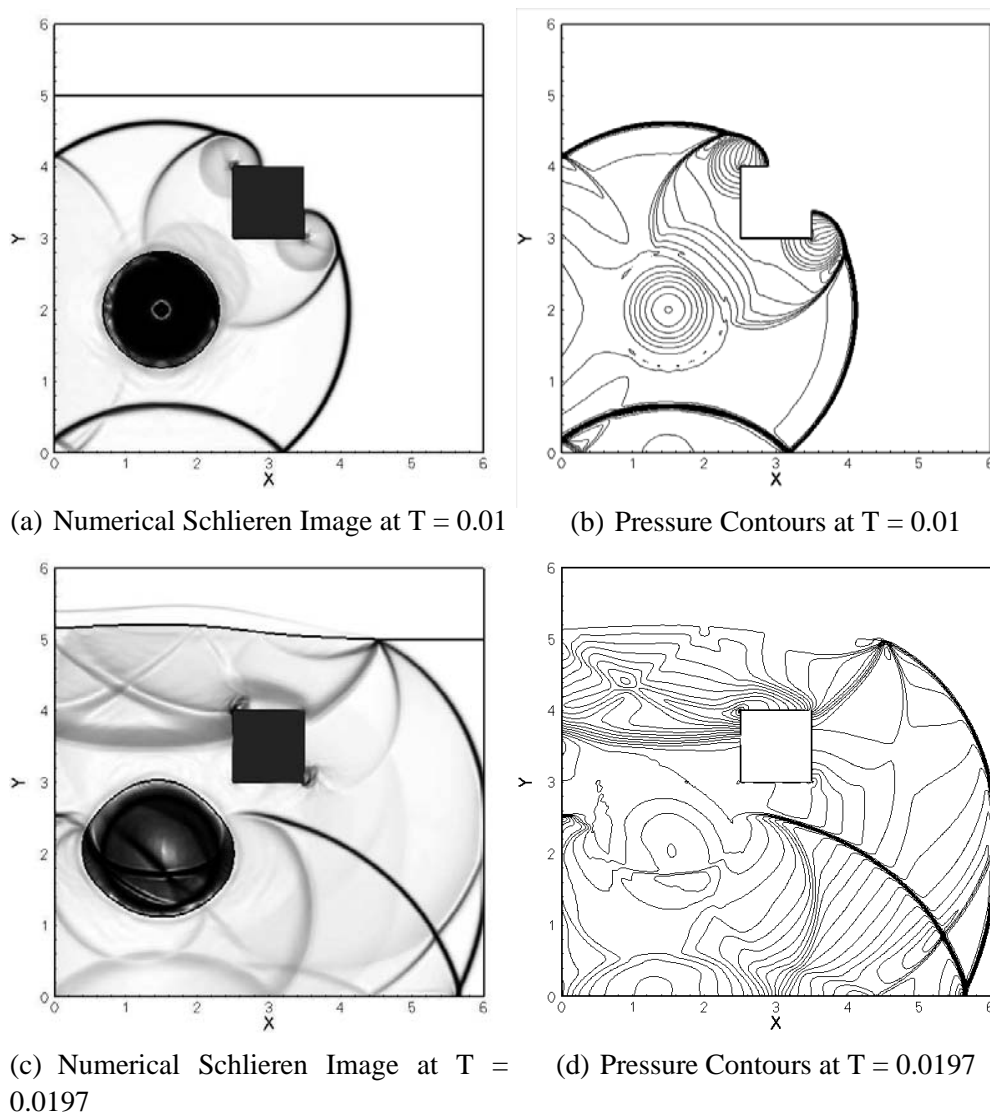
Figure 3.29: Snapshots of numerical Schlieren image (left) and corresponding pressure contours (right) at different instants in time.
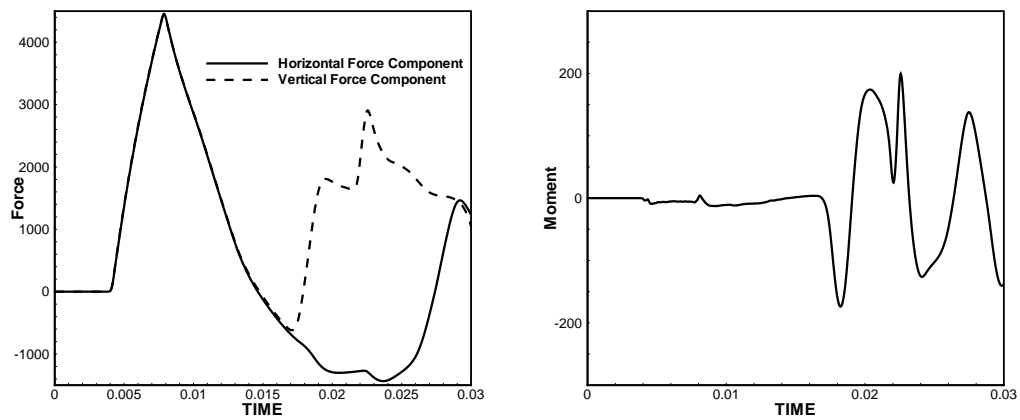
(a) Horizontal and Vertical Force Components

(b) Moment on the submerged square

Figure 3.30: Plots of non-dimensionalized force components (Figure 3.30(a)) and moment (Figure 3.30(b)) exerted on on the submerged square structure.
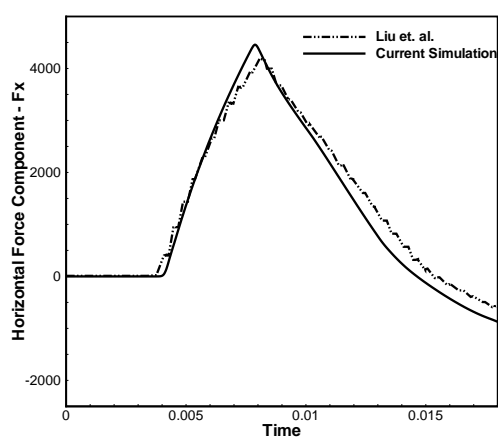
(a) Horizontal Force Component   (b) Vertical Force component
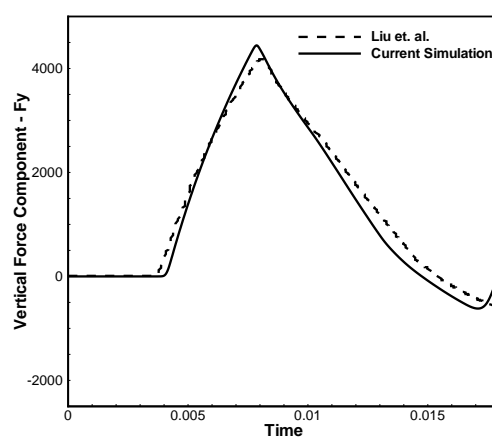
Figure 3.31: Comparison of non-dimensionalized horizontal (Figure 3.31(a)) and vertical (Figure 3.31(b)) force components exerted on the submerged square structure.
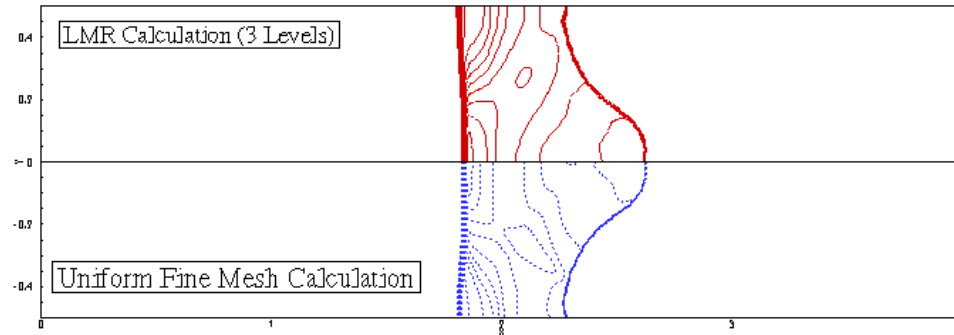
(a) Density contours for LMR and uniform mesh solutions at time T = 2.25
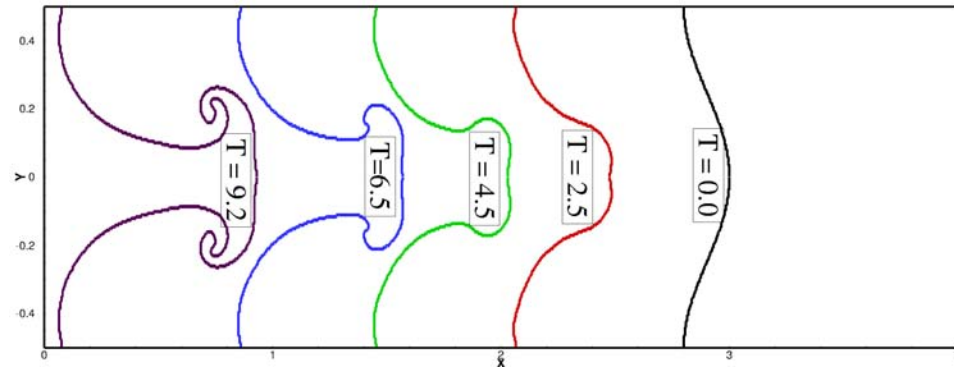
(b) Topology of the interface at different instants in time

Figure 3.32: Richtmyer-Meshkov Instability (RMI): (a) Comparison of density contours for LMR calculations, with 3 levels of mesh refinement, with the corresponding uniform fine mesh calculation (b) Topology of the interface at different instants in time.

(a) T = 2.5

(b) T = 4.5

(c) T = 6.5

(d) T = 9.2
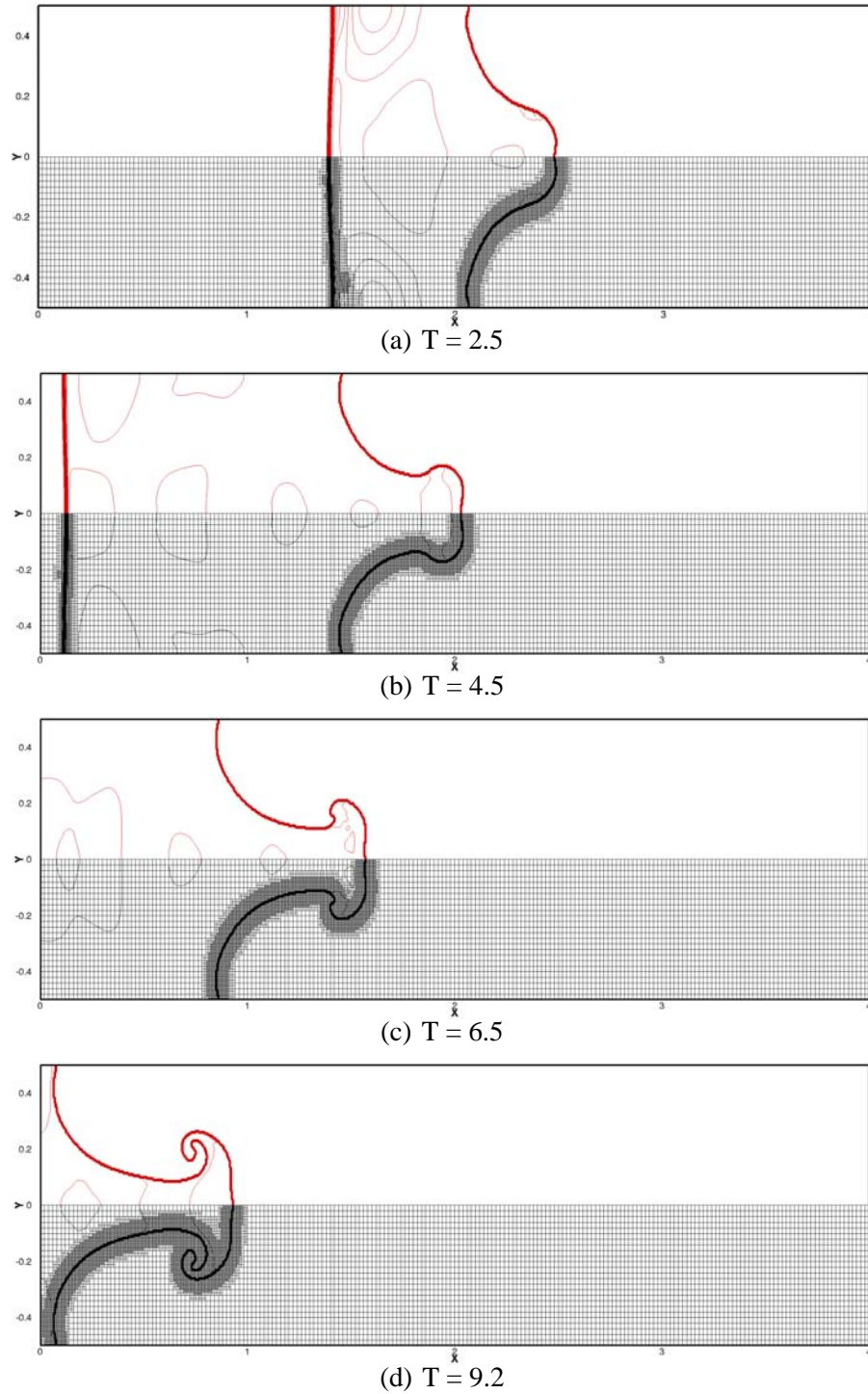
Figure 3.33: Snapshots of mesh evolution and density contours for the RMI at different instants in time.
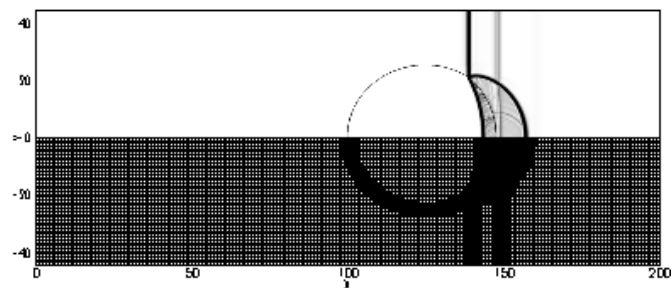
(a) T = $28\mu s$
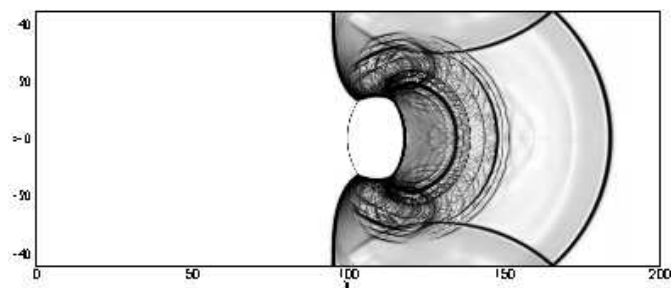
(b) T = $106\mu s$
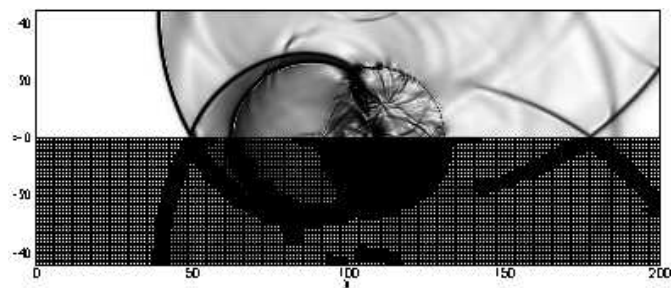
(c) T = $250\mu s$
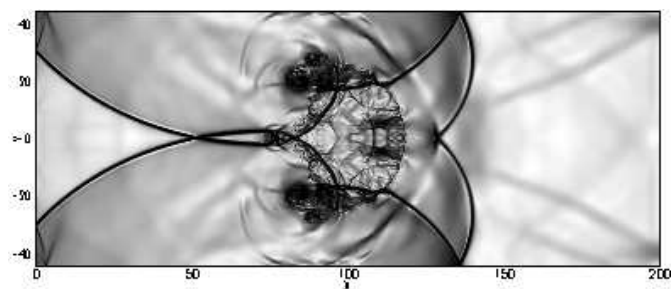
(d) T = $402\mu s$

Figure 3.34: Snapshots of mesh evolution and numerical Schlieren image for a planar shock (Mach 1.22) interacting with R_{22} cylindrical bubble at different instants in time.
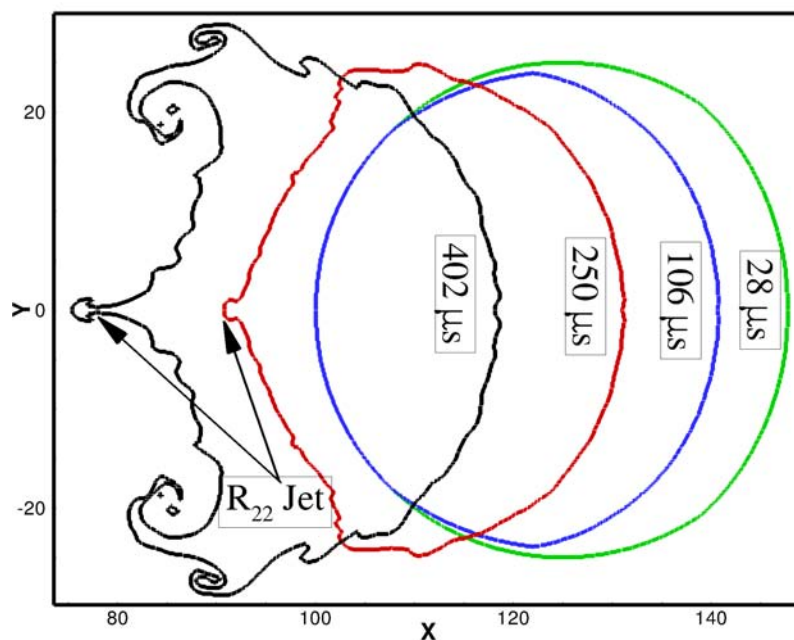
(a) Interface Evolution
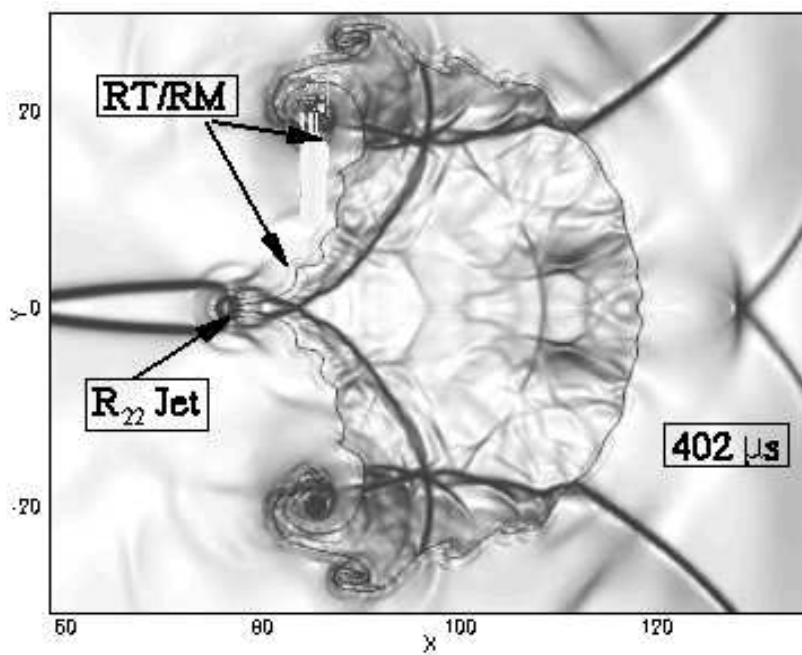
(b) RM/RT Instabilities

Figure 3.35: Mach 1.22 shock interacting with R_{22} cylindrical bubble: Enlarged view of the (a) interface evolution at different instants in time and (b) instabilities occurring at the interface.
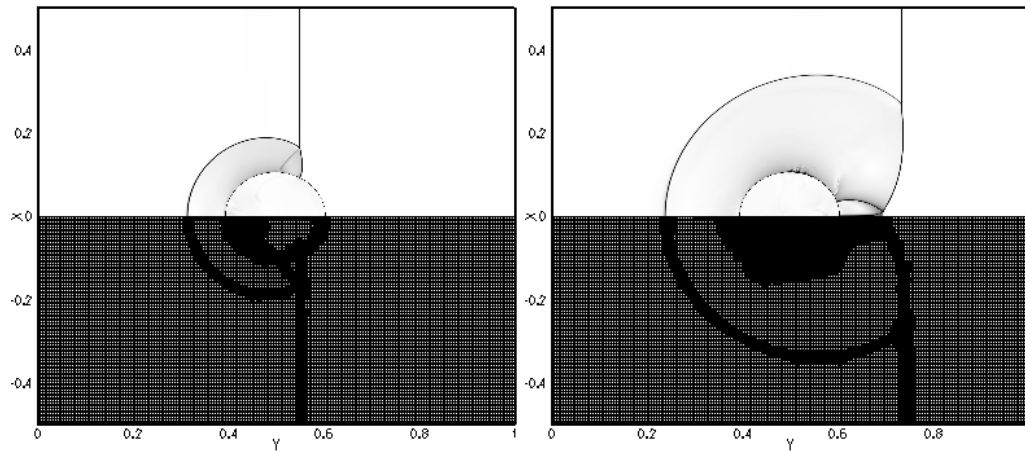
(a) Mesh and numerical Schlieren image at T = $0.376\mu s$

(b) Mesh and numerical Schlieren image at T = $0.75\mu s$
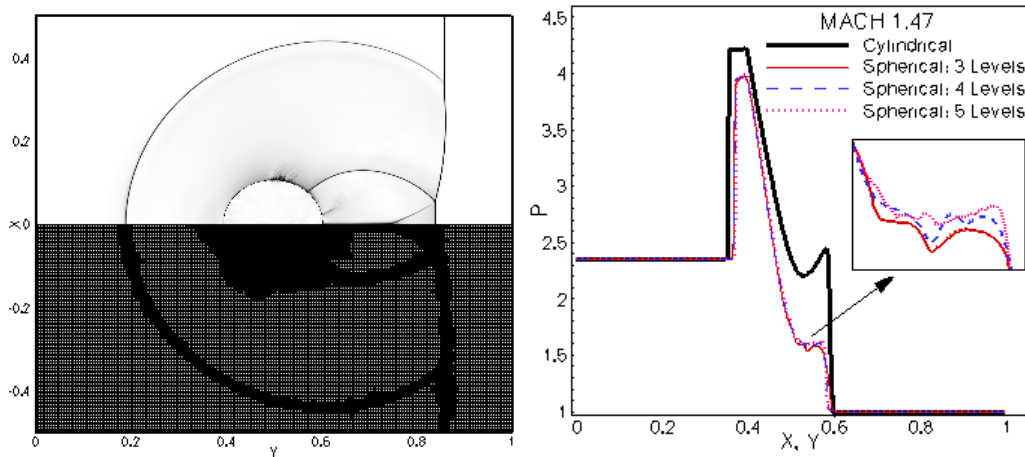
(c) Comparison of numerical Schlieren image at T = $1.128\mu s$

(d) Pressure distribution along the line of symmetry at T = $0.015\mu s$

Figure 3.36: Mach 1.47 shock interacting with spherical water droplet: (a), (b) and (c) Snapshots of mesh evolution and numerical Schlieren image computed on a base mesh $\Delta x_g = \frac{1}{200}$ with 5 levels of mesh refinement (d) Pressure distribution along the line of symmetry at T = $0.015\mu s$.
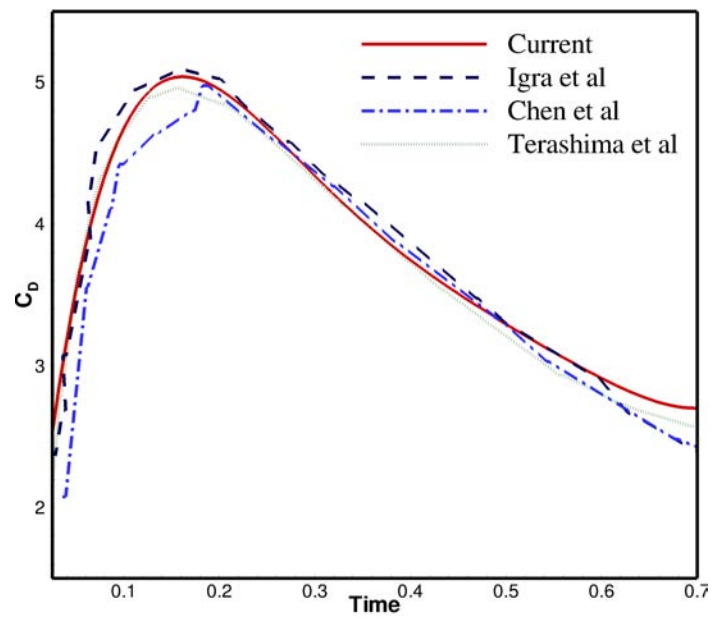
Figure 3.37: Comparison of unsteady drag coefficient computed on the surface of a cylindrical droplet

(a) Mesh and numerical Schlieren image at T = $0.02\mu s$

(b) Mesh and numerical Schlieren image at T = $0.037\mu s$

(c) Mesh and numerical Schlieren image at T = $0.06\mu s$

(d) Comparison of numerical Schlieren image at T = $0.015\mu s$
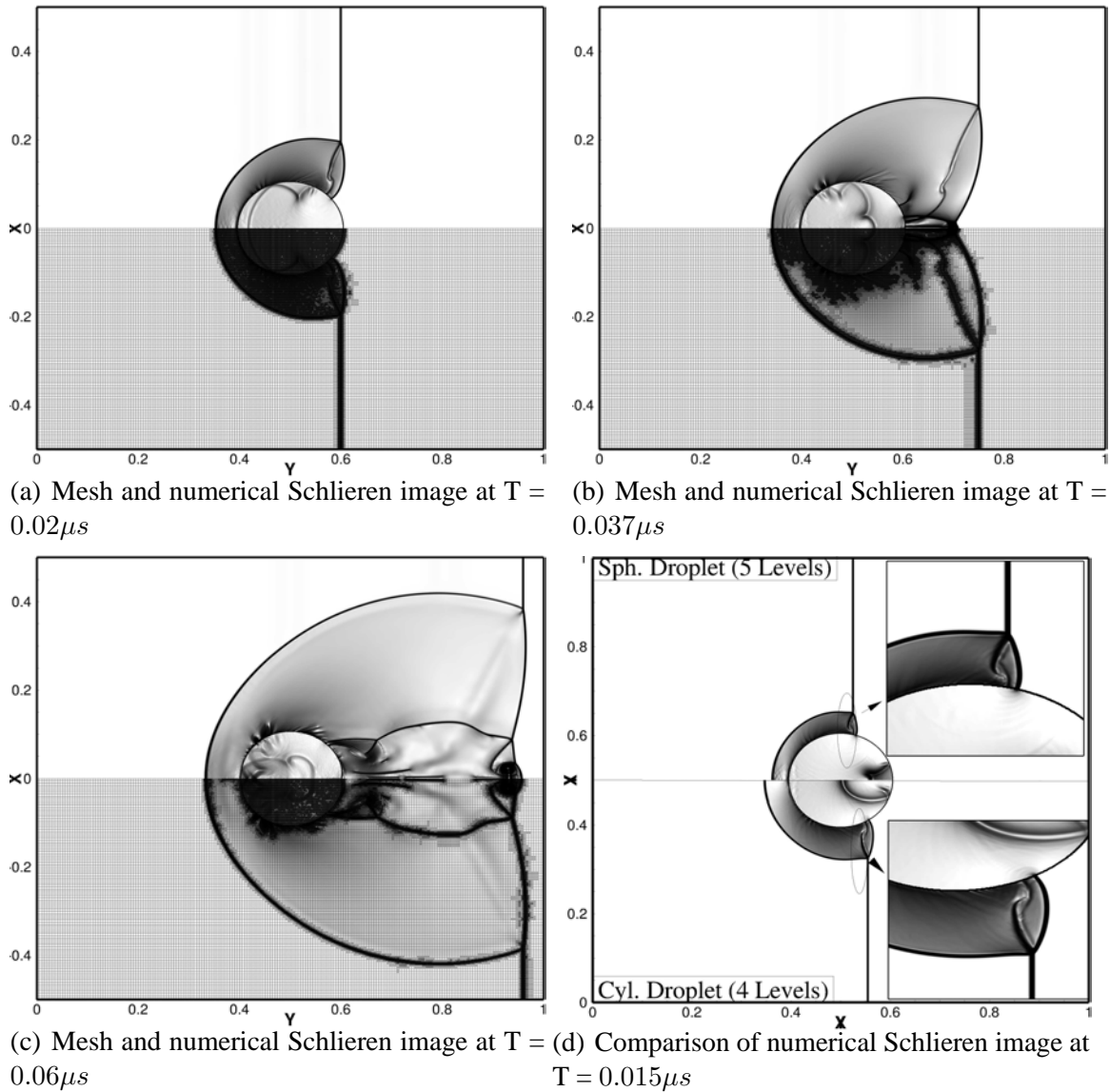
Figure 3.38: Mach 3 shock interacting with spherical water droplet: (a), (b) and (c) Snapshots of mesh evolution and numerical Schlieren image computed on a base mesh $\Delta x_g = \frac{1}{200}$ with 4 levels of mesh refinement (d) Comparison with cylindrical water column computed on a base mesh $\Delta x_g = \frac{1}{200}$ with 4 levels of mesh refinement.
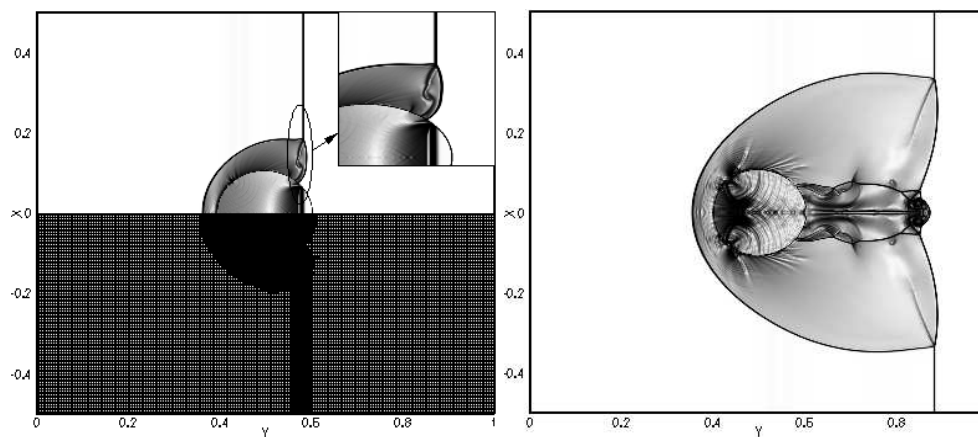
(a) Mesh and numerical Schlieren image at T = $0.01\mu s$

(b) Mesh and numerical Schlieren image at T = $0.026\mu s$
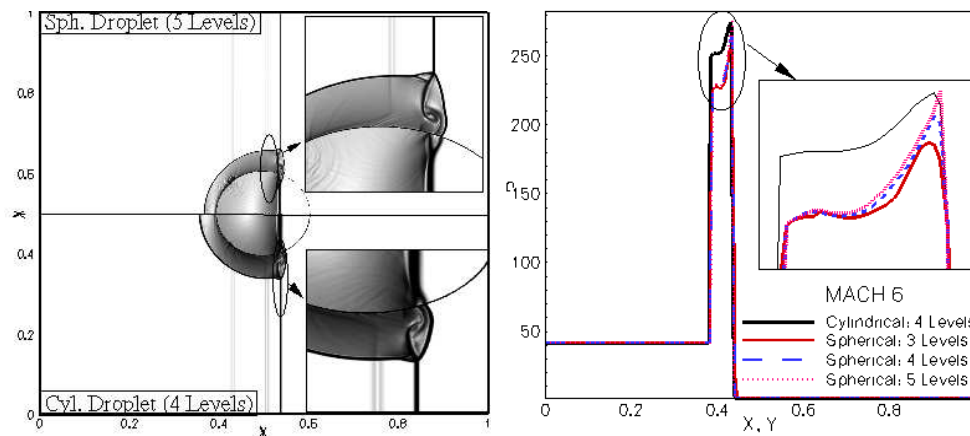
(c) Comparison of numerical Schlieren image at T = $1.128\mu s$

(d) Pressure distribution along the line of symmetry at T = $0.0031\mu s$

Figure 3.39: Mach 6 shock interacting with spherical water droplet: (a) and (b) Snapshots of mesh evolution and numerical Schlieren image computed on a base mesh $\Delta x_g = \frac{1}{200}$ with 4 levels of refinement (c) Comparison with cylindrical bubble computed on a base mesh $\Delta x_g = \frac{1}{200}$ with 4 levels of refinement; (d) Pressure distribution along the line of symmetry at T = $0.0031\mu s$.
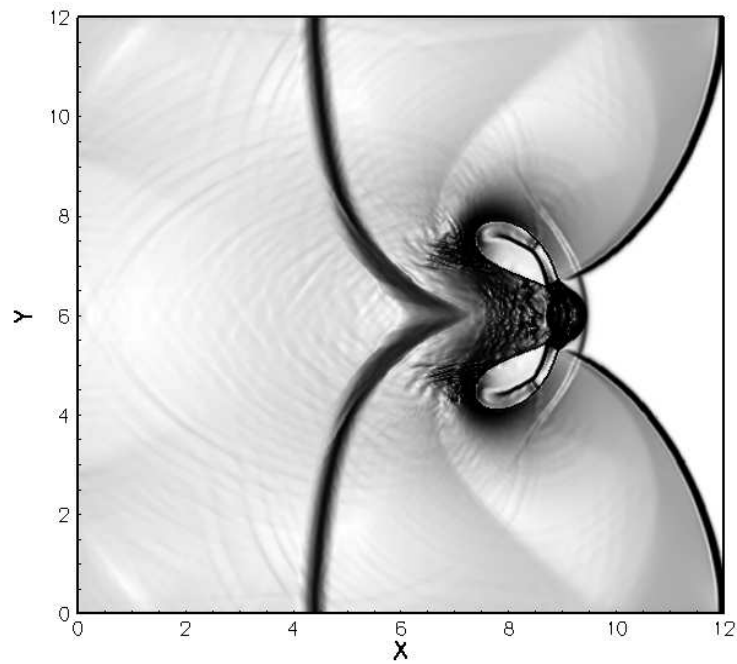
Figure 3.40: Numerical Schlieren image at T = 0.0316, for the collapse of cylindrical air cavity under the impact of a strong shock wave in water
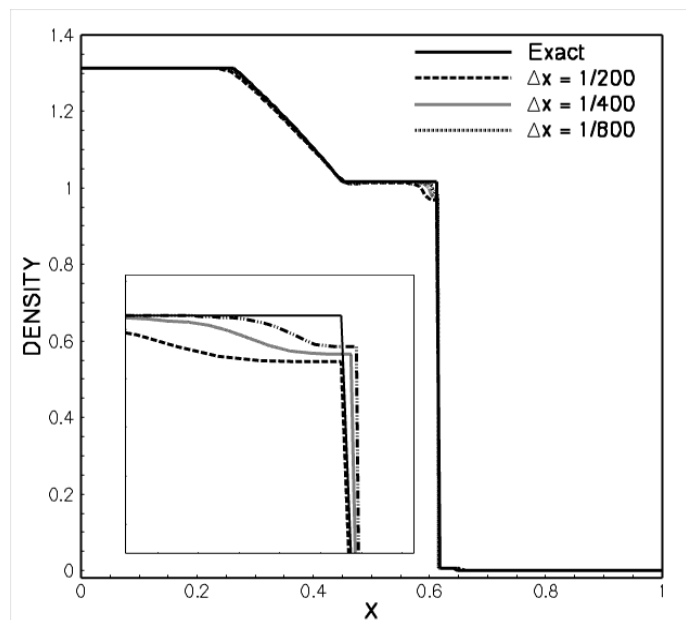
(a) Density
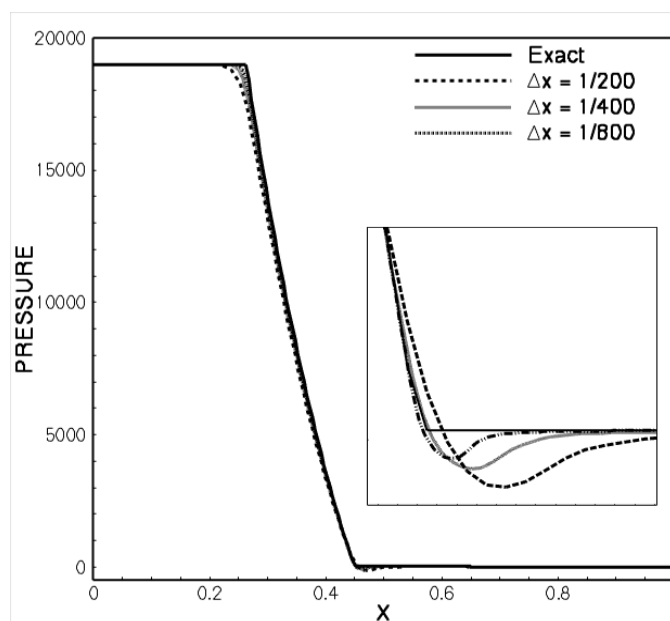
(b) Pressure

Figure 3.41: One dimensional water-air shock tube problem for the collapse of cylindrical air cavity in water. Inserts shown in the figures correspond to the variation close to the interface.

(a) Numerical Schlieren image at T = 0.005

(b) Numerical Schlieren image at T = 0.016

(c) Numerical Schlieren image at T = 0.03

(d) Mesh topology at T = 0.03
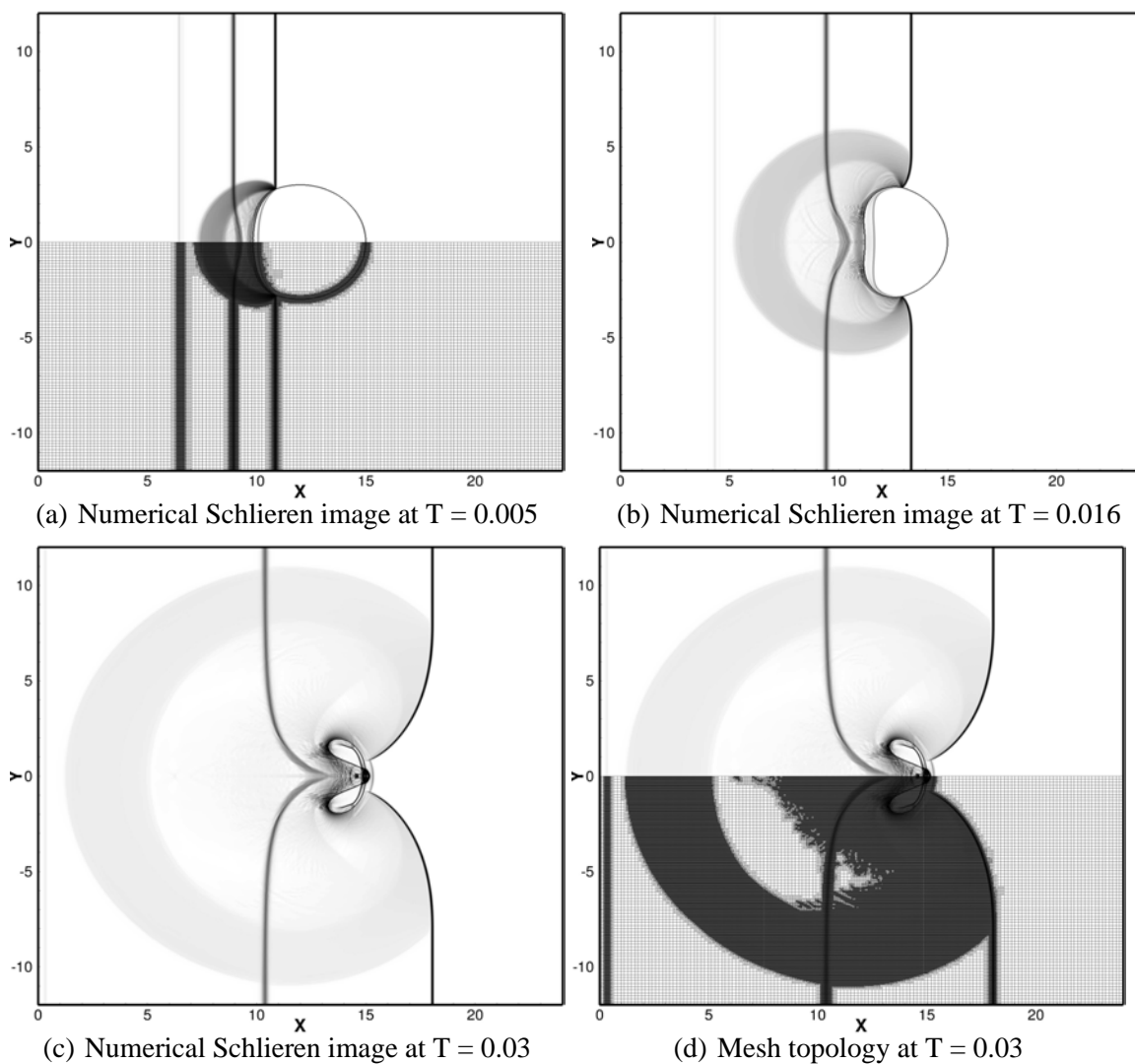
Figure 3.42: Numerical Schlieren image for the solution with 4 levels of mesh refinement on a base of size $\Delta x_g = 0.16$.

(a) Numerical Schlieren image at T = 0.03

(b) Mach contours at T = 0.03

(c) Velocity of the tail of the bubble

(d) Evolution of the interface
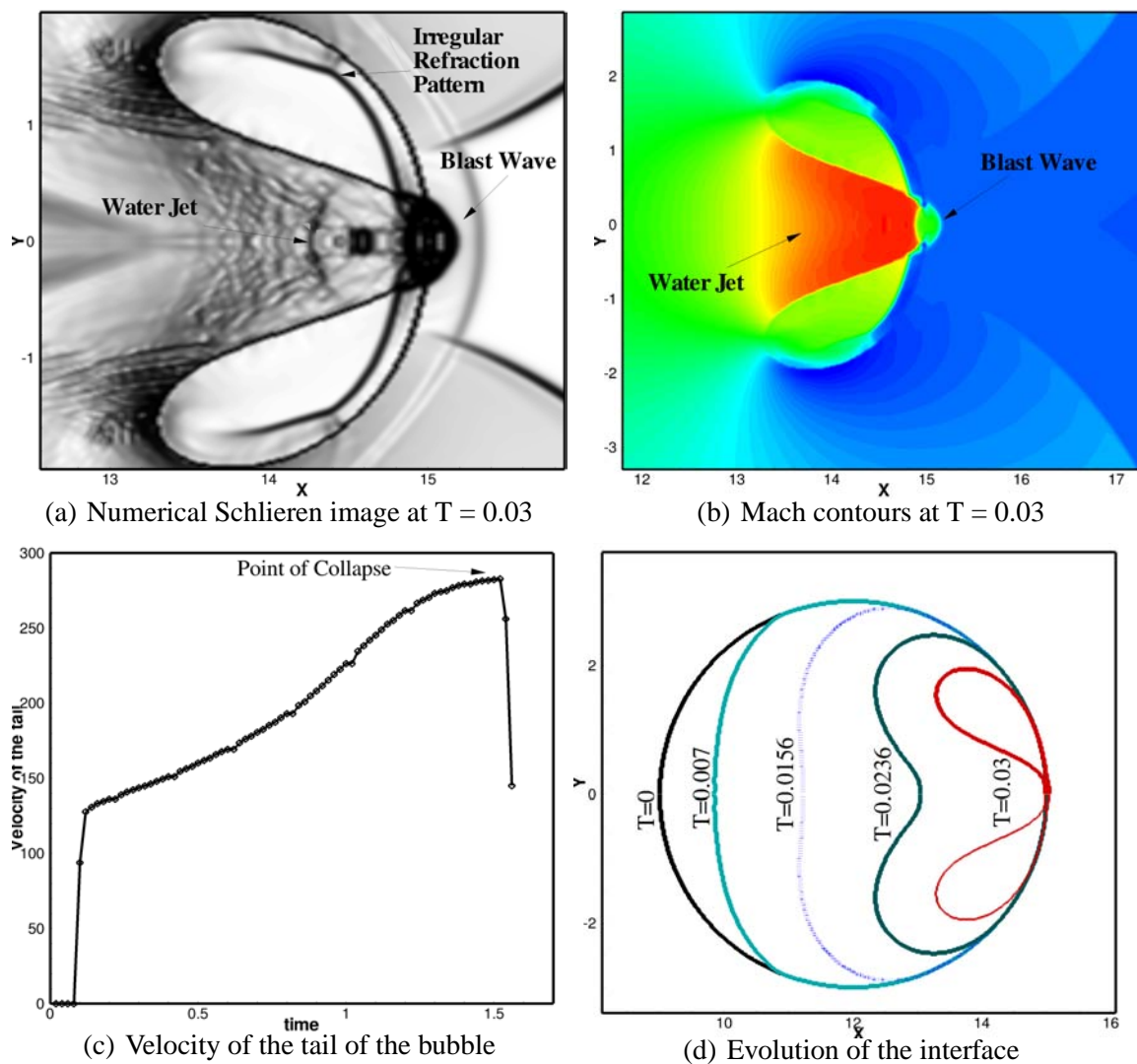
Figure 3.43: Collapse of cylindrical air cavity:(a) Close in view of the numerical Schlieren image at time T = 0.03 units; (b) Enlarged view of the Mach contours at time T = 0.03 units; (c) Velocity of the tail (rear end) of the bubble as a function of time; (d) Evolution of the interface (0-levelset).
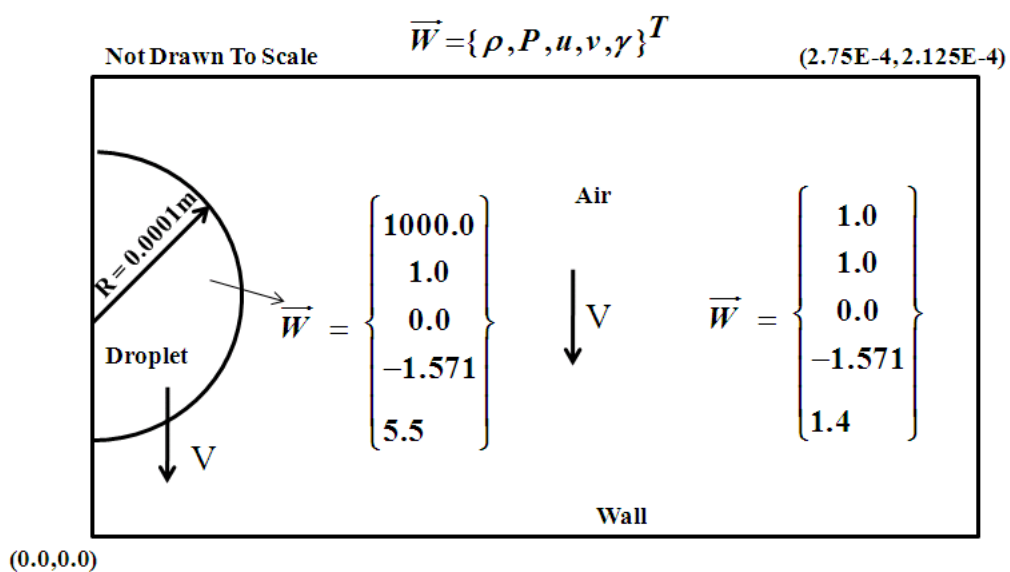
Figure 3.44: Initial configuration for high speed droplet impacting a flat substrate.

(a) Numerical Schlieren Image at 21.7 ns

(b) Numerical Schlieren Image at 37.54 ns

(c) Numerical Schlieren Image at 84.32 ns

(d) Numerical Schlieren Image at 118.8 ns
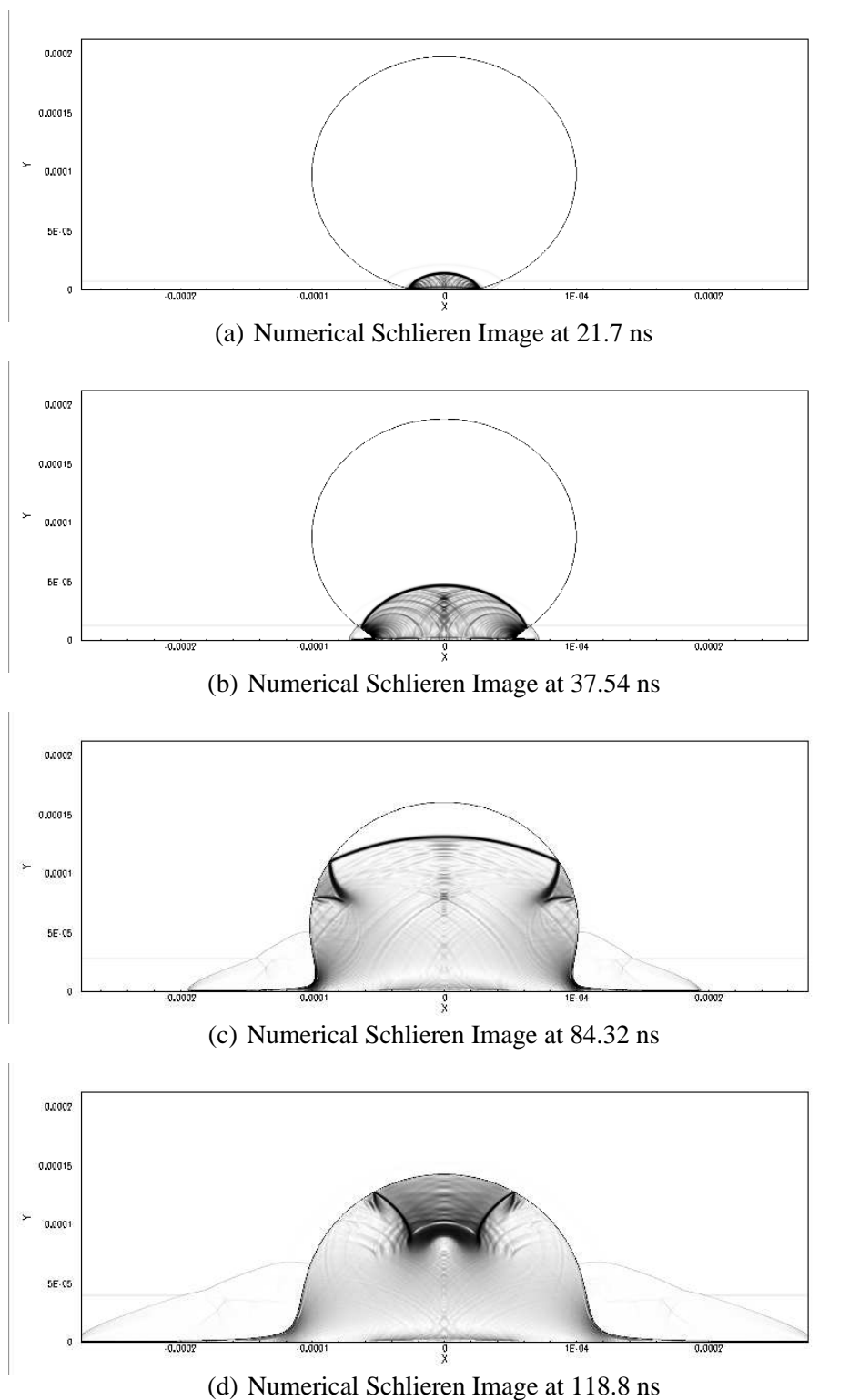
Figure 3.45: Snapshots of numerical Schlieren image illustrating the wave patterns generated from the impact of a high velocity droplet on a flat substrate at different instants in time.
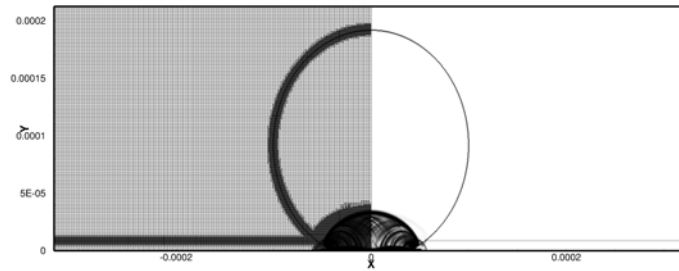
(a) Numerical Schlieren Image at 31.4 ns
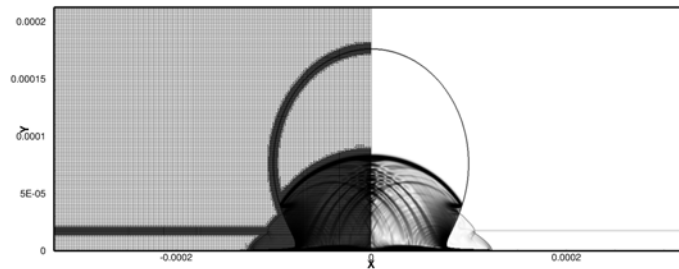
(b) Numerical Schlieren Image at 62.8 ns
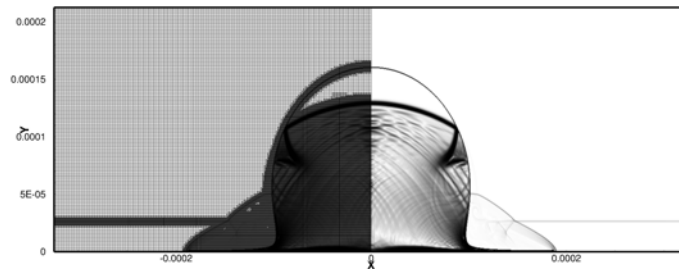
(c) Numerical Schlieren Image at 94.2 ns
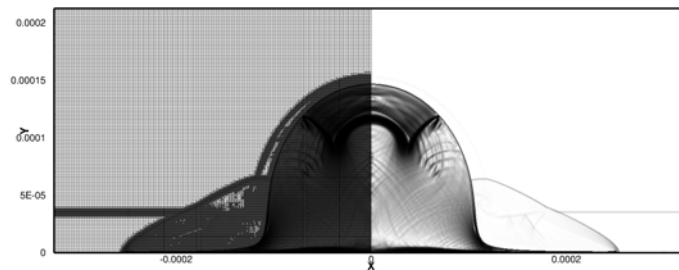
(d) Numerical Schlieren Image at 125.6 ns

Figure 3.46: Snapshots of numerical Schlieren image illustrating the wave patterns generated from the impact of a high velocity droplet on a flat substrate at different instants in time.

CHAPTER 4
SHARP INTERFACE TREATMENT FOR ELASTO-PLASTIC SOLIDS

4.1   Introduction

The phenomenology of high speed impact and penetration mechanics are of interest for plethora of applications including munition-target interactions [17, 212], geological impact dynamics [8, 150], shock-processing of powders [21, 22], vehicular collision crashworthiness [23, 214], formation of shaped charges [195, 199], etc.. In such applications, the propagation of elasto-plastic stress waves in the material dictates the deformation of the colliding bodies. The wave propagation in the interacting media is highly nonlinear, and often lead to localized phenomena such as shear bands, crack propagation, and complete failure of the material interface. In addition, the stress and strain fields are related through nonlinear elasto-plastic yield surfaces, the models for which must be included in the governing equations [192]. Capturing the response of the material interface subject to such intense loading conditions is the subject of this chapter.

In this chapter, the sharp interface GFM approach described in section 1.6 is extended to resolve the response of elasto-plastic solids due to high velocity impact and high intensity shock loading conditions. As pointed out in chapter 1, the fundamental challenges to a simulation capability designed to solve problems in the physical phenomena listed above arise from the large deformations occurring at high strain conditions suffered by the interacting materials [190]. Traditionally, the methods that have been used to solve such large deformation, finite strain transient problems have been termed hydrocodes [24].

Hydrocodes may be either based on a Lagrangian formulation, such as in EPIC and DYNA, where a moving unstructured mesh is used to follow the deformation, or an Eulerian formulation, such as in CTH, where a fixed mesh is used and the boundaries are tracked through the mesh [190]. The broad range of available hydrocodes has been reviewed by Anderson [9] and Benson [24]. In this work, an Eulerian fixed grid approach is proposed to resolve the multi-material high speed impact, collision, penetration and void collapse problems.

In contrast to the previous Cartesian grid approaches [190, 192], the present effort is attractive for the following reasons:

i. The interfaces are tracked and represented via traditional level set approach as opposed to the hybrid particle level set technique employed in [190] or the marker particles approach employed in [192].

ii. The GFM approach is applied to treat and represent the embedded interface. In contrast to [190], where the discretization scheme was modified to incorporate the boundary conditions at the interface, the present method decouples the discretization scheme from the interface capturing technique.

iii. A novel approach to infuse the boundary conditions to the ghost cells is proposed. The interaction of the embedded boundaries with each other and the evolution of free boundaries is treated by application of appropriate boundary conditions at the resulting material-material and material-void boundaries. The proposed method carefully takes into account of the subcell position and topology of the interface.

iv. A simple and a robust algorithm for tracking and detecting collision is developed. The algorithm is shown to be effective in resolving collisions at very high speeds of interaction.

v. Local mesh adaptation is employed for efficient resolution of disparate length scales and strong gradients.

vi. Plethora of numerical examples encompassing a broad spectrum of speeds of interaction (up to 7 km/s) are presented. Although the numerical examples illustrated in this chapter are limited to planar two-dimensional or axisymmetric problems, the formulation of the approach is carried out in three-dimensions. These examples demonstrate the robustness and accuracy of the present approach.

4.2   Governing Equations and Constitutive Models

The governing equations and constitutive relations along with the modeling assumptions are discussed at length in section 1.3. Because of the very high speeds involved in the interaction process, the governing equation constitutes a set of hyperbolic conservation laws. When cast in Cartesian coordinates, the equations take the form given in Eq 1.13. The governing equations are solved in its entirety, including the models for the strength of the materials. These equations are solved in an Eulerian setting on a fixed Cartesian mesh. Eigenvalue analysis performed in [194] ensure hyperbolicity of the governing equations for the impact velocity regime of interest. The equations are solved using a third-order TVD-based Runge-Kutta scheme for time integration and third-order convex ENO scheme [120] for spatial discretization.

4.3   Capturing the Response of the Material Interface

One of the exemplifying feature of the problems solved in this work is that the embedded material interface is subject to very severe deformations at high strain-rate conditions. These deformations occur almost instantaneously (typically $O(\mu s)$) and hence require meticulous treatment and resolution of the interface. In this work, the response of the material interface subject to high velocity impact and shock loading conditions is captured using the GFM approach outlined in section 1.6. As mentioned before, the GFM approach requires a definition of band of ghost points corresponding to each phase of the interacting material. When this band of ghost points are supplied with flow properties the ghost field together with the real field constitute a single flow field wherein a single equation of state can be used. Thus in the GFM approach it boils down to populating the ghost cells with suitable flow conditions.

4.3.1   Populating the Ghost Points

To populate the ghost cells appropriate boundary conditions need to be applied at the interface location. The conditions that must be enforced at the interface to populate the ghost cells depend on the material that the interface separates. For instance, the interface could separate a material from another material or void. Depending on the nature of the interface and the material that the interface separates, the conditions are modified and the ghost cells are populated accordingly. Section 1.6.2.2 enlists the conditions that must enforced for interfaces separating different materials. The set of conditions that must be

enforced at the interface can be concatenated in the following general set of conditions.

$$\text{Dirichlet condition: } \Psi_I \quad = \quad l_I \qquad (4.1)$$

$$\text{Neumann condition: } \frac{\partial \Psi_I}{\partial n} \quad = \quad m_I \qquad (4.2)$$

$$\text{Continuity of flow variables: } [\Psi_I] \quad = \quad n_I \qquad (4.3)$$

$$\text{Discontinuity of flow variables: } [\Psi_I] \quad \neq \quad 0 \qquad (4.4)$$

where Ψ_I correspond the flow variables for which the boundary conditions are applied. The ghost points are defined with flow conditions such that the real field along with the corresponding ghost field satisfy the boundary conditions (Eqs 4.1 - 4.4) accurately at the interface. In what follows, the numerical procedure to apply the boundary conditions is briefly reviewed.

4.3.1.1 Applying the Boundary Conditions at the Material Interface:

To apply the boundary conditions (Eqs 4.1 - 4.4) at the interface, a reflective boundary condition-based approach is adopted. For instance, to define the ghost states at point P (Figure 4.1), a probe is inserted to identify the reflected point IP1 and the point IP on the interface. Points IP and IP1 can be identified by using the level set distance function:

$$\vec{X}_{\text{IP}} \quad = \quad \vec{X}_P + \mid \phi_P \mid \vec{N}_P \qquad (4.5)$$

$$\vec{X}_{\text{IP1}} \quad = \quad \vec{X}_P + 2\mid \phi_P \mid \vec{N}_P \qquad (4.6)$$

where $\vec{X}$ is the position vector, ϕ_P the level set value at point P and $\vec{N}_P$ is the normal vector at point P. Once points IP and IP1 are identified, a Vandermonde matrix is constructed on the surrounding interpolation nodes to determine the flow properties at the ghost point

P. For instance, the surrounding interpolating points 1,2,3 and IP are determined for the reflected point IP1 (Figure 4.1). At the point IP on the interface, either the value of the flow variables (Dirichlet conditions) or the flow gradient (Neumann type conditions) is available. Thus it is necessary to embed the appropriate boundary conditions to complete the interpolation procedure. For bilinear interpolation we have

$$\Psi = a_1 + a_2 x + a_3 y + a_4 xy \tag{4.7}$$

where (x,y) are the coordinates of the surrounding interpolation nodes. For Dirichlet condition on IP, the Vandermonde matrix takes the following form:

$$\begin{pmatrix} 1 & x_1 & y_1 & x_1 y_1 \\ 1 & x_2 & y_2 & x_2 y_2 \\ 1 & x_3 & y_3 & x_3 y_3 \\ 1 & x_{IP} & y_{IP} & x_{IP} y_{IP} \end{pmatrix} \begin{pmatrix} a_1 \\ a_2 \\ a_3 \\ a_{IP} \end{pmatrix} = \begin{pmatrix} \Psi_1 \\ \Psi_2 \\ \Psi_3 \\ l_I \end{pmatrix} \tag{4.8}$$

For Neumann condition, the matrix is modified as follows

$$\begin{pmatrix} 1 & x_1 & y_1 & x_1 y_1 \\ 1 & x_2 & y_2 & x_2 y_2 \\ 1 & x_3 & y_3 & x_3 y_3 \\ 0 & n_x & n_y & n_x y_{IP} + n_y x_{IP} \end{pmatrix} \begin{pmatrix} a_1 \\ a_2 \\ a_3 \\ a_{IP} \end{pmatrix} = \begin{pmatrix} \Psi_1 \\ \Psi_2 \\ \Psi_3 \\ m_I \end{pmatrix} \tag{4.9}$$

The last row of the coefficient matrix in Eq (4.9) is obtained by differentiating Eq (4.7), noting that

$$\frac{\partial \psi}{\partial n} = \frac{\partial \psi}{\partial x} n_x + \frac{\partial \psi}{\partial n} n_y \tag{4.10}$$

where n_x and n_y are the normal vector components and m_I corresponds to the value of the normal gradient at the point IP. Once the coefficients are determined, the flow properties at

the reflected point can be deduced using Eq (4.7). For flow variables that are continuous across the interface, the ghost states at point P are obtained by directly injecting the corresponding flow properties from the real fluid present at point P. The discontinuous variables are extended to the ghost points via a constant extrapolation approach [15]. Alternatively, since a constant extrapolation approach ensures zero gradient condition at the interface, the ghost states corresponding to the discontinuous flow variables can be determined by enforcing Neumann condition with $m_I = 0$ in Eq 4.9. Once the flow conditions at the ghost points adjacent to the interface are determined, the values corresponding to the interior ghost cells are obtained by solving the extension equation.

4.3.2 Collision Detection Algorithm

In the present work, material interfaces are expected to collide with other interfaces or collapse and fragment. Such events need to be tracked and appropriate interface conditions applied on the interacting parts of the interface. In the current framework, multiple objects with different material properties are described by different level set functions. Only one material can possess a given computational grid point at any time, whether it be void or solid material.

At the beginning of the calculation, the material enclosed inside and outside the interface are identified as solids, liquids, voids or elsasto-plastic solids. Then one of these material is classified as bulk material indicating that the objects are immersed in the surrounding bulk material as shown in Figure 4.2(a). Thus unless a collision is detected, the embedded object is said to interact with the surrounding bulk material and the cor-

responding interface conditions are enforced to populate the ghost cells. For instance, in Figure 4.2(a) an elasto-plastic solid object is immersed in surrounding bulk material, which in this case corresponds to a free-surface. Thus for the interface separating the elasto-plastic solid and the bulk free surface, the conditions corresponding to the material-void interface, described in section 4.3, are enforced to populate the ghost points.

Various situations may arise when two different objects move toward each other as shown in Figure 4.2(b). Collisions between multiple objects are inevitable when the approaching objects are in close proximity. In such cases the interface conditions that must be applied to populate the ghost points must be different from the material-bulk material conditions. Thus it is necessary that the colliding objects are detected and the interface is resolved accordingly. For this purpose the following algorithm is adopted.

To begin with the points straddling the material interface (called the interfacial points) are tagged as "bulk nodes", indicating that the interfacial points are nodes that always interact with the surrounding bulk material. To detect collision, the distance between the interface of the current object and other interfaces are computed using the level set functions associated with each interface. For the sake of illustration consider the case of two levels sets approaching each other as shown in Figure 4.2(b). At any interfacial grid point, the values of each level set at that point represents the distance to their respective interfaces. Therefore, the difference in these values represents the distance between the two interfaces. If the distance between two approaching level sets is less than the tolerance limit, then the point is marked as a "colliding node". For instance, with reference to Figure 4.2(b), all the interfacial points are tagged as bulk nodes. Then the collision algorithm

is invoked to determine the colliding nodes. In Figure 4.2(b), the potential collision point P is identified by computing the approaching distance between the two colliding objects. The approaching distance in this case can be computed from the value of the level set field at point P as indicated in the figure. If this approaching distance is less then the tolerance limit then point P is tagged as colliding node. Once a point is marked as colliding node, the conditions corresponding to the material-bulk material are no longer enforced at that point. Instead the condition corresponding to the material-material interface are enforced to populate the ghost points. This process is repeated for each level set after the level set is advected. The tolerance limit to detect collisions are set at $\kappa \Delta x$ where κ corresponds to the CFL number with which the interface is advected. This prevents inter-penetration of level sets as any grid point can be contained within one level set.

For two level sets, each defining a moving boundary under impending collision, the normal velocity at the interface is continuous through the impact surface, whereas the tangential component may be discontinuous as sliding is permitted. No surface friction is accounted for in this work but can easily be included in the present framework. Thus unlike in [15], the level set field and level set velocities are unaltered and the inter-penetration of the level set field is prevented.

4.4   Numerical Examples

4.4.1   Impact of a Copper Rod over a Rigid Substrate - Axisymmetric Taylor Bar

Experiment

4.4.1.1   Impact at 227 m/s - Validation

Taylor test [185] on a copper rod is considered. The Taylor test analysis have been used as a canonical test problem to verify and validate numerical and experimental observations. Taylor [185], after an extensive analysis on the impact of cylindrical specimen over a rigid flat substrate, depicted the deformation process as a sequence of elastic and plastic wave propagation into the cylinder. In the two-dimensional setting, a cylindrical rod made of copper with an initial radius of 3.2 mm and a length of 32.4 mm impacts a rigid flat substrate at 227 m/s (Figure 4.3). A computational domain of radius 8 mm and length 34.0 mm is chosen for this simulation. The top and right end of the computational domain are prescribed with Neumann conditions. The presence of rigid wall on the bottom end of the domain is modeled by enforcing a reflective condition. The left end of the domain is prescribed with symmetry condition (with $S_{xy} = 0$). The deformation of the rod is presumed to be axisymmetric. The rod has an initial density of $8930\frac{kg}{m^3}$, Young's modulus $E = 117GPa$, Poisson's ratio $\nu = 0.35$, and yield stress $\sigma_Y = 400MPa$. The material is assumed to harden linearly with a plastic modulus of $100MPa$. The calculations are carried out up to a time of $80\mu s$ (at which point nearly all the initial kinetic energy has been dissipated as plastic work) on a base mesh of size $\Delta x_G = 0.5mm$ with 3, 4 and 5 levels of mesh refinement. The CFL number was set to 0.4 for this computation.

The impact of the rod with the bottom rigid surface results in a precursor, compres-

sive, elastic wave traveling in the bar followed by a slower nonlinear plastic wave front. The elastic wave travels the entire length and the width of the rod, and is reflected off the free surface as relief wave. The deformation of the rod ends with the reflected elastic wave interacting with the plastic wave, since the stress is reduced to zero [131]. Similar to the impact of the liquid droplet, the initial deformation of the rod is along the line of contact with the rigid substrate (Figure 4.4(a)). However, in contrast the droplet impact, the jetting of the rod continues along the line of contact up to 40 μs at which point the material begins to harden (Figure 4.4(b)). With the hardening of the material near the foot of the rod, the plastic wave (deformation) moves up the rod resulting in the bulging of the base as shown in Figure 4.4(c). At around 80 μs, the rod reaches a state of rest with the familiar mushroom like shape (Figure 4.4(d)).

In Figure 4.7(a), the evolution and the topology of the interface at different instants in time are plotted. The interface topology displayed in the figure corresponds to the solution obtained using 5 levels of mesh refinement. The interface evolution matches well with that reported in [180, 190]. To validate the present approach, the results obtained from the current calculations are compared with previous numerical simulations [180, 190, 192, 210]. The parameters, such as the final radius of the mushroom foot, the final length and the maximum effective plastic strain, characterizing the impact of the rod computed in the present study agree well with the previously reported values (Table 4.1). The methodology developed in this work is stable and accurate in capturing the extreme stress and velocity gradients developed in the rod at the moment of impact.

4.4.1.2   Impact Velocity of 400 m/s and 600 m/s

The Taylor test is repeated with impact velocities of 400 m/s and 600 m/s. The calculations are conducted with 5 levels of mesh refinement. The plots from the present calculations are displayed in Figures 4.5 & 4.6. As expected, with the increase in the impact velocity the deformation in the bar is much severe. For the sake of comparison, the evolution of the interface at different instants in time are plotted in Figure 4.7. Also shown in the figure is the final configuration of the bar at $80\mu s$. As can be seen from the figures, for the impact velocity of 600 m/s the bar has completely deformed before coming to rest. The final radius of the mushroom foot, the final length and the maximum effective plastic strain, corresponding to different impact velocities are tabulated in Table 4.2.

4.4.2   2D Axisymmetric Penetration of Steel Target by WHA Long Rod

The validation of the present method for two deformable objects with different material properties is carried out using a slender Tungsten heavy alloy (WHA) rod projectile penetrating an initially planar target made of a steel plate. Plates of 29.0 and 49.5 mm thick were tested at incident velocities of 1250 m/s and 1700 m/s. The thickness represent the previously determined ballistic limits for the impact velocities [180]. The cylindrical projectile of 2 mm in radius and 50 mm length impacted a cylindrical steel plate of 40 mm in radius. A schematic defining the problem is shown in Figure 4.8. The response of the materials were modeled by using a Johnson-Cook material model and the corresponding parameters for both materials are shown in Table 1.2. The friction between the two impacting surfaces is neglected in these calculations. The simulations are carried out on a base

mesh of size $\Delta x_G = 0.0005$ with 4 levels of mesh adaptation.

In the previous Eulerian calculation reported in [190], the solutions were obtained on a truncated domain (0.0125 m X 0.02 m) with a grid density of 100x688 mesh points. With the adaptive mesh refinement facility the current computations were performed on the actual size as employed in the previous experimental [10] and numerical calculations [180]. In Figures 4.9, 4.10 & 4.11, the contours of effective plastic strain (ϵ_P) and velocity, the evolution of mesh and the interface topology are plotted for the impact velocity of 1250 m/s. As can be seen from the figures, the response of the projectile and the target agrees well with the calculations reported in [180]. The ejecta, which were not captured by the previous particle level set approach [190], are predicted very well and matches with the results presented in [180]. The maximum equivalent plastic strain is found to be around 4.5, occurring mostly near the impact surfaces. The values of equivalent plastic strain are higher in the WHA material compared to those in the steel material. The plastic strains obtained in [180] using Lagrangian finite element method with an adaptive mesh agree very well with the present results, both in terms of the magnitude and distributions of the plastic strains. In particular, a trough in the plastic strain distribution is noticed in both results and occurs near the bottom surface in the steel plate at the symmetry axis, as seen in Figure 4.9(d). The ejection length of the WHA material also agrees well with [180]. The maximum positive v-component velocity is observed around $40\mu s$, occurring in the ejecting mass of the WHA material. Around $80\mu s$, the rod comes to rest and only small residual velocities remain. The maximum temperatures occur around the impacted surfaces as this is the region of maximum rate of conversion of plastic work to heat. The recorded maximum

temperature is around 1575 K in the WHA material, below the melting temperature of 1777 K for WHA and 1723 K for steel. The largest temperature occurs at around 40μs, and decreases as the rod goes to rest state. This shows that the largest plastic work done occurs before this time of 40μs.

Figures 4.12(a) & 4.12(b) show the projectile nose and tail trajectories and velocities as a function of time, and is compared with the superposed results from experiment [10] and from numerical calculations [180]. Also plotted are the original rear and impact surfaces. The results show excellent agreement with those of experiment and numerical observations. The predicted penetration depths is also in good agreement with experiments.

In Figures 4.13, 4.14 & 4.15, the contours of effective plastic strain (ϵ_P) and velocity, the evolution of mesh and the interface topology are plotted for the impact velocity of 1700 m/s. Similar to the impact velocity of 1250 m/s, the maximum equivalent plastic strain recorded is found to be 5.0. The plastic strains obtained in [180] using Lagrangian finite element method with an adaptive mesh agree very well with the present results, both in terms of the magnitude and distributions of the plastic strains. In contrast to the lower impact velocity, projectile is completely absorbed by the target forming a slightly larger crater and longer penetration length. Similar to the previous case, the rod comes to rest with only small residual velocities around 80μs. The results are in excellent agreement with that of [180]. Figures 4.16 & 4.16(b) show the projectile nose and tail trajectories and velocities as a function of time, and is compared with the superposed results from experiment [10] and from numerical calculations [180, 190]. The plots are in excellent agreement.

4.4.3 Shock Wave Interaction with Hemispherical Groove

Shock wave interacting with a hemispherical groove in a Copper matrix is considered. A planar shock wave generated by contact explosion interacts with a hemispherical groove of radius 15 mm. The generated shock wave corresponds to a particle velocity of 540 m/s and a pressure ratio of 230 Kbar [46]. The center of the groove is located at 29 mm from the bottom surface of the plate. The shock is initiated by quadratically accelerating the velocity of the bottom domain from 0 to 540 m/s. A computational domain of 250 mm X 30 mm is chosen. A base mesh of size $\Delta x_G = 0.003$ with 4 levels of mesh refinement is selected. The simulation is run till 100 μs. Johnson cook material model is employed to simulate the response of the Copper matrix.

The interaction of the shock wave with the hemispherical groove results in a reflected expansion wave and a formation of jet. The formation of the jet was confirmed in the experimental work reported in [123] and subsequently in the numerical work reported in [46]. The model can also be viewed as a prototype for hemispherical explosively formed projectile (EFP) where the formation of the jet resembles that of the EFP. The jet reaches a maximum velocity of 2750 m/s at about 12 μs and continues to jet until it reaches the target. For the sake of validation, the maximum jet velocity and the jet diameter obtained from the present calculations are compared with the previous computational [46] and experimental observation [123]. The values are reported in Table 4.3. The agreement is excellent. The mesh topology and the velocity contours are shown in Figure 4.17. In Figure 4.18, the interface topology at different instants in time are plotted. The evolution of the interface closely follows the trend reported in [46].

4.4.4 Void Collapse in a Copper Matrix

In this test case, a cylindrical void with a radius of 1 μm within a Copper matrix undergoes deformation due to a propagating shock created by imposing a particle velocity of 550 m/s at the bottom domain boundary. The schematic of the problem is given in [190]. The response of the Copper material is modeled using a Johnson-Cook model. The wave moves through the copper matrix and is transmitted out through the upper boundary. Both right and left boundaries are subjected to symmetric conditions. As pointed out in [46], void collapse is defined as the point at which the lower and upper boundary surfaces come into contact. The void collapse phenomenon has implications for the initiation process in energetic materials. Void collapse can occur in different modes depending on the strength of the impinging shock. As the shock strength increases the void collapse goes from a nearly cylindrical (visco-plastic) mode to a jet (hydrodynamic) mode where the lower surface of the void forms a jet which impacts on the upper surface at high velocity. The criterion for the transition from the visco-plastic to hydrodynamic mode is provided by the analysis of Khasainov [106] in terms of the ratio of shock passage time to the void deformation time scales. If the shock passage time scale is larger than the void collapse time scale the mode of collapse is visco-plastic, and when the shock passage time scale is comparable with the void collapse time scale the mode of collapse is hydrodynamic [190]. This latter mode is characterized by the formation of a jet of material which issues from the lower side of the void and impacts the upper side, leading to large temperatures on the impact location due to dissipation of kinetic energy of the jet [190].

The results from the current calculations are displayed in Figure 4.19. Formation

of a distinct jet can be observed, with the highest velocity of the jetting material being around 3360 m/s, much higher than the imposed particle velocity. Similar to the hydrodynamic case, the formation of the blast wave at the instant of collapse is also clearly visible 4.19(d). One can see that the void would be completely collapsed before the shock wave reaches the top boundary of the domain, i.e. this case represents the hydrodynamic mode of collapse in agreement with the criterion mentioned above. The evolution of the interface is displayed in Figure 4.20. As expected, the evolution closely follows the trend observed in the hydrodynamic case.

4.4.4.1 High Velocity Impact of a Metallic Sphere on a Metal Target

In this example, a high velocity impact of a metallic sphere over a flat metal substrate is studied. Two sets of material compositions are considered in this problem:

- Configuration 1: Impact of a heavy alloy Tungsten sphere on an infinitely thick Steel target

- Configuration 2: Impact of a Copper sphere on an infinitely thick Copper target

The impact velocity of the sphere is fixed at 2000 m/s for both configurations. Configuration 1 is a simple modification of the WHA rod penetration example considered in [180,190] whereas configuration 2 corresponds to the problem investigated in [192]. The dimension of the impinging sphere and the semi-infinite target are displayed in Figure 4.21. The response of the metallic sphere and the target are modeled using Johnson-Cook material model. The calculations are carried out in a domain of size 0.125 mm X 0.175 mm on a base mesh of size $\Delta x_g = 2\mu m$ with 4 levels of mesh adaptation. The results from the

present calculations are presented in Figure 4.22.

Figure 4.22 shows the response of the initially spherical impactor and the target. The initial response for the two configurations are very similar (Figures 4.22(a) & 4.22(d)). The impact sets off a compressive wave traveling in both the impactor and the target. Due to the difference in speed of sound in the media, the subsequent response of the material is vastly different. As can be seen in Figures 4.22(c) & 4.22(d), the size and shape of the ejecta for configuration 2 starts to differ from that of configuration 1. The depth of penetration (Figures 4.22(e) & 4.22(f)) and the width of the resultant crater (Figures 4.22(g) & 4.22(h)) are different for both the configurations. The topology and the evolution of the interface for the two configurations are displayed in Figure 4.23.

As can be seen from the figure, the depth of penetration for configuration 1 is much greater than that of configuration 2. On the other hand, the width of the crater for configuration 1 is significantly smaller than configuration 2. The heavier Tungsten sphere, due to its larger initial kinetic energy penetrates much deeper and comes to rest at about 250 μs. The lighter Copper sphere comes to rest at 200 μs. It is worth pointing out that the previous calculation reported in [192] failed to capture the formation of crater and ejecta. With the present framework, these features that are typical of hyper-velocity impact phenomena are depicted and predicted accurately.

4.4.5 Very High Speed Impact of Aluminum Sphere over Aluminum Target

In this example, a very high speed impact of Aluminum sphere into an effectively semi-infinite Aluminum target is investigated. The Aluminum sphere impacts the target

at 7000 m/s. An Aluminum sphere of 6.35 mm in diameter impacts a target also made

of Aluminum. The length and the radius of the semi-infinite cylindrical target are 10.0

mm and 2.9 mm respectively. The simulations are carried out with a base mesh of size

$\Delta x_G = 0.0005$ with 4 levels of mesh adaptation. A Johnson-Cook material model is

employed to compute the response of the Aluminum target and the impactor.

The problem was previously investigated in [213] using a two-dimensional explicit

Lagrangian FEM hydrocode ZeuS. The zoomed in view of the results obtained from the

current calculations are reported in Figures 4.24 & 4.25. As expected, due to the very

high velocity involved in the impact process, a shock wave is formed that travels both in

the impactor and the target. These shock waves are visible in Figure 4.25(a) in which the

mesh adaptation and the contours effective plastic strain (ϵ_P) are displayed. The mesh

adapting to the shock wave is also clearly visible in the figure. Subsequent evolution

of the mesh and the deformation of the impactor and the target are displayed in Fig-

ures 4.25(b), 4.25(c), & 4.25(d). As pointed in [213], the projectile is almost consumed

by 3 μs after impact (Figure 4.24(b)). Due to very large incident kinetic energy, the width

of the crater and the depth of the ejecta are very large compared to the corresponding low

velocity impact processes. Aluminum impactor eventually forms a very thin layer that set-

tles on the crater formed on the target (Figure 4.24(d)). Since the target is sufficiently large,

there are no reflected relief waves from the target to relieve the compressive strain in the

impactor. As a result, the impactor is always in a state of compression and continues to

penetrate the target. At the instant shown in Figure 4.24(d), the impactor has almost come

to a complete stop. The velocity of the head of the impactor at this instant is about 500

m/s which is about 14 times smaller than the initial impact velocity. The evolution and the topology of the interface at different instants in time are plotted in Figure 4.26. The example demonstrates the robustness of the present approach in capturing the high velocity impact phenomena.

4.4.6 Perforation of Aluminum Plates by Conical Nose Projectile

Numerical simulations of conical nosed projectile perforating cylindrical target plates are performed in this study. The conical nosed projectile is made of Tungsten and the cylindrical target plate is made of 5083-H131 Aluminum. The geometry and the problem set up can be found in the experimental studies conducted in [63]. Prior numerical calculations for this problem have been reported in [180]. Two plates of thickness 12.7 mm and 50.8 mm impacted at velocities 1195 m/s and 1176 m/s respectively are considered. The initial problem configuration is displayed in Figure 4.27. Johnson cook material model was employed to simulate the response of the projectile and the target. In consistent with the parameters selected in [180], the Taylor-Quinney coefficient β is set to zero. Both the simulations were carried out on a base mesh of size $\Delta x = \frac{1}{1000}$ with four levels of mesh refinement. The histories of effective plastic strain (ϵ_P) along with the mesh evolution are displayed in Figures 4.28 & 4.29.

The conical nosed projectile upon impacting the target forms a hole with cavity diameter equal to the shank diameter of the projectile [63]. As reported in [63, 180], the impacting projectile is practically undeformed for both incident velocities. This can be readily seen from the snapshots displayed in the Figures 4.28 & 4.29. The sharp conical

nose of the projectile is retained in tact even when the interface is moved using the traditional level set advection procedure (with no Lagrangian particles for correction). This clearly indicates that the diffusion errors that are intrinsic in the level set technique have very little influence in altering the shape and topology of the interface. Furthermore the adaptive mesh refinement facility employed in this work is effective in mitigating these diffusion errors. The mesh adaptation and evolution displayed in the figures clearly show that the regions with fine mesh are concentrated to those region with significant plastic strain. The maximum effective plastic strain computed for the 12.7 mm thick Aluminum plate is 1.52 which is close to the value (1.50) reported in [180]. However, the value registered for the 50.8 mm thick Aluminum plate is 2.05 which is greater than the value reported in [180]. Nevertheless, the response of the plate closely follows the trend reported in [63, 180].

4.4.6.1   Explosion Inside a Copper Tube

In this example, an explosion inside a Copper tube and the response of the Copper metal walls is simulated. The initial configuration of the problem is shown in Figure 4.30. A high pressure explosive core of gas is located at the center of a Copper tube containing water at ambient conditions. The initial conditions are given below:

$$(\rho, P, u, v, \gamma) = \begin{cases} (4000.0 kg/m^3, 500000.0 atm.0, 0.0, 0.0, 7.15) \text{ for} \\ \\ (1000.0 kg/m^3, 1.0 atm, 0.0, 0.0, 1.4) \text{ for water at ambient conditions.} \end{cases}$$

The size of the computational domain is 6m X 6m and the size of the base mesh employed is $\Delta x_g = 0.06$. The computations are carried out with four levels of mesh refinement. The explosive core is modeled using an ideal gas law and the surrounding bulk fluid (water) is

modeled using a stiffened equation of state (Eq 1.60). The Copper tube is idealized as a perfectly flowing plastic with no hardening model. Both the explosive core and the walls of the Copper tube are tracked and represented by level sets. The evolution of the explosive core is captured by solving the Riemann problem at the interface (Section 1.6.2.1) and the response of the metal tube is computed by enforcing the conditions listed in Section 1.6.2.2. A similar problem was investigated in [115] using the MGFM approach. In [115], the deviatoric response of the material was not computed explicitly but included in the hydro-elasto-plastic (HEP) equation of state used to model the dilatational response of the solid phase. Their model was based on the assumption that under such explosive loading conditions, the response of the material is predominantly compressive in nature. Hence the dilatational response is orders of magnitude larger than the deviatoric response of the structure. With such HEP equation of state, the MGFM approach developed in [118] was extended to model the structural response. In subsequent work [202, 203], the MGFM approach was used to couple the Eulerian fluid calculation to a Lagrangian solid calculation for exclusively modeling fluid-structure interaction problems. In direct contrast to the past efforts, the calculations reported in this section are performed with the generic sharp interface Eulerian framework. The results are displayed in Figure 4.31

The explosion sets off a shock wave that travels in the water medium and an expansion wave traveling in the core (Figure 4.31(a)). The shock wave in the water medium upon impacting the Copper tube walls, results in a transmitted and a reflected shock wave (Figure 4.31(b)). As seen in Figure 4.31(b), the impinging shock wave is strong enough to cause the Copper walls to deform. The reflected shock wave subsequently interacts with

the expanding explosive core and results in a secondary system of waves; a reflected relief wave in the water medium and a transmitted shock wave in the explosive core. The multiple reflection causes the fluid near the tube walls to cavitate and hence the calculation could not be carried out without adequate cavitation model. Development of such a model is beyond the scope of the present work and hence the computations were deliberately stopped before the cavitation phenomenon could arise. Figures 4.31(c) & 4.31(d) display the deformation of the tube walls at later instants in time. The deformation in this case is governed by the multiply reflected wave systems. Also seen in the figures is the expanding gas core with a significantly distorted shape.

4.4.6.2 Shock Wave Interacting with Deformable Metal Particle(s)

Shock waves interacting with metal particles and related momentum transfer are important in applications related to detonation and deflagaration in condensed media. Traditional models for detonation phenomena were based on frozen shock assumption wherein the momentum transfer and subsequent motion of the particles were ignored. The importance of such an assumption for heavy and light particles were analyzed in [209]. In this example, similar calculations are repeated in the current sharp interface framework. In particular, the planar shock wave interacting with spherical Aluminum and Tungsten particle of radius 5 μm are considered. An initially planar shock wave in water with initial conditions,

$$(\rho, P, u, v, \gamma) = \begin{cases} (1639kg/m^3, 1.013Kbar, 1987m/s, 0.0, 5.5) \text{ for y } \leq 2.6, \\ \\ (1000kg/m^3, 1.0bar, 0.0, 0.0, 5.5) \text{ for y } > 2.6 \end{cases}$$

is positioned at Y = 20 μm. The spherical particle is positioned at (0 μm, 25 μm) in a computational domain of size 25 μm X 50 μm. A base mesh of size $\Delta x_g = 0.5 \mu m$ with four levels of mesh refinement is used. The materials are assumed to behave perfectly plastic with no hardening model. The initial configuration of the problem is displayed in Figure 4.32.

The results from the current calculations are displayed in Figure 4.33. The initial interaction of the shock wave with the particle results in a reflected and a transmitted shock wave (Figure 4.33(a)). The transmitted shock wave upon arriving at the other end of the particle results in a reflected relieve wave and a transmitted shock wave (Figure 4.33(b)). The negative pressure values (inside the Aluminum particle) indicated in Figure 4.33(b) correspond to the tensile wave traveling in the particle. Such negative pressure contours may not be visible in [209] as a HOM equation of state was employed with no explicit correction for relief waves. As evident from Figures 4.33(c) & 4.33(d), the response of Aluminum particle is vastly different from that of Tungsten. This is because the shock wave imparts significantly higher pressure than the yield stress of the material and hence the response of the particle varies with materials [209]. The Aluminum particle not only undergoes considerable lateral expansion and distortion but also moves significantly with the incident shock wave. The evolution and the topology of the interface for Aluminum particle is shown in Figure 4.34(a). The location of the leading and trailing edge as a function of time is plotted in Figure 4.34(b). The transmission coefficient (the ratio of the velocity of the center of mass of the particle with the velocity of the incident shock wave) computed for Aluminum particle is 0.63 and the value reported in [209] is 0.6. Thus the

present calculations agree well with previous efforts [209].

Similar to the calculations performed in [209], shock wave interacting with a cluster of Aluminum particles are considered next. The strength of the shock wave is the same as the single particle. The cylindrical Aluminum particles of 5 μm radius are seeded in an orderly fashion in a computational domain of size 70 μm X 125 μm. A base mesh of size $\Delta x_g = 0.25 \mu m$ with four levels of mesh refinement is chosen for this calculation . The left and the right end of the domain are imposed with symmetry conditions to depict a periodic arrangement of particles. The solution obtained from the current calculations are displayed in Figure 4.35.

As expected the shape and topology of the particles is much different from the single particle case. This is due to the complex nature of reflected wave patterns generated from the neighboring particles. Although the present configuration is slightly different from [209], the overall interface evolution patterns are in good qualitative agreement.

4.4.7 High Velocity Impact Induced Explosion

When a high energy explosive material is impacted at sufficiently high velocity, the resulting energy deposition can cause the initiation of explosion. The facility to compute such high velocity impact driven explosion of high explosives is demonstrated in this example. The problem consist of a cylindrical WHA Tungsten projectile impacting on a cylindrical Steel casing containing HMX explosive. Three level sets, each for the Tungsten projectile, the steel casing and the HMX explosive, are employed to track and represent the interfaces. The problem demonstrates the robustness of the current approach in resolving

multiple interface collisions. The dimensions and initial configuration of the problem are shown in Figure 4.36. Johnson-cook material model are used for modeling the response of Steel casing and the Tungsten projectile. For the HMX explosive, perfect plastic flow model is assumed (neglecting the effects of viscosity). A base mesh of size $\Delta x_G = 0.0005$ along with 4 levels of mesh adaptation is used.

The impact of the projectile on the steel casing results in a momentary compressive wave, that later coalesce to form a shock wave, traveling in the projectile and the steel casing (Figure 4.37(a)). The shock wave generated as a result of this impact process (in the front end of the steel casing) is transmitted to the HMX explosive at the instant shown in Figure 4.37(a). This transmitted shock propagates through the HMX media and gets reflected and transmitted as a shock wave upon arriving at the back end of Steel casing. The secondary shock reflection process is visible Figure 4.37(b). This multiple shock reflection initiates a detonation phenomena in the HMX explosive and results in the deformation of back end of the steel casing (the part of the casing not in contact with the impactor). This deformation process is visible in Figures 4.37(c) & 4.37(d). For the sake of clarity, the evolution and topology of the interface are plotted in Figure 4.39. This deformation of the Steel enclosure and the projectile may not continue endlessly as depicted in Figure 4.37(d). With sufficient damage model, the shattering and collapse of the materials can be adequately modeled. Incorporation of damage models in the present framework is straightforward and the efforts in this direction will be reported in the future. In Figure 4.38, the mesh evolution and effective plastic strain (ϵ_P) contours at different instants in time are displayed. The mesh adaptation process is apparent in the figures.

4.4.8   Axisymmetric Dynamic-Tensile Large-Strain Impact-Extrusion of Copper

The experimental study on the influence of grain size on the response of Copper was conducted in [91]. In this section, the corresponding numerical simulations are presented. The example problem considered here consists of a Copper sphere of 7.6 mm in diameter undergoing a tensile extrusion process. The extrusion process is carried out by impact the Copper sphere fired at 400 m/s towards extrusion die. The Extrusion die made of hardened Steel is designed with an entrance diameter of 7.62 mm and an exit diameter of 2.28 mm; a reduction of 70 % as shown in the Figure 4.40. A base mesh of size $\Delta x_G = 0.0005$ is chosen with 4 levels of mesh adaptation. A Johnson Cook material model is employed to capture the response of the sphere and the extrusion die.

The evolution of the effective plastic strain (ϵ_P) and velocity contours at different instants in time are displayed in Figure 4.41. The initial impact of the sphere (at about 10 μ s corresponding to the instant shown in Figure 4.41(a)) on the extrusion die results in the acceleration of the leading edge of the sphere as it exits the die [91]. At about 20 μ s, corresponding to the instant shown in Figure 4.41(b), the conical-shaped portion of the sphere comes to rest in the extrusion die. This can be easily verified from the velocity contours registered in Figure 4.41(b) and in the subsequent Figures 4.41(c) & 4.41(d). The portion of the sphere continues to remain at rest while the leading edge of the sphere stretches to form a shape-charge jet. Figure 4.41(c) shows the onset of the initial necking process which subsequently forms three-major particle (as verified by the experimental observation conducted in [91]). These particles are clearly visible in the Figure 4.41(d). The jet continues to stretch and results in further splitting up of particles that can only be

captured with explicit damage models. Despite the lack of adequate damage model, the present calculations are able to predict the overall behavior of the extrusion process that matches well with the experimental predictions reported in [91]. The maximum equivalent plastic strain (ϵ_P) was observed during the jetting phase and corresponds to a value of 9.3. The numerical computations conducted in [91] reports a value of 9.0, which is in close agreement with the current predictions.

Figure 4.42 shows the evolution of the mesh. The enlarged view of the mesh adapting to the shape-charge jet is shown in Figure 4.42(c). The mesh adaptation is excellent and is apparent from the figures. In Figure 4.43, the evolution of the interface at different instants in time are displayed. It is clear that throughout the extrusion process, the shape of the extrusion die is unaltered.

Case	Final Length (mm)	Final Base Radius (mm)	Maximum ϵ_p
Current (3 Levels)	21.35	6.75	2.84
Current (4 Levels)	21.50	7.01	3.087
Current (5 Levels)	21.53	7.05	3.169
Tran et al [190]	21.15	7.15	2.86
Udaykumar et al [192]	-	6.8	6.97-7.24
Camacho et al [180]	21.42-21.44	7.21-7.24	2.97-3.25
Zhu et al [210]	21.26-21.40	6.97-7.18	2.75-3.03

Table 4.1: Comparison of results for the axisymmetric impact of Copper rod at 227 m/s.

Case	Final Length (mm)	Final Base Radius (mm)	Maximum ϵ_p
227 m/s (5 levels)	21.53	7.05	3.169
400 m/s (5 levels)	10.56	12.81	5.01
600 m/s (5 levels)	-	24.56	5.3

Table 4.2: Comparison of parameters for the axisymmetric impact of Copper rod for different impact velocities

	Velocity (cm/s)	Diameter (δ_c, cm)
Present	0.275	0.58
Computation [46]	0.264	0.16
Experiment [123]	0.27	0.6

Table 4.3: Comparison with experimental and computational results for the jet velocity and diameter.
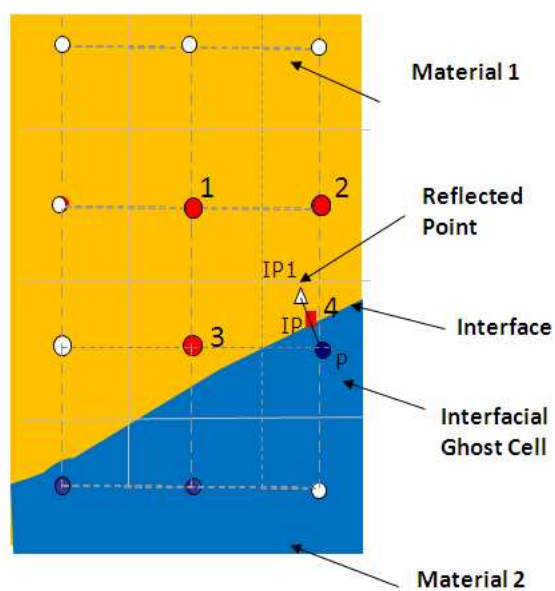
Figure 4.1: Embedding the boundary conditions with the interpolation procedure.
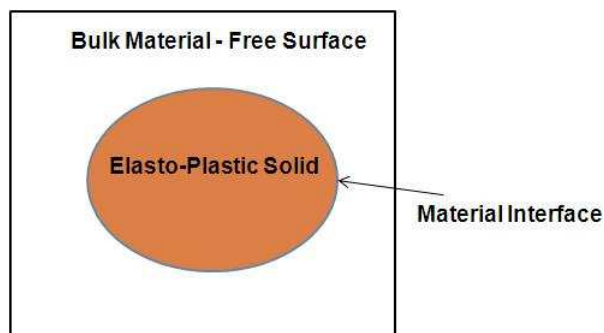
(a) Classification of materials
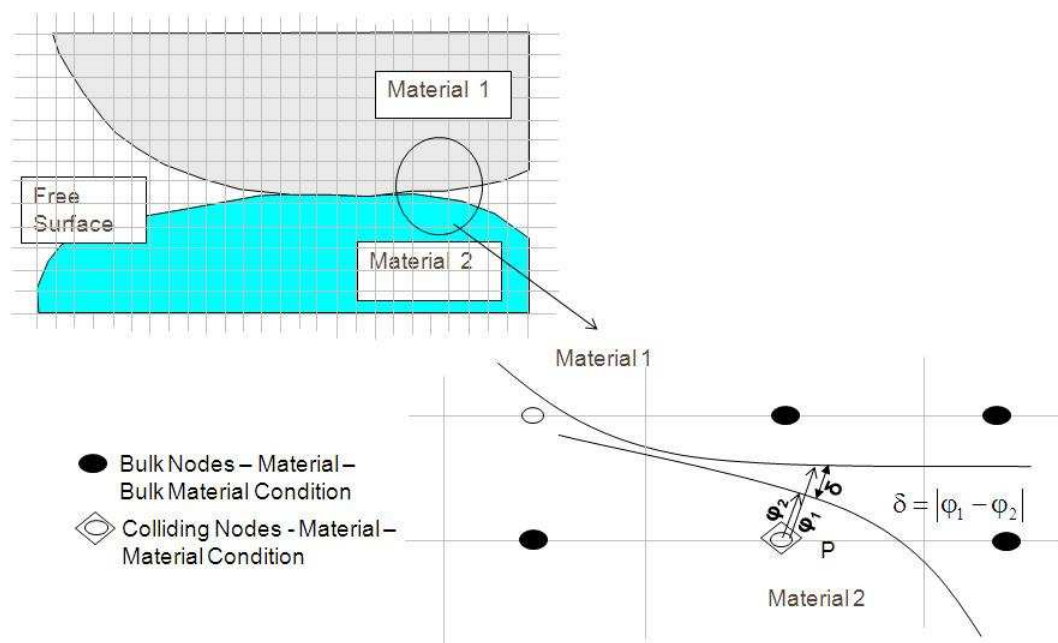
(b) Collision detection algorithm

Figure 4.2: Collision detection algorithm: (a) An elasto-plastic solid object immersed in a free surface. The surrounding free surface is flagged as bulk material (b) Algorithm to detect collision between any two level sets; ϕ_l indicate the value of the level set function corresponding to the lth material interface and δ is the distance between the approaching level sets at point P.
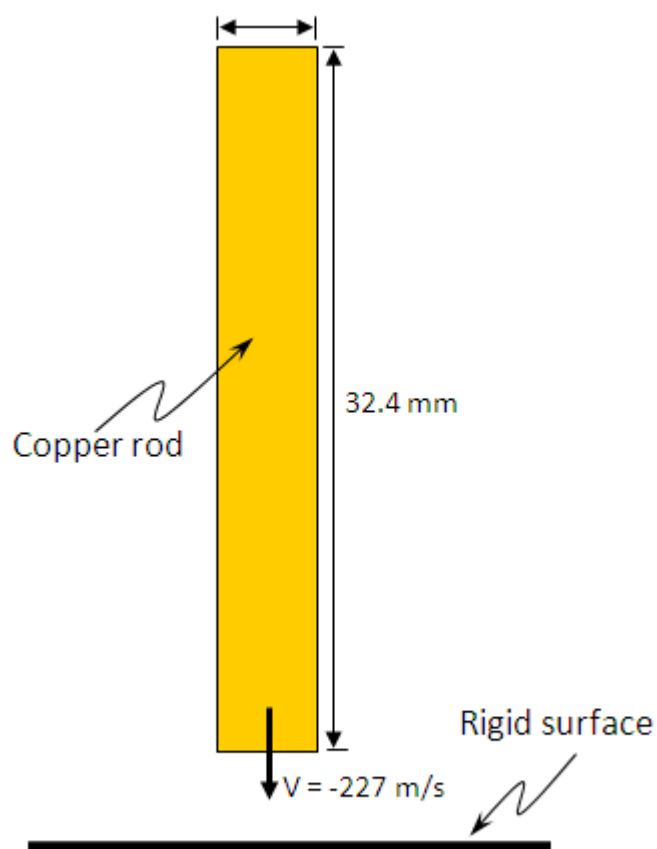
Figure 4.3: Initial configuration for two-dimensional axisymmetric Taylor test on a Copper rod.
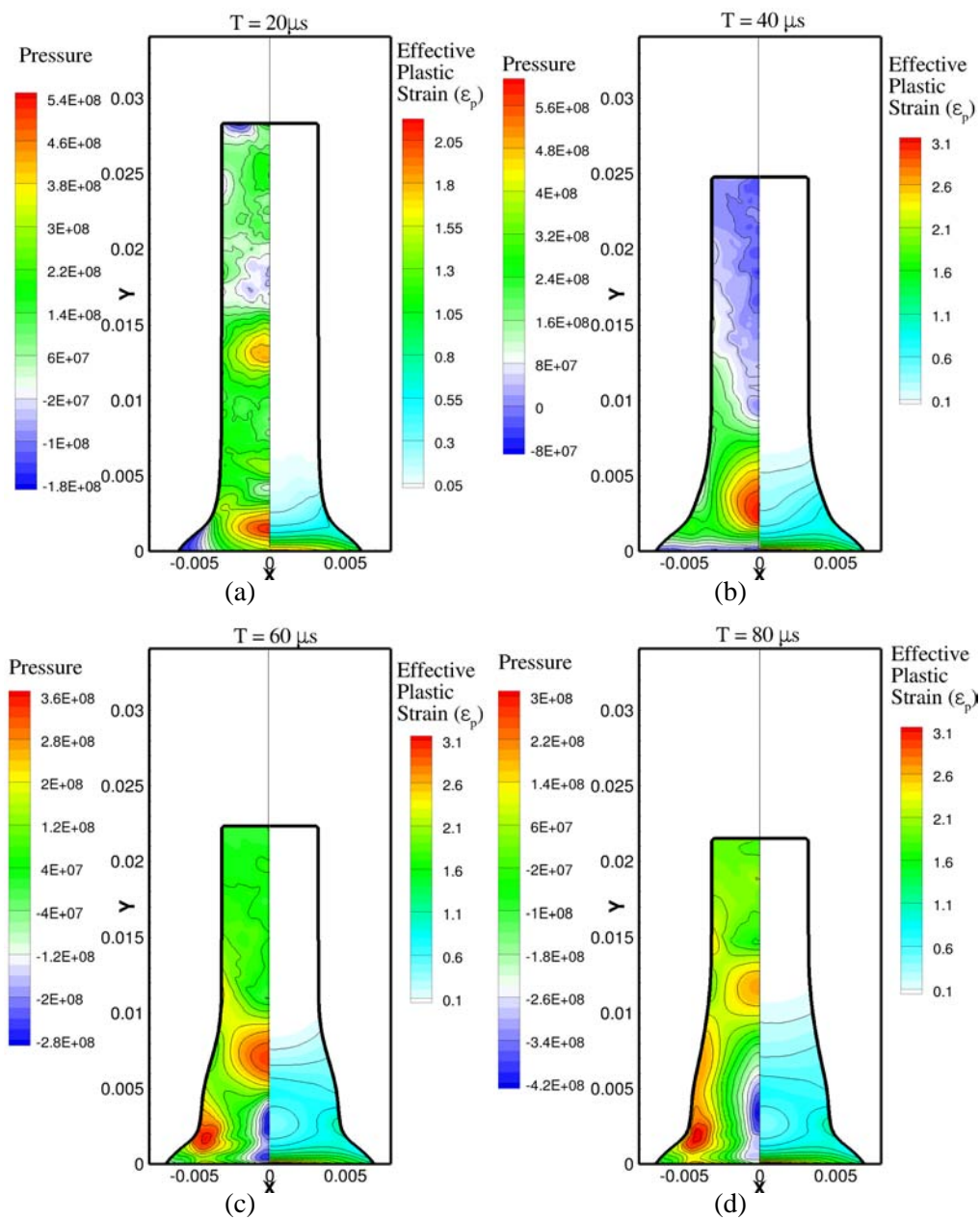
Figure 4.4: Snapshots of pressure and effective plastic strain (ϵ_P) contours at different instants in time for the axisymmetric impact of Copper rod at 227 m/s.
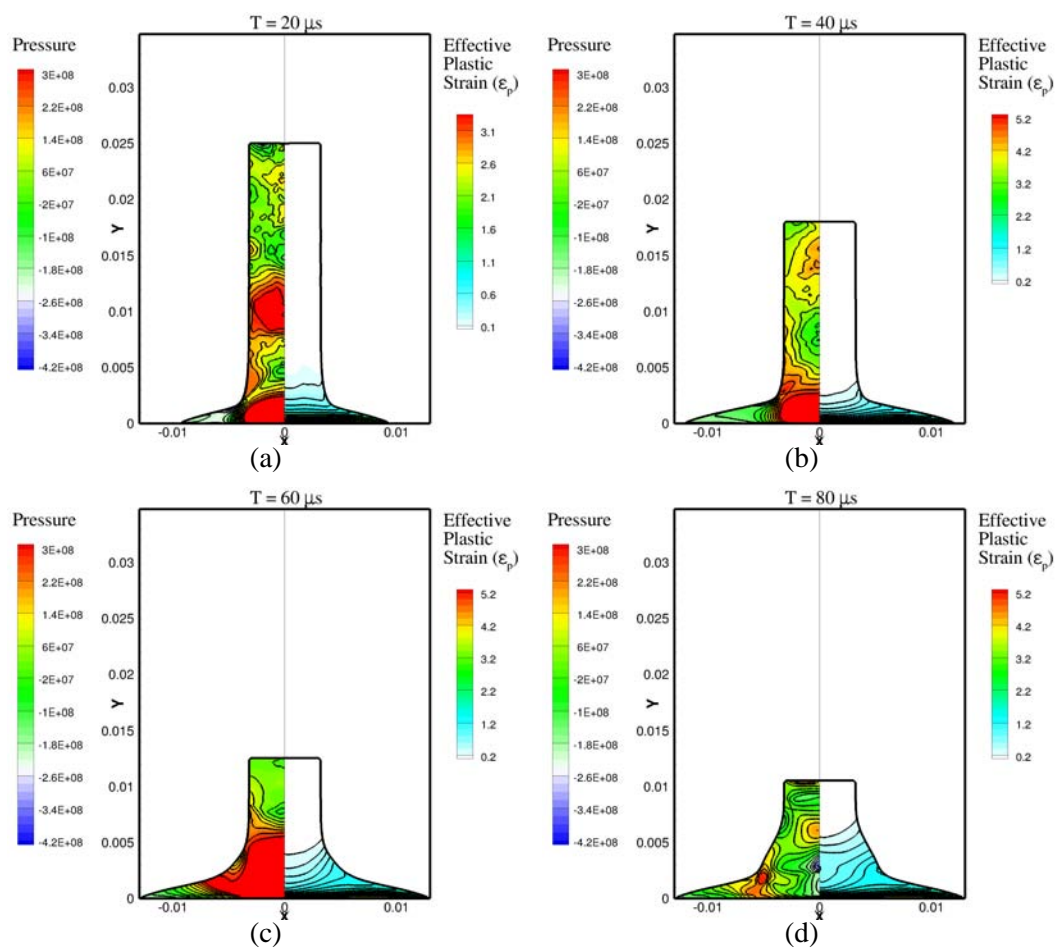
Figure 4.5: Snapshots of pressure and effective plastic strain (ϵ_P) contours at different instants in time for the axisymmetric impact of Copper rod at 400 m/s
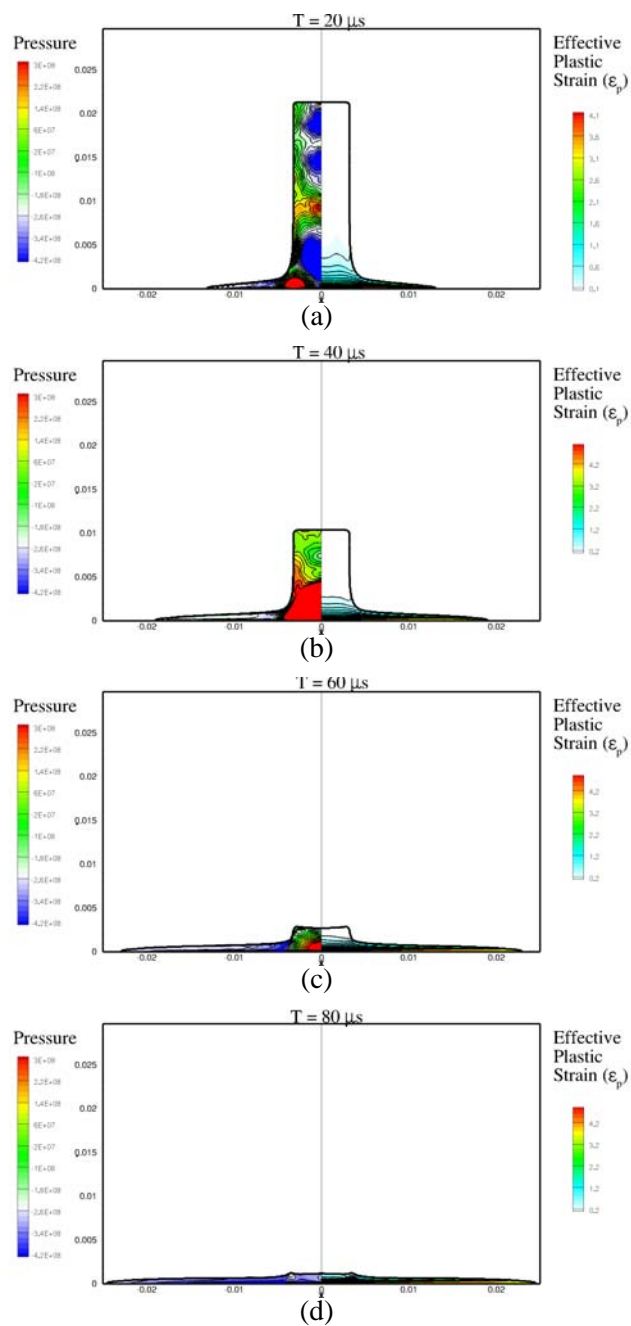
Figure 4.6: Snapshots of pressure and effective plastic strain (ϵ_P) contours at different instants in time for the axisymmetric impact of Copper rod at 600 m/s
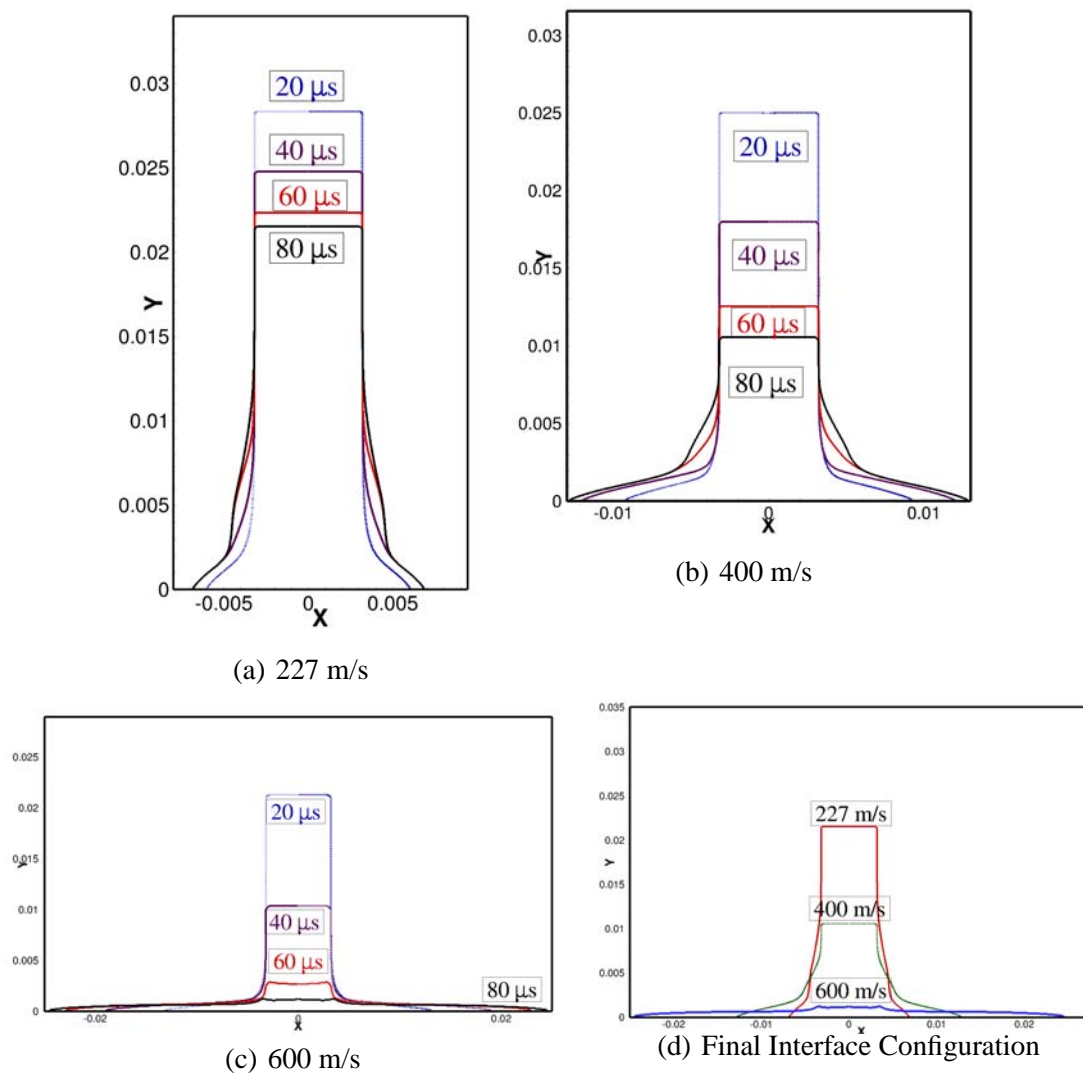
Figure 4.7: Axisymmetric Taylor bar experiment: Figures (a), (b), and (c) show the evolution and the topology of the interface at different instants in time for three different impact velocities (d) Final configuration of the interface at $80\mu s$.
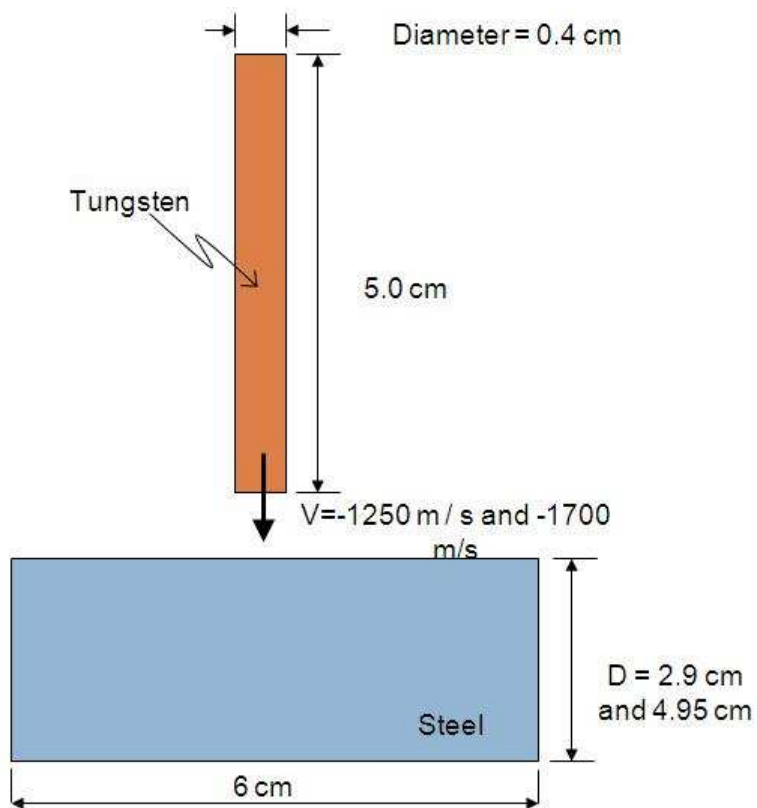
Figure 4.8: Initial configuration for the two-dimensional axisymmetric penetration of Steel target by WHA long rod
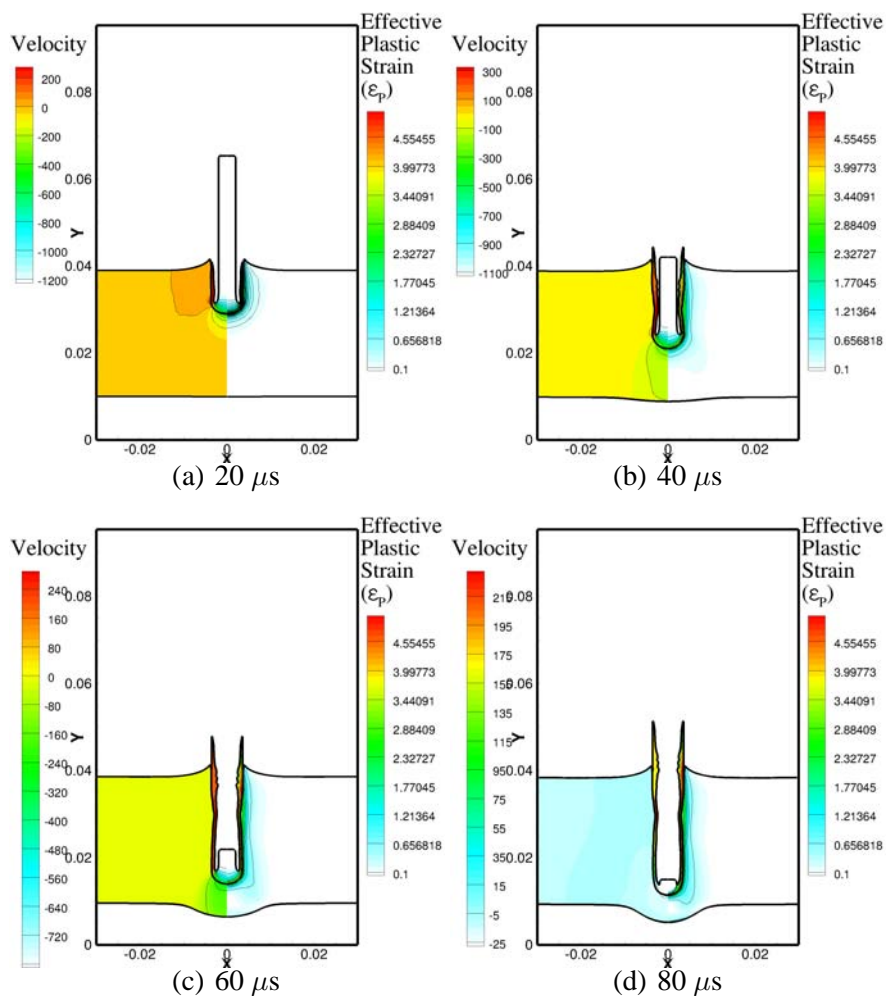
Figure 4.9: Contours of equivalent plastic strain (ϵ_p) and velocity of a Tungsten rod penetrating a steel plate at 1250 m/s.
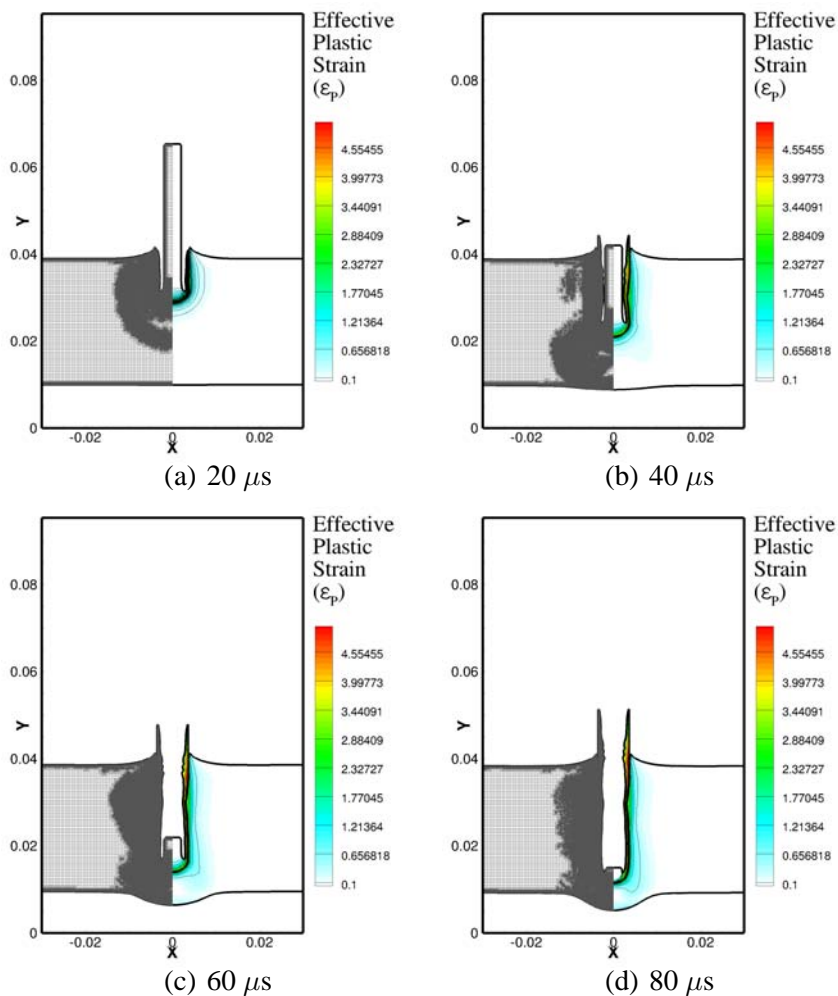
Figure 4.10: Contours of equivalent plastic strain (ϵ_p) and mesh evolution of a Tungsten rod penetrating a steel plate at 1250 m/s.

(a) 20 μs

(b) 40 μs

(c) 60 μs

(d) 80 μs
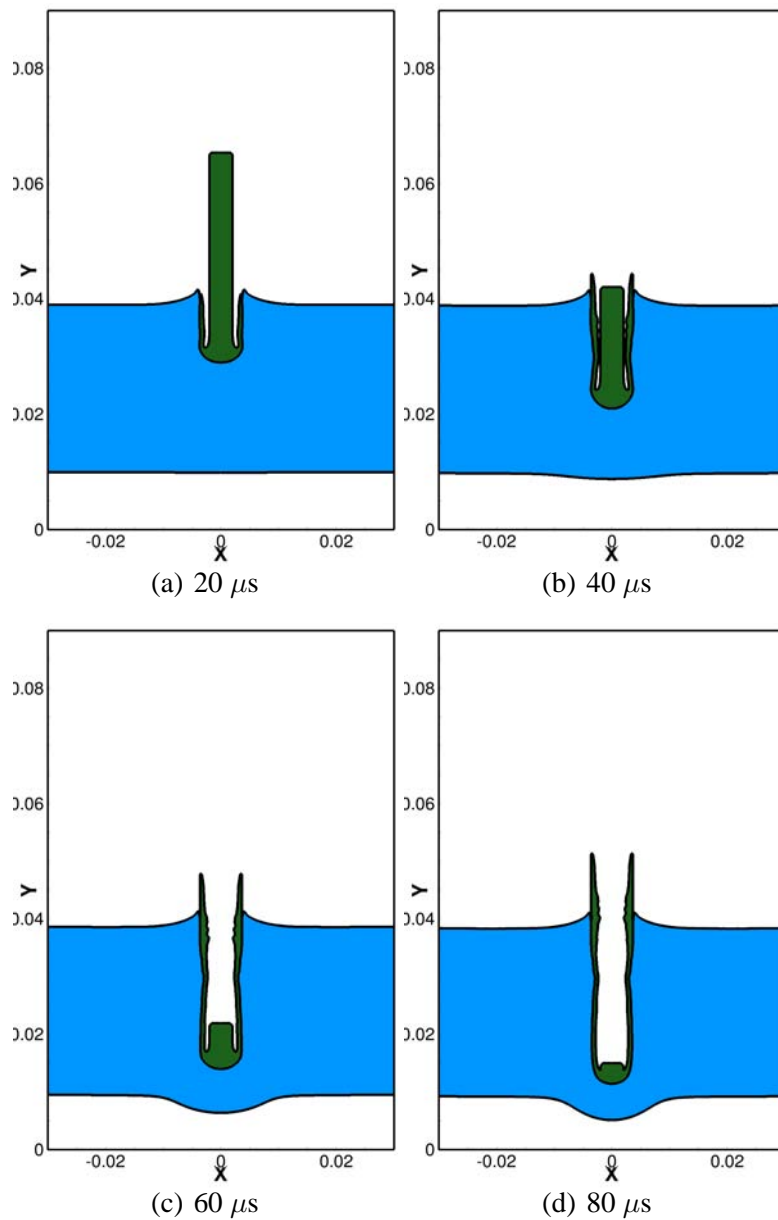
Figure 4.11: Snapshots of the interface topology of a Tungsten rod penetrating a steel plate at 1250 m/s.
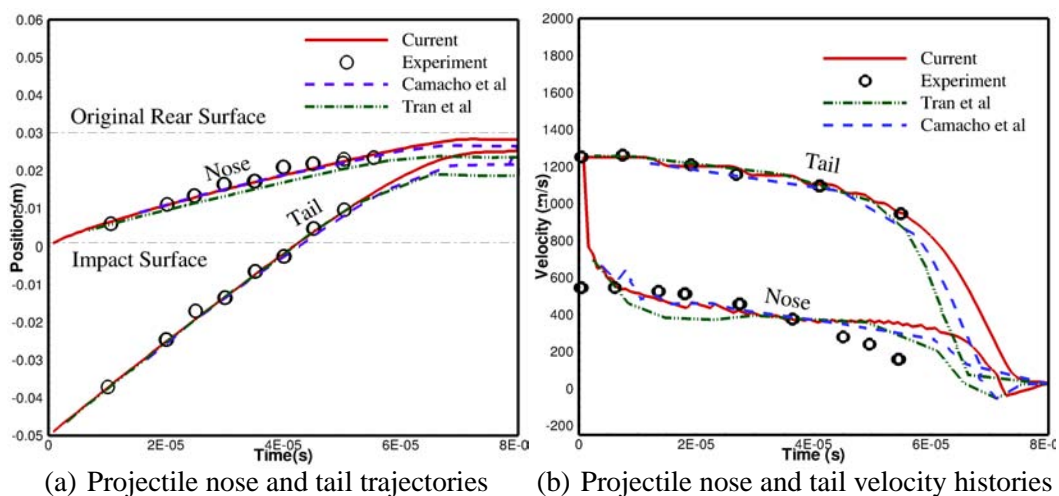
(a) Projectile nose and tail trajectories   (b) Projectile nose and tail velocity histories

Figure 4.12: Tungsten rod penetrating steel plate at 1250 m/s: (a) Trajectories and (b) velocities of the nose and tail of the projectile.
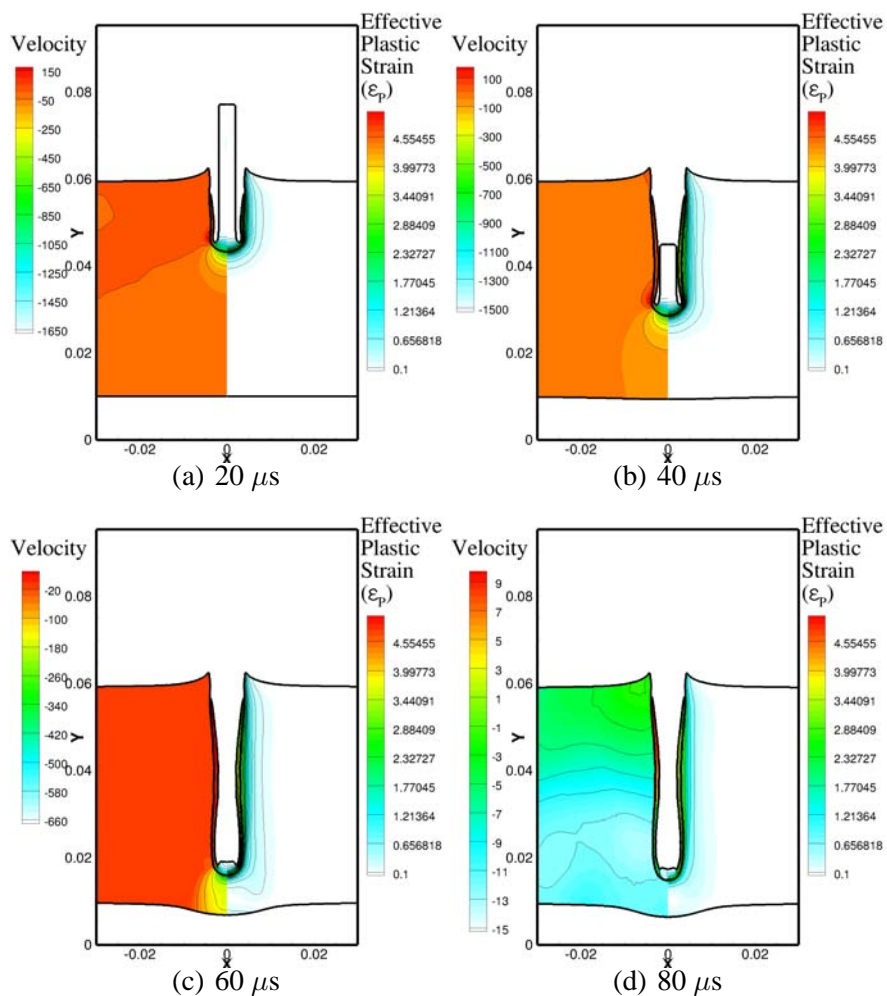
Figure 4.13: Contours of equivalent plastic strain (ϵ_p) and velocity of a Tungsten rod penetrating a steel plate at 1700 m/s.
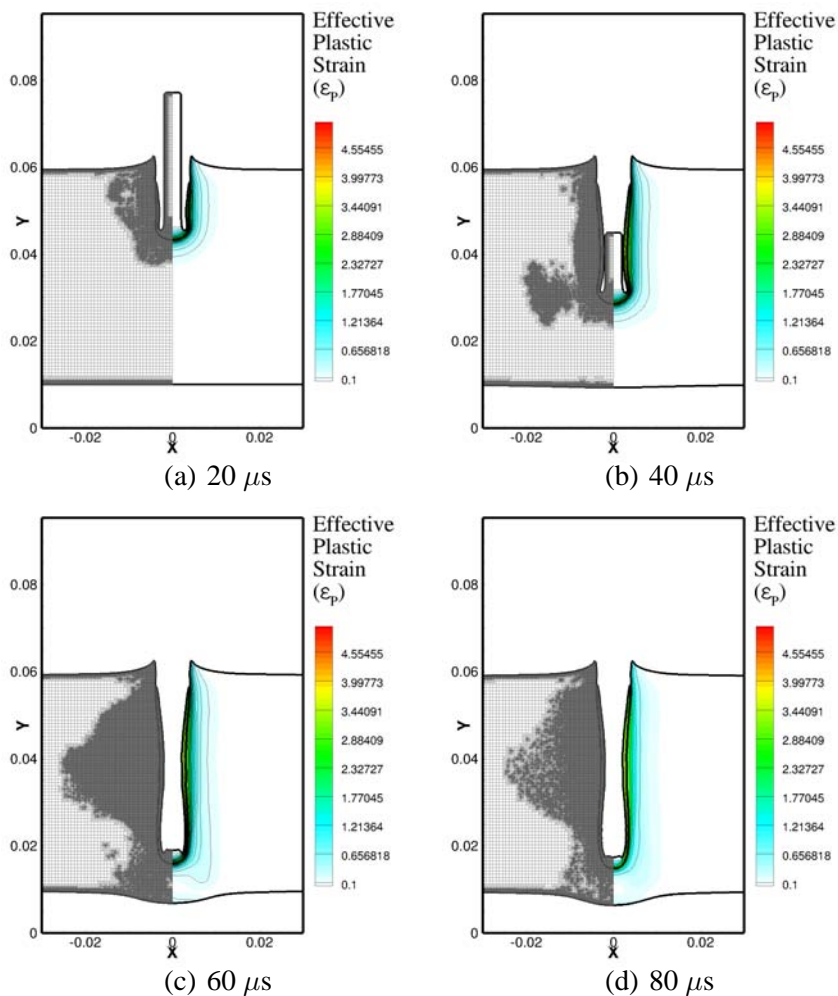
Figure 4.14: Contours of equivalent plastic strain (ϵ_p) and mesh evolution of a Tungsten rod penetrating a steel plate at 1700 m/s.
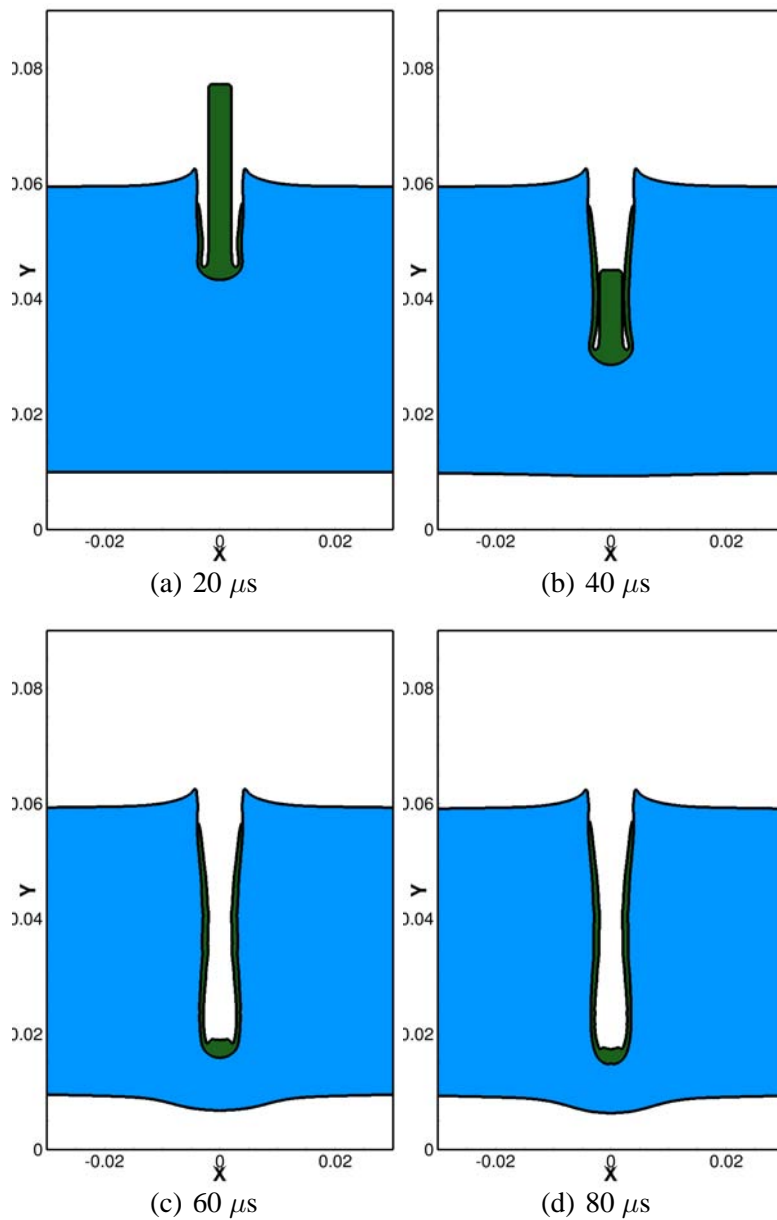
Figure 4.15: Snapshots of the interface topology of a Tungsten rod penetrating a steel plate at 1700 m/s.
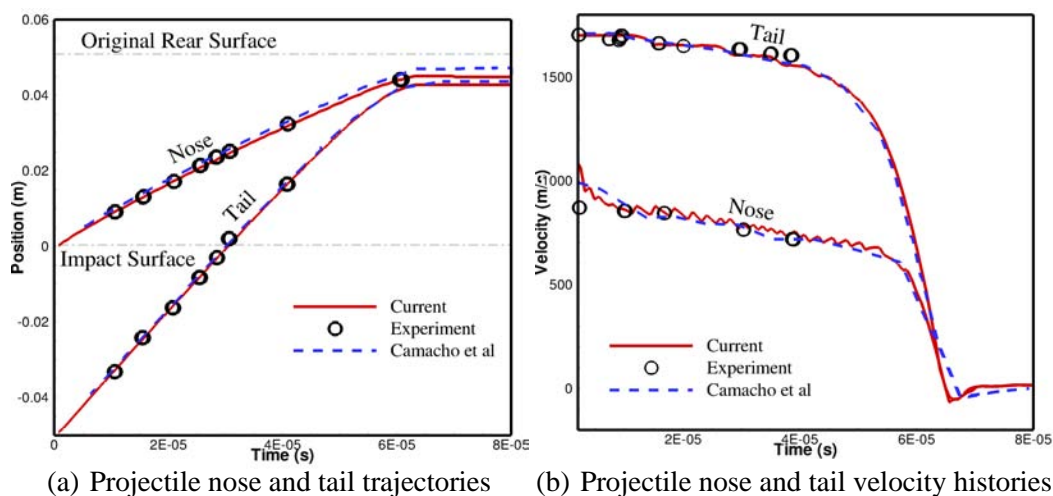
(a) Projectile nose and tail trajectories   (b) Projectile nose and tail velocity histories

Figure 4.16: Tungsten rod penetrating steel plate at 1700 m/s: (a) Trajectories and (b) velocities of the nose and tail of the projectile.
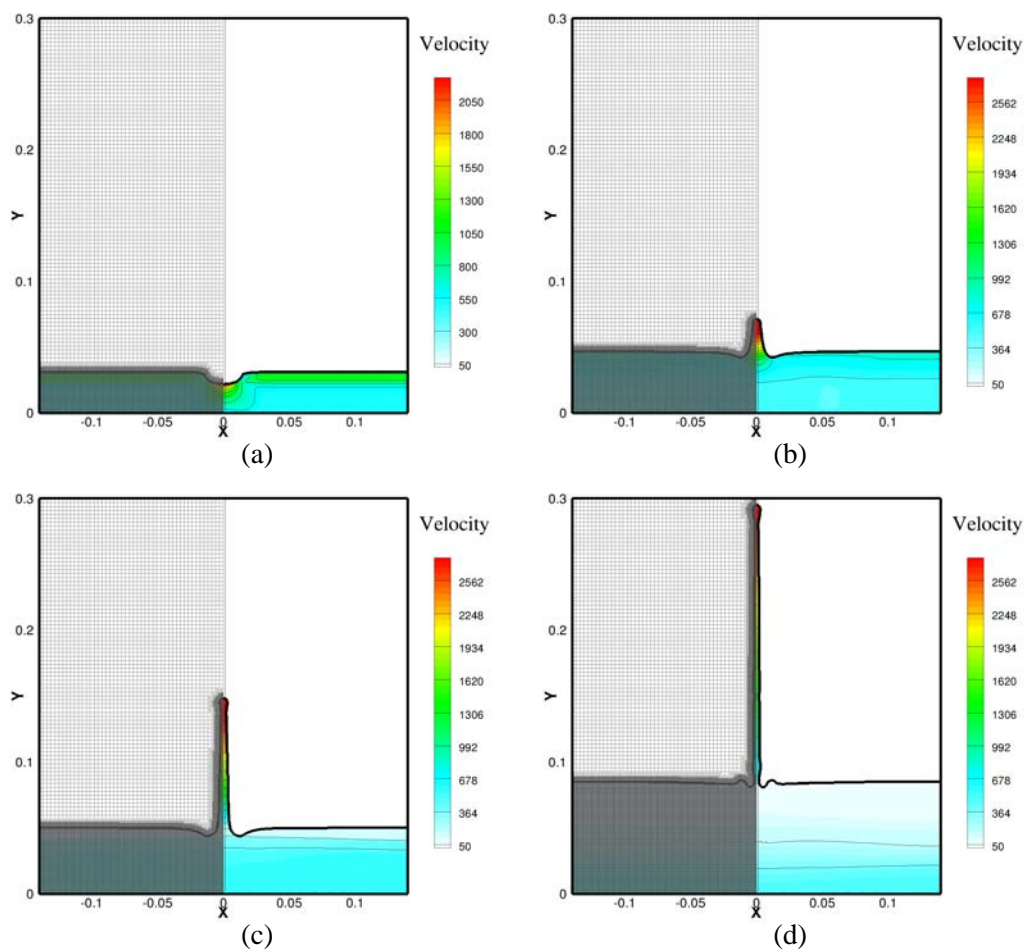
Figure 4.17: Snapshots of velocity contours and mesh evolution at different instants in time for the response of a hemispherical groove to a shock wave
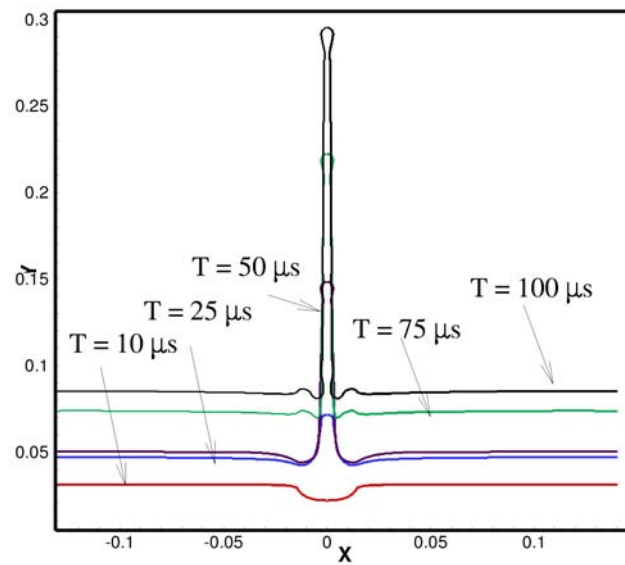
Figure 4.18: Topology and evolution of the interface at different instants in time for the response of a hemispherical groove to a shock wave
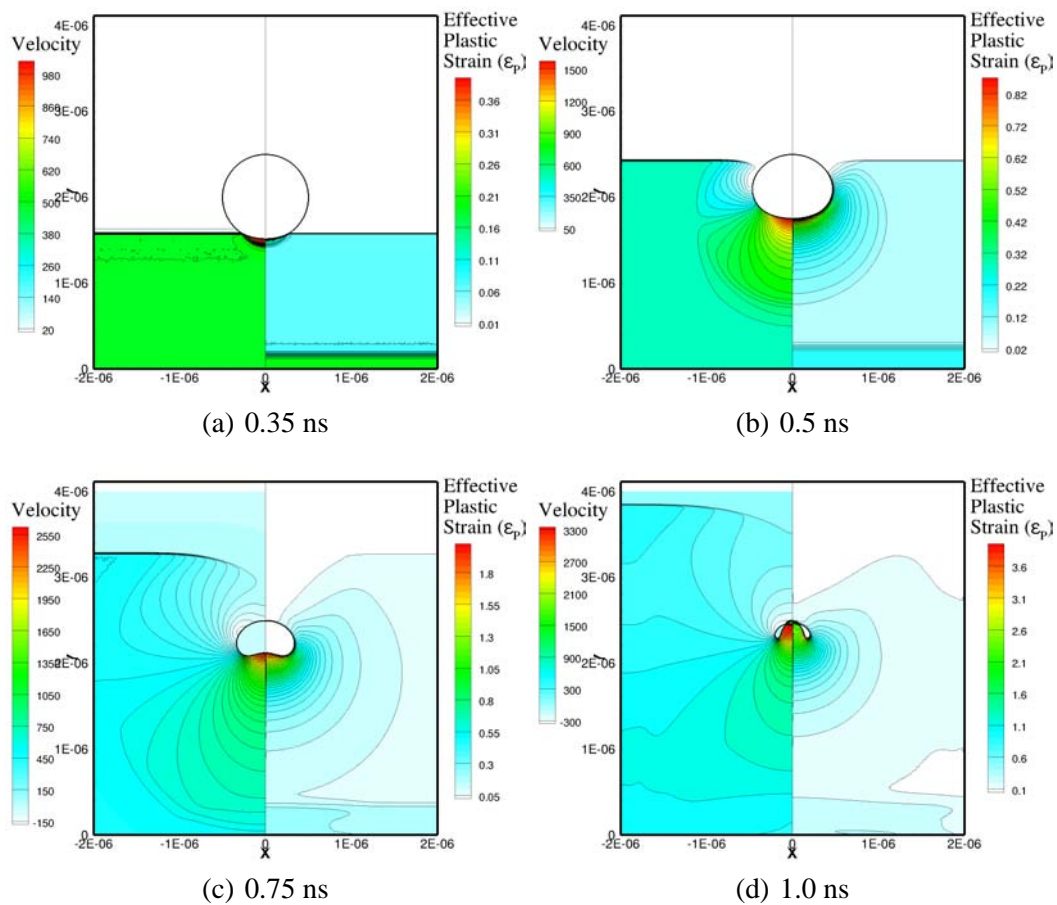
Figure 4.19: Snapshots of velocity and equivalent plastic strain (ϵ_p) contours at different instants in time for the collapse of a cylindrical void in a Copper matrix
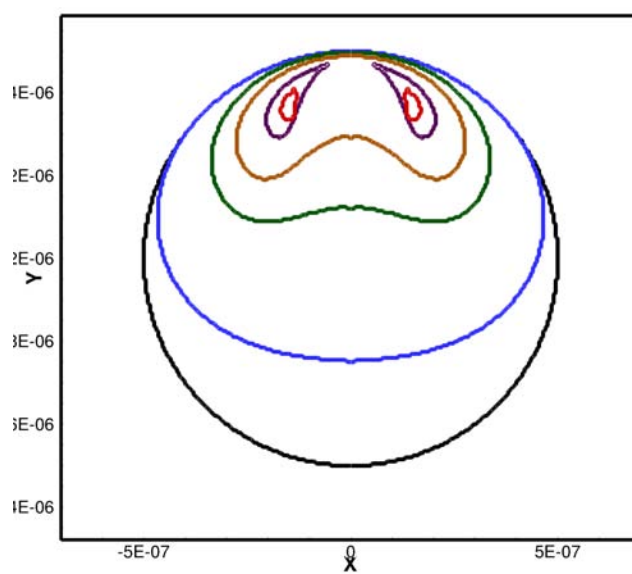
Figure 4.20: Topology and evolution of the interface for the collapse of a cylindrical void in a Copper matrix
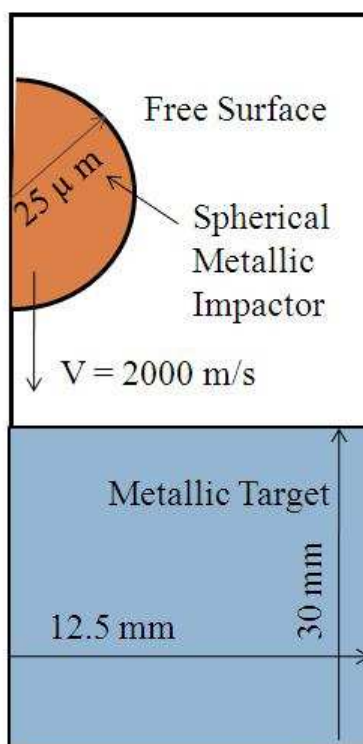
Figure 4.21: Initial configuration for the impact of a metallic sphere on a semi-infinite metallic target
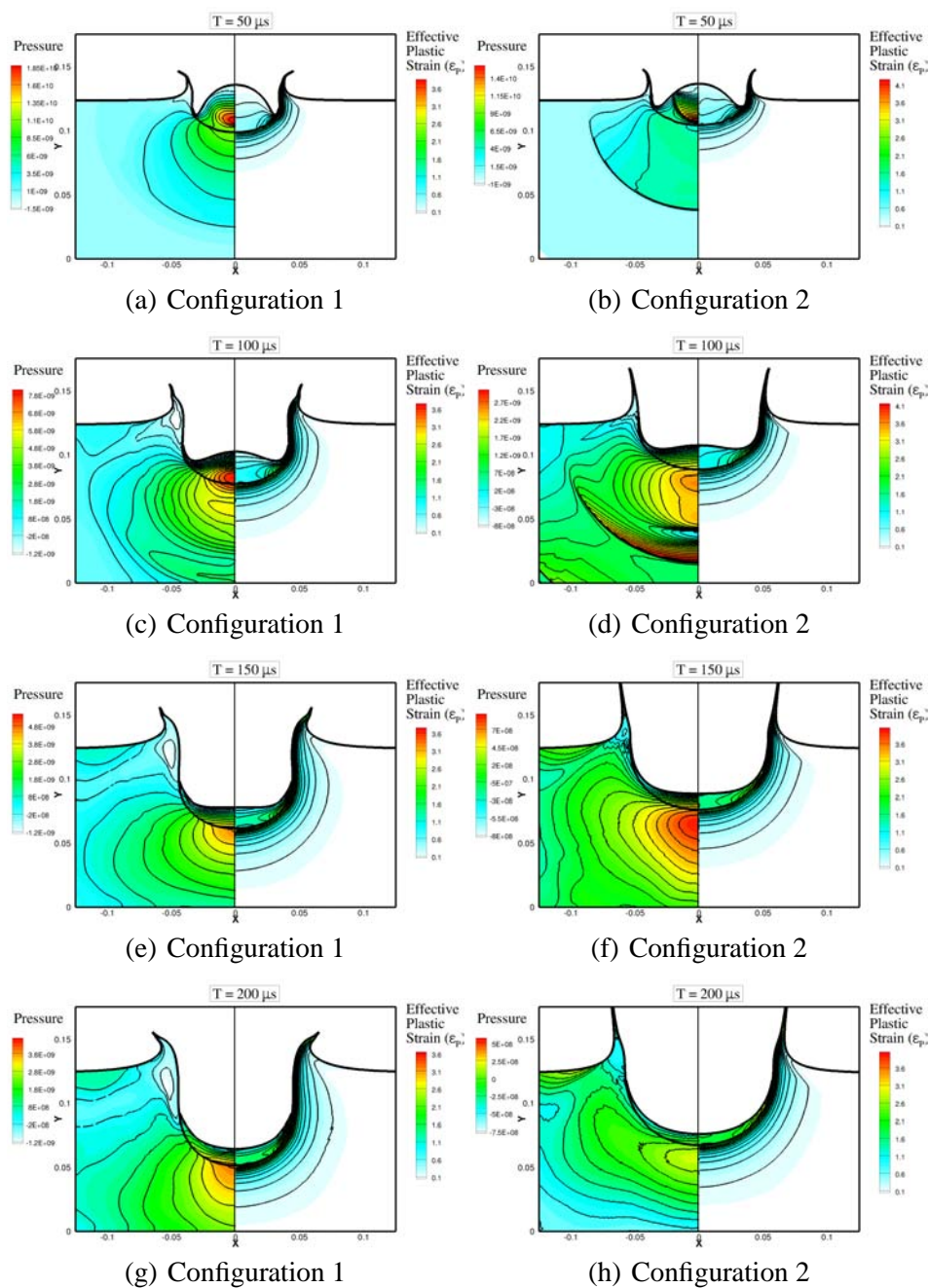
Figure 4.22: High velocity impact of metal sphere on a metal Surface: (a), (c), (e), and (g) correspond to configuration 1 - impact of a heavy alloy Tungsten sphere on an infinitely thick Steel target and (b), (d), (f), and (h) correspond to configuration 2 - impact of a Copper sphere on an infinitely thick Copper target
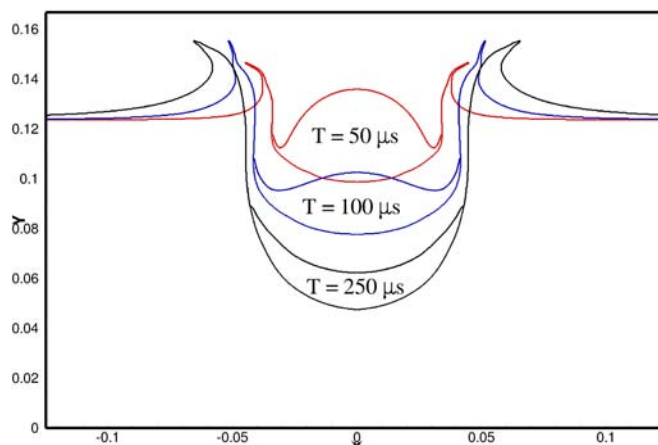
(a) Configuration 1
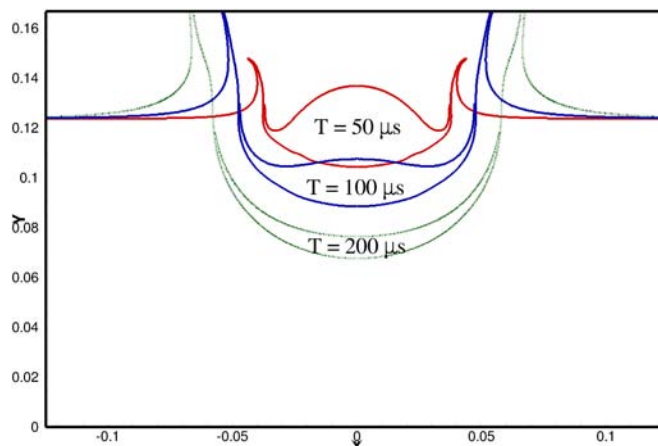
(b) Configuration 2

Figure 4.23: Toplogy and location of the interface at different instants in time: (a) configuration 1 - impact of a heavy alloy Tungsten sphere on an infinitely thick Steel target and (b) corresponds to configuration 2 - impact of a Copper sphere on an infinitely thick Copper target

(a) 0.4 μ s

(b) 2 μ s

(c) 4 μ s

(d) 6 μ s
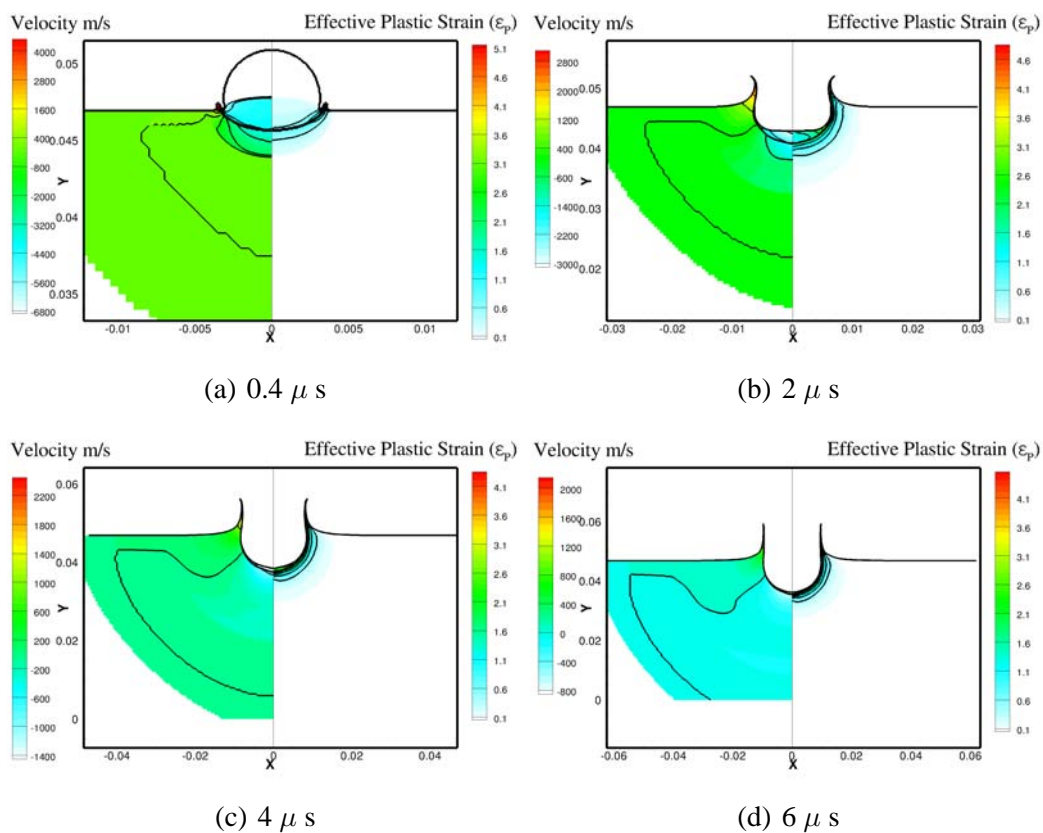
Figure 4.24: Snapshots of effective plastic strain (ϵ_P) and velocity contours at different instants in time for the dynamic tensile extrusion of Copper
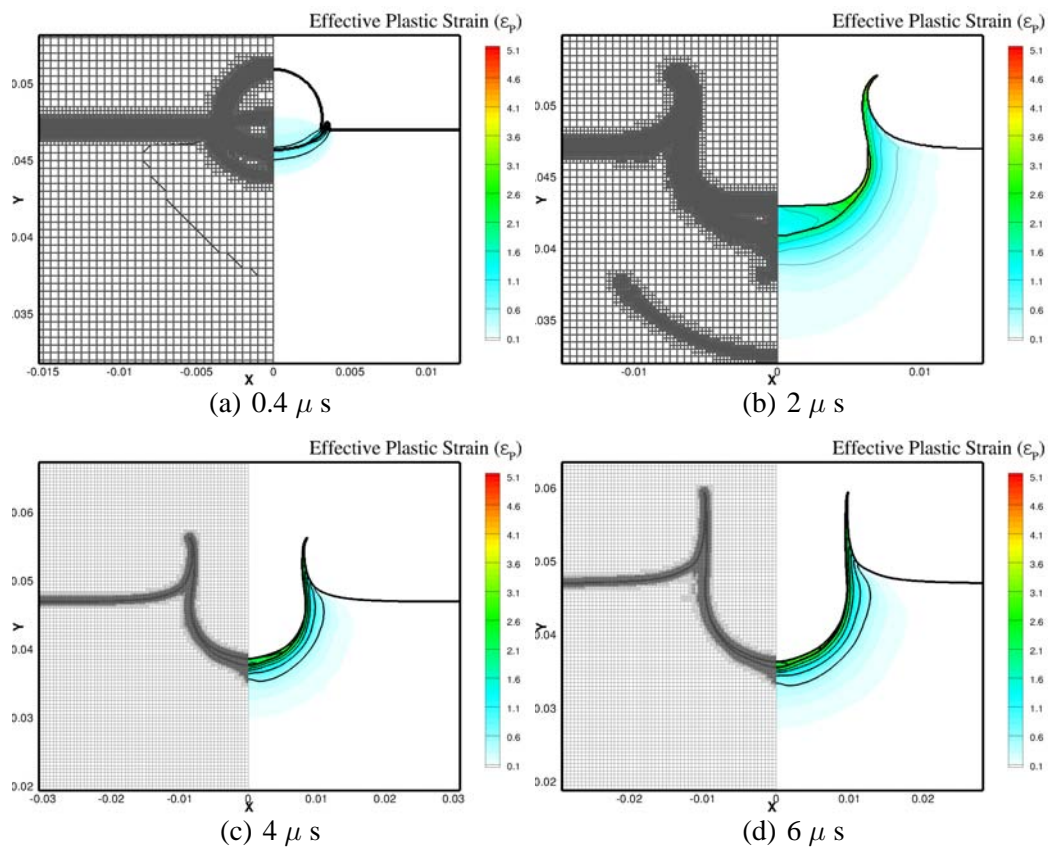
Figure 4.25: Snapshots of effective plastic strain (ϵ_P) and mesh topology at different instants in time for the 7000 m/s impact of Aluminum sphere on Aluminum target.
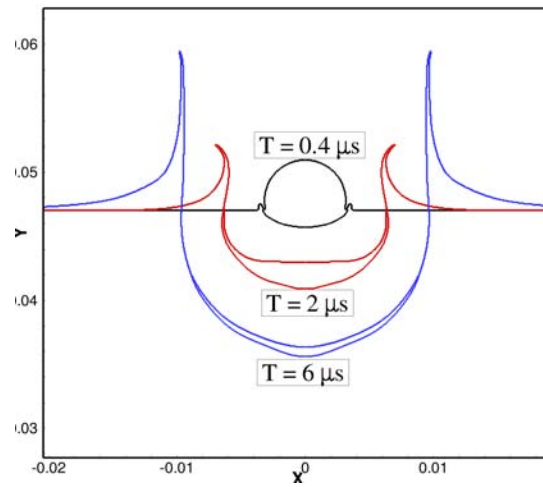
Figure 4.26: Topology and evolution of the interface at different instants in time for the 7000 m/s impact of Aluminum sphere on Aluminum target.
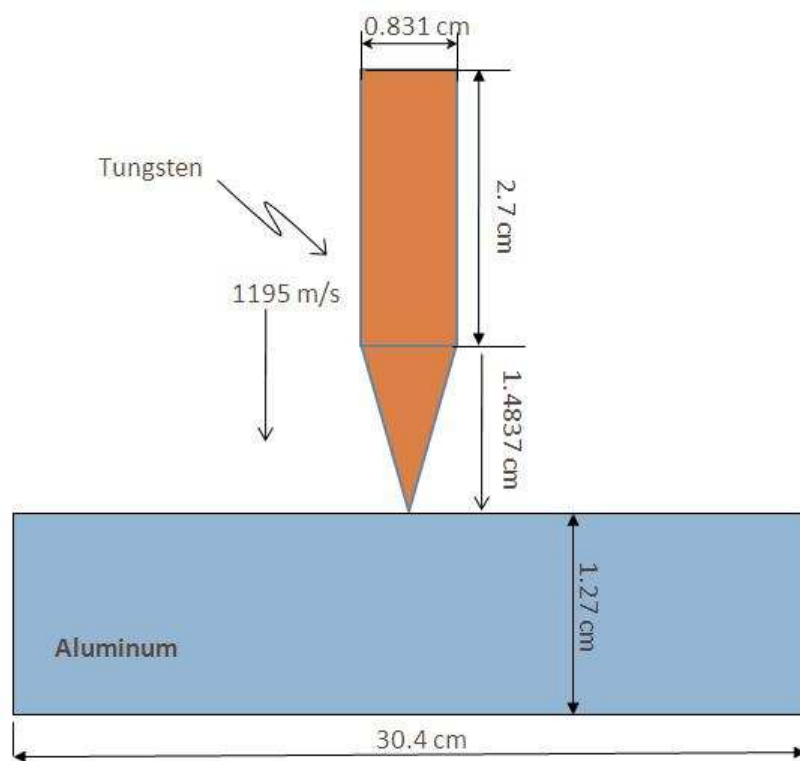
Figure 4.27: Initial configuration for the perforation of Aluminum plate by a conical nose projectile.
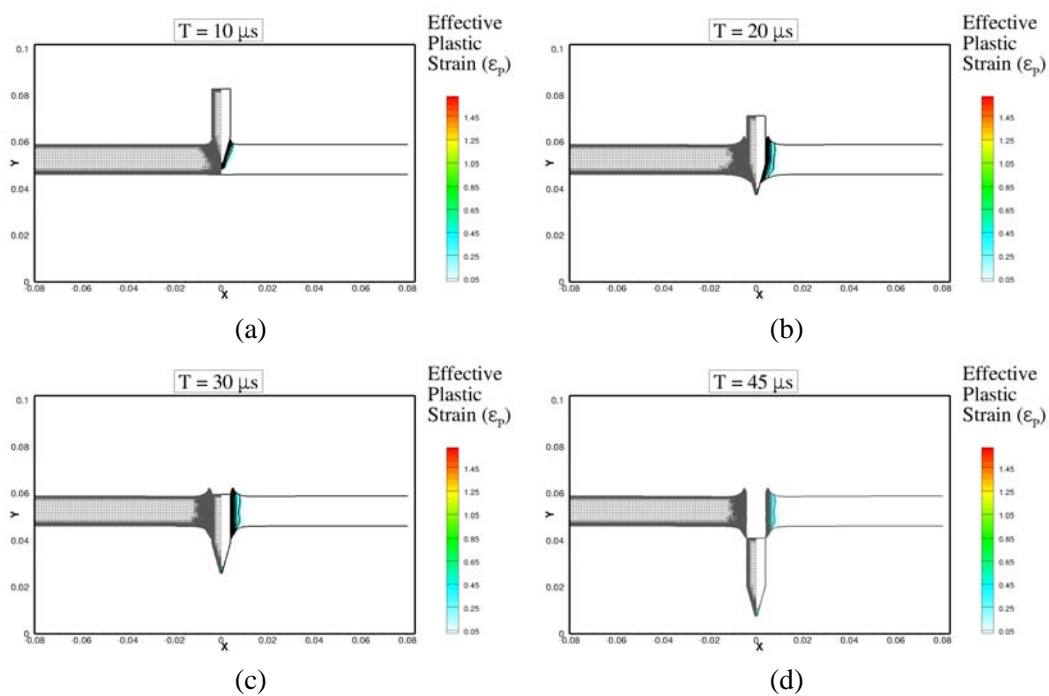
Figure 4.28: Snapshots of effective plastic strain (ϵ_P) contours and mesh evolution at different instants in time for the perforation of 12.7 mm thick Aluminum plate at an incident velocity of 1195 m/s.
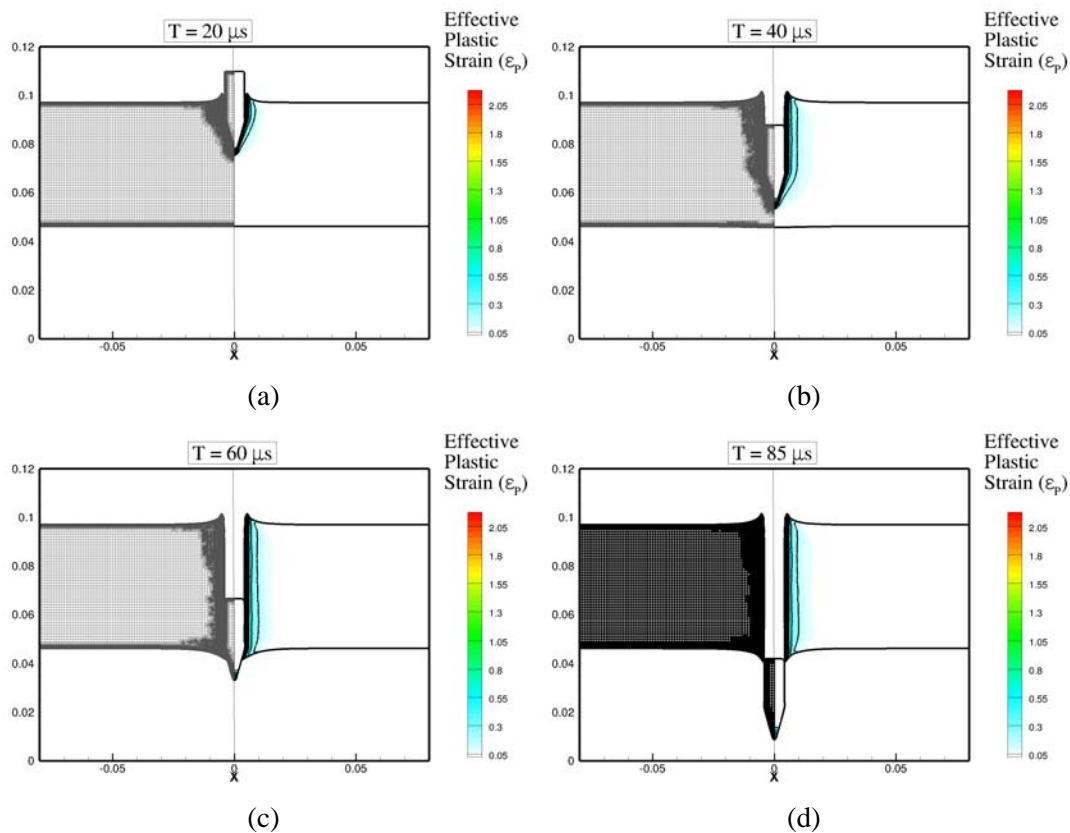
Figure 4.29: Snapshots of effective plastic strain (ϵ_P) contours and mesh evolution at different instants in time for the perforation of 50.8 mm thick Aluminum plate at an incident velocity of 1176 m/s.
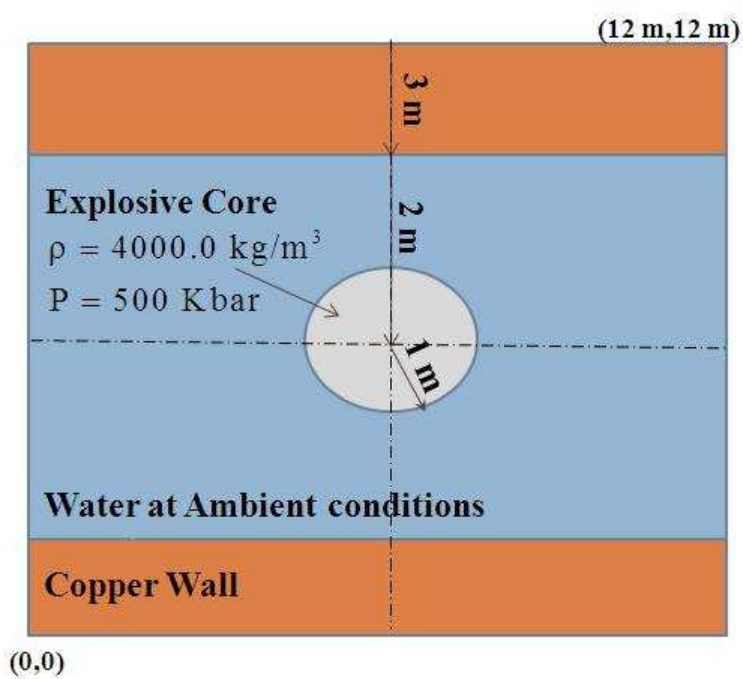
Figure 4.30: Initial configuration for the explosion inside a Copper tube.

(a) T = 112.5 μs

(b) T = 300.0 μs

(c) T = 600.0 μs

(d) T = 900.0 μs
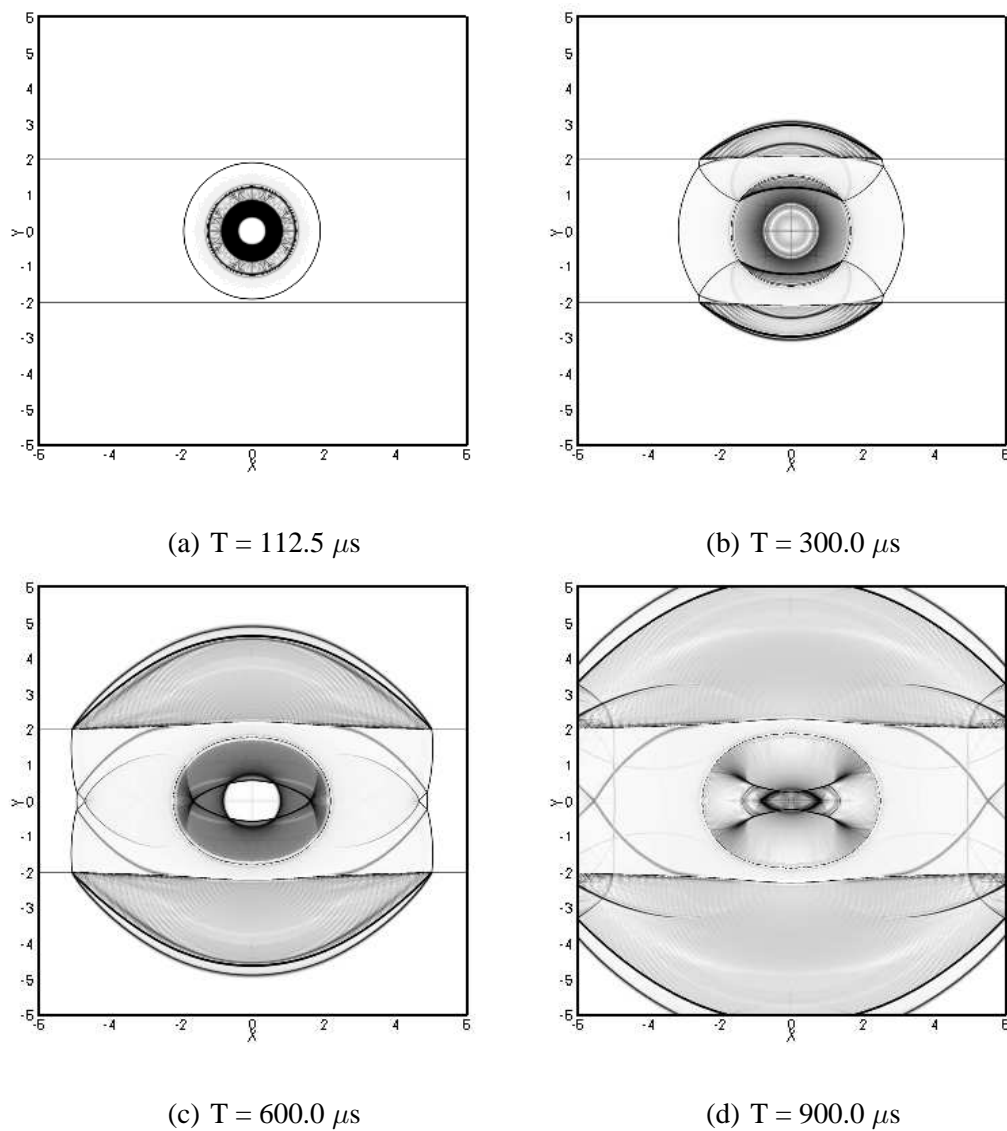
Figure 4.31: Snapshots of numerical Schlieren image, at different instants in time, for the response of a Copper tube to an explosion in water.
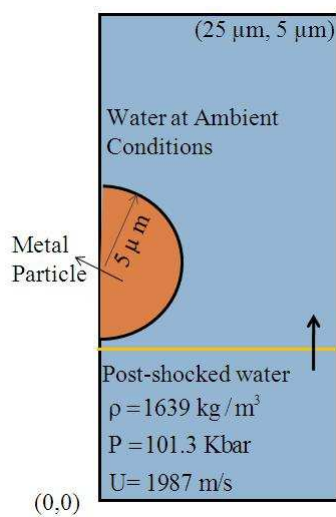
Figure 4.32: Initial configuration for a shock wave interacting with metal particle.

(a) T = 1 ns   (b) T = 2 ns

(c) T = 3 ns   (d) T = 5 ns
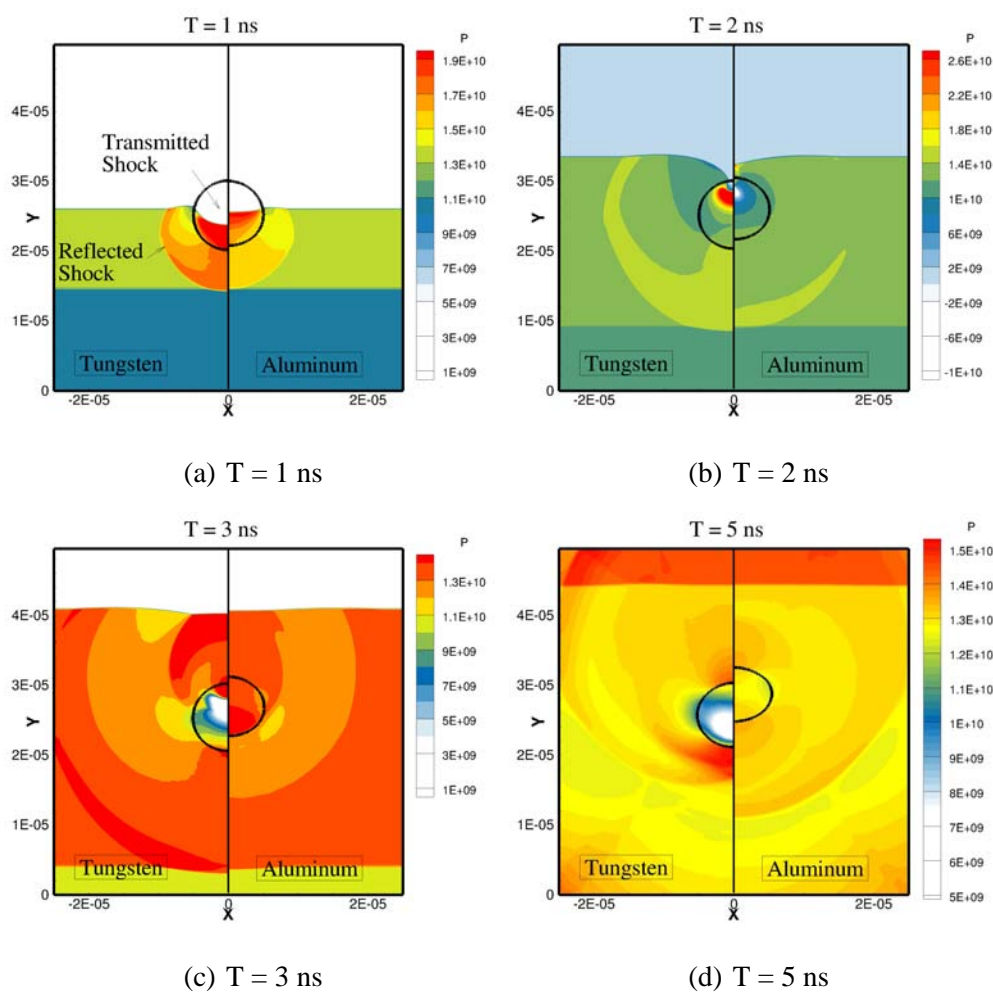
Figure 4.33: Snapshots of pressure contours for a Tungsten (left) and an Aluminum (right) particle subject to a shock wave in water.

(a) Toplogy and location of the interface   (b) Locus of leading and trailing edge
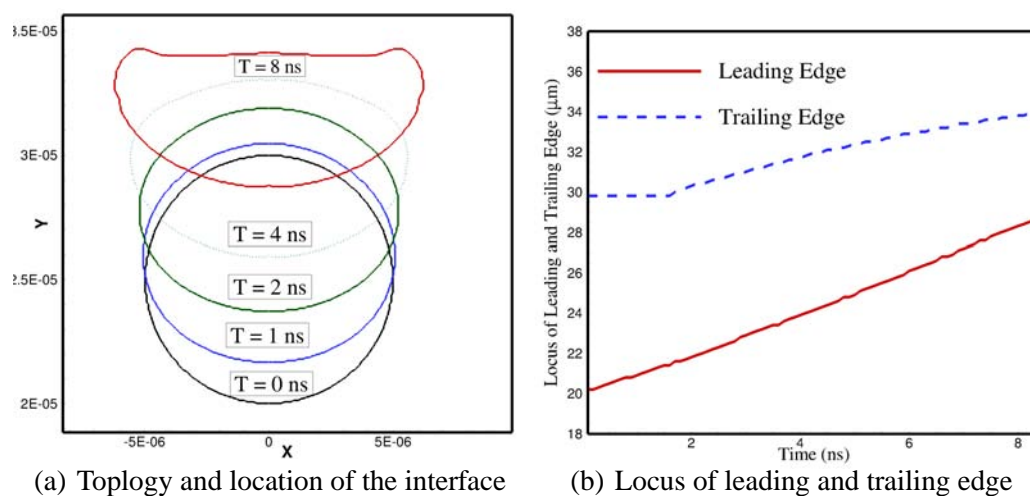
Figure 4.34: Aluminum particle subjected to a planar shock wave: (a)Topology and location of the interface at different instants in time; (b) locus of leading and trailing edge as function of time.
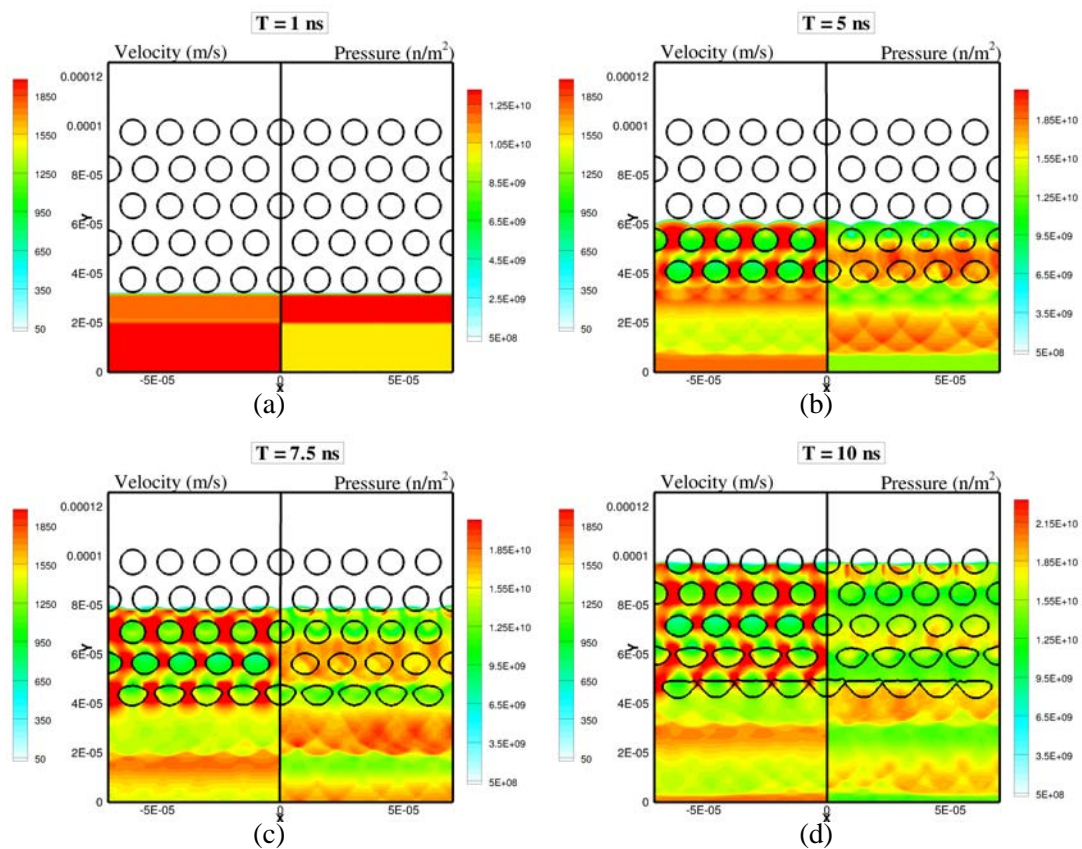
Figure 4.35: Snapshots of pressure contours for a cluster of Aluminum particles subject to a planar shock wave in water.
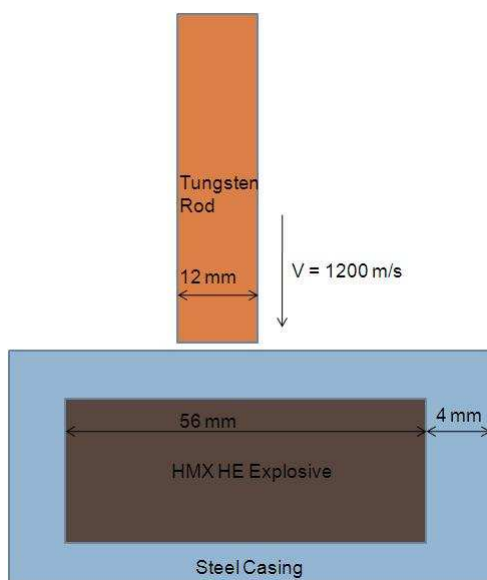
Figure 4.36: Initial configuration for the explosion initiated due to high velocity impact.

(a) 0.75 μ s

(b) 1.5 μ s

(c) 4.5 μ s
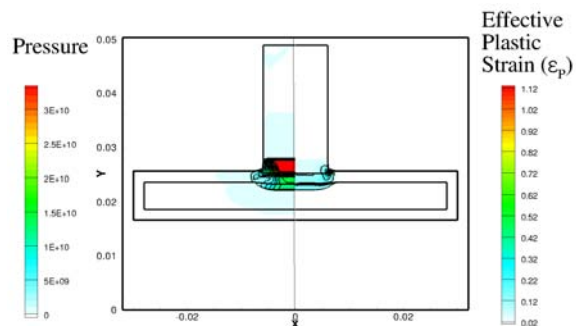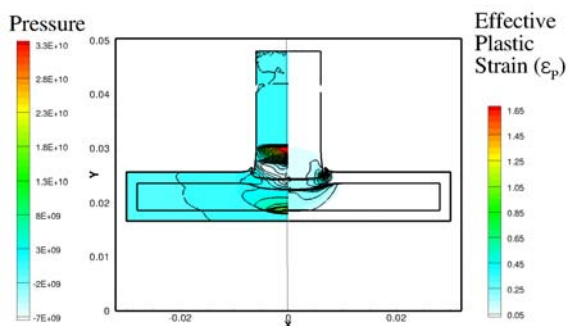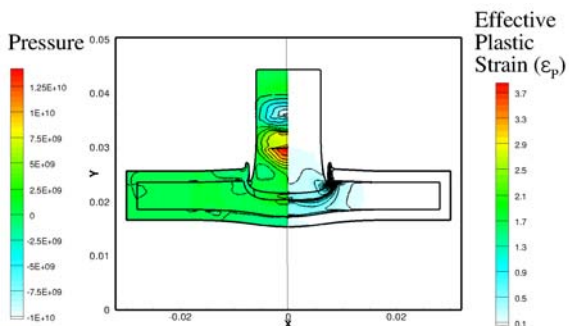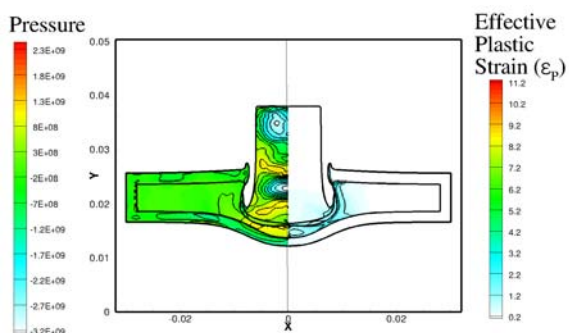
(d) 10 μ s

Figure 4.37: Snapshots of effective plastic strain (ϵ_P) and velocity contours at different instants in time for the impact driven explosion problem.
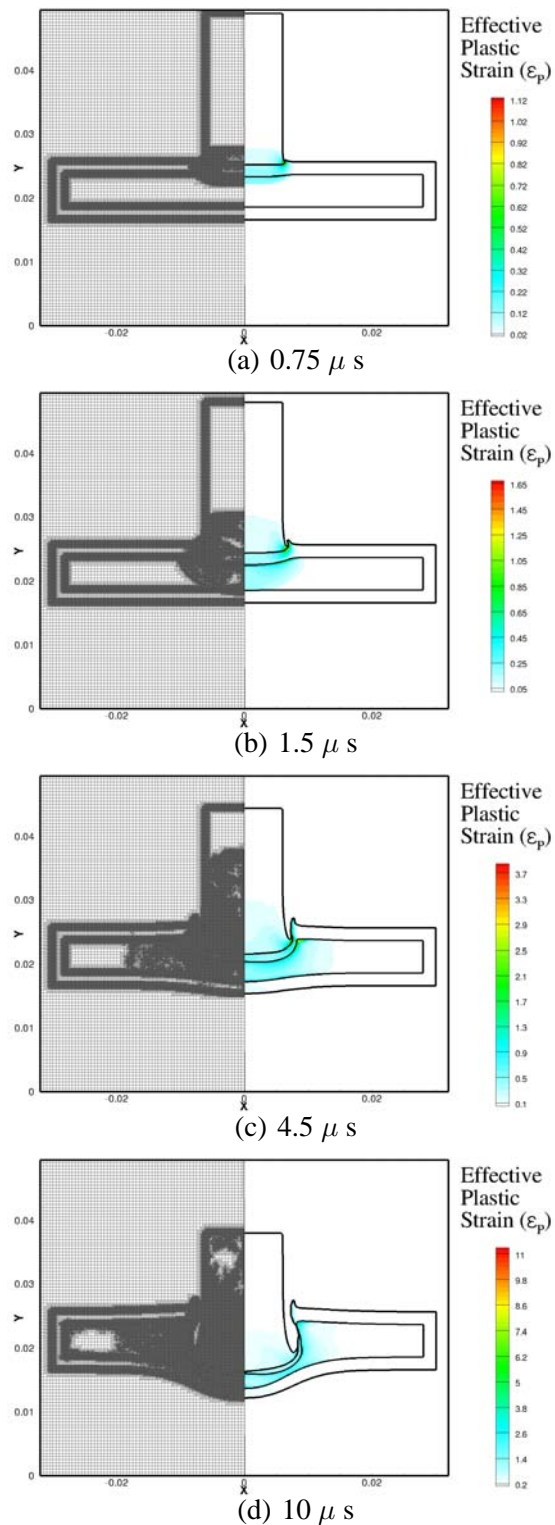
Figure 4.38: Snapshots of effective plastic strain (ϵ_P) contours and mesh evolution at different instants in time for the impact driven explosion problem.
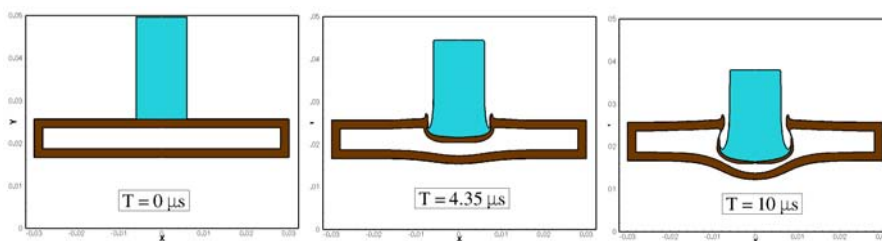
Figure 4.39: Topology and evolution of the interface at different instants in time for the impact driven explosion problem.
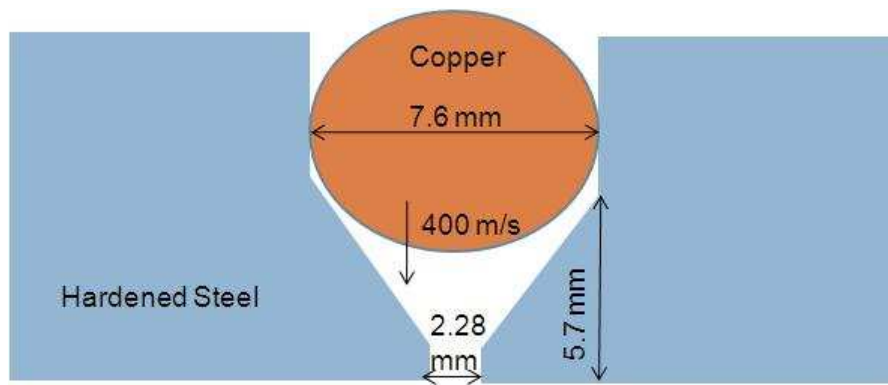
Figure 4.40: Initial configuration for the axisymmetric dynamic-tensile impact-extrusion of Copper.
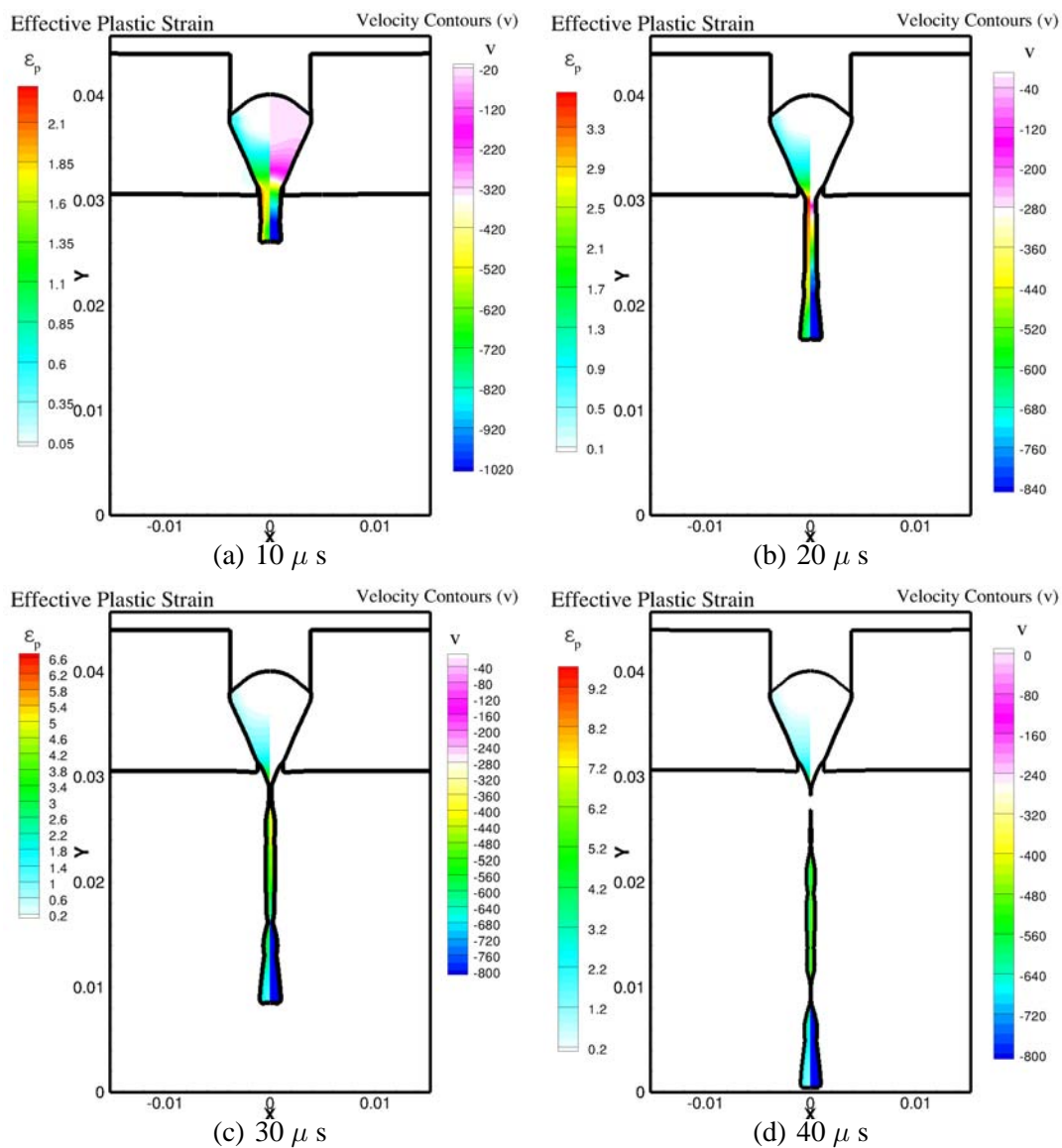
Figure 4.41: Snapshots of effective plastic strain (ϵ_P) and velocity contours at different instants in time for the dynamic tensile extrusion of Copper.
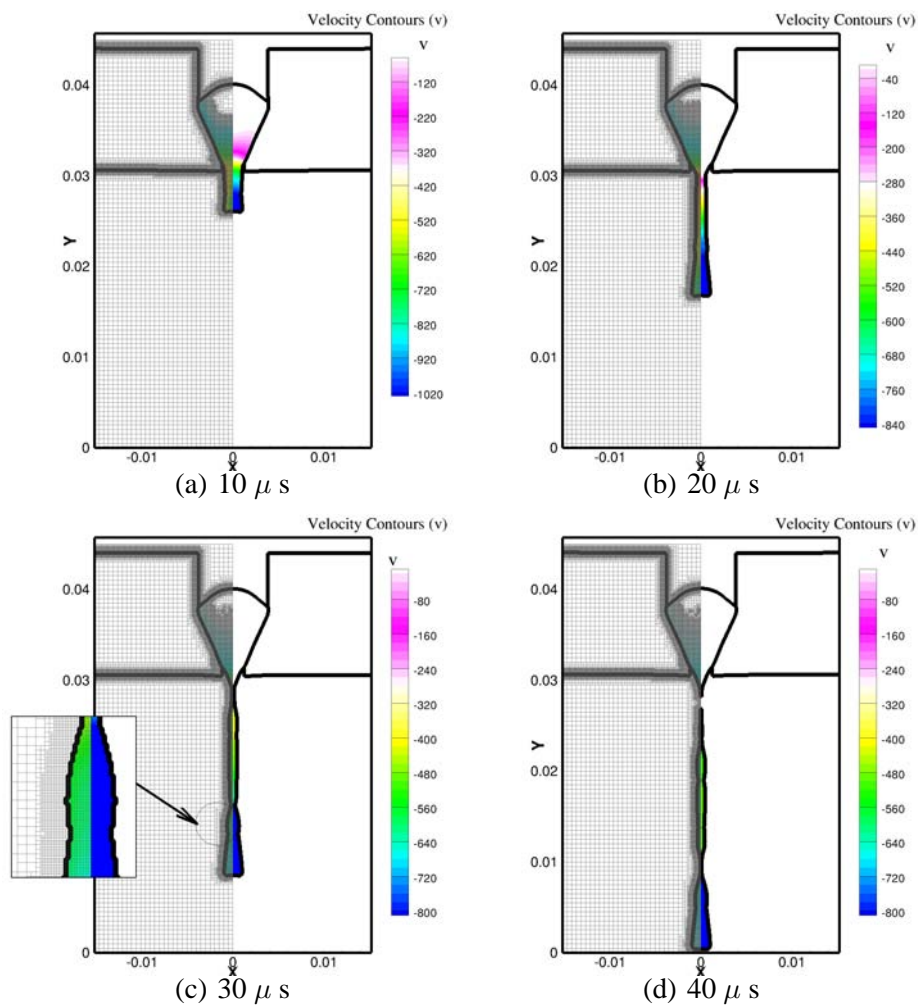
Figure 4.42: Snapshots of velocity contours and mesh evolution at different instants in time for the dynamic tensile extrusion of Copper.
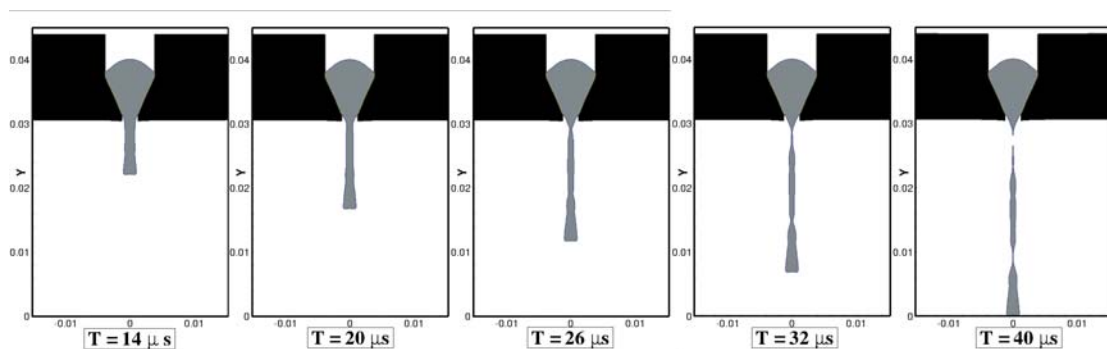
Figure 4.43: Topology and evolution of the interface at different instants in time for the dynamic tensile extrusion of Copper.

CHAPTER 5
SHARP INTERFACE TREATMENT FOR SOLID OBJECTS

5.1   Introduction

Recently, the use of embedded boundary methods for the representation of solid boundaries in incompressible [86, 124, 148, 177] and compressible [57, 58, 118, 133, 135, 190] flows has become popular. The Ghost Fluid Method (GFM) [58] (explained in the previous chapter) provides a simple framework to implicitly transmit the presence of an embedded interface to the flow field. However, when applied to shock interactions with stationary or moving solid objects embedded in compressible flows, the GFM was found to suffer from acute over-/under-heating numerical errors [60, 118]. In section 3.2.1.1, it was demonstrated that the naïve approach of entropy extrapolation (isobaric fix proposed by Fedkiw and coworkers [58]) failed to maintain non-oscillatory pressure field, particularly for strong shocks interacting with fluid-fluid interfaces. Furthermore, it was found that the failure of GFM to accurately resolve the interface can be alleviated by populating the ghost points by solving a local Riemann problem normal to the interface [118]. This was later adopted by several researchers both in the GFM and non-GFM framework [13, 14, 42, 49, 87, 118]. However, these methods were mostly developed to treat fluid-fluid interfaces and hence it is not clear how one could extend such methods to represent embedded solid objects. A variant of the GFM, the Characteristic Based Matching(CBM) method proposed by Nourgaliev et al [133] was found to be effective in reducing the shock-interface interaction errors significantly. In the present work, a unified

formulation to treat both solid-fluid and fluid-fluid interfaces is presented. Briefly, a simple Reflective Boundary Condition (RBC) method is used to populate the ghost points and the resulting heating errors are corrected by augmenting the solutions by solving a Riemann problem between the real field and the reflected ghost field. The Riemann problem constructed normal to the interface is solved using an exact Riemann solver and the resulting Riemann states are used to populate the ghost points. This approach of solving a Riemann problem is simpler to implement than the CBM approach and is also shown later to be computationally less expensive. As demonstrated in the results from the current simulations, the proposed method is found to yield satisfactory solutions for several complex configurations and shock diffraction phenomena. Shocks interacting with multiple particles and complex shapes have been computed and the method is currently being applied to study the dynamics of dense particulate compressible flows.

5.2   Boundary Conditions

The tracked interface has to be coupled with the flow solver such that the jump in the mass, momentum and energy fluxes along with the material properties across the interface are depicted accurately. In the GFM approach, this translates to suitably populating the ghost points. However, there is a significant difference between the treatment of fluid-fluid and (rigid) solid-fluid interfaces in the GFM framework. In the case of fluid-fluid interfaces the flow variables, such as velocity and pressure, that are continuous across the interface are injected into the ghost field directly. In the latter case, due to the absence of flow fields on one side of the interface (the solid side), it is not immediately clear how to populate the

ghost points with the virtual flow properties.

At the interface of a solid body immersed in compressible flows, the boundary conditions that hold true are enlisted in section 1.6.2.3. The set of boundary conditions given in Eqs (1.92) - (1.96) govern the behavior of the flow near the embedded solid body and must be enforced on the real fluid by suitably populating the ghost points. There are several approaches for applying these boundary conditions within the spirit of the Ghost Fluid Method. However, as will be demonstrated in the numerical examples (section 5.3), not all of them are successful in computing shock-interface interactions in a robust fashion.

5.2.1 Boundary Condition Type I: Reflective Boundary Condition (RBC)

The Reflective Boundary Condition (RBC) approach is widely adopted to depict the presence of a rigid body in the fluid [11, 48, 62, 109, 204]. RBC, as the name indicates, reflects the real flow fields across the interface. In the GFM framework, the fields from the real fluid are reflected onto the ghost points in the solid phase. The reflection operation is carried out such that the boundary conditions (Eqs (1.92) - (1.96)) are enforced exactly at the interface. Since the boundary conditions involve the flow properties in the normal and tangential directions, the reflection process must be carried out in the local body-fitted curvilinear coordinates (v_n, v_{t_1}, v_{t_2}), instead of the global Cartesian coordinates (u,v and w).

In order to carry out the reflection process accurately, the reflected point on the real fluid side for each interfacial ghost point on the solid phase must be determined. The reflected point IP1 on the real fluid side, corresponding to ghost point P, can be obtained

by inserting a probe through point P as shown in Figure 5.4. IP is the point of intersection of the probe with the interface. The absolute value of the levelset ($|\phi_P|$) gives the normal distance of point P from the interface. This value ϕ_P can then be used to march into the real fluid to determine the coordinates of the reflected point IP1,

$$\vec{X_{\text{IP1}}} = \vec{X_P} + 2|\phi_P|\vec{N_P}. \tag{5.1}$$

The flow properties at the reflected point can be obtained using a regular bilinear interpolation from the surrounding computational points as shown in Figure 5.4. It must be noted that one or more of these neighboring computational points may lie inside the solid, in which case the corresponding ghost fluid properties are used in the interpolation procedure. Once the flow properties at the reflected point are determined, it is straightforward to reflect the flow properties on to point P.

5.2.1.1   Embedding Boundary Conditions with the Interpolation Procedure

Sometimes, an interfacial ghost point, like point P in Figure 4.1, may lie very close to the interface. In such cases, using a direct bilinear interpolation procedure will involve the (as yet unknown) ghost point. Hence in order to avoid interpolating from the ghost point in consideration, the methodology outlined in section 4.3.1.1 is employed to embed the boundary conditions in the interpolation procedure. Accordingly, the value of the flow variables at the reflected point IP1 can be obtained using a bilinear interpolation of the form

$$\psi = a_1 + a_2 x + a_3 y + a_4 xy \tag{5.2}$$

where (x, y) are the coordinates of the reflected point IP1 and ψ corresponds to the flow variables. In order to determine the coefficients $a_1 - a_4$, Eq (4.7) is applied to the sur-

rounding points chosen for the interpolation procedure. Hence, for Dirichlet type boundary conditions Eq (5.2) reduces to,

$$
\begin{pmatrix}
1 & x_1 & y_1 & x_1y_1 \\
1 & x_2 & y_2 & x_2y_2 \\
1 & x_3 & y_3 & x_3y_3 \\
1 & x_{IP} & y_{IP} & x_{IP}y_{IP}
\end{pmatrix}
\begin{pmatrix}
a_1 \\
a_2 \\
a_3 \\
a_4
\end{pmatrix}
=
\begin{pmatrix}
\psi_1 \\
\psi_2 \\
\psi_3 \\
\psi_4
\end{pmatrix}
\tag{5.3}
$$

and for Neumann type conditions, we have

$$
\begin{pmatrix}
1 & x_1 & y_1 & x_1y_1 \\
1 & x_2 & y_2 & x_2y_2 \\
1 & x_3 & y_3 & x_3y_3 \\
0 & n_x & n_y & n_xy_{IP} + n_yx_{IP}
\end{pmatrix}
\begin{pmatrix}
a_1 \\
a_2 \\
a_3 \\
a_4
\end{pmatrix}
=
\begin{pmatrix}
\psi_1 \\
\psi_2 \\
\psi_3 \\
S_4
\end{pmatrix}
\tag{5.4}
$$

The last row of the coefficient matrix in Eq (5.4) is obtained by differentiating Eq (4.7), noting that

$$
\frac{\partial \psi}{\partial n} = \frac{\partial \psi}{\partial x}n_x + \frac{\partial \psi}{\partial y}n_y
\tag{5.5}
$$

where n_x and n_y are the components of the normal vector at point P and S_4 corresponds to the value of the normal gradient at the interface. After determining the coefficients, the flow properties at the reflected point can be determined using Eq (4.7).

5.2.1.2   Determining the Flow Properties at the Interfacial Ghost Points

Once the flow properties at the reflected point IP1 are determined, the next step is to incorporate the boundary conditions (Eqs (1.92) - (1.96)) at the interface. In the RBC framework, the boundary conditions take the following form: The no-penetration condition

is satisfied by reflecting the normal velocity, as given by,

$$v_{n_P} = 2U_{n_{\text{IP}}} - v_{n_{\text{IP1}}}, \tag{5.6}$$

where $U_{n_{\text{IP}}}$ is the velocity of the center of mass of the solid body. For the tangential veloci-

ties, Eq (1.93) must be satisfied at the interface. The Neumann condition for the tangential

velocities in the RBC framework then becomes,

$$v_{t_{1_P}} = 2U_{t_{1_{\text{IP}}}} - v_{t_{1_{\text{IP1}}}}, \tag{5.7}$$

$$v_{t_{2_P}} = 2U_{t_{2_{\text{IP}}}} - v_{t_{2_{\text{IP1}}}}, \tag{5.8}$$

where, for slip,

$$U_{t_{1_{\text{IP}}}} = v_{t_{1_{\text{IP1}}}}, \tag{5.9}$$

$$U_{t_{2_{\text{IP}}}} = v_{t_{2_{\text{IP1}}}}, \tag{5.10}$$

and for no slip,

$$U_{t_{1_{\text{IP}}}} = 0, \tag{5.11}$$

$$U_{t_{2_{\text{IP}}}} = 0, \tag{5.12}$$

where $U_{t_{1_{\text{IP}}}}$ and $U_{t_{2_{\text{IP}}}}$ are the tangential velocities at IP. Along the same lines, the pressure

field can be obtained from Eq (1.96),

$$P_P = P_{\text{IP1}} - (\frac{\rho_p v_{t_{1_P}}^2}{R_P} - \rho_p a_{n_P})2 \mid \phi_P \mid, \tag{5.13}$$

where a_{n_P} is the acceleration of the solid. The density ρ_p used in Eq (5.13), is obtained by

reflecting the value at IP1, i.e.,

$$\rho_P = \rho_{IP1}. \tag{5.14}$$

Once the flow properties corresponding to the interfacial ghost points in the solid phase are determined, these properties are then extended to populate the interior ghost points using a suitable multi-dimensional extrapolation procedure. Linear and other higher-order extrapolation procedures have been discussed in Aslam et al [15]. However, the numerical experiments carried out in this work indicate that the order of the extrapolation procedure has little or no significant influence over the accuracy of the solution, and hence a simple constant extrapolation procedure was found to be sufficient for the problems attempted in this paper. Thus in the current formulation the subcell postion of the interface and the topology of the interface are carefully embedded in the interpolation procedure. With the reflected ghost field, the problem is reduced effectively to a single fluid (real fluid - ghost fluid) problem which can be solved with known (fluid - fluid) interface treatment techniques.

5.2.1.3   Correction for Over-/Under-Heating Problems

The reflection of strong shocks from moving or stationary walls can cause numerical artifacts such as excessive over-/under-heating errors [127, 132]. The over-/under-heating errors are the result of lack of dissipation in the numerical model. In reality, the viscous effects are not negligible in the regions occupied by the shock and when a shock reflects of the interface, the excessive heat generated are dissipated due the viscous effects (conducted away from the wall). Since the numerical schemes, do not have such strong dissipative mechanism, the heat generated accrue over time and result in over-/under-prediction of field variables. Donat et al [52] developed a flux-splitting scheme which had a

built-in mechanism to dissipate the excessive heat generated at the wall. Fedkiw et al [60] proposed an isobaric fix, which is a simple extrapolation of entropy from the real fluid side onto the corresponding ghost field (Figure 5.2(a)), to suppress the over-/under-heating errors.

Several interface treatment techniques developed in the past [58, 60, 133, 135] were prone to these heating errors and RBC is no exception. As mentioned above, with RBC, the solid-fluid interface is converted to a relatively simple (real) fluid - (ghost) fluid interface problem. The interaction between the real and the corresponding ghost fields result in strong shock or rarefaction waves or both, which travel into the real and ghost fields. The problem becomes accentuated for a strong shock impacting the interface due to the following three reasons.

i. Due to the implementation of reflective conditions, which uses bilinear interpolation to obtain the flow properties at the reflected point: Using any form of interpolation techniques across strong discontinuities will result in interpolation errors. These errors, although generated locally near the interface, accrue over time and afflict the solution way from the interface. It is important to point out that the errors arising from the interpolation procedure can be significantly reduced by employing lower/higher-order MUSCL [193]/ENO [163] based adaptive polynomial interpolation procedure. However, such schemes require wider stencils and gradient evaluation, which becomes complicated to compute and computationally expensive particularly when the mesh becomes highly unstructured; i.e. when additional mesh enrichment techniques like Adaptive Mesh Refinement (AMR) [26] or tree-based Local Mesh Refinement

(LMR) [108] is employed.

ii. Due to the over-/under-heating errors arising from shock reflection phenomena.

iii. Due to over-/under-specification of boundary conditions: The characteristic analysis (discussed in section 5.2.4) of the governing hyperbolic equations dictates that the variables corresponding to incoming characteristic waves must be supplied with flow conditions independent of the flow field, and the variables corresponding to the outgoing characteristic waves must be evolved in time based on the flow properties within the computational domain [133, 135]. Since the RBC approach does not conform to the restriction imposed by the characteristic waves at the interface (except for supersonic inflow condition), it results in over-/under-specification of the boundary conditions, which in turn causes spurious waves to enter the computational domain.

The isobaric fix [60] is one approach to annihilate the growth of over-/under-heating shock interaction errors. However, it was shown in the previous chapter that the isobaric fix does not perform adequately for strong shocks interacting with a fluid-fluid interface. Furthermore, it was shown that the most effective way of dynamically correcting such errors was to accurately resolve the wave interactions occurring at the interface. To this effect, a Riemann problem was solved locally, normal to the interface, to decompose the singularities in wave patterns and material properties. In section 3.1.2, the methodology to construct the Riemann problem at the interface of a fluid object immersed in the flow was reviewed. The same methodology can be extended to correct the heating errors arising due to shocks interacting with the solid-fluid interfaces. Moreover, the Riemann solver constructed locally

at the interface essentially solves the mass, momentum and energy balances at the interface (Rankine-Hugoniot jump conditions), and implicitly adheres to the nature of the waves arriving/leaving the interface. Hence the Riemann states obtained from the Riemann solver are devoid of shock interaction errors and could be used to mitigate the growth of such errors. The procedure described in section 3.1.2 is adopted here. Once the flow properties at the interfacial ghost points are determined, the flow field corresponding to the interior ghost points (located inside the solid) can be obtained by extending the flow properties using a suitable multi-dimensional extrapolation procedure [15].

5.2.2 Boundary Condition Type II: Simple Boundary Condition (SBC)

SBC approach is the most direct way to enforce the boundary conditions (Eqs (1.92) - (1.96)) accurately at the interface. This is a simple extension of the approach discussed in Marella et al [124], where a methodology was developed to treat the presence of embedded objects in an incompressible flow. A version of this approach was also discussed by Arienti et al [11]. As shown in Figure 5.2(b), a probe is inserted through each interfacial ghost point P in the solid phase. Coordinates of IP, the point of intersection of the probe with the interface, are determined from Eq (3.1). Along the same lines, the coordinates of points IP1 and IP2 are determined as follows:

$$\vec{X}_{IP1} = \vec{X}_{\text{IP}} + \Delta x \vec{N}_P, \tag{5.15}$$

$$\vec{X}_{IP2} = \vec{X}_{\text{IP}} + 2\Delta x \vec{N}_P. \tag{5.16}$$

Flow properties at points IP1 and IP2 are obtained using bilinear interpolation from the surrounding computational points. The normal derivatives required in Eqs (1.92) - (1.96)

can now be easily computed as

$$\frac{\partial \psi}{\partial n} = \frac{\psi_{IP} - 4\psi_{IP1} + \psi_{IP2}}{3\Delta x},$$
(5.17)

where ψ corresponds to temperature T, or tangential velocities v_{t_1} & v_{t_2} or the pressure P. The density at the interface can be obtained from the equation of state. The velocity of the center of mass is specified as the normal velocity at the point IP. After determining the flow properties at the interface, the values are extended to define the ghost field in the solid phase.

It is important to note that this method suffers from severe over-/under-heating errors. In particular, these errors are amplified during the transient shock-interface interaction process. Evaluation of derivatives with the use of probes, especially during the initial stages of the shock interaction with the interface, result in severe interpolation errors. If these start-up errors are left uncorrected, they are fed back into the real fluid through the ghost field. It was found that these errors cannot be corrected by augmenting this approach with a local Riemann solver. This is because, populating the ghost points with SBC results in an abrupt change in flow properties. Employing a Riemann solver would yield intermediate states which together with the real fluid would not satisfy the boundary conditions (Eqs (1.92) - (1.96)) at the interface. Therefore, for strong shock interactions with the embedded solid boundaries, the SBC approach is ill-advised.

5.2.3 Boundary Condition Type III: Simple Boundary Condition using Coordinate Transformation (SBC-CT)

Another method for treating the presence of embedded solid bodies is to use the coordinate transformation/rotation technique [133, 135]. In this method, the discretization of Eqs (1.92) - (1.96) are carried out in global Cartesian coordinates for each interfacial ghost point in the solid phase, and then transformed to the local (body-fitted) curvilinear coordinates by means of a suitable transformation matrix. Thus the normal and tangential derivatives can be computed as follows;

$$
\begin{pmatrix} \frac{\partial \psi}{\partial n} \\[2mm] \frac{\partial \psi}{\partial t_1} \\[2mm] \frac{\partial \psi}{\partial t_2} \end{pmatrix} = \mathbb{J} \begin{pmatrix} \frac{\partial \psi}{\partial x} \\[2mm] \frac{\partial \psi}{\partial y} \\[2mm] \frac{\partial \psi}{\partial z} \end{pmatrix}, \tag{5.18}
$$

$$
\mathbb{J} = \begin{pmatrix} n_x & n_y & n_z \\[2mm] t_{1x} & t_{1y} & t_{1z} \\[2mm] t_{2x} & t_{2y} & t_{2z} \end{pmatrix}. \tag{5.19}
$$

where $\mathbb{J}$ is the Jacobian matrix and the unit vectors $\hat{n}, \hat{t}_1$ and $\hat{t}_2$ are the normal and tangential vectors computed from the level-set field [101, 133, 135]. This method minimizes interpolation across the discontinuity and hence localizes the over-/under-heating errors to few points close to the interface. Although this method appears to be very simple and robust, there is a slight smearing of the interface due to the following reason: Eqs (1.92) - (1.96) are valid at the interface and hence the normal and tangential derivatives must be evaluated at the interface itself. Evaluating the derivatives at the interfacial ghost points results in diffusing the interface over few grid points and hence using Eq (5.18) would not

ensure the application of boundary conditions strictly at the interface.

5.2.4 Boundary Condition Type IV: Characteristic Based Matching (CBM) [133, 135]

Another promising approach to treat the presence of embedded objects in compressible flows is to use the characteristic wave analysis at the interface [133, 135, 188]. As the governing equations are a set of hyperbolic conservation laws, the equations can be recast in characteristic form using a suitable transformation matrix. The sign of the eigenvalues determine whether the waves are incoming or outgoing, and hence the direction of propagation of information. The incoming waves carry information into the flow field and hence correspond to the physical boundary conditions that need to be supplied independent of the flow field. The outgoing waves carry information from within the flow field and hence correspond to the numerical boundary conditions (obtained via extrapolation) that need to computed from within the flow field. The characteristic analysis was carried out by Thomson [188] for the domain boundaries and was extended by Poinsot et al [141] for compressible turbulent flows. The method was applied for complex configurations in curvilinear coordinates by Kim et al [107]. Nourgaliev et al [133,135] extended the method to treat interfaces embedded in a Cartesian mesh in the GFM framework. The discussion in this section follows from Thomson [188] and Nourgaliev et al [135] and interested readers should refer to the original papers for additional information.

5.2.4.1 Coordinate Transformation

In order to obtain a non-oscillatory pressure field and to maintain sharp transition in the field variables across the interface, it is desirable to work with primitive variables.

Hence it is required to transform the conservative variable formulation of the governing equations to the corresponding primitive (non-conservative) variable formulation [5, 102]. The associated transformation matrix along with the governing equations in the primitive variable formulation is

$$\frac{\partial \vec{U}}{\partial t} + \frac{\partial \vec{F}}{\partial x} + \frac{\partial \vec{G}}{\partial y} + \frac{\partial \vec{H}}{\partial z} = \vec{S}, \tag{5.20}$$

$$\frac{\partial \vec{U}}{\partial \vec{\vec{U}}} \frac{\partial \vec{\vec{U}}}{\partial t} + \frac{\partial \vec{F}}{\partial \vec{\vec{U}}} \frac{\partial \vec{\vec{U}}}{\partial x} + \frac{\partial \vec{G}}{\partial \vec{\vec{U}}} \frac{\partial \vec{\vec{U}}}{\partial y} + \frac{\partial \vec{H}}{\partial \vec{\vec{U}}} \frac{\partial \vec{\vec{U}}}{\partial z} = \vec{S}. \tag{5.21}$$

where

$$\vec{\vec{U}} = \begin{pmatrix} \rho \\ P \\ u \\ v \\ w \end{pmatrix} \tag{5.22}$$

Thus there exist an unique transformation matrix [P] = $\frac{\partial \vec{U}}{\partial \vec{\vec{U}}}$ with inverse given by $[P]^{-1} = \frac{\partial \vec{\vec{U}}}{\partial \vec{U}}$ However, in order to apply the the boundary conditions (Eqs (1.92) - (1.96)) at the interface, the conservative variable $\vec{U}$ must be transformed to the corresponding primitive variable formulation in the local curvilinear coordinates $\vec{\vec{U}}^{\star}$, where $\vec{\vec{U}}^{\star}$ is defined as

$$\vec{\vec{U}}^{\star} = \begin{pmatrix} \rho \\ P \\ v_n \\ v_{t_1} \\ v_{t_2} \end{pmatrix}, \tag{5.23}$$

where v_n, v_{t1} and v_{t2} are defined in Eq (1.97). The Jacobian matrix that enables the transformation to the local curvilinear coordinates is defined in Eq (5.19). The transformation matrix [P], that transforms $\vec{U}$ to the primitive variable formulation $\vec{\tilde{U}}^\star$ in the local body fitted coordinate, then becomes

$$[P] = \frac{\partial \vec{U}}{\partial \vec{\tilde{U}}^\star} = \begin{pmatrix} 1 & 0 & 0 & 0 & 0 \\ KE & \frac{1}{\gamma - 1} & \rho v_n & \rho v_{t_1} & \rho v_{t_2} \\ u & 0 & \rho n_x & \rho t_{1_x} & \rho t_{2_x} \\ v & 0 & \rho n_y & \rho t_{1_y} & \rho t_{2_y} \\ w & 0 & \rho n_z & \rho t_{1_z} & \rho t_{2_z} \end{pmatrix}, \tag{5.24}$$

where

$$\mathrm{KE} = \frac{1}{2}\left(u^2 + v^2 + w^2\right) = \frac{1}{2}\left(v_n{}^2 + v_{t_1}{}^2 + v_{t_2}{}^2\right). \tag{5.25}$$

Thus, pre-multiplying Eq (5.20) with the transformation matrix [P] we get,

$$[P]\frac{\partial \vec{\tilde{U}}^\star}{\partial t} + [\tilde{A}^\star]\frac{\partial \vec{\tilde{U}}^\star}{\partial n} + [\tilde{B}^\star]\frac{\partial \vec{\tilde{U}}^\star}{\partial t_1} + [\tilde{C}^\star]\frac{\partial \vec{\tilde{U}}^\star}{\partial t_2} - \vec{S}^\star = 0, \tag{5.26}$$

where

$$[\tilde{A}^\star] = \frac{\partial \vec{\mathbb{F}}\left(\vec{\tilde{U}}^\star\right)}{\partial \vec{\tilde{U}}^\star}, \tag{5.27}$$

$$[\tilde{B}^\star] = \frac{\partial \vec{\mathbb{G}}\left(\vec{\tilde{U}}^\star\right)}{\partial \vec{\tilde{U}}^\star}, \tag{5.28}$$

$$[\tilde{C}^\star] = \frac{\partial \vec{\mathbb{H}}\left(\vec{\tilde{U}}^\star\right)}{\partial \vec{\tilde{U}}^\star}, \tag{5.29}$$

and $\mathbb{F}\left(\vec{\tilde{U}^\star}\right)$, $\mathbb{G}\left(\vec{\tilde{U}^\star}\right)$, $\mathbb{H}\left(\vec{\tilde{U}^\star}\right)$ are the projections of the Cartesian flux vectors on to the local curvilinear coordinates [135],

$$
\begin{pmatrix}
\frac{\partial \mathbb{F}\left(\vec{\tilde{U}^\star}\right)}{\partial n} \\[6pt]
\frac{\partial \mathbb{G}\left(\vec{\tilde{U}^\star}\right)}{\partial t_1} \\[6pt]
\frac{\partial \mathbb{H}\left(\vec{\tilde{U}^\star}\right)}{\partial t_2}
\end{pmatrix}
= \begin{bmatrix} J \end{bmatrix}
\begin{pmatrix}
\frac{\partial F\left(\vec{U}\right)}{\partial x} \\[6pt]
\frac{\partial G\left(\vec{U}\right)}{\partial y} \\[6pt]
\frac{\partial H\left(\vec{U}\right)}{\partial z}
\end{pmatrix}.
\tag{5.30}
$$

Pre-multiplying Eq (5.26) with $[P]^{-1}$ we obtain

$$
\frac{\partial \vec{\tilde{U}^\star}}{\partial t} + [P]^{-1}[\tilde{A}^\star]\frac{\partial \vec{\tilde{U}^\star}}{\partial n} + [P]^{-1}[\tilde{B}^\star]\frac{\partial \vec{\tilde{U}^\star}}{\partial t_1} + [P]^{-1}[\tilde{C}^\star]\frac{\partial \vec{\tilde{U}^\star}}{\partial t_2} - [P]^{-1}\vec{S}^\star = 0.
\tag{5.31}
$$

where

$$
[P]^{-1} = \frac{\partial \vec{\tilde{U}^\star}}{\partial \vec{U}} =
\begin{pmatrix}
1 & 0 & 0 & 0 & 0 \\[8pt]
(\gamma - 1)\,KE & (\gamma - 1) & -(\gamma - 1)\,u & -(\gamma - 1)\,v & -(\gamma - 1)\,w \\[8pt]
-\frac{v_n}{\rho} & 0 & \frac{n_x}{\rho} & \frac{n_y}{\rho} & \frac{n_z}{\rho} \\[8pt]
-\frac{v_{t_1}}{\rho} & 0 & \frac{t_{1_x}}{\rho} & \frac{t_{1_y}}{\rho} & \frac{t_{1_z}}{\rho} \\[8pt]
-\frac{v_{t_2}}{\rho} & 0 & \frac{t_{2_x}}{\rho} & \frac{t_{2_y}}{\rho} & \frac{t_{2_z}}{\rho}
\end{pmatrix}.
\tag{5.32}
$$

It is important to note that in the derivation of [P] and $[P]^{-1}$, an ideal gas equation of state has been used. With a more generalized equation of state (such as the Mie-Gruneisen equation of state), the computation of matrices [P] and $[P]^{-1}$ may become exceedingly complicated. Equation (5.31) is the required primitive variable formulation in the local curvilinear coordinate.

5.2.4.2   Compatibility Relation

Equation (5.31) is a hyperbolic equation which can be diagonalized to obtain the compatibility relation. However, it is not always possible to simultaneously diagonalize

the matrices $[P^{-1}][\tilde{A}^\star]$, $[P^{-1}][\tilde{B}^\star]$, $[P^{-1}][\tilde{C}^\star]$. Since we are interested in analyzing the characteristic waves arriving at the interface, diagonalization of Eq (5.31) can be carried out with respect to the normal direction (i.e., with respect to $\left([P^{-1}][\tilde{A}^\star]\right)$ [188]. Grouping all the transverse terms together Eq (5.31) can be written as,

$$\frac{\partial \vec{U}^\star}{\partial t} + \underbrace{[\chi]}_{[P]^{-1}[\tilde{A}^\star]}\frac{\partial \vec{U}^\star}{\partial n} + \underbrace{[\vec{S}^\star]}_{[P]^{-1}([\tilde{B}^\star]\frac{\partial \vec{U}^\star}{\partial t_1}+[\tilde{C}^\star]\frac{\partial \vec{U}^\star}{\partial t_2}-\vec{S}^\star)} = 0. \tag{5.33}$$

Diagonalizing Eq (5.33) with respect to $[\chi]$ we get the compatibility relation [84, 188],

$$[L]^{-1}\frac{\partial \vec{U}^\star}{\partial t} + [\mathcal{L}] + [L]^{-1}[\vec{S}^\star] = 0. \tag{5.34}$$

where

$$\vec{U}^\star = \begin{pmatrix} \rho \\ P \\ v_n \\ v_{t_1} \\ v_{t_2} \end{pmatrix}, \tag{5.35}$$

$$[\mathcal{L}] = \begin{pmatrix} \mathcal{L}_1 \\ \mathcal{L}_2 \\ \mathcal{L}_3 \\ \mathcal{L}_4 \\ \mathcal{L}_5 \end{pmatrix} = \begin{pmatrix} \lambda_1 \left(\frac{\partial p}{\partial n} - \rho c \frac{\partial v_n}{\partial n} \right) \\ \lambda_2 \left(c^2 \frac{\partial \rho}{\partial n} - \frac{\partial p}{\partial n} \right) \\ \lambda_3 \left(\frac{\partial v_{t_1}}{\partial n} \right) \\ \lambda_4 \left(\frac{\partial v_{t_2}}{\partial n} \right) \\ \lambda_5 \left(\frac{\partial p}{\partial n} + \rho c \frac{\partial v_n}{\partial n} \right) \end{pmatrix}, \tag{5.36}$$

and

$$\lambda_1 = v_n - c, \tag{5.37}$$

$$\lambda_2 = v_n, \tag{5.38}$$

$$\lambda_3 = v_n, \tag{5.39}$$

$$\lambda_4 = v_n, \tag{5.40}$$

$$\lambda_5 = v_n + c. \tag{5.41}$$

are the eigenvalues, c is the speed of sound, $[L]^{-1}$ is the matrix with left eigenvectors as its rows and $[\mathcal{L}]$ is correction term matrix [133, 135] which is used to infuse the boundary conditions at the interface. The eigenvalues λ_1 and λ_5 represent the sound waves moving in the negative and positive direction normal to the interface, λ_2 corresponds to the velocity of the entropy advection , λ_3 and λ_4 correspond to the velocities with which v_{t_1} and v_{t_2} are advected normal to the interface [188]. At any point on the interface, the sign of the eigenvalues determine the direction (positive for inflow and negative for outflow) of propagation of characteristic waves and the Mach number determines the flow condition at that point. For example, if the Mach number $M \leq 1$, then the flow condition is subsonic. If the normal velocity $v_n \geq 0$, then there are four incoming waves corresponding to λ_2, λ_3, λ_4, & λ_5, and one outgoing wave corresponding to λ_1. This combination of flow with wave direction is categorized as "subsonic inflow" with respect to the interface. Therefore, for a subsonic inflow condition, four boundary conditions corresponding to the three velocity components and temperature must be supplied. Equation (5.34) can be written in a convenient form by pre-multiplying with [L] to obtain,

$$\frac{\partial \vec{\tilde{U}}^\star}{\partial t} + [L][\mathcal{L}] + [\vec{\tilde{S}}^\star] = 0, \tag{5.42}$$

$$[\mathfrak{L}] = [L][\mathcal{L}] = \begin{pmatrix} \frac{1}{c^2}\left(\mathcal{L}_2 + \frac{1}{2}\left(\mathcal{L}_5 + \mathcal{L}_1\right)\right), \\ \frac{1}{2}\left(\mathcal{L}_5 + \mathcal{L}_1\right) \\ \frac{1}{2\rho c}\left(\mathcal{L}_5 - \mathcal{L}_1\right) \\ \mathcal{L}_3 \\ \mathcal{L}_4 \end{pmatrix}. \tag{5.43}$$

The correction terms ($\mathfrak{L}$) given in Eq (5.43) are used to evolve variables corresponding to the outgoing waves in time. The variables corresponding to incoming waves are specified as boundary conditions. This way of applying the boundary conditions prevents over-/under-specification of boundary conditions which in turn prevents spurious disturbances from entering the flow field [188]. To solve Eq (5.42) in Cartesian coordinates at the interface of the embedded object, requires the evaluation of the tangential and normal derivatives and fluxes. This calls for a meticulous treatment of cut cells and explicit conservation of fluxes at the interface which becomes a monumental task especially for a system of equations like Eq (5.42). However, the difficulties associated with the cut cell treatment and with the evaluation of derivatives can be alleviated if the characteristic analysis of Eq (5.42) is carried out for the interfacial ghost points, as done in the CBM approach of Nourgaliev et al [133, 135].

As the fluxes in Cartesian coordinates are computed for all points in the computational domain, one can make use of these fluxes to compute the normal and tangential

derivatives occurring in Eq (5.42). Carrying out the diagonalization procedure yields,

$$\frac{\partial \vec{\tilde{U}}^\star}{\partial t} + \underbrace{[\delta\mathfrak{L}]}_{\begin{pmatrix} \frac{1}{c^2}\left(\delta\mathfrak{L}_2 + \frac{1}{2}\left(\delta\mathfrak{L}_5 + \delta\mathfrak{L}_1\right)\right) \\[2mm] \frac{1}{2}\left(\delta\mathfrak{L}_5 + \delta\mathfrak{L}_1\right) \\[2mm] \frac{1}{2\rho c}\left(\delta\mathfrak{L}_5 - \delta\mathfrak{L}_1\right) \\[2mm] \delta\mathfrak{L}_3 \\[2mm] \delta\mathfrak{L}_4 \end{pmatrix}} + \underbrace{[\vec{\tilde{\mathbb{S}}}^\star]}_{[P]^{-1}\left(\frac{\partial \vec{F}}{\partial x} + \frac{\partial \vec{G}}{\partial y} + \frac{\partial \vec{H}}{\partial z} - \vec{S}\right)} = 0. \qquad (5.44)$$

The form of Eq (5.44) is similar to that of Eq (5.42) except now the source term in Eq (5.44) includes fluxes in Cartesian coordinates pre-multiplied with the transformation matrix. The characteristic analysis can now be performed on the interfacial ghost points using Eq (5.44) [135]. As mentioned before, at each interfacial ghost point, the Mach number and the sign of the normal velocity determine the flow condition and the flow direction respectively. Based on the flow condition and the flow direction, the boundary treatment at the ghost point fall into one of the four categories;

   i. subsonic inflow - four incoming waves and one outgoing wave,

  ii. subsonic outflow - four outgoing waves and one incoming wave,

 iii. supersonic inflow - All five waves are incoming waves,

 iv. supersonic outflow - All five waves are outgoing waves

Thus for the variables corresponding to the incoming waves, the respective boundary conditions from Eqs (1.92) - (1.96) must be used to find the values. Once the variables corresponding to the incoming waves are evaluated, the correction terms can be computed by

inverting Eq (5.44). For the outgoing waves, the corresponding variables must be evolved in time depending on the flow field at that instant. The correction term for the outgoing wave is set to zero (as the normal derivative terms are taken into account in the modified source term defined in Eq (5.44), the explicit evaluation of the correction terms will be annulled by the corresponding terms in the source term). For example, for a subsonic inflow case, there are four incoming waves corresponding to λ_2, λ_3, λ_4, & λ_5 and hence the correction terms $\delta\mathfrak{L}_2$, $\delta\mathfrak{L}_3$, $\delta\mathfrak{L}_4$, & $\delta\mathfrak{L}_5$ must be evaluated from Eq (5.44), and one outgoing wave corresponding to λ_1 and hence $\delta\mathfrak{L}_1$ is set to zero [135].

$$\delta\mathfrak{L}_1 = 0, \tag{5.45}$$

$$\delta\mathfrak{L}_3 = -\left(\frac{\partial v_{t_1}}{\partial t} - \tilde{\mathbb{S}\star}_4^n\right), \tag{5.46}$$

$$\delta\mathfrak{L}_4 = -\left(\frac{\partial v_{t_2}}{\partial t} - \tilde{\mathbb{S}\star}_5^n\right), \tag{5.47}$$

$$\delta\mathfrak{L}_5 = \delta\mathfrak{L}_1 - (2\rho c)\left(\frac{\partial v_n}{\partial t} - \tilde{\mathbb{S}\star}_3^n\right), \tag{5.48}$$

$$\delta\mathfrak{L}_2 = -\left(\frac{1}{2}\left(\delta\mathfrak{L}_5 + \delta\mathfrak{L}_1\right)\right) - c^2\left(\tilde{\mathbb{S}\star}_1^n + \frac{\partial\rho}{\partial t}\right) \tag{5.49}$$

Using the correction terms $\delta\mathfrak{L}_1 - \delta\mathfrak{L}_5$, pressure term in Eq (5.44) can be computed as follows

$$P^{n+1} = P^n - \Delta t(\tilde{\mathbb{S}\star}_2^n + \frac{1}{2}(\delta\mathfrak{L}_1 + \delta\mathfrak{L}_5)). \tag{5.50}$$

Density can then be retrieved by using the equation of state. Iterations are performed until convergence in the computed values of pressure and density are achieved [135]. The same procedure is repeated for all interfacial ghost points and all flow variables can be evaluated. These flow variables are then extended to the interior ghost points in the ghost band.

5.2.4.3   Other Methods

Other methods for applying interface conditions on embedded solid boundaries have been discussed at length by Arienti et al [11]. The methods include mirroring technique, reflection method and direct injection method. In the mirroring technique [62], the flow properties on the real fluid side are mirrored onto the ghost fluid by multiplying with a suitable rotation/reflection matrix. The reflection method discussed in Arienti et al [11] simply extends the flow properties at the real fluid interfacial nodes, but with an inverted sign of the normal velocity to satisfy the no-penetration boundary condition. The injection method formulated by Arienti et al [11] is a variation of SBC. In this approach, flow variables at the real fluid interfacial points are extended to the ghost points, but now the normal velocity is set to zero, preserving the tangential velocities to depict the slip condition at the interface. These methods are mentioned here only for the sake of completeness and will not be considered in the numerical examples to be discussed in the next section.

5.3   Numerical Examples

5.3.1   One Dimensional Examples

The one-dimensional examples shown here demonstrate the performance of various (interface treatment) methods in handling regular shock reflections. It is found that the choice of method impacts significantly on the accuracy and stability of the computations.

5.3.1.1   Rotated Shock Tube

A variant of the one-dimensional shock tube problem due to Nourgaliev et al [135] is considered first. As shown in Figure 5.3, the walls of the shock tube are embedded in

the computational domain by defining a suitable level set field. The shock tube is oriented at an angle to the regular Cartesian mesh so that a two-dimensional problem is solved, but the problem is one-dimensional along the centerline of the shock tube.

The discontinuity at T = 0 is at the center of the shock tube. The shock tube is placed at different orientations relative to the grid lines. Rotation angles corresponding to $\alpha_{rot} = 30^o, \alpha_{rot} = 45^o,$ and $\alpha_{rot} = 60^o$ with respect to the horizontal have been considered. The size of the computational domain is 2×2 units. The length and the height of the shock tube were chosen to be 1.5 and 1.0 units respectively. The simulations were carried out to T = 0.164. The results obtained from the current simulations are shown in Figure 5.4. RBC augmented with local Riemann solver (henceforth RBC-RS), SBC and the CBM approaches were used to simulate this problem. Figure 5.4 shows good agreement between these methods and with the exact solution, in capturing the shock and the contact discontinuity. The simulations were stopped to prevent the shock from reflecting off the wall, so that the resulting numerical solution could be compared with the exact solution.

5.3.1.2 Woodward Colella (Bang Bang) Problem

Unlike the previous case, this example involves strong shock reflections and shock collisions. The initial conditions along with the geometrical set up is given in Figure 5.5. As in the previous example, the shocktube is placed at different orientations ($\alpha_{rot} = 30^o,$ and $\alpha_{rot} = 60^o$) so that the problem is not strictly one-dimensional and the impact of the interface treatment and mesh orientation can be examined. The simulations were run to time T = 0.038 units and the plots of density, pressure and entropy along the centerline

of the shocktube are displayed in Figure 5.6. Note that the SBC, unable to suppress the initial transient shock development errors, failed in the first few times steps of the shock reflection process.

From the entropy plots displayed in Figures 5.6(e) & 5.6(f), it is evident that RBC suffers from extensive over-heating errors that appear to be problem dependent (over-/under-heating errors were not observed in the previous example). Clearly the over-heating errors associated with the RBC cannot be neglected and hence must be corrected in order to obtain better solutions in the presence of strong shocks. On the other hand, the RBC-RS shows no significant over-/under-heating errors. Both CBM and the SBC-CT produce under-heating errors which are small. This example clearly illustrates the requirement of an additional correction procedure to suppress the errors associated with shock-interface interactions.

5.3.1.3   Shock Reflecting off a Stationary Wall

This is strictly one-dimensional test case with Mach 10 and Mach 20 shocks reflecting off a stationary wall. The wall is positioned at x = 0.25 and the incident shock is initially located at x = 0.35 in a computational domain of unit length. The shock impinges on the wall and reflects back bringing the oncoming fluid to rest. Again SBC failed exactly at the instant when the shock impinged on the wall. Clearly, this shows that the SBC suffers from severe interpolation errors especially in the presence of strong shocks near the interface. The results obtained from the current simulations can be found in Figure 5.8. The position of the reflected shock obtained from the RBC with and without the Riemann correction

differs by a fraction of a grid cell from that obtained using CBM. This discrepancy in the shock location can be attributed to the mass conservation errors occurring during the initial shock formation process. Once the shock has developed and detaches from the surface, the interface recovers back to its normal motion and hence the conservation errors are localized to the few time steps [118] during which the shock impinges on the interface.

Thus, it is clear from the one-dimensional examples presented in this section that the SBC approach suffered from severe over-/under-heating errors that had catastrophic consequences in the final outcome of the solution. The RBC approach incurred over-/under-heating errors that were problem dependent (Figures 5.6(e), 5.6(f), & 5.8). In contrast, the RBC-RS and CBM method resulted in lower levels of over-/under-heating errors and were consistent in predicting satisfactory solutions. This clearly favors the use of CBM and RBC approach with Riemann solver correction over other methods.

5.3.2   Two-Dimensional Examples

In the one-dimensional test cases considered in the preceding section, the shocks interacted with interfaces to produce regular reflections. Multi-dimensional shock diffraction patterns can be irregular (consisting of Mach stem, slip lines emanating from Mach stem and eventual roll up of slip lines due to baroclinic vorticity generation, etc.). In this section a series of multi-dimensional test cases are presented to illustrate the performance of the GFM-based approaches in such situations.

5.3.2.1   Shock Diffraction over Wedge

The first two-dimensional test case considered in this work, is the diffraction of a Mach 1.3 shock wave past a wedge. The details of the initial configuration of the problem can be found in Sivier et al [166]. This problem has received considerable attention in the past, and extensive numerical and experimental documentations are available for comparison [166]. Snapshots of the numerical Schlieren image, at different instants in time, obtained from using both the RBC-RS and the CBM approach are displayed in Figures 5.9 & 5.10. Although the contour plots generated using the two approaches look very similar, there are subtle differences that are worth noting. As mentioned in Sivier et al [166], the planar shock, upon impacting the wedge, forms a cylindrical reflected "bow" shock centered at the wedge tip with a Mach stem attached to the wedge surface (Figures 5.9(a) and 5.9(b)). All typical features of Mach reflections are captured well by both (RBC-RS & CBM) methods. However, both methods fail to capture the slip line originating from the wedge surface which is clearly visible in Sivier et al. But in Sivier et al, an Adaptive Mesh Refinement (AMR) technique was employed which provides sufficient mesh enrichment to capture such fine details. Figures 5.9(c) and 5.9(d) correspond to the instant when the incident shock wave has passed over the wedge surface. As observed by Siver et al, the roll up of slip layers to form vortices that engulf the vertex of the entropy fan are clearly visible. At this instant, the opposite shock systems from the symmetrical side of the wedge have crossed and have begun to interact with these vortices. The expansion fan, which is produced as a result of the diffraction of the Mach stem around the corner [166] and which subsequently moves down the wedge surface, is also visible in the

figures. Figures 5.9(e) - 5.9(h) show that the vortices have shifted to the right, downstream of the wedge. The slip layer emanating from these vortices are now visible along with a new triple point formed at the vortex center. All of these features typical of the shock diffraction phenomena past a wedge are consistent with other numerical results [166] and with experimental observations [156].

Plots of the primary shock distance from the wedge surface are shown in Figure 5.11. Shown in the figure, in accordance with Sivier et al, are the horizontal shock detachment distance "a" of the reflected bow shock from the foot of the wedge (Figure 5.11(a)), vertical distance "r" from the tip of the wedge to the diffracting shock (Figure 5.11(b)), and the horizontal distance "x" between the tip of the wedge and the incident shock (Figure 5.11(c)). The plots show excellent agreement between the two methods in determining the position of the primary shocks and are consistent with the predictions made by Sivier et al [166].

5.3.2.2 Shock Diffraction over a Circular Cylinder - Comparison with CBM

A Mach 2.81 planar shock wave negotiating a cylindrical obstacle in a shock tube is considered. As pointed out by Bazhenova et al [20], the initial interaction of the planar shock with the cylinder is a regular reflection with the shock reflecting normally along the axis of symmetry. The reflected shock begins traversing the cylinder before transitioning to a Mach reflection. The Mach reflection consists of the incident shock, the reflected shock, Mach stem and slipstream. Ripley et al [149] pointed out that this curved Mach stem travels down the cylinder and interacts with the shock system from the symmetrical part of

the cylinder to form a wake. Several papers documenting this phenomenon are available for comparison [20, 31, 149, 158, 176, 204].

Due to the symmetry of the problem, only one-half of the problem was modeled using a symmetry condition at the bottom wall. Reflective boundary condition for the top wall and Neumann condition for outlet were imposed. At the inlet, a Dirichlet condition corresponding to Mach 2.81 shock was enforced. The semi-circular obstacle with radius 0.105 units was positioned at x = 0.5 and y = 0.0. The simulations were performed with 500×250 mesh points in a 1×0.5 computational domain. The initial discontinuity was located at x = 0.385 units so that the sharp discontinuity relaxes to a numerical shock profile before impacting the obstacle.

Results from the current simulations are shown in Figures 5.12, 5.13 and 5.14. Experimental results obtained by Bazhenova et al [20] are shown in Figures 5.12(e) - 5.13(e). Figure 5.12 shows the curved Mach stem, with the reflected and incident shock, just before interacting with the opposite shock system. Both CBM and RBC-RS agree well with each other and also with the experimental results. Figure 5.13 shows the triple point and wake formed after the shock interaction. The contact discontinuities, upper and lower triple points, and the Mach systems are captured well. Although the density contours in Figure 5.14 shows a somewhat wider wake for the CBM approach, there is no other discernable difference between the results. The figures also indicate that the large scale features of the diffraction pattern observed particularly in the wake region appear more prominent for the RBC-RS approach in comparison with CBM method. For a quantitative comparison between the two methods, the bow shock detachment distance over time and the locus of

upper triple point were tracked [20]. Figure 5.15 shows the plots obtained from the current calculations. Figure 5.15(a) predicts a parabolic behavior for the shock detachment distance which is consistent with the numerical results obtained by Ripley et al [149]. The angle, made by the locus of the upper triple point with the horizontal, obtained using the RBC-RS is 31.3^o and that obtained using CBM is 30.5^o. The correlation obtained from experimental observations predicts an angle of 33° [100, 149] which is in close agreement with the current numerical calculation.

5.3.2.3 Diffraction of a Planar Shock Wave Negotiating a Cylindrical Obstacle - LMR Calculations

The shock-cylinder interaction problem is repeated but with dynamic mesh adaptation. The purpose of this example is to investigate the impact of LMR on the final solution, present guidelines for selecting refinement criteria and to validate the proposed RBC-RS approach. To validate the current method, the coefficient of drag (C_D) obtained from the current simulations are plotted against experimental [182] and numerical [53] results (Figure 5.16) for two different shock strengths (Mach 1.3 and 2.6). The simulations were carried out with a base mesh of size $\Delta x = \frac{1}{200}$ with 4 levels of refinement. As is evident from the Figure 5.16, the drag vs time obtained is in good agreement with experimental and numerical predictions. The peak values are predicted accurately for both cases. For the Mach 1.3 shock wave, the trend starts to depart when the shock wave starts to diffract off the lee side of the cylinder, i.e. in the wake region. This is because, in the current computations viscous effects are not taken into account, whereas the numerical predictions

reported in [53] were obtained by solving Navier Stokes equations. Effect of viscosity becomes predominant in the wake region, particularly for shocks of moderate strength. For strongly shocked flows, the drag coefficient C_D is dominated by form drag. This can be verified by comparing the trend observed for the Mach 2.6 case. By doubling the Mach number, the prediction for drag coefficient obtained by solving (inviscid) Euler equations approaches more closely the trend obtained from experimental observations.

High Fidelity Calculation for Mach 2.81 Shock Wave Negotiating a Cylindrical Obstacle:

Next, the diffraction patterns observed for a Mach 2.81 shock wave negotiating a stationary cylindrical obstacle is considered. For this purpose, a fine base mesh of size $\Delta x_g = \frac{1}{300}$ with 4 levels of mesh refinement was selected (an effective resolution of 3 million grid points). δ_1 and δ_2 were set at 10.0 and 250.0 respectively. The results from the current calculations are presented in Figure 5.17. The Mach reflection consisting of the incident shock, the reflected shock, the Mach stem and the slipline are visible in Figure 5.17(a). The slipline emanating from the Mach stem, that was not captured in Figure 5.20, is clearly visible in Figure 5.17(a). In addition, the roll up of slipline is also captured accurately. The curved Mach stem travels down the cylinder and interacts with the shock system from the symmetrical part of the cylinder to form the wake region (Figures 5.17(b), 5.17(c) & 5.17(d)). The enlarged view of the wake regions at two different instants in time are displayed in Figure 5.18. In Figure 5.18(b), the onset of Kelvin-Helmholtz instability in the wake region, that were previously not reported in the literature, can be seen. For the

sake of comparison, the enlarged view of the wake region from a uniform mesh calculation

($\Delta x = \frac{1}{800}$) is presented (Figure 5.18(a)). As can be seen from Figures 5.18(a) & 5.18(b),

the onset of instability is only apparent with sufficiently high mesh refinement. The sub-

sequent development of the instability at a later instant in time (T = 2.4 μs) is shown in

Figure 5.18(d). Figure 5.18(c) shows the enlarged view of the mesh in the wake region at T

= 1.1 μs. The mesh adaptation is excellent and closely follows the delicate contours in the

wake region. The OR computed for this simulation is only 8.7 %. In Figure 5.19, the locus

of upper and lower triple point are plotted with experimental [182] and numerical [53] pre-

dictions. The trends are in excellent agreement. In Figure 5.19(b), a perfect parabolic fit

is obtained which is consistent with the predictions made in [149]. Furthermore, the angle,

made by the locus of the upper triple point with the horizontal is 33° and which is the exact

value reported in the experimental observations in [100].

Computational Time Study:

As the diffraction patterns are rich with features typical of shock-interface interaction

phenomena, the problem is selected as a prototype for performing timing analysis. The

simulations were evolved to time T = 6.28 μs. The refinement criteria for the LMR calcu-

lations were set to $\delta_1 = 10.0$ & $\delta_2 = 25.0$. For a representative measure of computational

time, the percentage CPU time ratio were computed with respect to the CPU time taken by

the uniform fine mesh calculation ($\Delta x = \frac{1}{800}$). The solutions were evolved for 4 different

(3, 4, 5 & 6) levels of mesh refinement while maintaining the size of the fine mesh cells

constant, i.e. $\Delta x_f = \frac{1}{800}$ & $\Delta x_g = \Delta x_f \times 2^{k-1}$ where k is the refinement level. The details

from the current calculations are displayed in Table 5.1.

As is evident from the table, although the OR remains almost constant, the % CPU time increases with increase in the levels of mesh refinement. Particularly for the case with 6 levels of mesh refinement (on a coarse base mesh of size $\Delta x_g = 0.04$), the CPU time is well above 100%. The reason for this increase in CPU time can be attributed to a coarse base mesh used in the calculation, and the interpolations performed over different grid levels at the fine-coarse mesh boundary. Hence, for fast computations with a given OR, the recommended limit on the mesh refinement level is 5. Furthermore, considering speed and accuracy of the calculation, 4 levels of mesh refinement can be chosen as an optimal refinement level.

In Figure 5.20, the LMR-based solution with 6 levels (corresponding to a refinement factor of 32) of mesh refinement (top portion of the figure) are compared with the corresponding fine mesh calculations with $\Delta x = \frac{1}{800}$ (bottom reflected portion of the figure). As can be seen from the figure, the shock locations and the wake regions are resolved accurately. The density contours (Figures 5.20(a), 5.20(c) & 5.20(e)) reveal striking similarity between the two solutions. The numerical Schlieren image (Figure 5.20(f)), indicate that the LMR-based calculation was not able to adequately resolve the slipline (visible in Figure 5.20(d)) in the wake region. Features such as slip lines and other weak structures in the flow domain can be accentuated by suitably tuning the threshhold limit for the refinement criteria. The pressure distribution on the surface of the cylinder are plotted in Figure 5.21. As the interface is always maintained at the finest level, the pressure distribution for different levels of mesh refinement are in excellent agreement with the uniform

mesh solution.

Sensitivity to Refinement Criteria:

Next, the sensitivity of the solution to the refinement criteria is examined. For this purpose, the calculations were repeated on a base mesh of size $\Delta x_g = 0.01$ with 4 levels of refinement. To examine the impact of δ_1 on the solution, simulations were performed for a range of values of δ_1 with δ_2 held constant (at arbitrary large value). A similar approach was adopted to examine the effect of δ_2 on the solution. The two sets of data are presented in Figure 5.22. As is apparent from the figure, with the decrease in the threshold limit, the $L_2(S)$ error decreases with increase in the occupancy ratio. The trend observed with respect to the $L_2(S)$ error for δ_1 & δ_2 are similar. This is because the primary shock systems are resolved with decrease in threshold limit. In contrast, the trend observed with the occupancy ratio differ significantly from one another. This is because, with the decrease in the threshold limit for δ_2, weak features/gradients are accentuated and resolved to the finest level. Thus to balance accuracy and speed of the calculation, the suggested range for the threshold limits, δ_1 and δ_2, are $\delta_1 \Delta x_g \approx (\Delta x_g - \frac{1.0}{\Delta x_g})$ and $\delta_2 \Delta x_g \approx (100\Delta x_g - 2.5\Delta x_g)$ respectively, where Δx_g is the size of the global base mesh.

5.3.2.4 Shock Diffraction over Multiple Cylinders

This test case is considered to demonstrate the ability of the interface treatment methods to handle multiple embedded objects. This example is similar to the previous one except that, in this case there are three asymmetrically placed cylindrical obstacles in the path of a planar shock wave. The cylinders of radius 0.1 units were placed at (0.3,0.3),

(0.35,0.7), and (0.5,0.1) in a 1×1 computational domain with 500 mesh points in each direction. A Mach 3 planar shock was initially positioned at x = 0.19. The results obtained from the current simulations are shown in Figure 5.23. Table 5.2 shows a comparison of CPU time taken by the two methods for one complete time step. Since the simulations were carried out on a fine mesh and due to the presence of multiple embedded objects, the CPU time for this example is a good representation of typical computation time for the problems attempted in the present work. Note that the transformation matrix computed in obtaining the compatibility relation is a function of time and when subject to strong transient shocks, the inherent linearization process assumed in obtaining the characteristic equations does not hold true [133]. As pointed out by Nourgaliev et al [133], these errors can be minimized by employing sub-iterations, i.e. by advancing in a series of small time steps for each RK time iteration. Although the CPU time taken by CBM without sub-iterations and RBC-RS are comparable, the CBM method with sub-iterations takes larger amount of CPU time to converge. Therefore the CBM and RBC-RS methods are comparable in terms of computational time. The choice of RBC-RS is however attractive due to the relative simplicity of implementation of the approach, since one can operate in the primitive-variable Cartesian formulation. Despite the simplicity of formulation and implementation of RBC-RS approach, the results produced by these two methods are in good agreement.

5.3.2.5   Shock Diffraction over Rectangles and Squares

The next example considered is the interaction of a planar shock with a square and rectangular cylinder respectively. Previous attempts to simulate the shock interactions with

rectangular cylinders have been reported by Sun et al [176] and Ripley et al [149]. Both Sun et al and Ripley et al have used unstructured body fitted grids while in the present work the interfaces are embedded in an underlying Cartesian mesh. The problem consists of a Mach 2 shock impinging on a rectangular cylinder with a length to breadth ratio of 4. The cylinders were placed at an angle of 60° (angle made by the minor axis with horizontal). The center of the cylinder was located at (2.75,1.5) in a 7.5X3.3 domain. A 750 X 303 mesh was used and the simulations were run till non-dimensional time T = 3.0. The top and the bottom walls were imposed with reflective boundary condition and the inlet with Dirichlet condition corresponding to a Mach 2 shock. The density contours and numerical Schlieren image obtained from the current simulations are shown in Figure 5.24. Both methods employed are in good qualitative agreement in capturing most of the typical features of shock diffraction phenomena, such as the multiple shock reflections, diffractions, and the vorticity generated due to baroclinic torque [176].

5.3.2.6   Dynamics of a Cylinder Subject to Mach 3 Shock

The first two-dimensional moving boundary problem demonstrated in this work is the dynamics of a cylindrical object subject to a Mach 3 shock. This problem was considered by Falcovitz et al [55] and later by several others [11,61]. The problem consists of a Mach 3 shock impacting a cylindrical object which is initially at rest and located at the bottom of the domain. The subsequent motion of the cylinder results in the cylinder lifting off the lower surface. The motion of the cylinder is computed by integrating the fluid forces acting on the cylinder at each instant. The numerical Schlieren image from

the current calculations are displayed in Figures 5.26(a) & 5.26(b). The locus of the center of mass of the cylinder is shown in Figure 5.26(c) for comparison. Thus, it is clear from Figure 5.26(c) that the numerical predictions of the postion of the cylinder made by the two approaches are in excellent agreement with each other. Furthermore, the numerical Schlieren image displayed in Figures 5.26(a) & 5.26(b) closely follows the trend observed by Forrer et al [61].

Thus, despite of few subtle differences, it can be inferred from the numerical examples shown above that there are no significant discrepancies in the numerical results obtained using CBM and RBC-RS methods. Considering the relative ease of implementation and speed of computation, RBC-RS is preferred over the CBM method. In the following examples, the robustness and versatility of the RBC-RS approach are demonstrated for shocks of different strengths interacting with embedded (stationary and moving) objects of complex shapes and orientations.

5.3.2.7 Double Mach Reflection of a Strong Shock

This is a popular test case and has been used in the past to test the numerical accuracy of several hydrocodes. Extensive discussion on the performance of different shock capturing schemes for this problem can be found in Woodward et al [200]. Pember et al [138] have used this example to test the accuracy of their adaptive refinement method. The problem consist of a Mach 10 shock impacting a ramp. The Ramp is inclined at 30° with the horizontal and located at x = 0.3. The shock, which is initially located at the foot of the ramp, upon impacting the ramp forms a double Mach reflection. Several grid sizes

were considered in the current simulation, and the resulting plot of density variation along the ramp are shown in Figure 5.28. For all grid sizes, the position of the reflected shock and the double Mach reflection formed are in close agreement. The contours of density and the corresponding Schlieren image for this case can be found in Figure 5.27. The results concur well with those obtained by Woodward et al [200] and Pember et al [138].

5.3.2.8 Mach 3 Wind Tunnel with a Forward Facing Step

This example was introduced by Emery et al [54] and since then has been used extensively to test the accuracy of several numerical schemes [200]. A Wind tunnel 3 units long and 1 unit high, has a backward facing step of height 0.2 units, located at 0.6 units from the entrance of the tunnel. The tunnel is continuously supplied with a gas having properties, $\rho = 1.4, u = 3.0, v = 0.0, P = 1.0$ and $\gamma = 1.4$. The presence of the step in the tunnel constricts the flow forming a bow shock, which interacts with the top wall and the horizontal portion of the step forming multiply reflected shock structure. Initially the reflections are regular, but as time elapses these reflections become Mach reflections with Mach stem formed both at the top wall and at the horizontal portion of the step. The slip streams emanating from these Mach stems are subject to Kelvin-Helmoholtz instability which can be captured with sufficiently high mesh resolution. The results from the current simulations are shown in Figure 5.29. The results show the Mach stem along with the slipstreams generated during the shock reflection phenomenon. Also, the numerical Schlieren image show the formation of the Kelvin-Helmoholtz instability. Clearly, as can be seen from plots, with the increase in mesh resolution, the instability becomes more predominant.

5.3.2.9   Shock Diffracting of a Backward Facing Step

A wide range of numerical and experimental data can be found for a shock diffracting around a backward facing step. The resulting shock diffraction pattern consists of features which are self similar and Mach number dependent. For instance, if the post shock flow is supersonic then the reflected supersonic rarefaction wave demarcates the shocked and unshocked region with the reflected wave being on the edge of the Prandtl Meyer expansion wave otherwise the reflected wave forms a smooth transition between the shocked and the unshocked region. For a detailed discussion of the flow features in this system, the reader is directed to Hiver et al [85]. In the current work, we have considered three examples; Mach 1.3 shock, a Mach 2.4 shock and a Mach 20 shock diffracting of a 90° corner. The first two cases can be compared with numerical [149] and experimental [157] results available in literature, while the third case is considered mainly to illustrate the performance of the method in high Mach number flows. The density contours and the corresponding Schlieren images generated from the current simulations have accurately captured the vortex roll up mechanism, the associated Prandtl Meyer expansion waves, the secondary shock wave formed in the diffraction phenomenon and the curved incident shock wave.

5.3.2.10   Mach 2.1 Shock Negotiating a Curved Channel

In this example, a Mach 2.1 shock traverses through a curved channel with a diverging exit. The resulting shock diffraction phenomenon consist of a curved Mach stem, slip line roll up and several other interesting features. The problem has been discussed in detail

by Nourgaliev et al [135] and hence only the results obtained from the current simulations (using RBC-RS approach) are presented here. Interested readers may refer to Nourgaliev et al [135] for additional details. The simulations were carried out with a particle negotiating a curved channel with a prescribed motion [135]. Figure 5.35 shows the numerical Schlieren image and the density contours obtained from the current simulations. As can be readily seen, the results obtained using RBC-RS approach compare very well with that of Nourgaliev et al [135].

5.3.2.11   Mach 3 shock interacting with multiple (120) stationary objects

A Mach 3 shock wave interacting with randomly oriented stationary obstacles is considered. The problem consists of 120 arbitrarily oriented and randomly positioned elliptical and cylindrical obstacles in a 25×6 computational domain. Although the coordinates of the center of mass of the particles were generated randomly, care was taken in placing the particles particularly on the bottom boundary so as to depict a symmetrical problem of 60 particles that are distributed randomly in the x direction. These stationary particles which are immersed in quiescent air, were subject to a Mach 3 shock. As seen from Figure 5.36, the shock after negotiating through these (fixed) obstacles develops a complex diffraction pattern, in addition to the reflected and the transmitted shock wave that emerge from the diffraction pattern. This example demonstrates the potential of the present method for the application to state of the art Direct Numerical Simulations (DNS) of a shock wave traversing through a porous medium or a dusty gas [152, 168].

5.3.2.12   Mach 8 spherical shock interacting with multiple (24) moving objects

The second example considered in this section, is an explosion corresponding to Mach 8 cylindrical shock in the presence of 24 symmetrically positioned particles that are free to move under the influence of the shock wave. Again, due to the symmetry of the problem, only one quadrant of the problem was modeled. As in the example considered in section 5.3.2.6, the velocity of the center of mass of the particles were obtained from a simple force balance. The external fluid force acting on the particles were computed by integrating the pressure force around each particle. The density and size of the particles were (randomly) chosen so that the collisions between the moving particles and with the domain boundaries were averted. Hence collision models, such as in Nourgaliev et al [134], in the presence of shocks were not included in this calculation. Figures 5.37 & 5.38 show a series of numerical Schlieren image and vorticity contours at different instants in time. The initial cylindrical shock, upon interacting with the particles disperse the particles from their initial positions. The cylindrical shock front, after reflecting off the walls of the domain, interacts again but now in the opposite direction to the motion of the particles, thereby slowing the particles.

5.3.2.13   Diffraction Patterns Generated by Supersonic Bluff-body Projectile(s)

Previous investigations [95, 97, 155] on ballistics of projectiles were limited to stationary or moving projectiles with simple square or rectangular shapes that conform with the computational mesh. The experimental and the numerical simulations documented for this problem were focused on the initial unsteady shock wave diffraction phenomena (such

as the blast wave, the jet flow, the vortex ring etc.) generated due to the movement of the projectile at the vicinity of the outlet of the launch tube. In this example, a realistic scenario of a bluff body projectile fired at transonic Mach number (M = 1.22) moving through the mesh (as opposed to solving in a moving coordinate system attached to the projectile) is studied. Attention is paid to the later part of the projectile motion and the resultant diffraction patterns. Configuration of the system and the computational domain are displayed in the Figure 5.39. The simulation was carried out with base mesh of size $\Delta x_g = 0.02$ with 5 levels of mesh refinement. The threshhold for the refinement criteria were set at $\delta_1 = 1.0$ & $\delta_2 = 1.0$.

The numerical Schlieren image along with the mesh topology generated from the current simulations are displayed in Figure 5.40. The initial movement of the projectile results in a series of compression waves that coalesce to form the "bow shock" that stands off from the nose of the projectile (Figure 5.40(a)). The diffraction pattern observed at the rear end of the projectile is similar to that of shock wave negotiating 90° step. Figure 5.40(a) shows the Prandtl-Meyer expansion waves and slip lines generated at the rear end of the projectile. As expected, the slip lines produced eventually roll up to form vortices (vortex rings in this case) that are exemplary of diffraction patterns of shock wave negotiating a 90° step [175]. These vortices are clearly visible in Figure 5.40(b). Figures 5.40(c) & 5.40(d) correspond to the instant at which the projectile has moved sufficiently far away from the launch tube/pad. At the front end of the projectile, the bow shock formed stands off sufficiently far away from the nose of the projectile. At the rear end of the projectile, the baroclinic vortices generated are convected downstream relative to the movement of the

projectile (Figure 5.41(a)). In Figure 5.41(b) the front end bow shock stand-off distance is plotted tracked as a function of time. The shock stand-off distance increases linearly with time for time $T \leq 0.5$ ms and subsequently reaches a steady state value of 0.22 units (0.55 body diameter) which is typical of projectile fired at transonic Mach numbers [1]. Figures 5.40(a) through 5.40(d) indicate that evolution of the mesh closely follows the primary features in the flow field. The occupancy ratio computed for this simulation is 23.25 %.

5.3.2.14   Dynamics of Particles in High Speed Flows

The shock wave processes in particle laden flows are significantly different from the single phase gaseous counterpart, owing to the momentum and energy exchange between the solid and the gaseous phase which modifies the shock wave diffraction pattern. Typical applications include shock interaction and resultant ignition/detonation of solid propellants/explosives [112], explosive dispersion of pollutants and particles [114, 208], hypervelocity thermal spray and coating technologies [51] etc. Previous simulations reported in the literature were limited to heuristic models that predict forces due to planar, and in some cases, spherical shock - (point) particle interactions. The corresponding DNS simulations were restricted to single, stationary or moving particle [53, 90, 153, 174]. In this example, an attempt is made towards DNS simulations of multiple particles interacting with planar and curved bow shocks. The example focuses on determining the dynamics of particles introduced in a (planar) shocked flow, and later impacted by a Reflected Bow Shock (RBS) wave. The configuration of the problem along with the initial location of the

shock are depicted in Figure 5.42. A computational domain of size 10×10 is chosen for the current simulation. A planar shock wave of Mach 2.81 is located at x = 4.75 units. Cylindrical particles with densities 10 times the fluid (air in this case) density are introduced in the post-shocked flow as shown in the Figure 5.42. A stationary bluff body with a semicircular front edge is positioned at the bottom of the domain. The presence of the stationary body generates the RBS wave that later interacts with the oncoming particles. A base mesh of size $\Delta x_g = 0.1$ with 4 levels of refinement are employed for the simulation. The threshold for the refinement criteria were set at $\delta_1 = \delta_2 = 10.0$. The simulation was run to time T = 10.0 ms.

The results from the current simulations are presented in Figure 5.44. The initial motion of the particles is due to the relative velocity between the fluid and the particles. Due to this relative motion, a bow shock wave (with pressure ratios 2.67 for objects 4-5 and 1.86 for objects 1-3) develops that is typical of shock wave interacting with cylindrical/spherical particles. As a result of the development of the bow shock wave, a steep rise in the drag force on the particle is observed. This can be verified from the plots shown in Figure 5.43(c). The trend observed is similar to a shock interacting with single particle. These features are clearly visible in Figure 5.44(a). Also visible in Figure 5.44(a) is the initial stage of the development of the RBS wave and the incident shock wave near the bluff body. The pressure ratio across the RBS wave is about 4.13 which corresponds to a Mach number of 2. At about T = 3.5 ms, particle 1 is initiated by the RBS (Figure 5.43(d)). As can be seen, until the instant at which the RBS impacts particle 1, the $C_D \& C_L$ trends are symmetrical. The impact of the RBS on particle 1 generates a steep increase in the

lift coefficient. Particle 2, which is always under symmetrical loads does not experience any lift force until T = 5.9 ms. This is the instant at which particle 2 is impacted by the RBS. The numerical Schlieren image at this instant is shown in Figure 5.44(b). The figure shows that the vortices generated in the wake regions of particles 1 & 2, are shifted upwards due to the impact of the RBS wave. At the instant shown in the figure, the incident normal shock has passed through the computational domain and hence is not visible in the figure. Figure 5.44(c) corresponds to the instant at which all the particles are impacted by the RBS. The mesh adaptation during this process is apparent from the figures. The OR for this simulation is 22.3 %.

5.3.2.15   Shock Diffraction Patterns in a Dusty Cloud

In this example, the DNS of a planar shock wave traversing through a dusty gas layer is performed. In [56], the problem was investigated by solving the Euler equations using a mixture model. Here the corresponding DNS calculations for two different Mach numbers (1.67 & 3) are performed. The initial configuration of the system is shown in Figure 5.45. A layer of (100) particles, with density $\rho = 1000$, were randomly seeded (Figure 5.45) in a computational domain of size $60mm \times 40mm$. The radius of the particles (d = $0.2mm$) and the mass fraction (M = 0.005) chosen for the current calculations are slightly higher than in [56]. The present computations were performed on a base mesh of size $\Delta x_g = 0.25d$ with 4 levels of mesh refinement (13 points per diameter) resulting in an effective resolution of about 2.45 million grid points. The threshold for the refinement criteria were set at $\delta = 1.0$ & $\delta = 25.0$. Figures 5.46 & 5.47 show the numerical Schlieren

image and vorticity contours for shocks of Mach 1.67 and 3.0 respectively. The inserts show in Figure 5.46 correspond to the enlarged view of the complex shock diffraction and the vortex shedding pattern observed in the wake region. The mesh topology shown in the inserts closely follow the intricate vortices and the shock wave diffraction pattern. The wake patterns shown in Figures 5.46 & 5.47 were not reported in the previous mixture model-based calculations [56]. Furthermore, the effect of viscosity on the wake patterns is an open subject of investigation. It is believed that the current effort is a step towards DNS of such large scale computations. Presently, efforts are underway for large scale computations (with large number of particles ($O(1000)$) with smaller radius ($O(1\ \mu m)$)) and the results will be reported in a separate work.

5.4   Conclusions

The issue of treatment of a rigid solid-fluid interface interacting with strong shock waves was studied. Several approaches for numerical treatment of such interactions were considered and evaluated for a range of test problems. A Riemann solver based GFM approach formulated to resolve the interface dynamics for embedded fluid-fluid interfaces was extended in conjunction with the Reflective Boundary Conditions (RBC) to treat the presence of solid objects in compressible flows. It was shown in the numerical examples that this method was robust, accurate and significantly reduced (but did not entirely eliminate) the over-/under-heating errors at the material interface. Both the Characteristic-Based Matching method (CBM) and the RBC augmented with Riemann correction (RBC-RS) approaches were found to be consistent in generating satisfactory solution for several com-

plex configurations and shock diffraction phenomena, and significantly reduced the shock interaction errors. However, the associated complexity involved in carrying out the characteristic decomposition and the wave analysis in the characteristic space at the interface render the CBM approach less attractive than the RBC-RS approach. Shocks interacting with multiple particles and complex shapes have also been computed.

Ref. Levels	Δx_g	CPU Time (in %)	OR	$L_2(\rho)$
1	0.0025	100	100	-
3	0.005	36.6	46.72	3.918×10^{-5}
4	0.01	39.15	46.1725	4.198×10^{-5}
5	0.02	60.98	47.286	4.746×10^{-5}
6	0.04	163.8	51.88	5.439×10^{-5}

Table 5.1: Timing analysis for a Mach 2.81 shock negotiating a stationary cylindrical obstacle, for different levels of refinement with $\Delta x_f = \frac{1}{800}$.

Interface Treatment Methods	CPU Time ratio
Reflective Boundary Condition With Riemann Solver	1.0
CBM without sub-iterations	1.0483
CBM with five sub-iterations	1.2276

Table 5.2: CPU time taken for one complete (third-order) RK time iteration
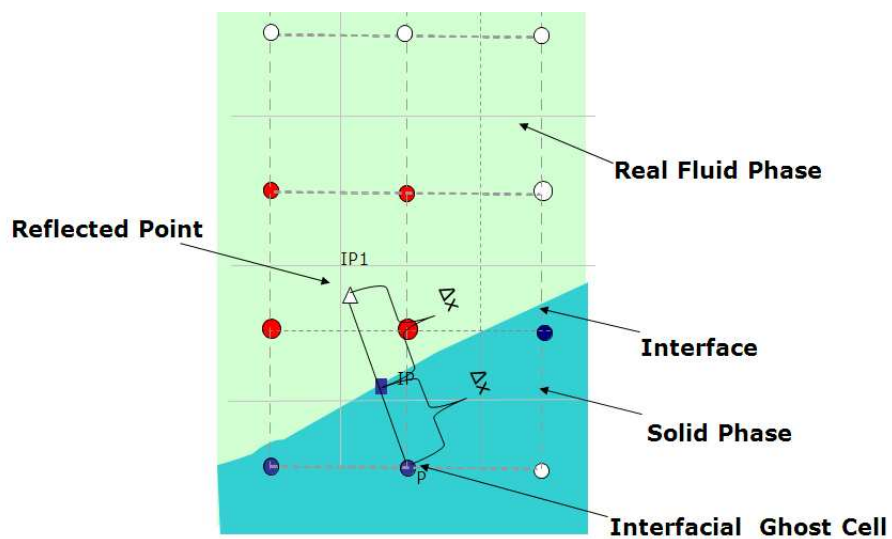
Figure 5.1: Illustration of grid points used in RBC
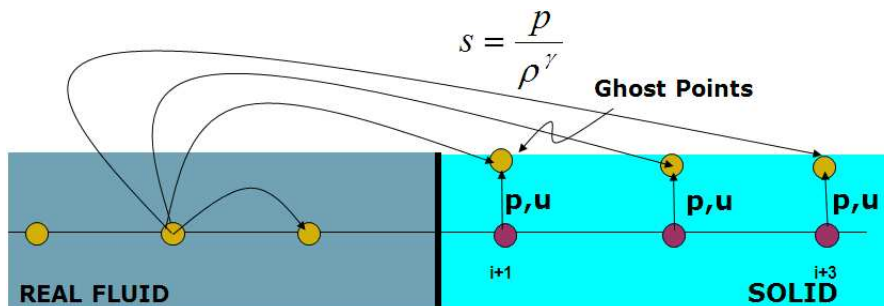
(a) Isobaric fix
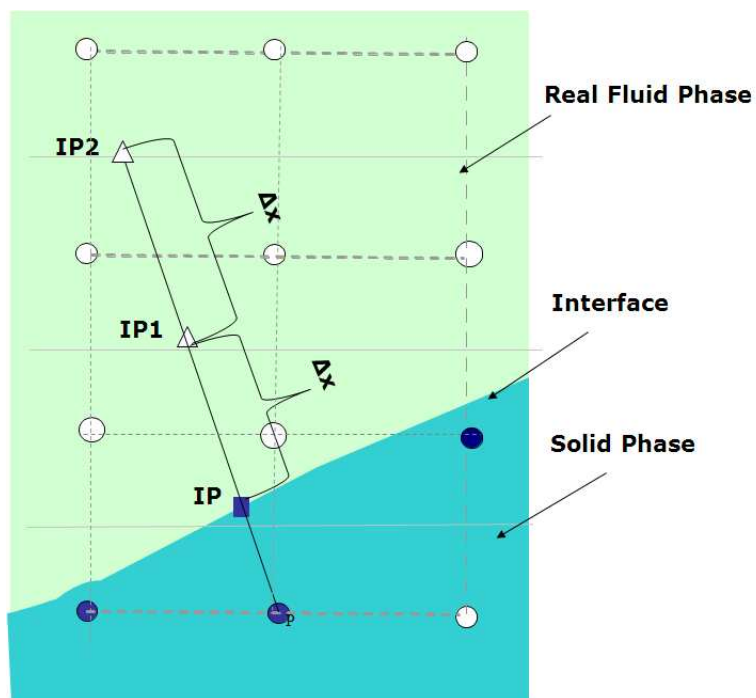
(b) SBC procedure

Figure 5.2: Isobaric fix and the SBC procedure: (a) Simple entropy extrapolation to correct the density field for the interfacial points; (b) Evaluating the normal derivatives at the interface.
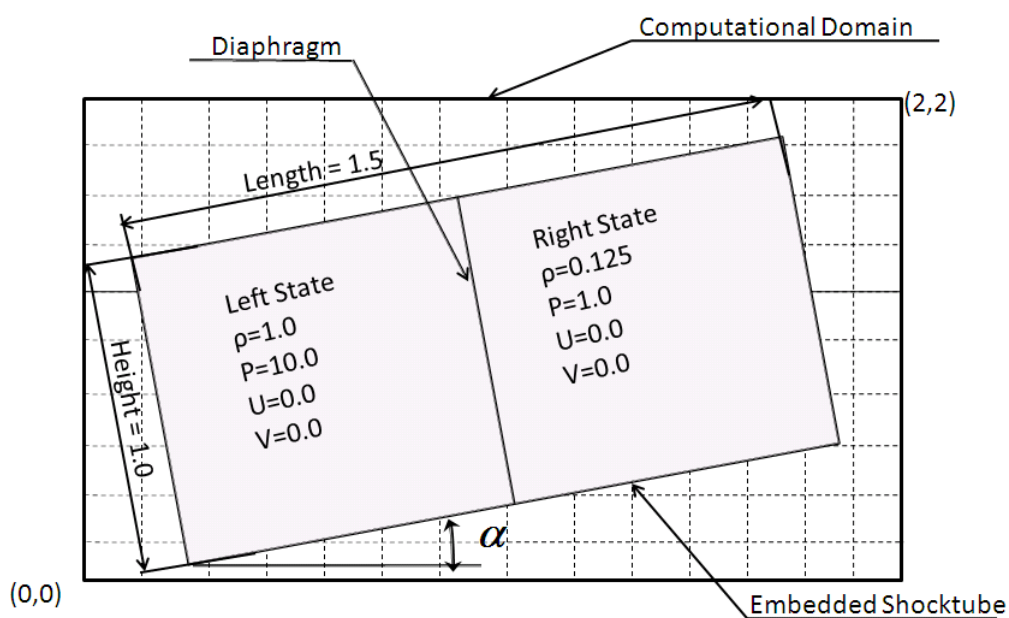
Figure 5.3: Configuration of a rotating shock tube embedded in the computational domain

(a) $\alpha = 30^0$

(b) $\alpha = 45^0$
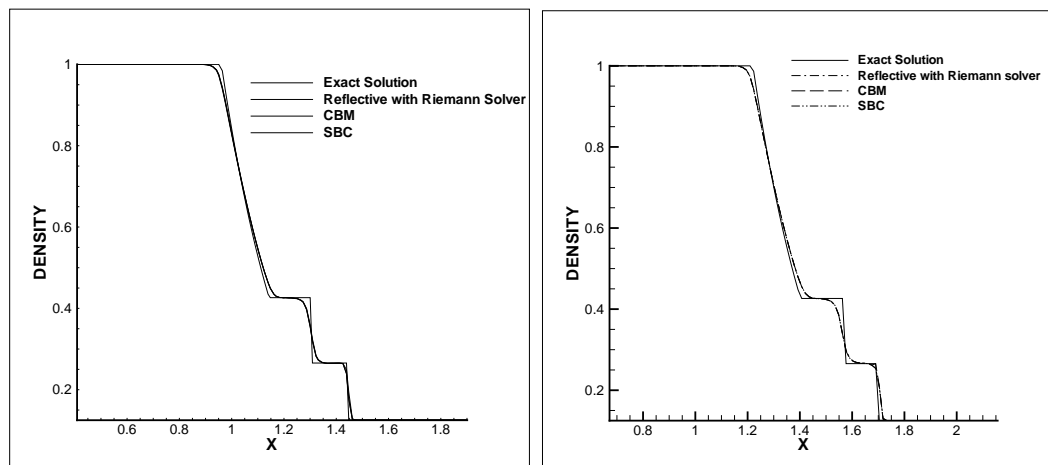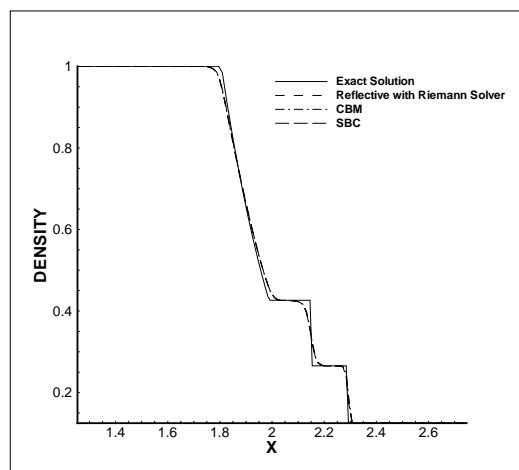
(c) $\alpha = 60^0$

Figure 5.4: Plots of density along the centerline of the shock tube placed at different orientations
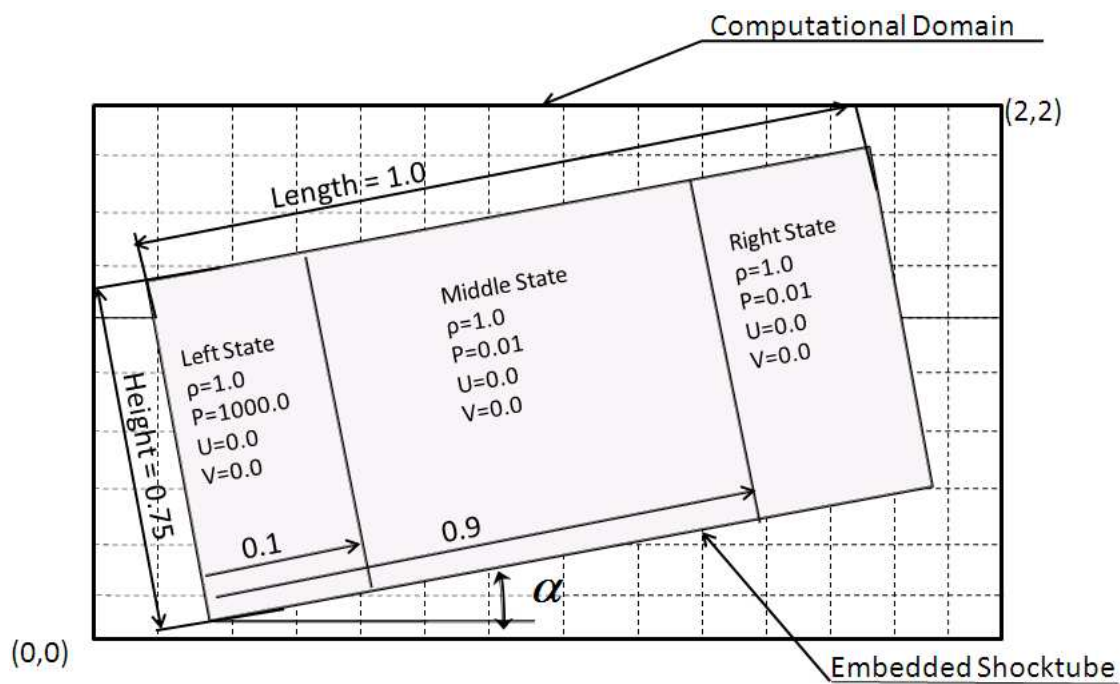
Figure 5.5: Configuration of a rotating shock tube embedded in the computational domain

(a) $\alpha = 30^0$ (b) $\alpha = 60^0$

(c) $\alpha = 30^0$ (d) $\alpha = 60^0$
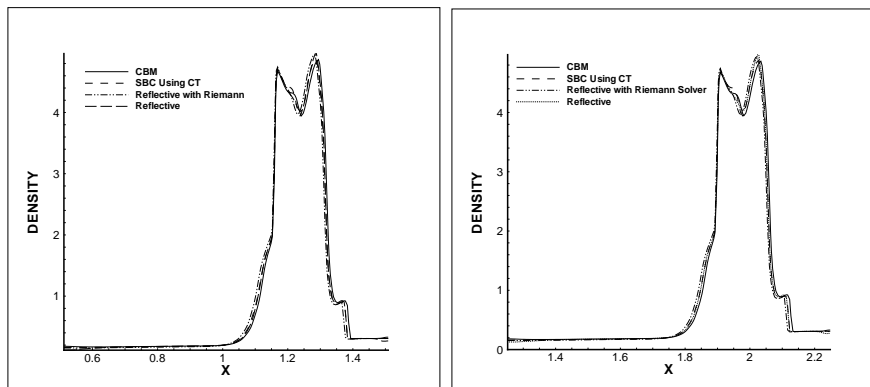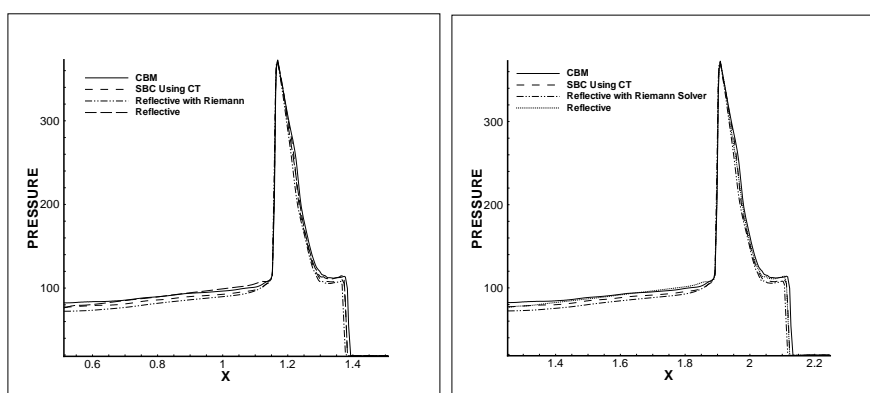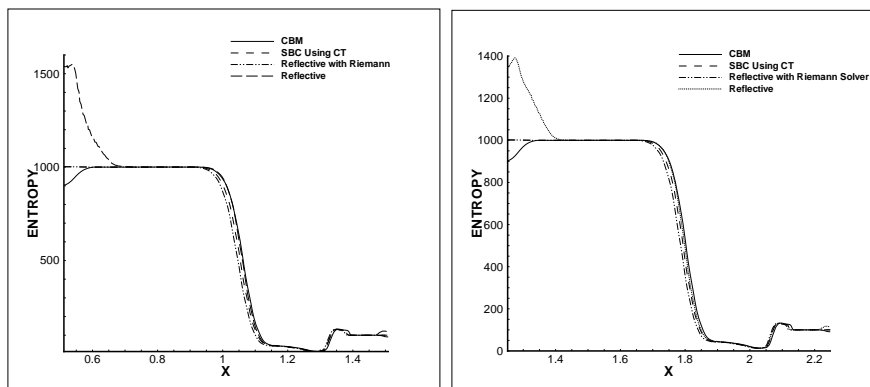
(e) $\alpha = 30^0$ (f) $\alpha = 60^0$

Figure 5.6: Woodward Colella "Bang Bang" Problem: Plots of Density (Figures 5.6(a) and 5.6(b)), Pressure (Figures 5.6(c) and 5.6(d)) and Entropy (Figures 5.6(e) and 5.6(f)) along the centerline for different orientations ($\alpha = 30^0$ on the left and $\alpha = 60^0$ on the right) of the shock tube
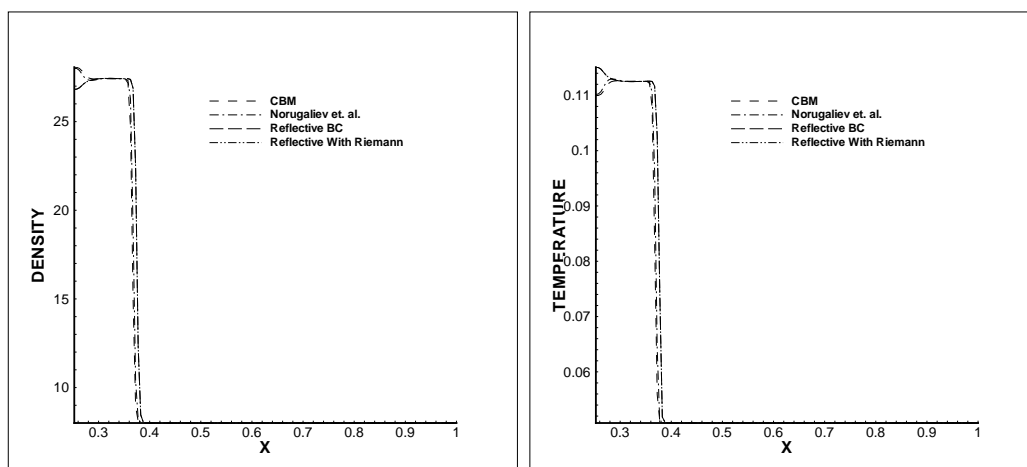
Figure 5.7: Plots of density and temperature for a Mach 10 shock reflecting off a stationary wall
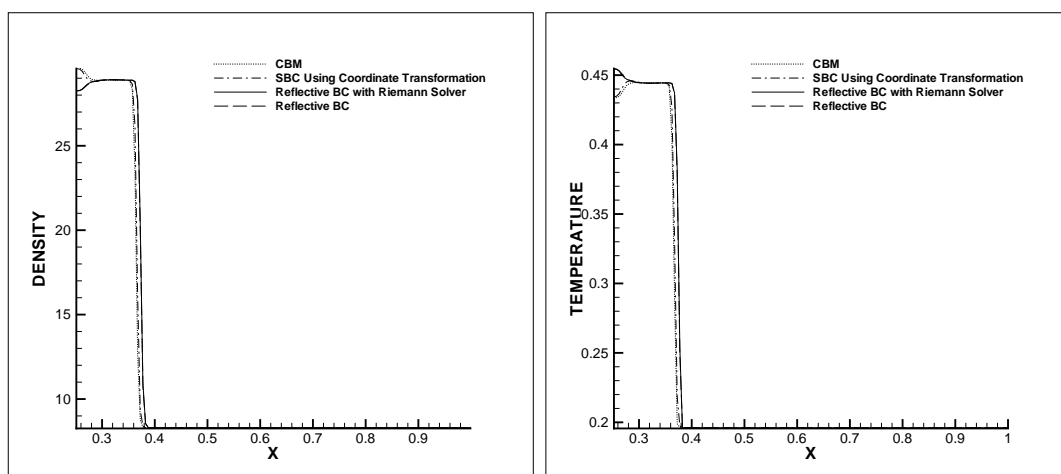
Figure 5.8: Mach 20 shock reflecting off a stationary wall: Plots of density (Figure 5.8(a)) and temperature (Figure 5.8(b))

(a) RBC-RS; T = 1.9

(b) CBM; T = 1.9

(c) RBC-RS; T = 4.9

(d) CBM; T = 4.9

(e) RBC-RS; T = 6.9

(f) CBM; T = 6.9

(g) RBC-RS; T = 8.9

(h) CBM; T = 8.9
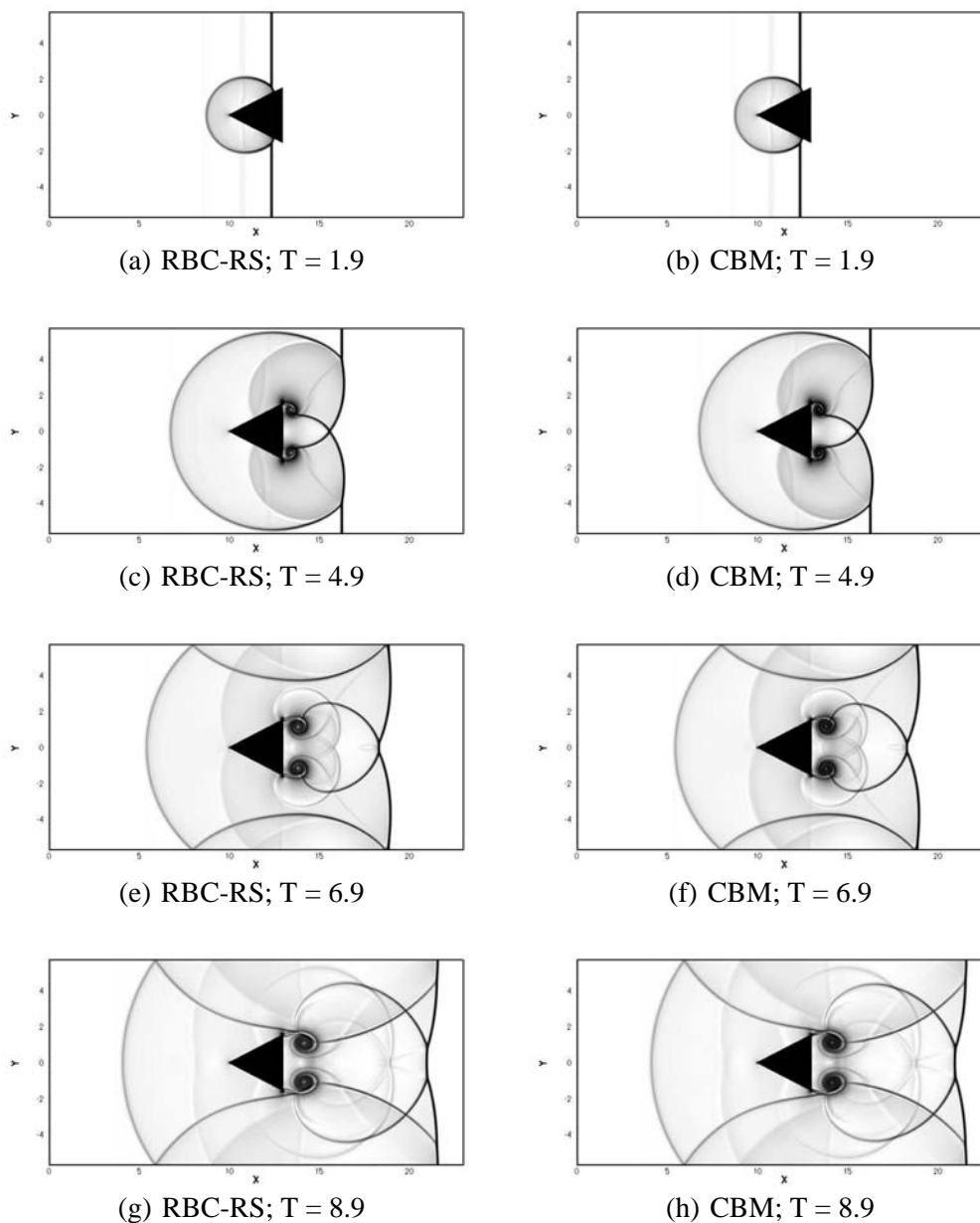
Figure 5.9: Snapshots of numerical Schlieren image of a Mach 1.3 shock diffracting a wedge: Results from RBC-RS are shown in Figures 5.9(a), 5.9(c), 5.9(e) and 5.9(g) and the the corresponding plots obtained from CBM are displayed in Figures 5.9(b), 5.9(d), 5.9(f) and 5.9(h).

(a) RBC-RS T = 1.9

(b) CBM; T = 1.9

(c) RBC-RS; T = 4.9

(d) CBM; T = 4.9

(e) RBC-RS; T = 6.9

(f) CBM; T = 6.9

(g) RBC-RS; T = 8.9

(h) CBM; T = 8.9
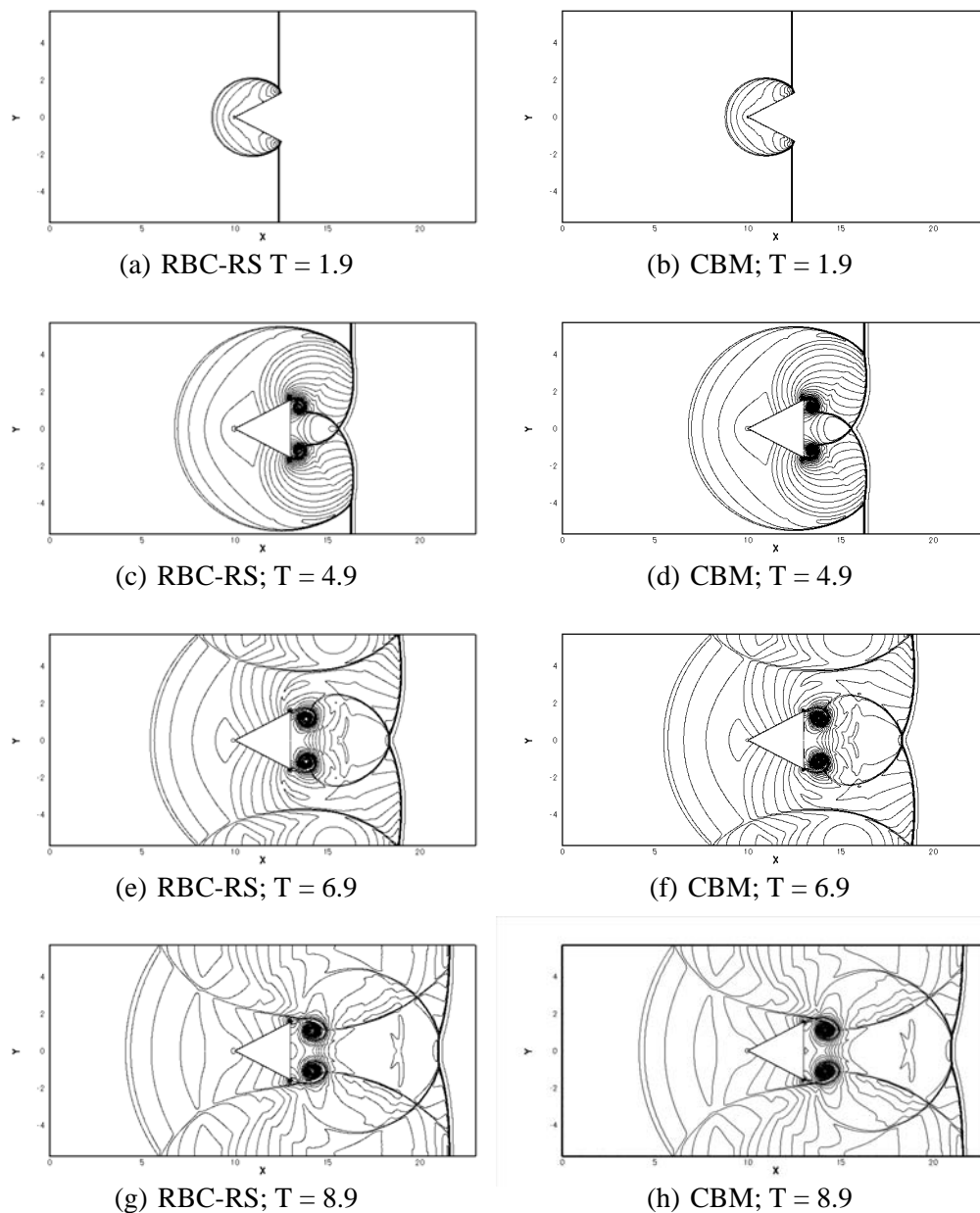
Figure 5.10: Snapshots of density contours of a Mach 1.3 shock diffracting a wedge: Results from RBC-RS are shown in Figures 5.9(a), 5.9(c), 5.9(e) and 5.9(g) and the the corresponding plots obtained from CBM are displayed in Figures 5.9(b), 5.9(d), 5.9(f) and 5.9(h).
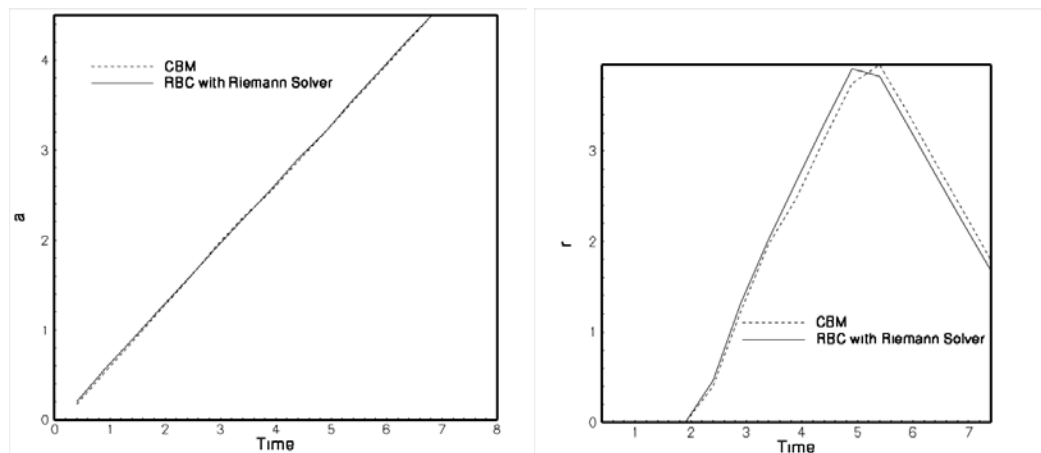
(a) Horizontal shock detachment distance of the reflected bow shock from the foot of the wedge

(b) Vertical distance from the tip of the wedge to the diffracting shock
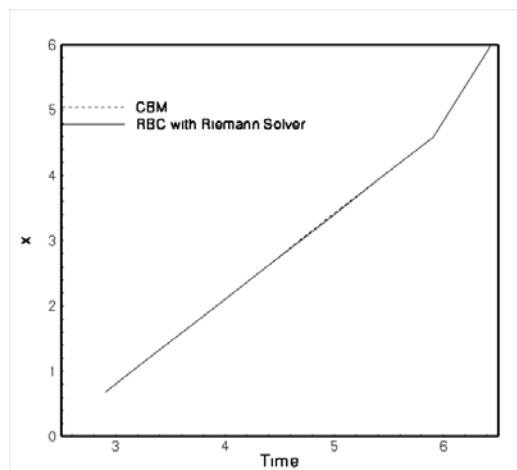
(c) Horizontal distance between the tip of the wedge and the incident shock

Figure 5.11: Comparison of primary shock detachment distance over time between CBM and RBC-RS

(a) Density Contours

(b) Numerical Schlieren Image

(c) Density Contours

(d) Numerical Schlieren Image

(e) Experimental Schlieren Image from Bazhenova et al [20]
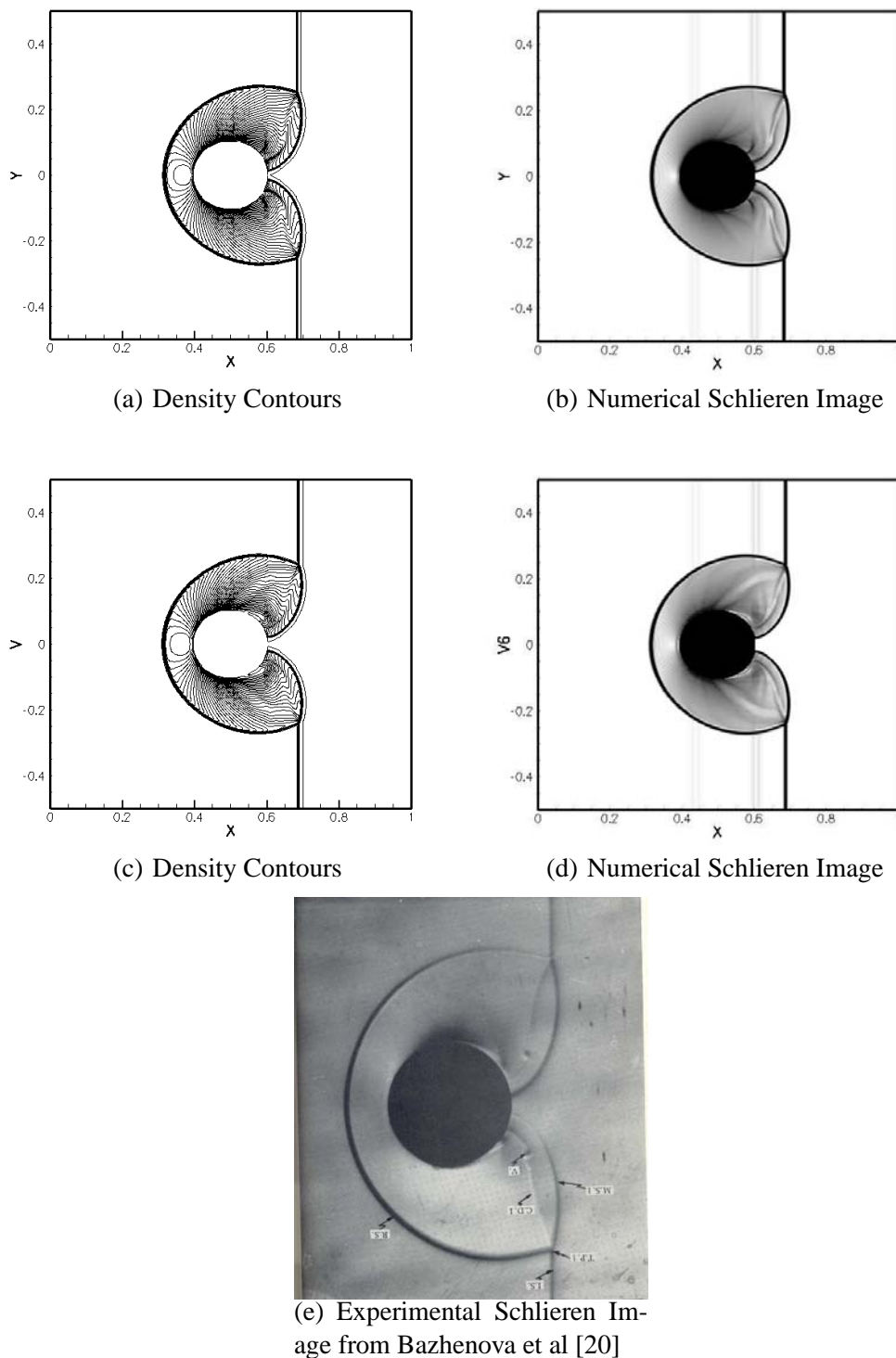
Figure 5.12: Contours of density and corresponding numerical Schlieren image at time T = 0.11: Results from RBC-RS are shown in figures 5.12(a) and 5.12(b) and CBM in 5.12(c) and 5.12(d); Figure 5.12(e) corresponds to the experimental Schlieren image

(a) Density Contours

(b) Numerical Schlieren Image

(c) Density Contours

(d) Numerical Schlieren Image

(e) Experimental Schlieren Image from Bazhenova et al [20]
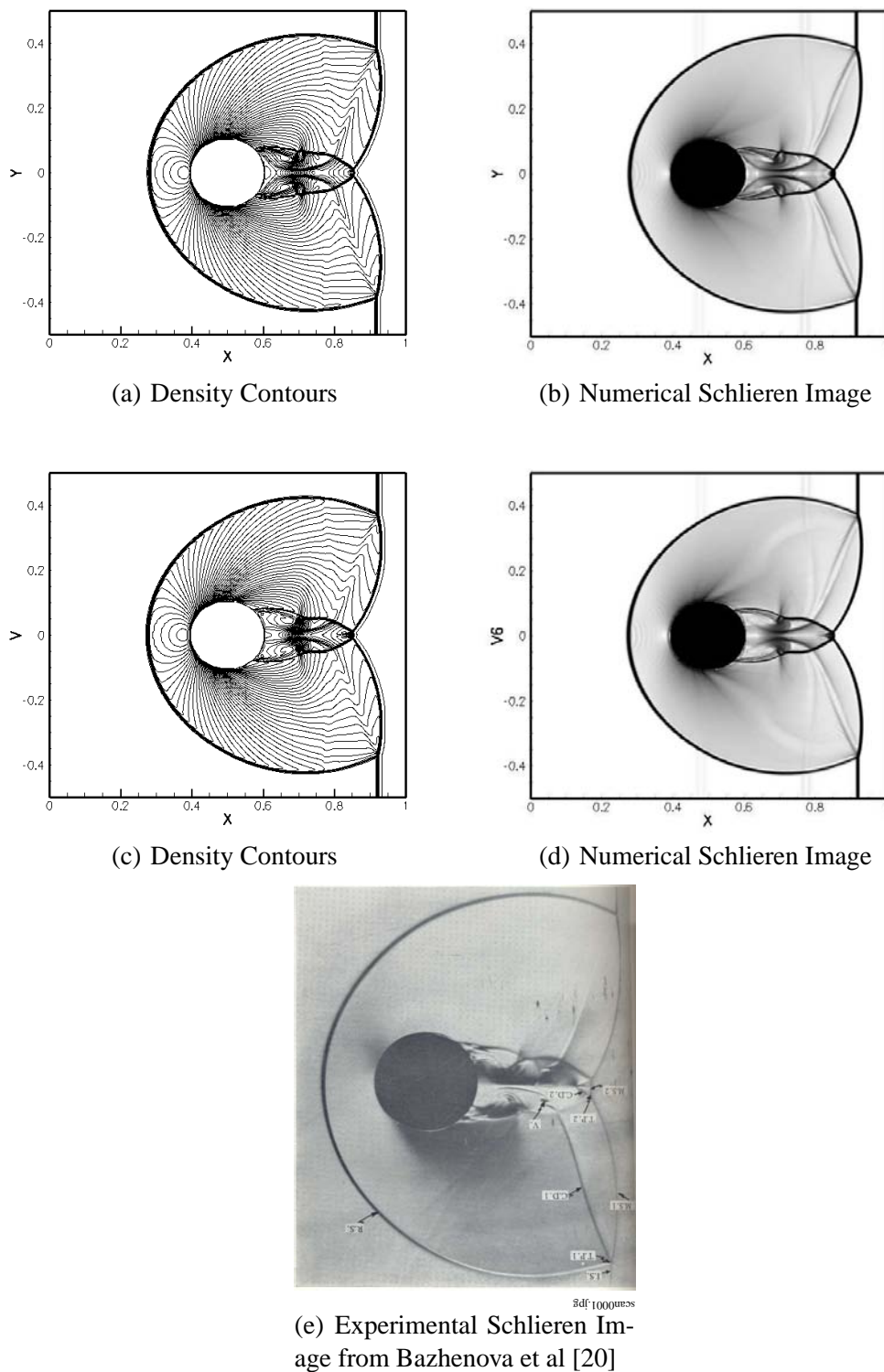
Figure 5.13: Contours of density and corresponding Schlieren image at time T = 0.2: Results from RBC-RS are shown in Figures 5.13(a) and 5.13(b) and CBM in 5.13(c) and 5.13(d); Figure 5.13(e) corresponds to the experimental Schlieren image.

(a) Density Contours

(b) Numerical Schlieren Image

(c) Density Contours

(d) Numerical Schlieren Image
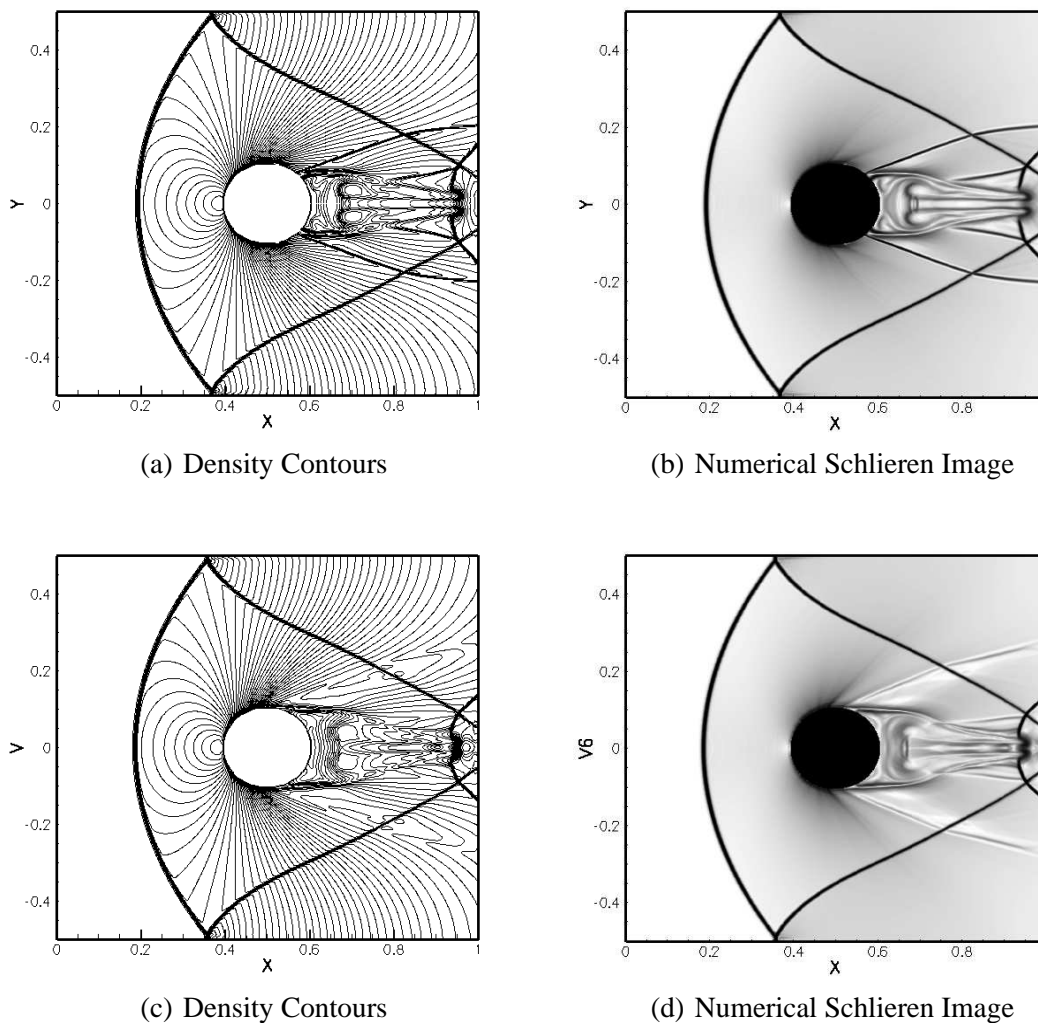
Figure 5.14: Contours of density and corresponding Schlieren image at time T = 0.5: Results from RBC-RS are shown in Figures 5.14(a) and 5.14(b) and CBM in 5.14(c) and 5.14(d)
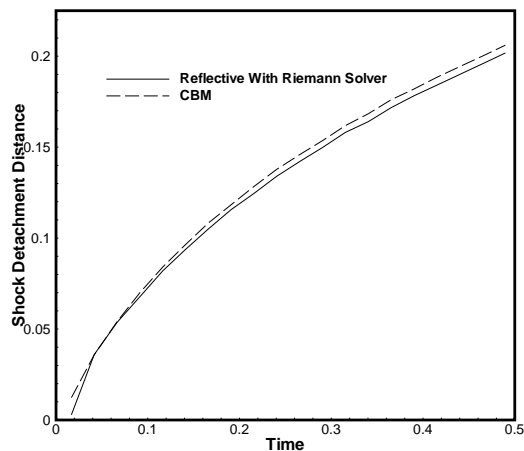
(a) Shock detachment distance vs time
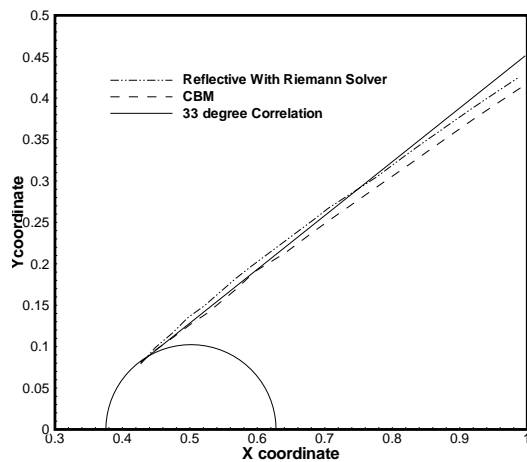
(b) locus of upper ripple point

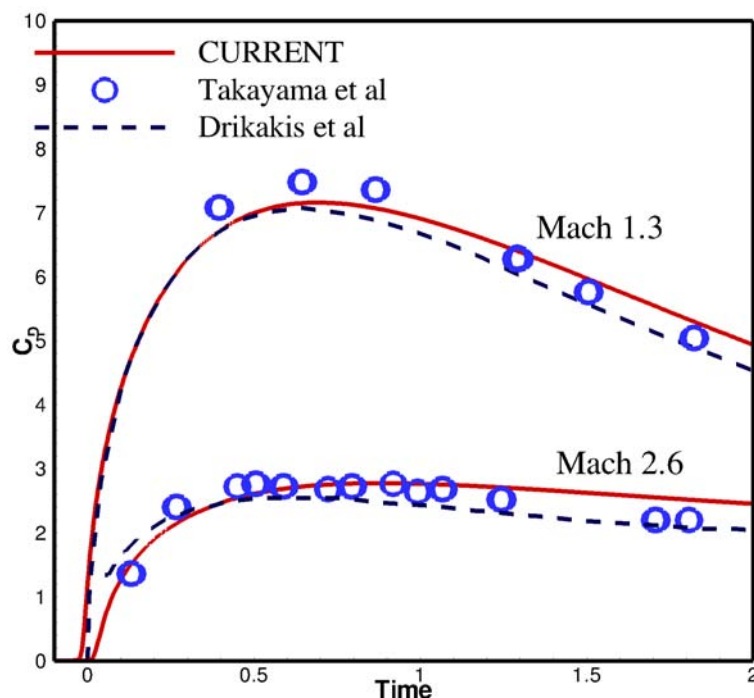Figure 5.15: Comparison between CBM and the RBC-RS : Shock detachment distance vs time (a) and locus of upper triple point (b)

Figure 5.16: Comparison of drag coefficient (C_D) with experimental and numerical predictions, for Mach 1.3 and 2.6 shock waves negotiating stationary cylindrical obstacles. The experimental image was obtained from "Takayama, K. and Itoh, K.,*Unsteady drag over cylinders and aerofoils in transonic shock tube ows*, Proceedings of the 15th International Symposium on Shock Waves and Shock Tubes, Stanford, California, U.S.A., PP 439 485, 1985". The corresponding numerical image was obtained from "D. Drikakis and D. Ofengeim and E. Timofeev and P. Voionovich, *Computation Of Non-Stationary Shock-Wave/Cylinder Ineraction Using Adaptive-Grid Methods*, Journal of Fluids and Structures,11(6),665 - 692,1997".

(a) Numerical Schlieren image at T = 0.314 μs

(b) Numerical Schlieren image at T = 0.612 μs

(c) Numerical Schlieren image at T = 1.1 μs
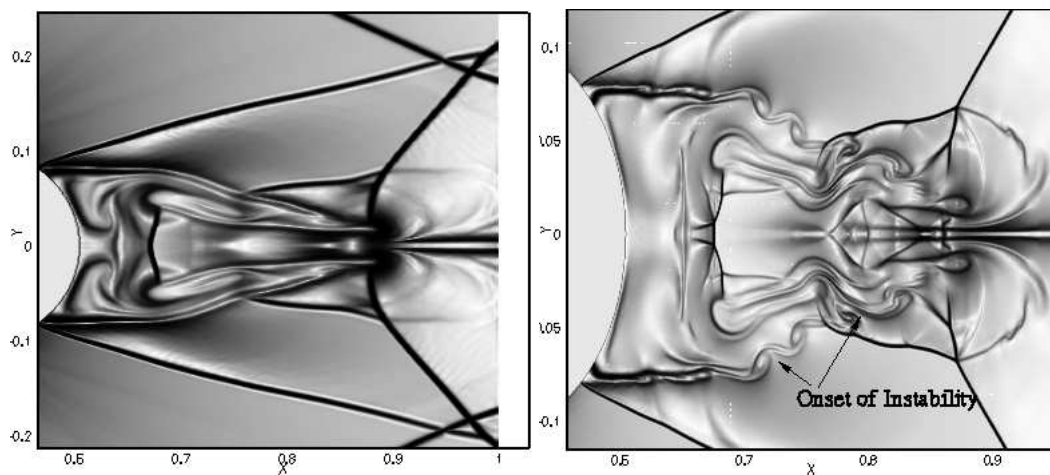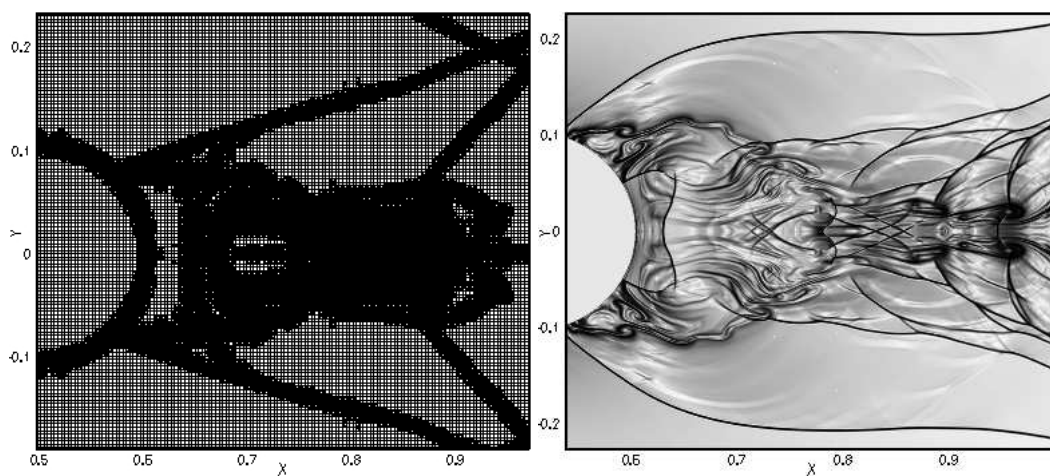
(d) Numerical Schlieren image at T = 2.4 μs
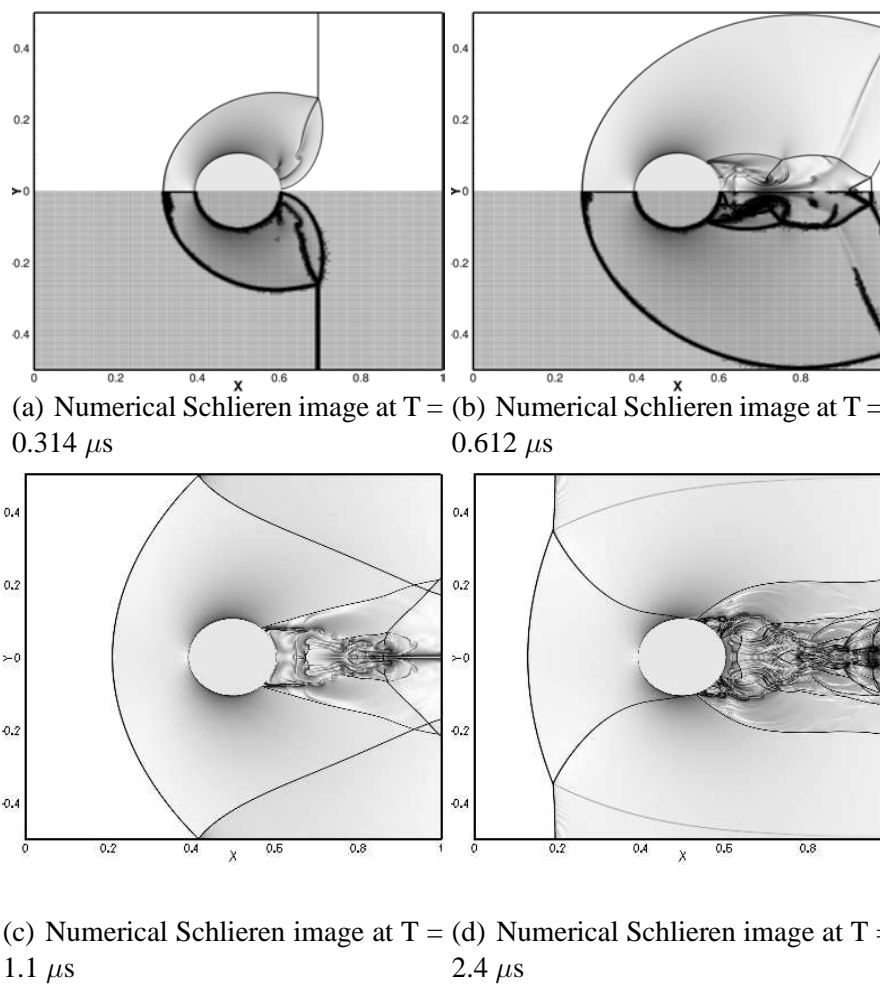
Figure 5.17: Numerical Schlieren image for the solution with 4 levels of mesh refinement on a base of size $\Delta x_g = \frac{1}{300}$ at different instants in time: (a) T = 0.314 μs; (b) T = 0.612 μs; (c) T = 1.1 μs; (d) T = 2.4 μs;

(a) The wake region at T = 1.1 μs (Uniform Mesh Calculation)

(b) The wake region at T = 1.1 μs

(c) The Mesh in the wake region at T = 1.1 μs

(d) The wake region at T = 2.4 μs

Figure 5.18: Enlarged view of the wake region of the numerical Schlieren image at two different instants in time: (a) Uniform mesh calculation with $\Delta x = \frac{1}{800}$ at 1.1 μs; (b) LMR calculation at T = 1.1 μs; (c) Mesh topology in the wake region at T = 1.1 μs; (d) LMR calculation at T = 2.4 μs;

(a) Locus of upper and lower triple point with experimental [182] and numerical [53] predictions

(b) Polynomial Fit
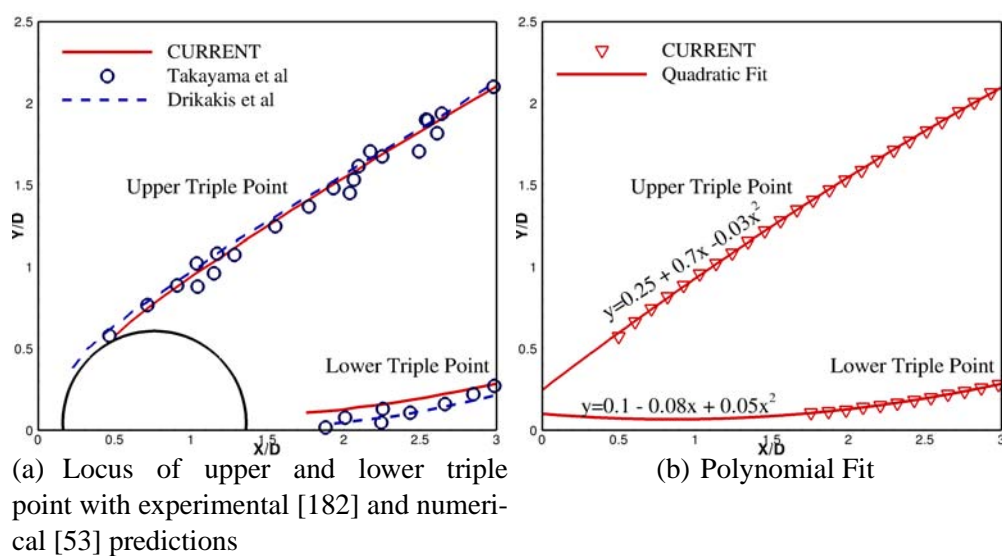
Figure 5.19: Shock-cylinder interaction validation: (a) Comparison of locus of upper and lower triple point (b) A parabolic fit for the locus of the upper and lower triple point
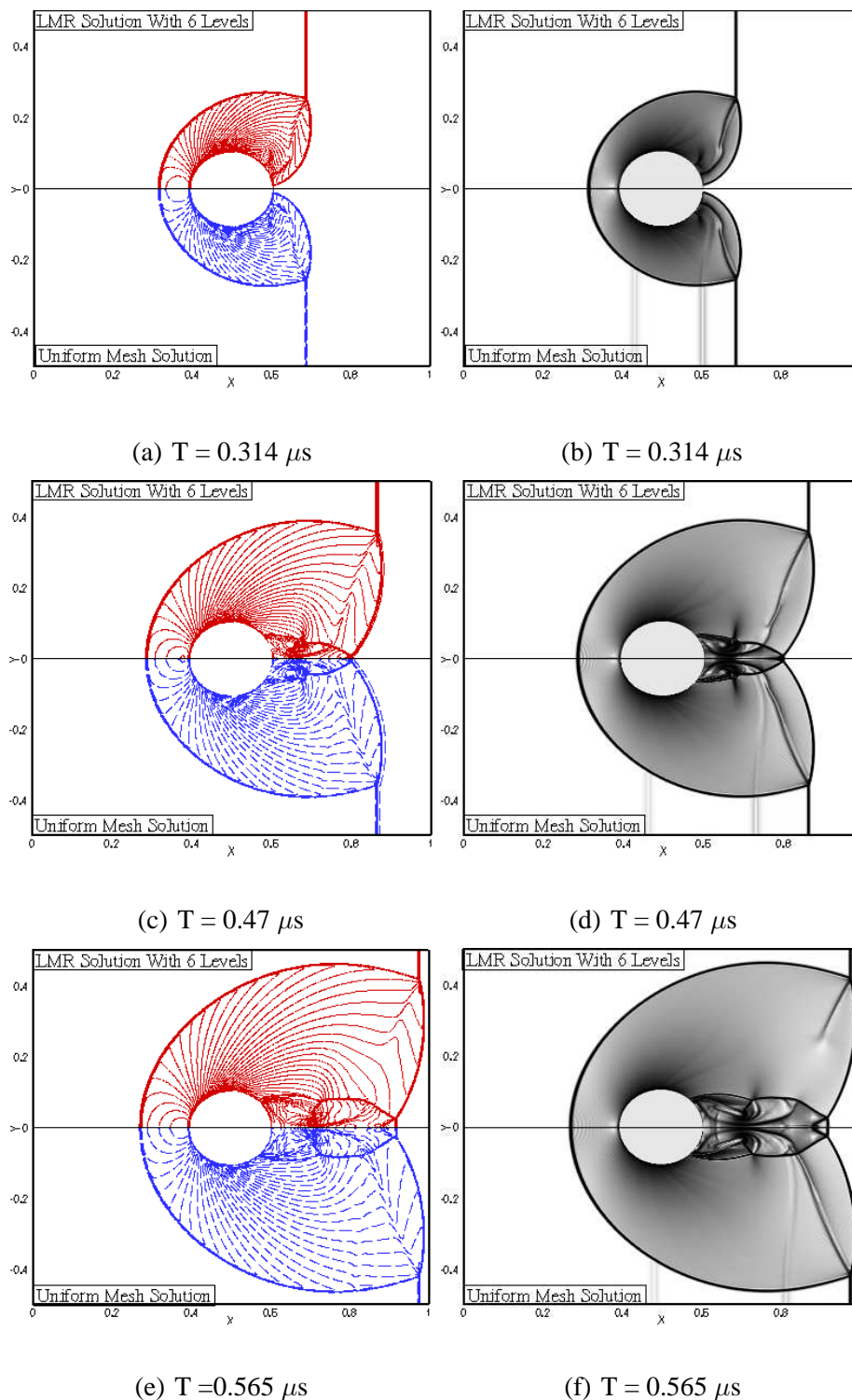
(a) T = 0.314 μs

(b) T = 0.314 μs

(c) T = 0.47 μs

(d) T = 0.47 μs

(e) T =0.565 μs

(f) T = 0.565 μs

Figure 5.20: Comparison of density contours ((a), (c) and (e)) and numerical Schlieren image ((b), (d) and (f)) for LMR-based calculation with 6 levels of mesh refinement, with the uniform fine mesh computations (with $\Delta x = \frac{1}{800}$) at different instants in time: (a) and (b) at T = 0.314 μs, (c) and (d) at T = 0.47 μs and (e) and (f) at T = 0.565 μs
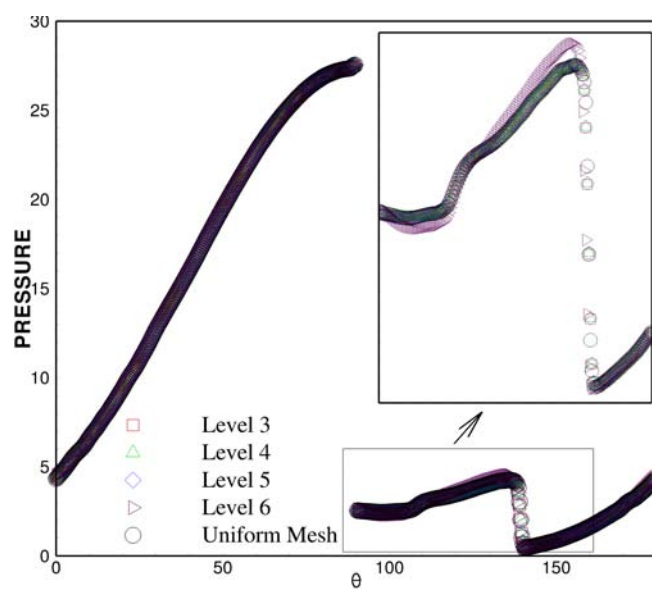
Figure 5.21: Comparison of pressure distribution on the surface of the cylinder for different levels of mesh refinement at time T = 5.65 μs
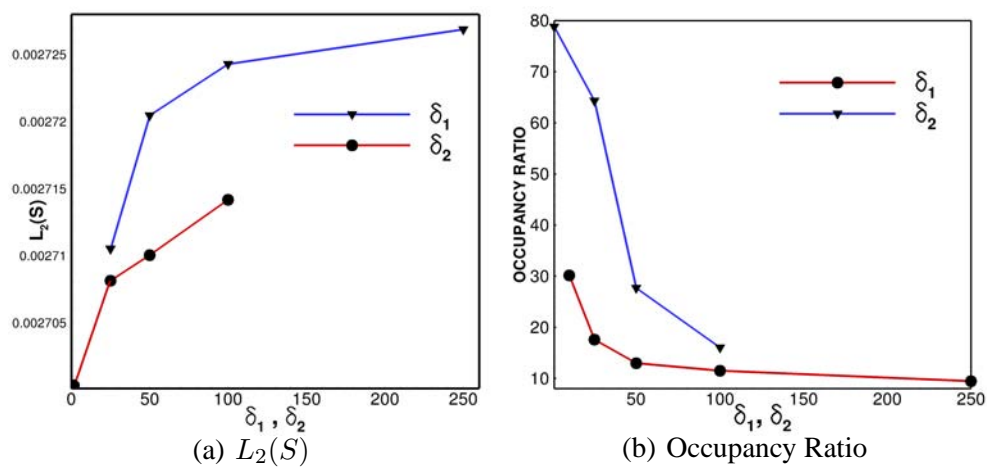
Figure 5.22: Sensitivity of the solution to the refinement criteria: (a) $L_2(S)$ for entropy (b) % Mesh occupancy ratio

(a) RBC-RS; T = 0.09

(b) CBM; T = 0.09

(c) RBC-RS; T = 0.125
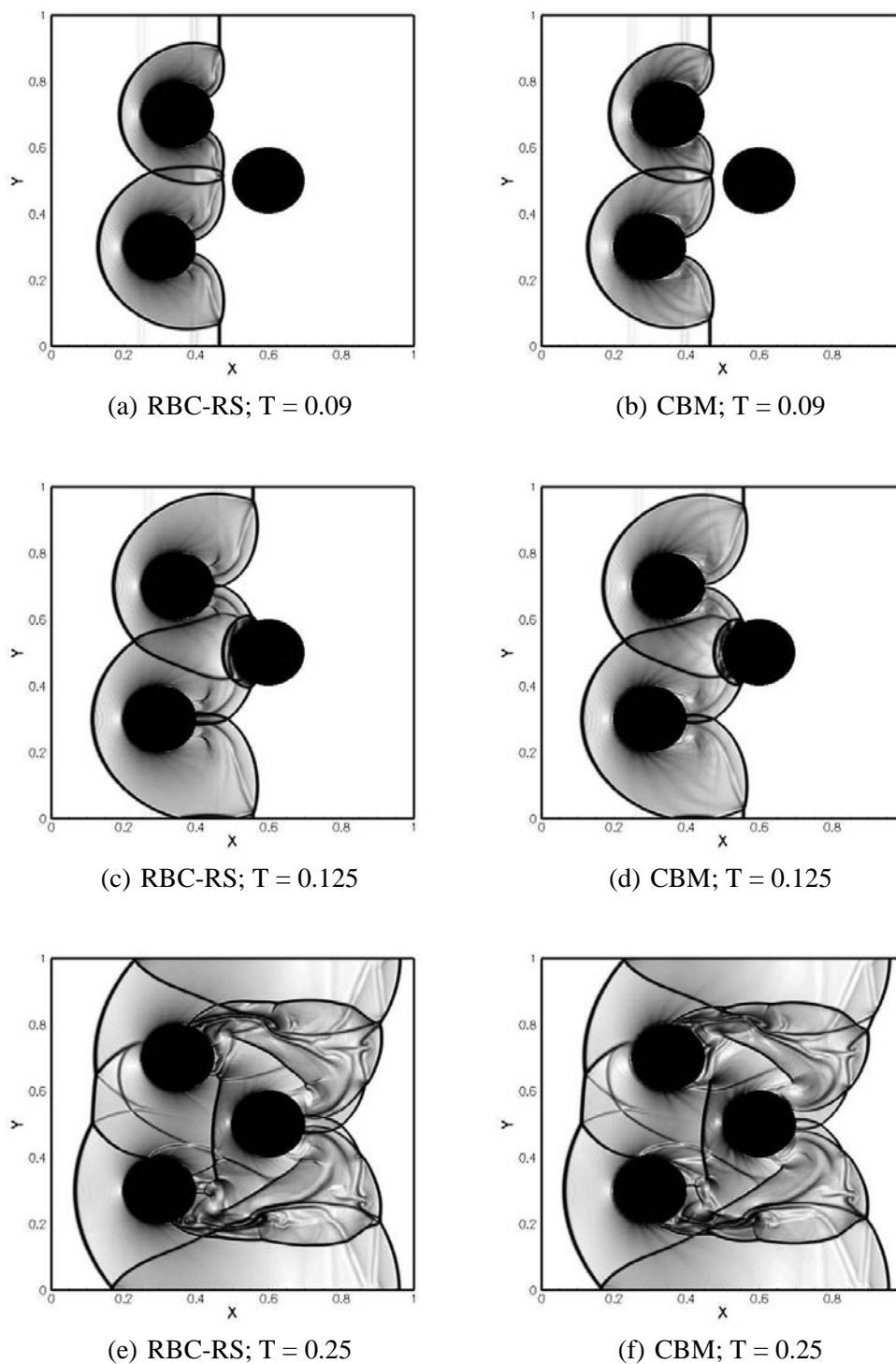
(d) CBM; T = 0.125

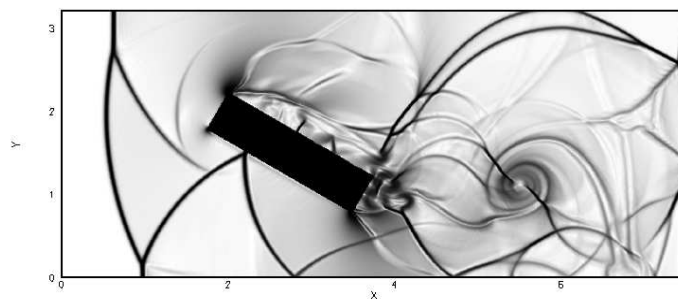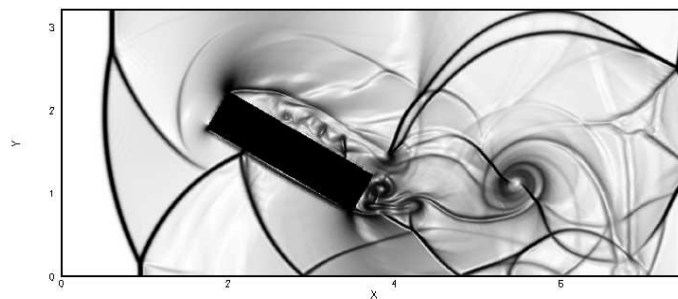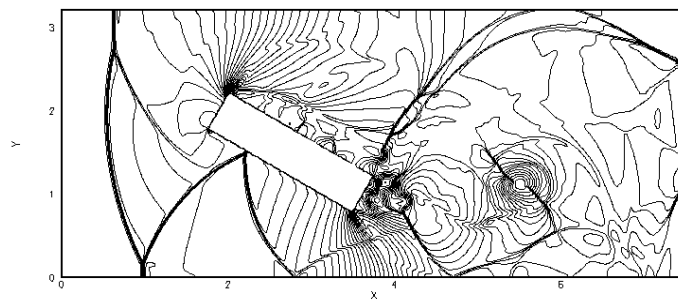(e) RBC-RS; T = 0.25

(f) CBM; T = 0.25

Figure 5.23: Snapshots of numerical Schlieren image for a Mach 3 shock interacting with multiple stationary cylinders at different instants in time: Results from RBC-RS are shown in Figures 5.23(a), 5.23(c) and 5.23(e) and the corresponding plots for the CBM approach are displayed in Figures 5.23(b), 5.23(d) and 5.23(f).
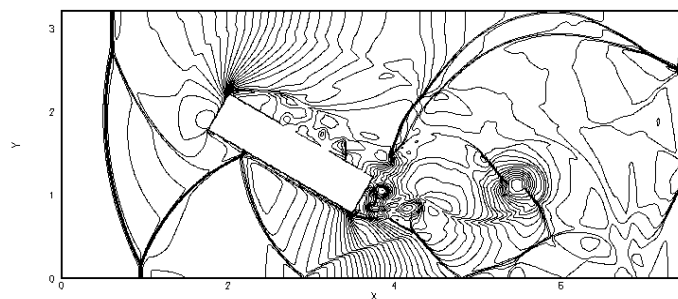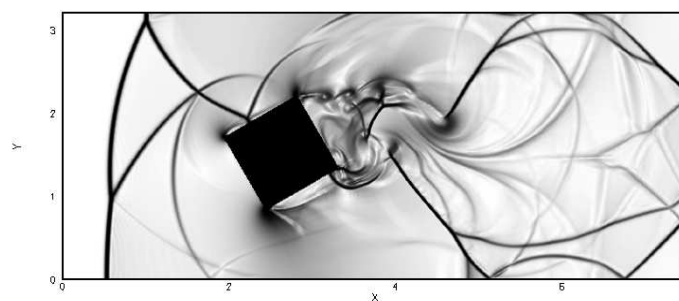
(a) RBC-RS
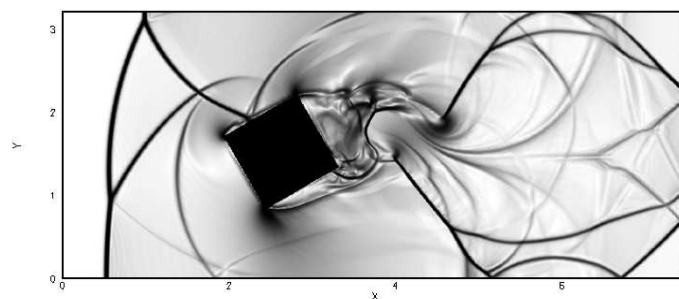

(b) CBM

(c) RBC-RS

(d) CBM

Figure 5.24: Mach 2 shock interaction with a square inclined at 60° with the horizontal: Figures (a) and (c) correspond to numerical Schlieren image and figures (d) and (e) correspond to the density contours

(a) RBC-RS
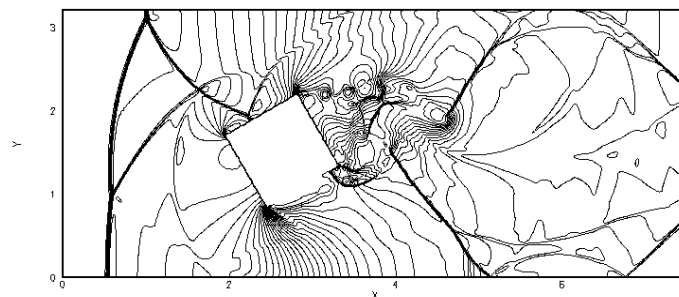

(b) CBM

(c) RBC-RS

(d) CBM

Figure 5.25: Mach 2 shock interaction with a square inclined at 60° with the horizontal: Figures (a) and (c) correspond to numerical Schlieren image and figures (d) and (e) correspond to the density contours
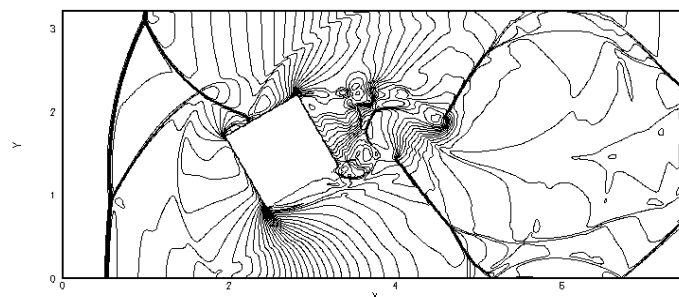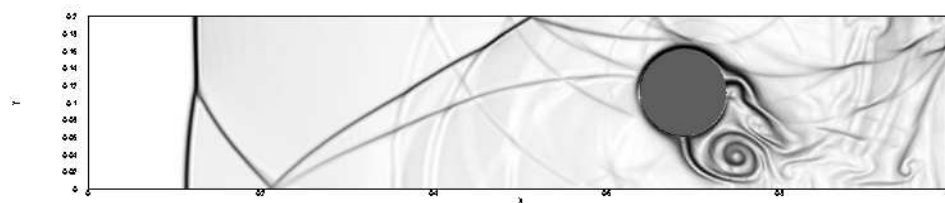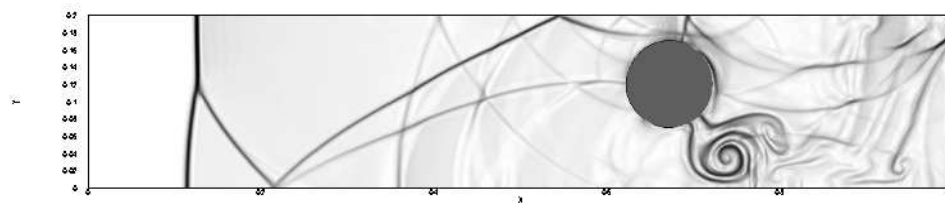
(a) RBC-RS

(b) CBM
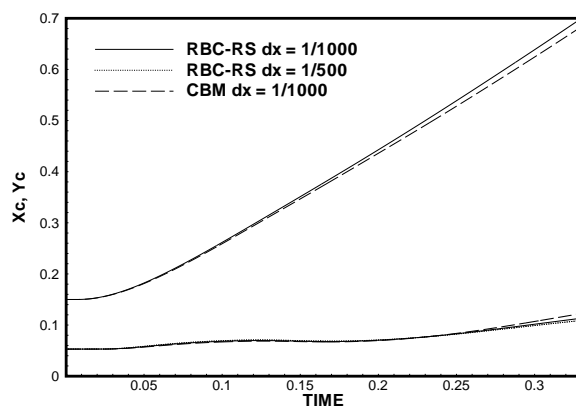
(c) Locus of center of mass as a function of time

Figure 5.26: Cylinder subject to Mach 3 shock: Numerical Schlieren image (RBC-RS in Figure 5.26(a) and CBM in Figure 5.26(b)) and locus of center of mass (Figure 5.26(c))
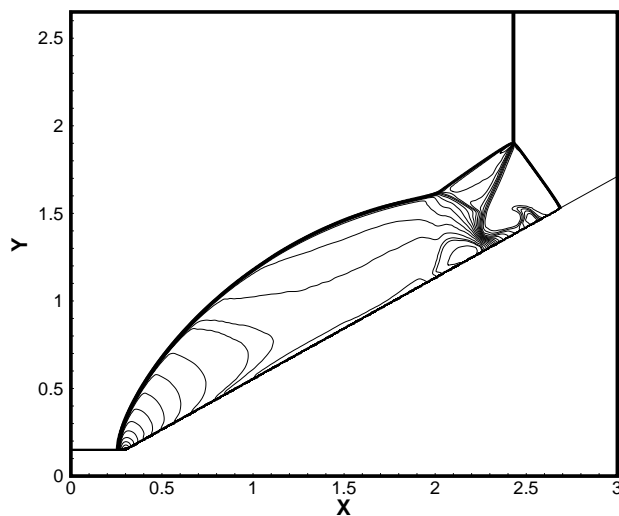
(a) Density contours at T = 0.22
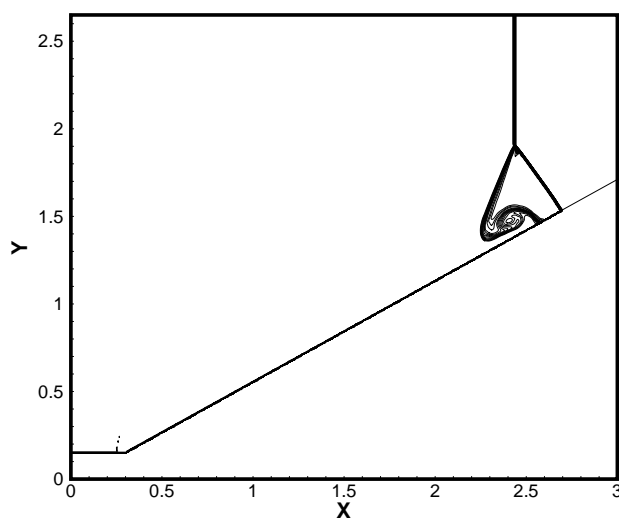
(b) Entropy Contours at T = 0.22

Figure 5.27: Mach 10 shock interacting with a 30° ramp at T = 0.22: Contours of (a) density and (b) entropy.
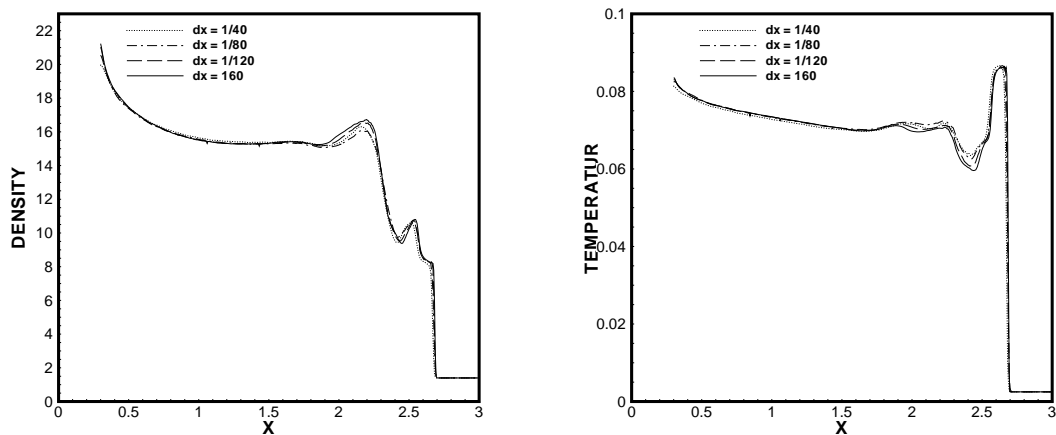
(a) Density

(b) Pressure
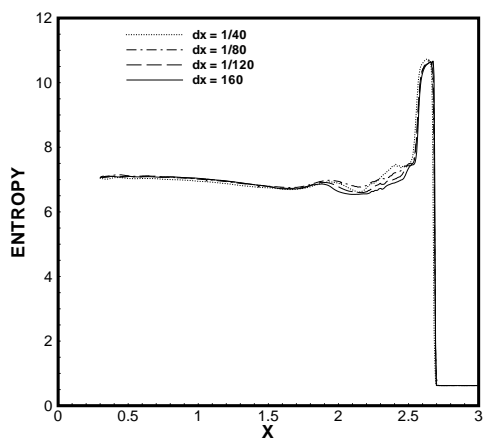
(c) Entropy

Figure 5.28: Grid refinement study - (a) Density, (b) Pressure and (c) Entropy plots along the ramp at T = 0.22

(a) Density contours for $\Delta x = \frac{1}{120}$

(b) Numerical Schlieren image for $\Delta x = \frac{1}{120}$

(c) Density contours for $\Delta x = \frac{1}{160}$

(d) Numerical Schlieren image for $\Delta x = \frac{1}{160}$

(e) Density contours for $\Delta x = \frac{1}{240}$

(f) Numerical Schlieren image for $\Delta x = \frac{1}{240}$

(g) Density contours for $\Delta x = \frac{1}{300}$

(h) Numerical Schlieren image for $\Delta x = \frac{1}{300}$
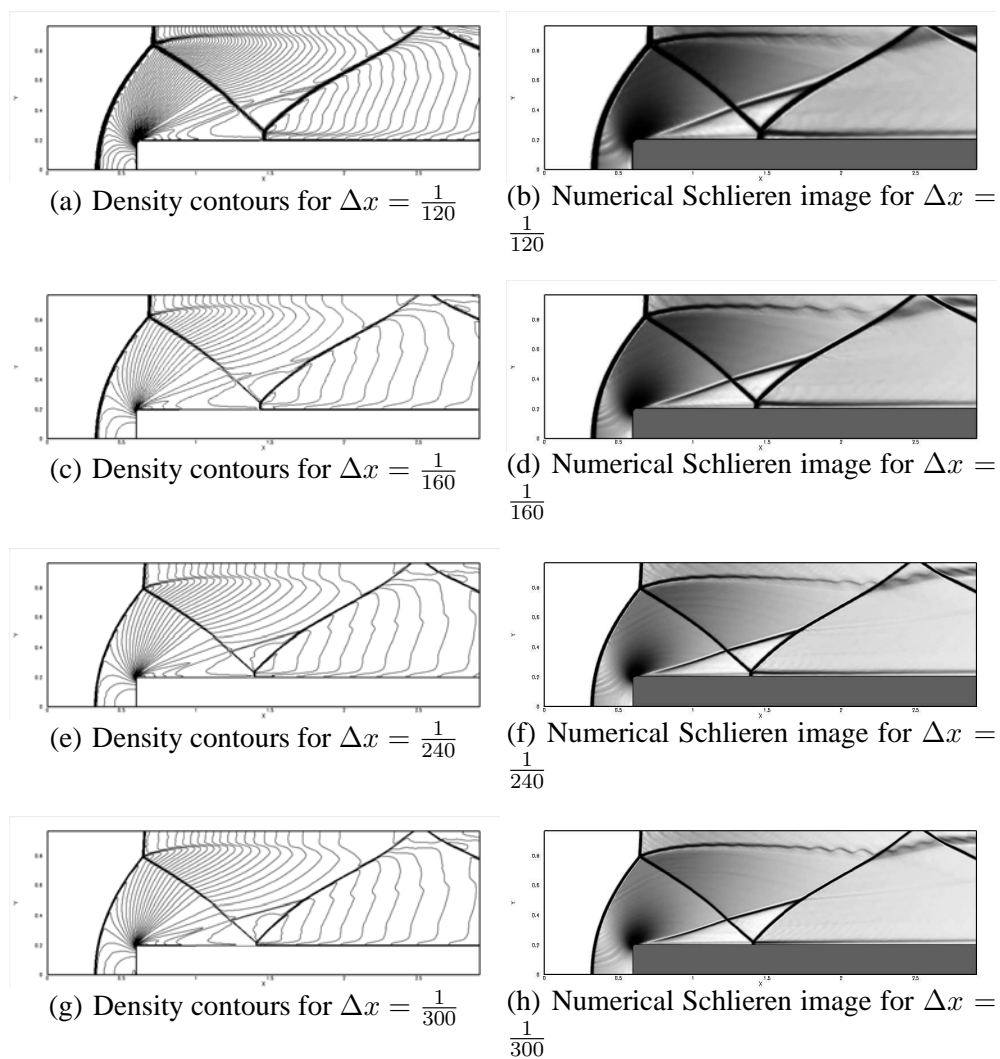
Figure 5.29: Mach 3 wind tunnel with a backward facing step: Density contours ((a), (c) and (e)) and numerical Schlieren image ((b), (d) and (f))
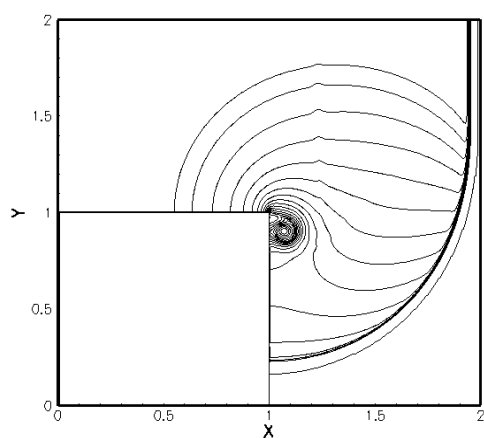
(a) Density Contours
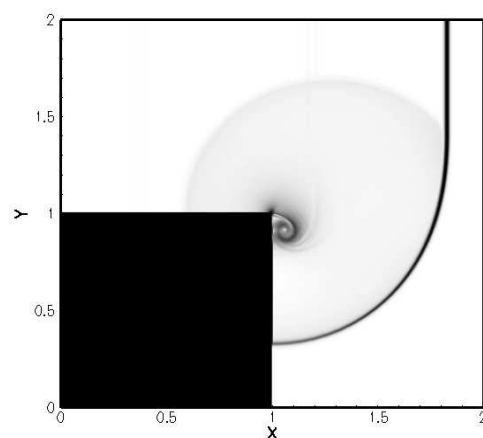
(b) Numerical Schlieren Image Contours
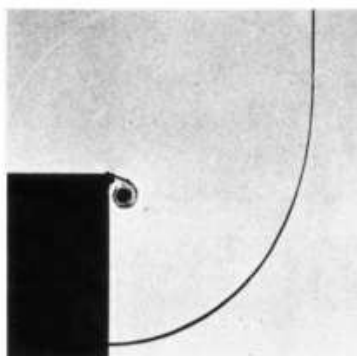
(c) Experimental Schlieren Image

Figure 5.30: Mach 1.3 shock diffracting a 90° corner: (a) Density contours, (b) numerical Schlieren image and (c) experimental Schlieren image
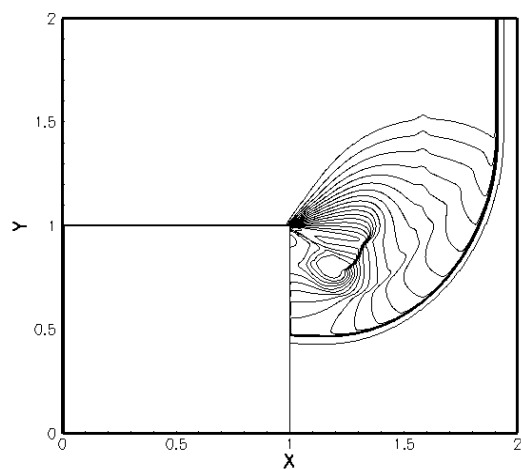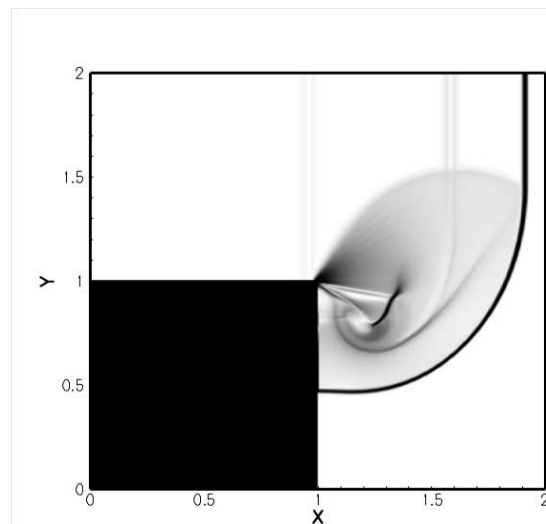
(a) Density contours

(b) Numerical Schlieren Image
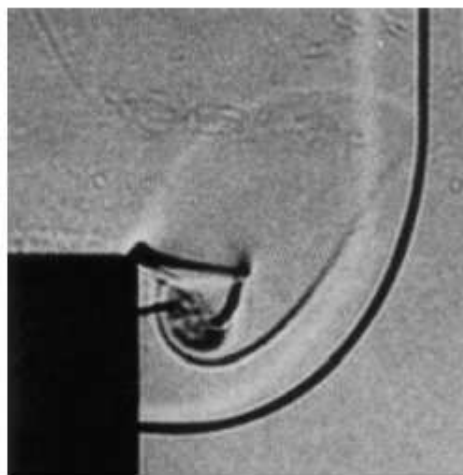
(c) Experimental Schlieren Image

Figure 5.31: Mach 2.4 shock diffracting a 90° corner: (a) Density contours, (b) numerical Schlieren image and (c) experimental Schlieren image

(a) Density contours

(b) Numerical Schlieren Image
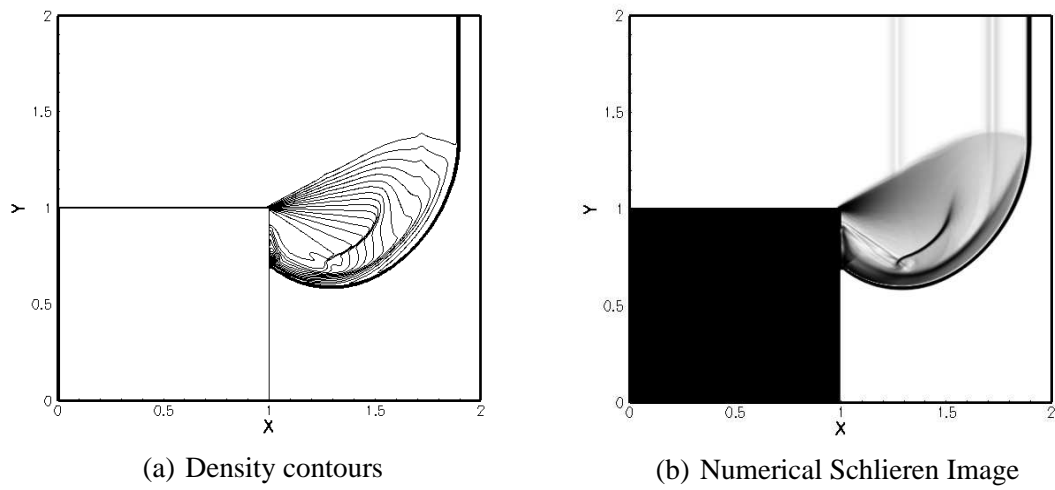
Figure 5.32: Mach 20 shock diffracting a 90° corner: (a) Density contours and (b) numerical Schlieren image
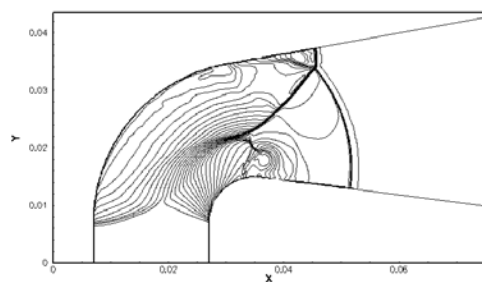
(a) Density contours at T = 0.0205
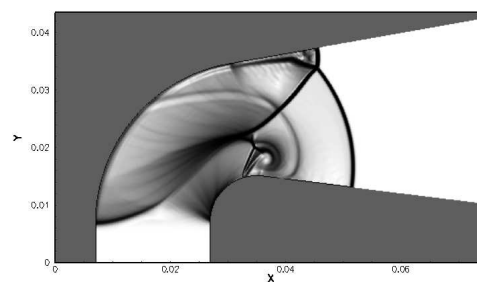
(b) Numerical Schlieren image at T = 0.0205
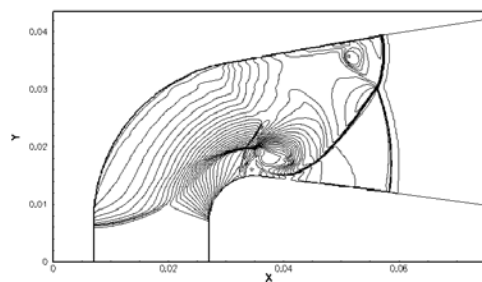
(c) Density contours at T = 0.035
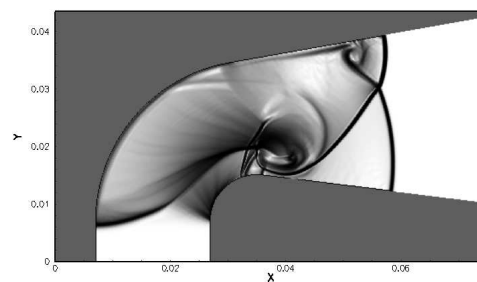
(d) Numerical Schlieren image at T = 0.035

Figure 5.33: Mach 2.1 shock negotiating a curved channel without obstacles: Density contours ((a) and (c)) and numerical Schlieren image ((b) and (d)) at two different instants in time

(a) Density contours at T = 0.0156

(b) Numerical Schlieren image at T = 0.0156

(c) Density contours at T = 0.035

(d) Numerical Schlieren image at T = 0.035
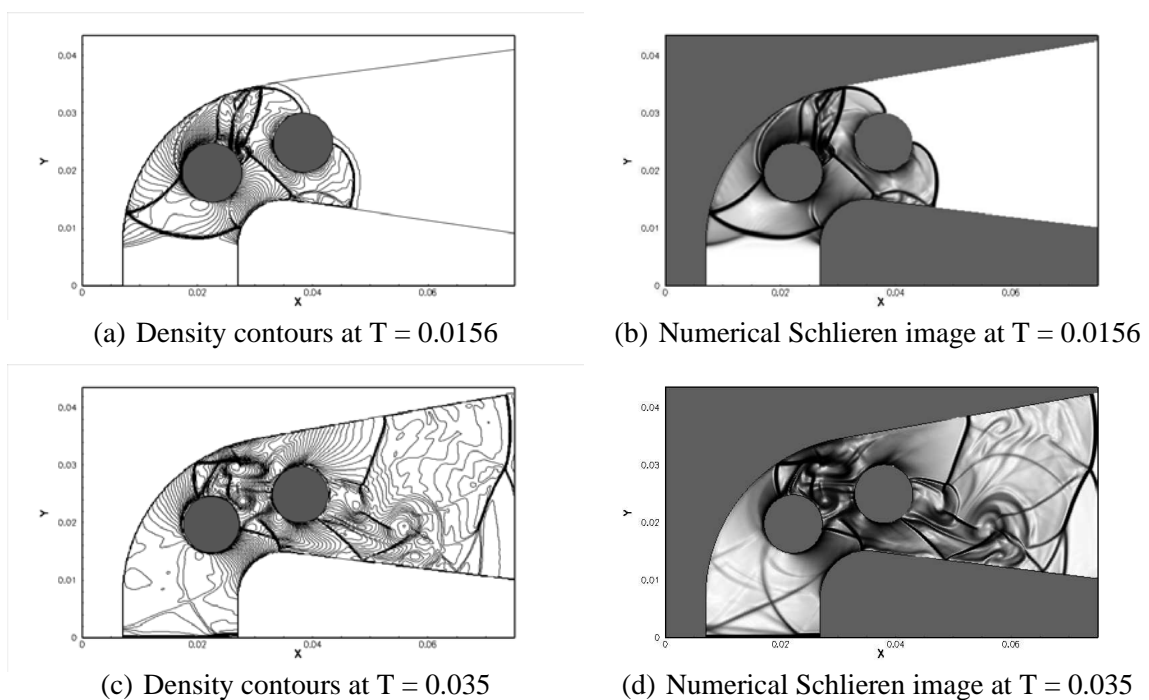
Figure 5.34: Mach 2.1 shock negotiating a curved channel with stationary obstacles: Density contours ((a) and (c)) and numerical Schlieren image ((b) and (d)) at two different instants in time

(a) Density contours at T = 0.014

(b) Numerical Schlieren image at T = 0.014

(c) Density contours at T = 0.025

(d) Numerical Schlieren image at T = 0.025
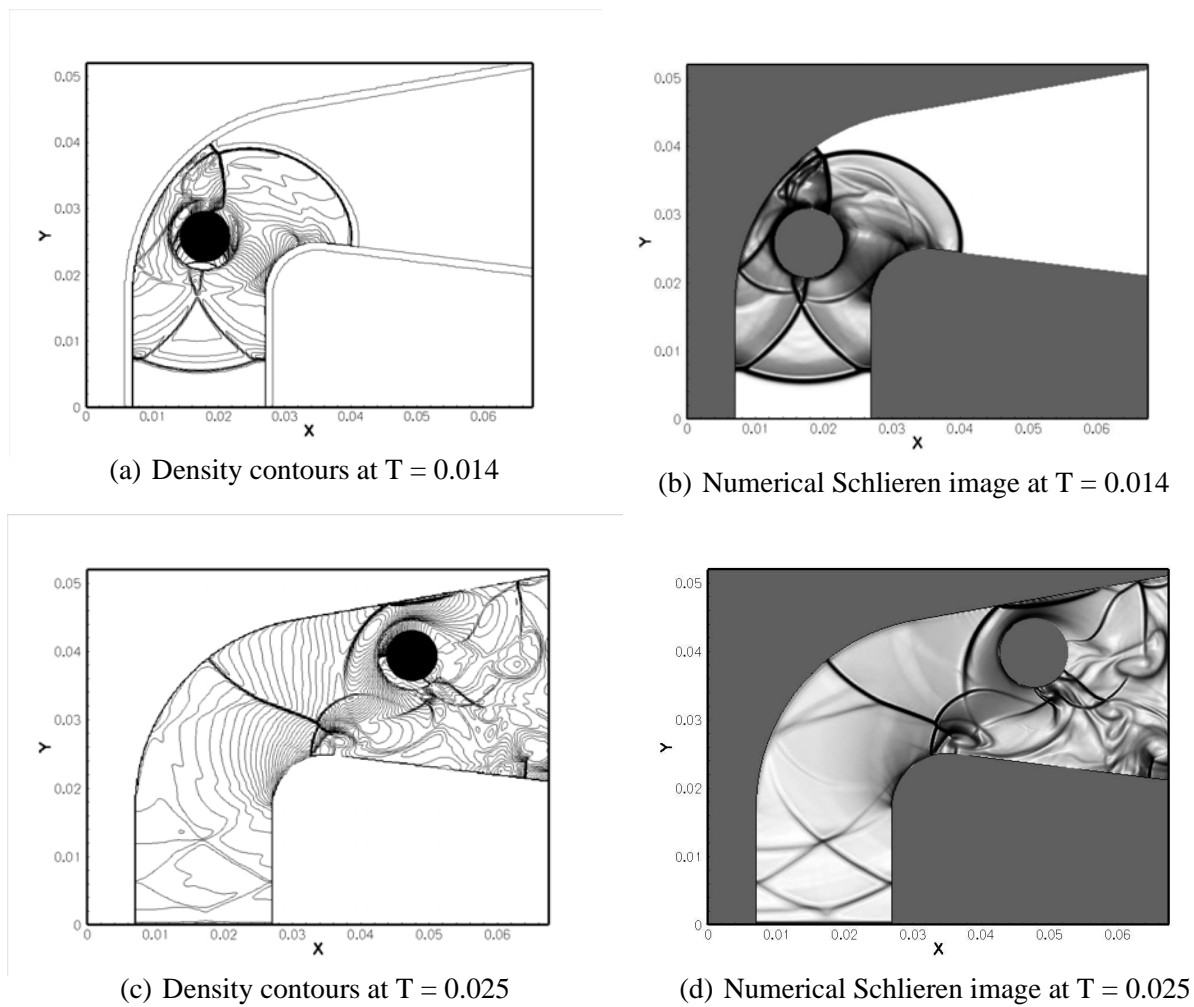
Figure 5.35: Mach 2.1 shock negotiating a curved channel with a moving obstacle: Density contours ((a) and (c)) and numerical Schlieren image ((b) and (d)) at different instants in time
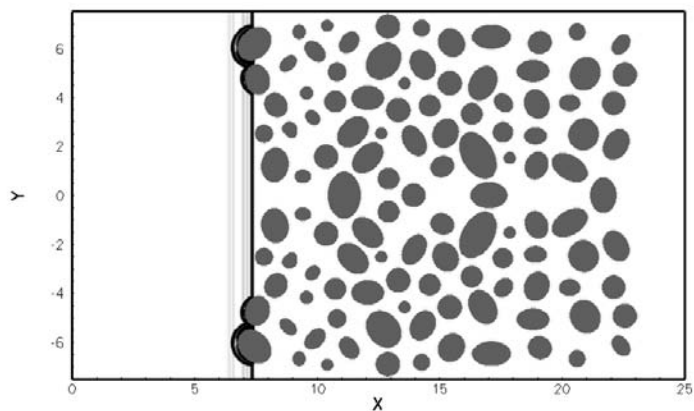
(a) Numerical Schlieren Image at T = 0.36
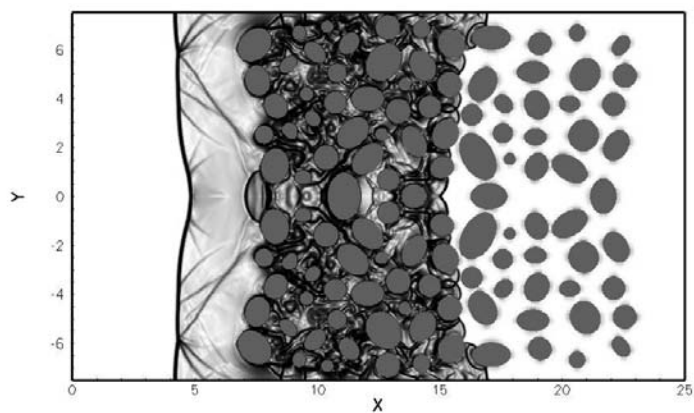
(b) Numerical Schlieren Image at T = 4.0
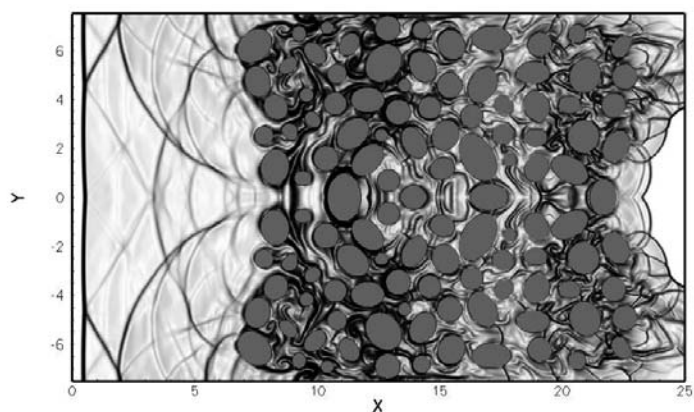
(c) Numerical Schlieren Image at T = 9.16

Figure 5.36: Series of numerical Schlieren image for a Mach 3 shock traversing through 120 randomly oriented stationary particles

(a) Numerical Schlieren at T = 0

(b) Vorticity Contours at T = 0.725

(c) Numerical Schlieren at T = 1.62

(d) Vorticity Contours at T = 3.0
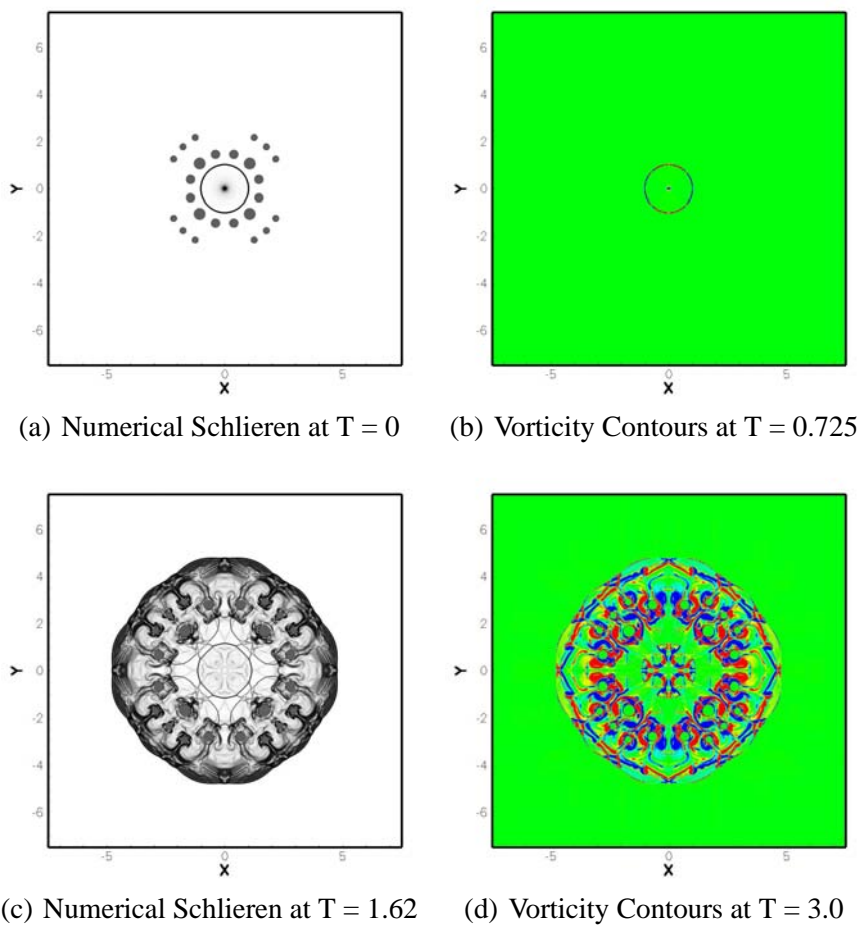
Figure 5.37: Series of numerical Schlieren image (Right) and vorticity contours (Left) for Mach 8 spherical shock interacting with 12 particles; Series correspond to the shock wave dispersing initially stationary particles
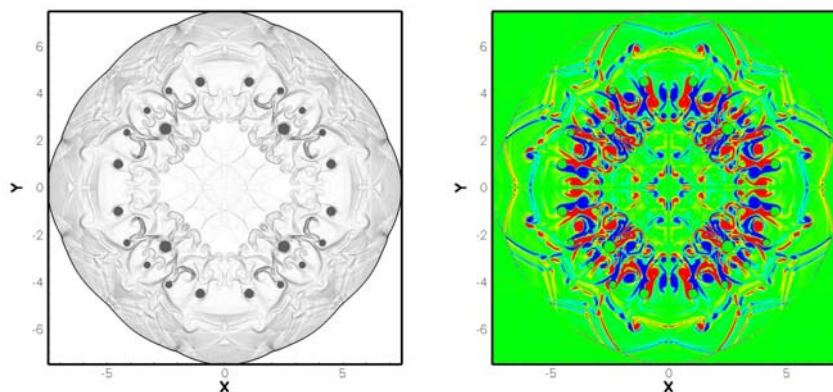
(a) Numerical Schlieren Image at T = 0

(b) Vorticity Contours Image at T = 0.725
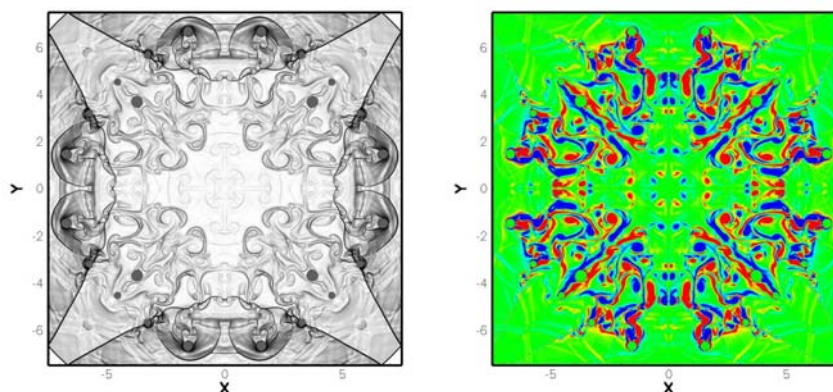
(c) Numerical Schlieren Image at T = 1.62

(d) Vorticity Contours Image at T = 3.0

Figure 5.38: Series of numerical Schlieren image (Right) and vorticity contours (Left) for Mach 8 spherical shock interacting with 12 particles; Series correspond to the shock wave reflecting off the domain walls.
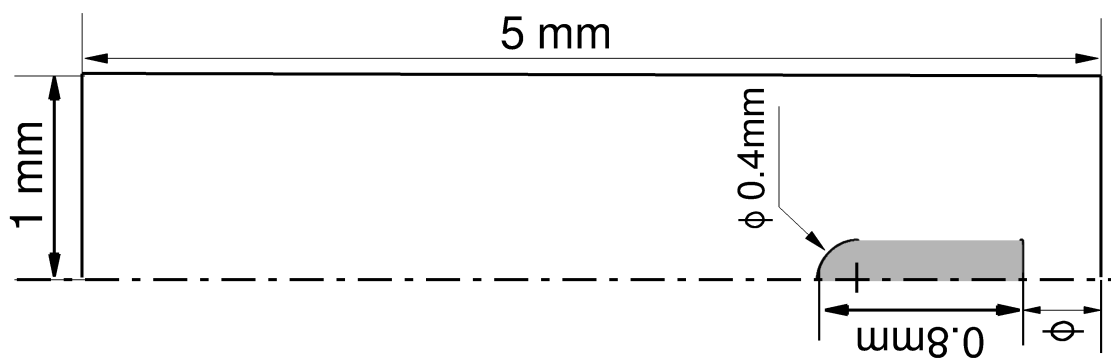
Figure 5.39: Configuration of a projectile travelling at Mach 1.22

(a) T = 0.25 ms   (b) T = 0.565 ms   (c) T = 4.65 ms   (d) T = 7.03 ms
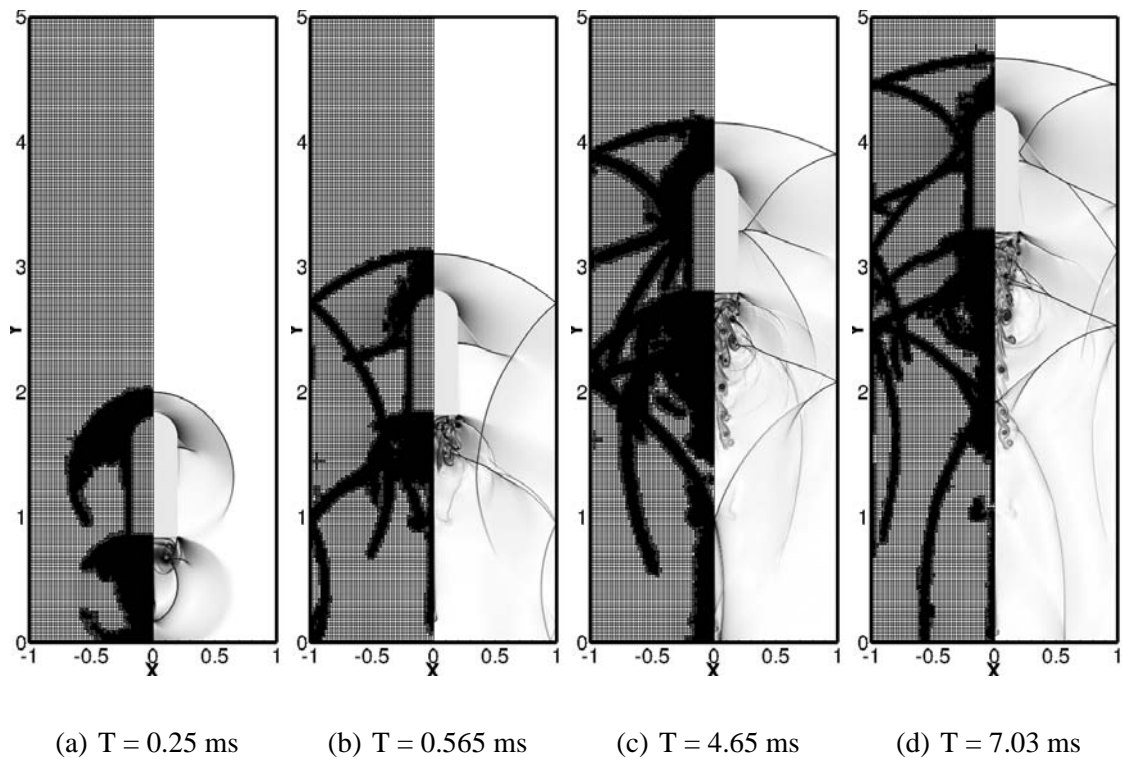
Figure 5.40: Numerical Schlieren image and the mesh topology for a supersonic projectile fired at Mach 1.22 at different instants in time.
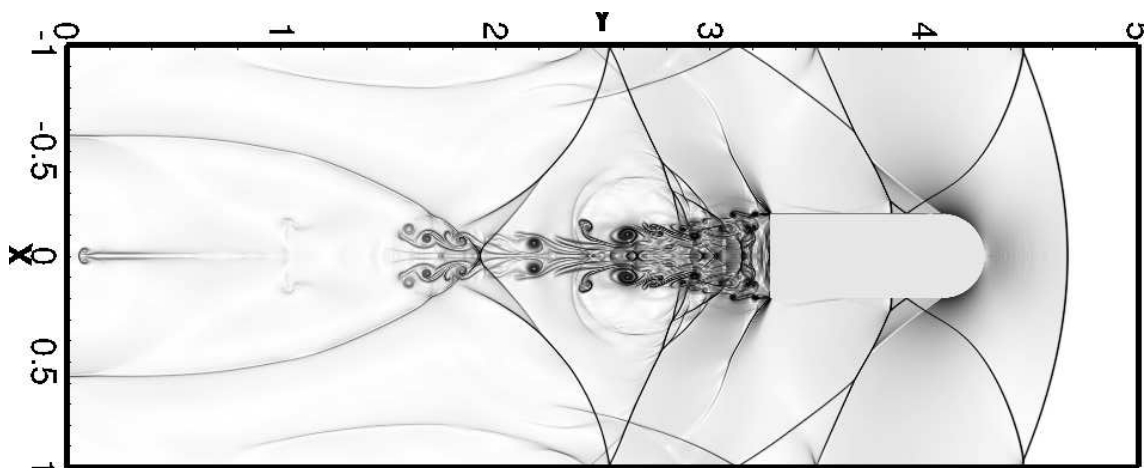
(a) Numerical Schlieren image at T = 7.03 ms
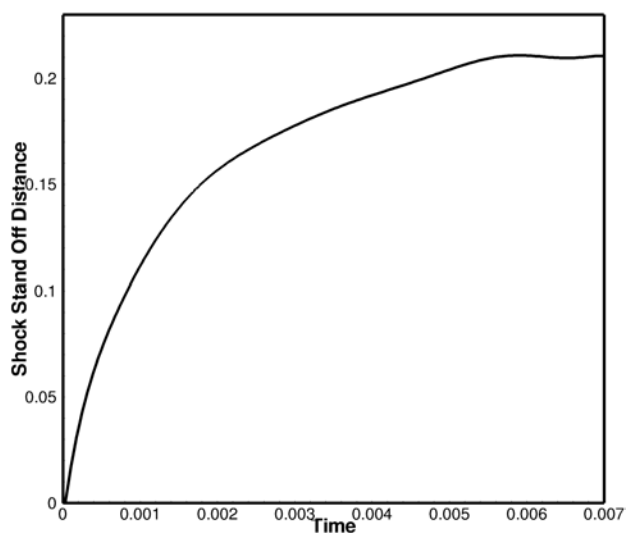
(b) Shock stand off distance with respect to time

Figure 5.41: Bluff body projectile fired at Mach 1.22: (a) Numerical Schlieren image at time T = 7.03 ms; (b) Shock stand off as a function of time
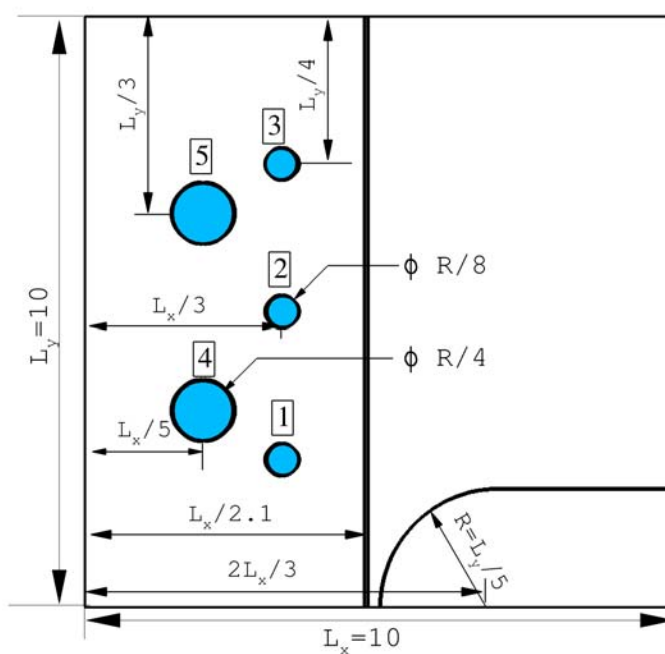
Figure 5.42: Problem configuration for the dynamics of multiple particles introduced in high speed flow

(a) Horizontal coordinate of the center of mass

(b) Vertical coordinate of the center of mass

(c) Drag Coefficient
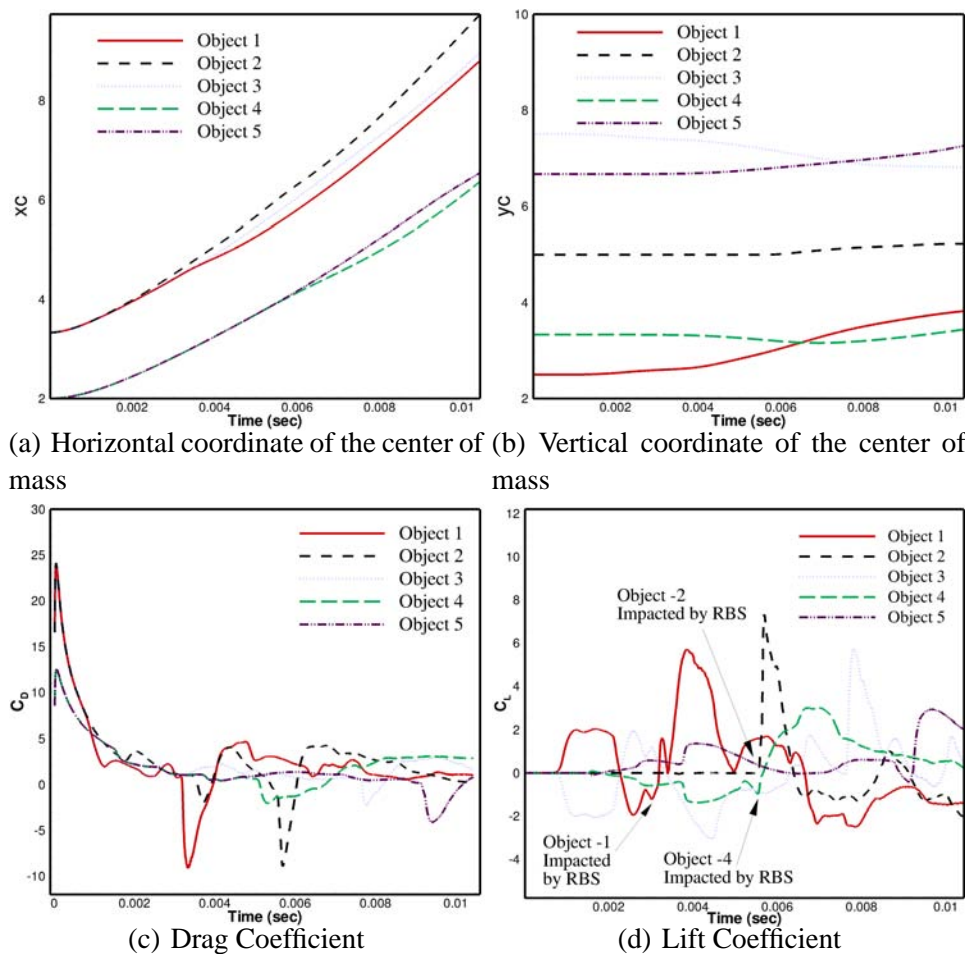
(d) Lift Coefficient

Figure 5.43: Dynamics of multiple particles introduced in high speed flow: (a) Locus of horizontal coordinate of the center of mass; (b) Locus of vertical coordinate of the center of mass; (c) Drag coefficient (d) Lift coefficient
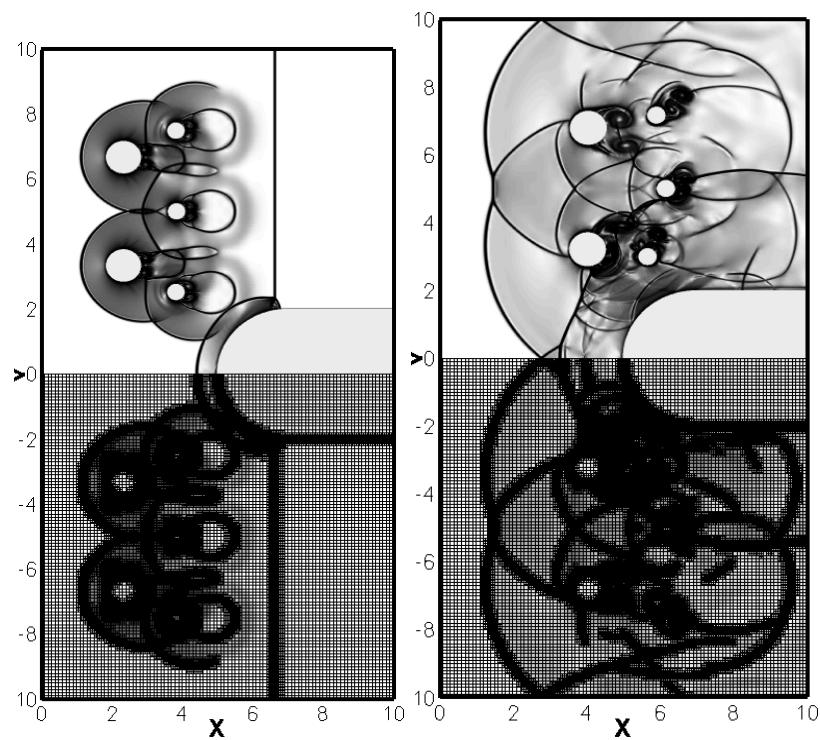
(a) Mesh Topology at T = 1.79 (b) Mesh Topology at T = 5.9 ms
ms
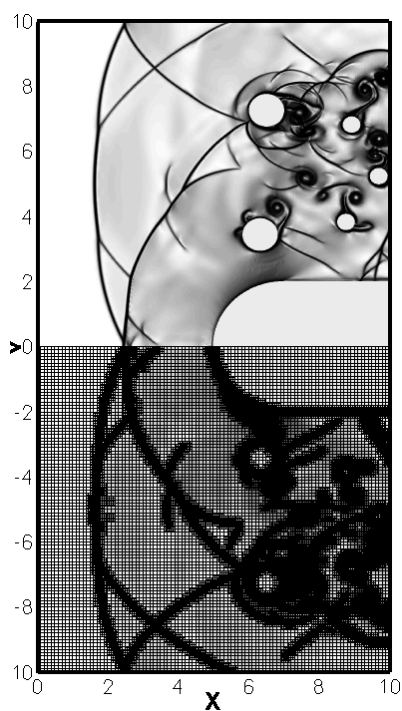
(c) Mesh Topology at T = 10.0
ms

Figure 5.44: Numerical Schlieren image and the mesh topology of cylindrical particles
introduced in high speed flows (a) T = 1.79 ms; (b) T = 5.9 ms; (c) T = 10.0 ms

338
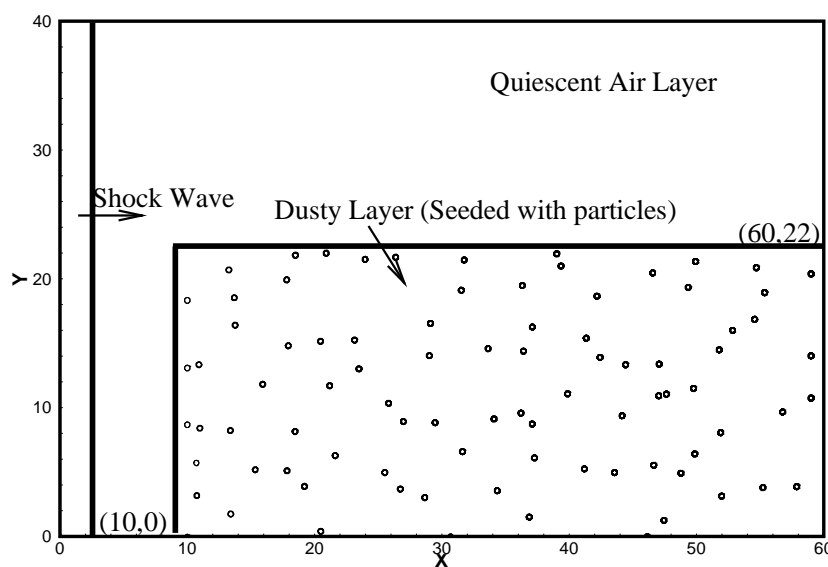
Figure 5.45: Initial configuration of the system for DNS of shock wave traversing through a dusty layer of gas
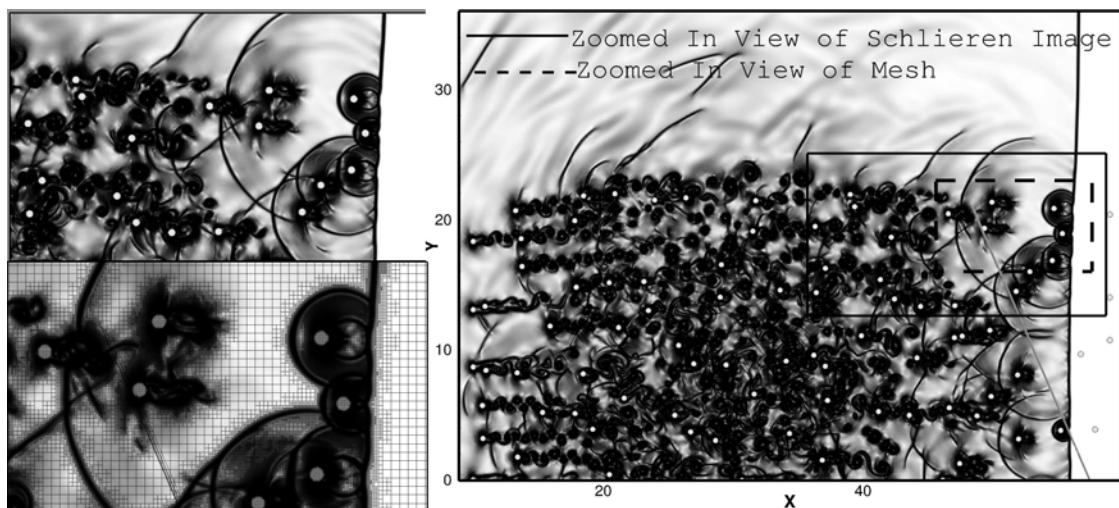
(a) Numerical Schlieren Image
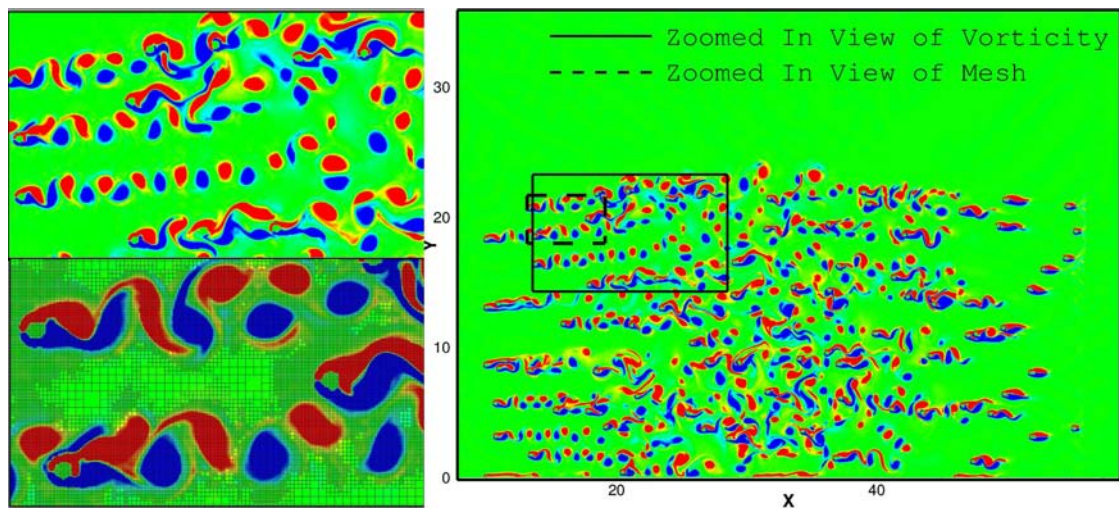
(b) Vorticity Contours

Figure 5.46: Mach 1.67 shock wave traversing through a dusty layer of gas at time T = 76.15 μ s: (a) Numerical Schlieren image and (b) vorticity contours
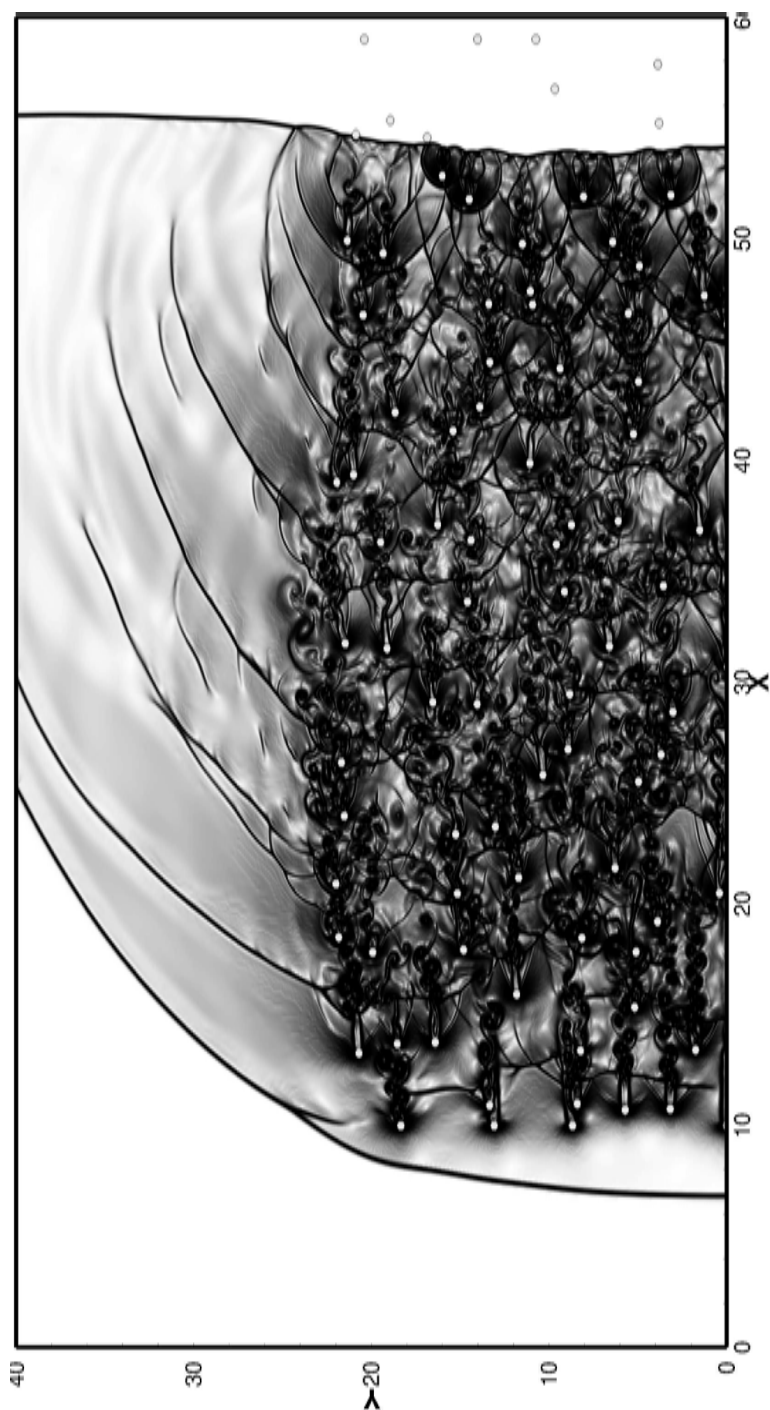
(a) Numerical Schlieren Image

Figure 5.47: Numerical Schlieren image for a Mach 3 shock wave traversing through a dusty layer of gas at time T = 41.17 μ s

CHAPTER 6
CONCLUSIONS AND RECOMMENDATIONS FOR FUTURE WORK

6.1 Conclusions

The primary goal of this thesis is to develop a robust, high-fidelity, Eulerian, Cartesian grid framework to solve high-speed multi-material interaction problems. The novelty of the work lies in the fact that an Eulerian approach is adopted for resolving the response of both solids and fluids. Another unique and distinguishing feature of this work is that the framework developed is applicable for a wide class of materials and for a broad spectrum of speeds of interactions. In addition, the robustness, versatility and simplicity of the approach makes it an attractive choice for solving several complex multi-material interaction problems. The examples that are solved in this thesis cover a plethora of applications and the stability of the framework in solving these problems has been well established.

6.2 Significant Contributions of this Thesis

To summarize some of the main contributions of this thesis are listed below:

- A generic sharp interface Cartesian grid method is formulated to capture the response of the embedded interface subject to intense loading conditions

- A robust Riemann problem approach is devised to resolve shock-droplet/shock-bubble interactions. The approach is found to be stable and accurate in decoupling the nature of the waves interacting at the embedded interface

- Physically consistent boundary conditions are formulated to capture the response of elasto-plastic solids under intense loading conditions

- A simple, robust and general formulation is devoloped to infuse interface conditions to the ghost nodes

- A conservative approach is devised to enforce flux conservation at mesh interfaces

6.3 Recommendations for Future Work

The framework can be extended in the following aspects:

- Although the implementation of the framework was carried out to include three-dimensions, the computations reported in this theses were limited to two-dimensional applications. In order to to perform real time, three-dimensional computations, multi-core computing facility must be incorporated in the present implementation. The efforts in this direction are currently underway and the results from such calculations will be reported in the future.

- The high-velocity impact and penetration studies conducted in this work typically involve fragmentation and failure of the interacting media. To accurately simulate these phenomena suitable fracture, damage and failure models have to be incorporated in concomitant with the interface capturing technique. To emphasize on the importance of these models, a sample computation of an Explosively Formed Projectile (EFP) is presented.

As shown in Figure 6.1(a), a conventional EFP consists of a metal liner held against

an explosive core. When the explosive core is initiated a detonation wave sets in the explosive charge. When this detonation wave impinges on the metallic liner, the liner material undergoes very large deformation resulting in the formation of high speed jet. The formation of high speed jet is shown in Figure 6.1(b). This hypervelocity jet of metal is capable of penetrating great depths into steel armor; however, in travel over some distance the jet breaks up along its length into particles that drift out of alignment, greatly diminishing its effectiveness at a distance.

In Figure 6.2(a), the initial formation of the jet process computed in this work is presented. For the sake of comparison, the jet formation process as depicted in [131] is displayed in Figure 6.2(b). As can be seen from the two figures, the present methodology is able to predict the initial jet formation process quite accurately. However, the present methodology was not able to predict the evolution of the jet at later stages as this would require the material to break apart from the explosive mold. To model this process a suitable void growth model has to be incorporated. In addition, the fragmentation of jet requires sophisticated damage and fracture models. These models exist and can be directly coupled with the numerical facility developed in this thesis.

- The computations reported in this thesis were performed for inert configurations, where-in the energetics of the interacting materials were neglected. In those cases, the interacting materials where treated as thermo-mechanically non-participating region. In reality, the resulting temperatures are very high, particularly for high shock loadings and high velocity impact problems, that the participating materials undergo

phase compression and chemical reactions that significantly alter the energy deposition mechanism. Thus for performing chemically reactive compressible flow calculations, the numerical facility developed in this thesis can be coupled with appropriate detonation models.
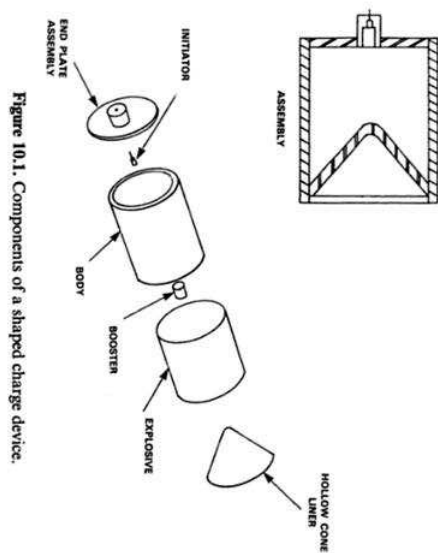
Figure 10.1. Components of a shaped charge device.

(a) Components of EFP [131]
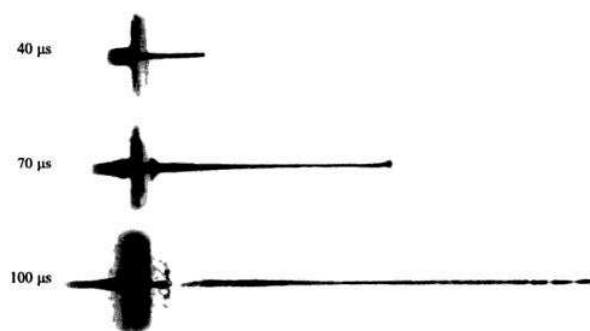
Figure 10.3. Flash radiographs of a 75 mm diameter shaped charge.

(b) Radiograph Images of Jet formation [131]

Figure 6.1: Explosively Formed Projectile: (a) Components of EFP and (b) Radiograph images of the jet formation process

(a) Current Calculation of EFP

Figure 10.2. Shaped charge jet and slug formation.

(b) Shaped Jet Formation as depicted in [131]
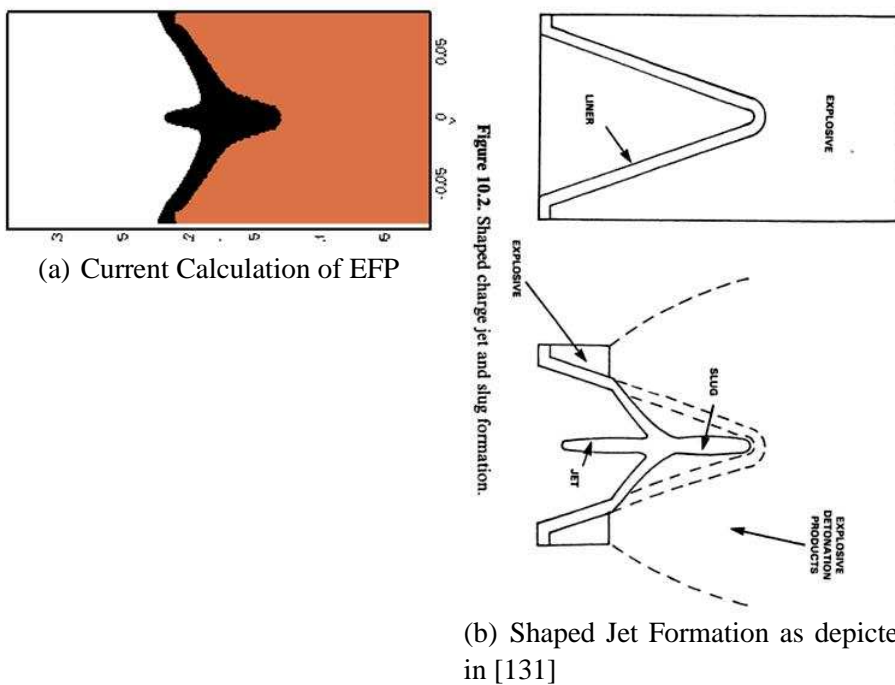
Figure 6.2: The jet formation process: (a) Current calculations (b) Theoretical prediction

REFERENCES

[1] *Shock Waves and Man*. The University of Toronto Press, 1974.

[2] *Analysis and Numerics for Conservation Laws*, chapter Wave Processes at Interfaces. Springer Berlin Heidelberg, 2005.

[3] A.M. Abd-El-Fattah and L.F. Henderson. Shock waves at a slow-fast gas interface. *Journal of Fluid Mechanics*, 89:79–95, 1978.

[4] R. Abgrall. On essentially non-oscillatory schemes on unstructured meshes: analysis and implementation. *J. Comput. Phys.*, 114(1):45–58, 1994.

[5] R. Abgrall. How to prevent pressure oscillations in multicomponent flow calculations: A quasi conservative approach. *Journal of Computational Physics*, 125:150–160, 1996.

[6] R. Abgrall and S. Karni. Computations of compressible multi-fluids. *Journal of Computational Physics*, 169:594–623(30), 20 May 2001.

[7] G. Agresar, J. J. Linderman, G. Tryggvason, and K. G. Powell. An adaptive, cartesian, front-tracking method for the motion, deformation and adhesion of circulating cells. *J. Comput. Phys.*, 143(2):346–380, 1998.

[8] Thomas J. Ahrens and John D. O'Keefe. Impact on the earth, ocean and atmosphere. *International Journal of Impact Engineering*, 5:13 – 32, 1987.

[9] Charles E. Anderson. An overview of the theory of hydrocodes. *International Journal of Impact Engineering*, 5:33 – 59, 1987.

[10] Charles E. Anderson, Volker Hohler, James D. Walker, and Alois J. Stilp. Time-resolved penetration of long rods into steel targets. *International Journal of Impact Engineering*, 16(1):1 – 18, 1995.

[11] M. Arienti, P. Hung, E. Morano, and Shepherd J.E. A levelest approach to Eulerian-Lagrangian coupling. *Journal Of Computational Physics*, 185:213–251, 2003.

[12] M. Arienti, E. Morano, and Shepherd J.E. Shock and detonation modeling with the mie-grüneisen equation of state. Technical report, Graduate Aeronautical Laboratories Report, 2004.

[13] T.D. Aslam. A level set algorithm for tracking discontinuities in hyperbolic conservation laws I: Scalar equations. *Journal Of Computational Physics*, 167:413–438, 2001.

[14] T.D. Aslam. A level set algorithm for tracking discontinuities in hyperbolic conservation laws II: Systems of equations. *Journal of Scientific Computing*, 19(1-3):37–62, 2003.

[15] T.D. Aslam. A partial differential equation approach to multidimensional extrapolation. *Journal Of Computational Physics*, 193:349–355, 2004.

[16] A. Bagabir and D. Drikakis. Mach number effects on shock-bubble interaction. *Shock Waves*, 11:209–218, 2001.

[17] J. Baker and A. Williams. Hypervelocity penetration of plate targets by rod and rod-like projectiles. *International Journal of Impact Engineering*, 5:101 – 110, 1987.

[18] G.J. Ball, B.P. Howell, T.G. Leighton, and M.J. Schofield. Shock induced collapse of a cylindrical air cavity in water : A free Lagrange simulation. *Shock Waves*, 10:265 – 276, 2000.

[19] J. W. Banks, D. W. Schwendeman, A. K. Kapila, and W. D. Henshaw. A high-resolution godunov method for compressible multi-material flow on overlapping grids. *J. Comput. Phys.*, 223(1):262–297, 2007.

[20] T.V. Bazhenova, L.G. Gvozdeva, and M.A. Nettleton. Unsteady interactions of shock waves. *Progress in Aerospace Sciences*, 21:249–331, 1984.

[21] D. J. Benson and W. J. Nellis. Dynamic compaction of copper powder: Computation and experiment. *Applied Physics Letters*, 65(4):418–420, 1994.

[22] D. J. Benson, W. Tong, and G. Ravichandran. Particle-level modeling of dynamic consolidation of ti-sic powders. *Modelling and Simulation in Materials Science and Engineering*, 3(6):771–796, 1995.

[23] D. L. Benson, J. O. Hallquist, M. Igarashi, K. Shimomoki, and M. Mizuno. The application of DYA3D to large scale crashworthiness calculations. In *Proceedings of the ASME Computers in Engineering Conference*, New York, July 20 - 24 1986. ASME.

[24] David J. Benson. Computational methods in lagrangian and eulerian hydrocodes. *Comput. Methods Appl. Mech. Eng.*, 99(2-3):235–394, 1992.

[25] David J. Benson. Volume of fluid interface reconstruction methods for multi-material problems. *Applied Mechanics Reviews*, 55(2):151–165, 2002.

[26] M. J. Berger and P. Colella. Local adaptive mesh refinement for shock hydrodynamics. *J. Comput. Phys.*, 82(1):64–84, 1989.

[27] Marsha J. Berger and Joseph E. Oliger. Adaptive mesh refinement for hyperbolic partial differential equations. Technical report, Stanford, CA, USA, 1983.

[28] N.K. Bourne and J.E. Field. Shock induced collapse of single cavities in liquids. *Journal of Fluid Mechanics*, 244:225 – 240, 1992.

[29] Jean Braun and Malcolm Sambridge. A numerical method for solving partial differential equations on highly irregular evolving grids. *Nature*, 376:655–660, Aug 1995.

[30] Greg L. Bryan. Fluids in the universe: adaptive mesh refinement in cosmology. *Comput. Sci. Eng.*, 1(2):46–53, 1999.

[31] A.E. Bryson and R.W.F. Gross. Diffraction of strong shocks by cones, cylinders and spheres. *Journal of Fluid Mechanics*, 10:1–16, 1960.

[32] R. Eatock Taylor C. W. Smith, J. Zang. Wavelet-based adaptive grids as applied to hydrodynamics. *International Journal for Numerical Methods in Fluids*, 2008.

[33] R. Caiden, R.P. Fedkiw, and C. Anderson. A numerical method for two-phase flow consisting of separate compressible and incompressible regions. *Journal of Computational Physics*, 166:1–27, 2001.

[34] Jay Casper and H. L. Atkins. A finite-volume high-order eno scheme for two-dimensional hyperbolic systems. *J. Comput. Phys.*, 106(1):62–76, 1993.

[35] Thomas C. Cecil, Stanley J. Osher, and Jianliang Qian. Simplex free adaptive tree fast sweeping and evolution methods for solving level set equations in arbitrary dimension. *J. Comput. Phys.*, 213(2):458–473, 2006.

[36] Thomas C. Cecil, Stanley J. Osher, and Jianliang Qian. Essentially Non-Oscillatory adaptive tree methods. *J. Sci. Comput.*, 35(1):25–41, 2008.

[37] J. W. Chalmersa, S. W. Hodsona, K. H. A. Winklera, P. R. Woodward, and N. J. Zabusky. Shock-bubble interactions : Generation and evolution of vorticity in two-dimensional supersonic flows. *Fluid Dynamics Research*, 3(4):392–394, 1988.

[38] C.H. Chang and M.S. Liou. A robust and accurate approach to computing compressible multiphase flow: Stratified flow model and AUSM+ - up scheme. *Journal of Computational Physics*, 225:840 – 873, 2007.

[39] H. Chen and S.M. Liang. Flow visualization of shock/water interactions. *Shock Waves*, 17:309 – 321, 2008.

[40] D. Cheng, G. Trapaga, J.W. McKelliget, and E.J. Lavernia. Mathematical modelling of high velocity oxygen fuel thermal spraying of nanocrystalline materials: An overview. *Modelling and Simulation in Materials Science and Engineering*, 11:1 – 31, 2003.

[41] Dae-Il Choi, J. David Brown, Breno Imbiriba, Joan Centrella, and Peter MacNeice. Interface conditions for wave propagation through mesh refinement boundaries. *Journal of Computational Physics*, 193(2):398–425, 2004.

[42] J.P. Cocchi and R. Saurel. A Riemann problem based method for the resolution of compressible multi-material flows. *Journal of Computational Physics*, 137:265–298, 1997.

[43] J.P. Cocchi, R. Saurel, and J.C. Loraud1. Treatment of interface problems with Godunov-type schemes. *Shock Waves*, 5(6):347–357, 1996.

[44] William J. Coirier and Kenneth G. Powell. An accuracy assessment of Cartesian-mesh approaches for the euler equations. *J. Comput. Phys.*, 117(1):121–131, 1995.

[45] William John Coirier. *An Adaptively-Refined, Cartesian, Cell Based Scheme for the Euler and Navier-Stokes Equations.* PhD thesis, Ann Arbor, MI, USA, 1994.

[46] S. R. Cooper, D. J. Benson, and V. F. Nesterenko. A numerical exploration of the role of void geometry on void collapse and hot spot formation in ductile materials. *International Journal of Plasticity*, 16(5):525 – 540, 2000.

[47] Nguyen D., F. Gibou, and Fedkiw R.P. A fully conservative Ghost Fluid Method and stiff detonation waves. In *Proceedings of the 12th International Detonation Symposium*, San Diego, CA, August, 11 - 16 2002.

[48] A. Dadone and B. Grossman. Ghost cell method for inviscid three dimensional flows on Cartesian grids. In *Presented at the 43rd AIAA Aerospace Sciences Meeting and Exhibit*, Reno, NV,USA, January 10-13 2005. AIAA 2005-0874.

[49] S. F. Davis. An interface tracking method for hyperbolic systems of conservations laws. *Applied Numerical Mathematics*, 10:447 – 472, 1992.

[50] M. D. de Tullio, P. De Palma, G. Iaccarino, G. Pascazio, and M. Napolitano. An immersed boundary method for compressible flows using local grid refinement. *J. Comput. Phys.*, 225(2):2098–2117, 2007.

[51] A. Dolatabadi, J.. Mostaghimi, and V. Pershin. Modeling dense suspension of solid particles in highly compressible flows. *International Journal of Computational Fluid Dynamics*, 18:125 – 131, 2004.

[52] R. Donat and A. Marquina. Capturing shock reflections: An improved flux formula. *Journal of Computational Physics*, 125:42–58, 1996.

[53] D. Drikakis, D. Ofengeim, E. Timofeev, and P. Voionovich.

[54] A.F. Emery. An evaluation of several differencing methods for inviscid fluid flow problems. *Journal of Computational Physics*, 2(3):306–331, 1968.

[55] J. Falcovitz, G. Alfandary, and G. Hanoch. A two dimensional conservation laws scheme for compressible flows with moving boundaries. *Journal of Computational Physics*, 138:83–102, 1997.

[56] A. V. Federov, Yu. V. Kharlamova, and T. A. Khmel. Reflection of a shock wave in a dust cloud. *Combustion, Explosion and Shock Waves*, 43(1):104 – 113, 2007.

[57] R. Fedkiw. Coupling an Eulerian fluid calculation to a Lagrangian solid calculation with the Ghost Fluid Method. *Journal of Computational Physics*, 175:200 – 224, 2002.

[58] R.P. Fedkiw, T.D. Aslam, B. Merriman, and S. Osher. A non oscillatory Eulerian approach to interfaces in multi-material flows (the Ghost Fluid Method). *Journal of Computational Physics*, 152(2):457 – 492, 1999.

[59] R.P. Fedkiw, T.D. Aslam, and S. Xu. The Ghost Fluid Method for deflagration and detonation discontinuities. *Journal of Computational Physics*, 154(2):393 – 427, 1999.

[60] R.P. Fedkiw, A. Marquina, and B. Merriman. An isobaric fix for the overheating problem in multi-material compressible flows. *Journal of Computational Physics*, 148:545–578, 1999.

[61] H. Forrer and M. Berger. Flow simulations on Cartesian grids involving complex moving geometries flows. *International Series of Numerical Mathematics*, 129(315):139–178, 1998. Birkhuser, Basel 1.

[62] H. Forrer and R. Jeltsch. A higher order boundary treatment for Cartesian grid methods. *Journal Of Computational Physics*, 140:259–277, 1998.

[63] M.J. Forrestal, V.K. Luk, and N.S. Brar. Perforation of aluminum armor plates with conical-nose projectiles. *Mechanics of Materials*, 10(1-2):97–105, 1990.

[64] J. Glimm, J. W. Grove, X. Li, K. M. Shyue, Y. Zeng, and Q. Zhang. Three-dimensional front tracking. *SIAM Journal on Scientific Computing*, 19(3):703–727, 1998.

[65] J. Glimm, C. Klingenberg, O. McBryan, B. Plohr, D. Sharp, and S. Yaniv. Front tracking and two-dimensional Riemann problems. *Advances in Applied Mathematics*, 6(3):259–290, 1985.

[66] J. Glimm, X. L. Li, and N. Zhao. Conservative front tracking and levelset algorithms. *Proceedings of the National Academy of Sciences*, 98(25):14198 – 14201, 2001.

[67] J. Glimm, D. Marchesin, and O. McBryan. A numerical method for two phase flow with an unstable interface. *Journal of Computational Physics*, 39:179 – 200, 1981.

[68] D. M. Greaves and A. G. L. Borthwick. On the use of adaptive hierarchical meshes for numerical simulation of separated flows. *International Journal for Numerical Methods in Fluids*, 26(3):303 – 322, 1998.

[69] D. M. Greaves and A. G. L. Borthwick. Hierarchical tree-based finite element mesh generation. *International Journal for Numerical Methods in Fluids*, 45(4):447 – 471, 1999.

[70] Deborah M. Greaves. Hierarchical tree-based finite element mesh generation. *International Journal for Numerical Methods in Fluids*, 44(10):1093 – 1117, 2004.

[71] Deborah M. Greaves. A quadtree adaptive method for simulating fluid flows with moving interfaces. *J. Comput. Phys.*, 194(1):35–56, 2004.

[72] Boyce E. Griffith, Richard D. Hornung, David M. McQueen, and Charles S. Peskin. An adaptive, formally second order accurate version of the immersed boundary method. *J. Comput. Phys.*, 223(1):10–49, 2007.

[73] J.W. Grove and R. Menikoff. Anomalous reflection of a shock wave at a fluid interface. *Journal of Fluid Mechanics*, 219:313–336, 1990.

[74] Shan Guang-Jiang and Wang Chi-Shu. Efficient implementations of Weighted ENO schemes. Technical report, 1995.

[75] J.F. Haas and B. Sturtevant. Interaction of weak shock waves with cylindrical and spherical inhomogeneities. *Journal of Fluid Mechanics*, 181:41–76, 1987.

[76] K. K. Haller. *High-Velocity Impact of a Liquid Droplet on a Rigid Surface: The Effect of Liquid Compressibility*. PhD thesis, Swiss Federal Institute of Technology Zurich, 2002.

[77] K.K Haller, D. Poulikakos, Y. Ventikos, and P. Monkewitz. Shock wave formation in droplet impact on a rigid surface: Lateral liquid motion and multiple wave structure in the contact line region. *Journal of Fluid Mechanics*, 490:1–14, 2003.

[78] K.K Haller, Y. Ventikos, and D. Poulikakos. Computational study of high speed liquid droplet impact. *Journal of Applied Physics*, 92(5):2821–2828, 2002.

[79] K.K Haller, Y. Ventikos, and D. Poulikakos. Wave structure in the contact line region during high speed droplet impact on a surface: Solution of the Riemann problem for the stiffened gas equation of state. *Journal of Applied Physics*, 93(5):3090–3097, 2003.

[80] R.K.S. Hankin. The Euler equations for multiphase compressible flow in conservation form. *Journal of Computational Physics*, 172:808 – 826, 2001.

[81] L.F. Henderson. On the refraction of shock waves. *Journal of Fluid Mechanics*, 198:365–386, 1989.

[82] W.D. Henshaw and D. W. Schwendeman. Moving overlapping grids with adaptive mesh refinement for high-speed reactive and non-reactive flow. *J. Comput. Phys.*, 216(2):744–779, 2006.

[83] Stefan Hiermaier. *Structures Under Crash and Impact*. Springer US, 2008.

[84] Charles Hirsch. *Numerical Computation of Internal and External Flows - Volume:II, Computational Methods for Inviscid and Viscous Flows*. Wiley, 1988.

[85] R. Hivier. Computation of shock wave diffraction at a ninety degrees convex edge. *Shock Waves*, 1:89–98, 1991.

[86] J.M. Hong, T. Shinar, M. Kang, and R. Fedkiw. On boundary condition capturing for multiphase interfaces. *Journal of Scientific Computing*, 31:99 – 125, 2007.

[87] X. Y. Hu and B. C. Khoo. An interface interaction method for compressible multi-fluids. *Journal of Computational Physics*, 198:35–64, 2004.

[88] X. Y. Hu, B. C. Khoo, N. A. Adams, and F.L. Huang. A conservative interface method for compressible flows. *Journal of Computational Physics*, 219(2):553 – 578, May 2006.

[89] D. Igra and K. Takayama. Numerical simulation of shock wave interaction with water column. *Shock Waves*, 11:219–228, 2001.

[90] O. Igra and K. Takayama. Shock tube study of the drag coefficient of a sphere in a non-stationary flow. *Proceedings: Mathematical and Physical Sciences*, 442(1915):231–247, 1993.

[91] G. T. Gray III, E. Cerreta, C. A. Yablinsky, L. B. Addessio, B. L. Henrie, B. H. Sencer, M. Burkett, P. J. Maudlin, S. A. Maloy, C. P. Trujillo, and M. F. Lopez. Influence of shock prestraining and grain size on the dynamic-tensile-extrusion response of copper: Experiments and simulation. *AIP Conference Proceedings*, 845(1):725–728, 2006.

[92] A. R. Jamaluddin, G. J. Ball, and T. G. Leighton. Free-Lagrange simulations of shock/bubble interaction in shock wave Lithotripsy. In *Shock Waves : Proceedings of the 24th International Symposium on Shock Waves*.

[93] Leland Jameson. AMR vs high order schemes. *J. Sci. Comput.*, 18(1):1–24, 2003.

[94] P. Jenny, B. Muller, and H. Thomann. Correction of conservative Euler solvers for gas mixtures. *Journal of Computational Physics*, 132:91–107, 1997.

[95] Xiaohai Jian, Zhihua Chen, Baochun Fan, and Hongzhi Li. Numerical simulation of blast flow fields induced by a high-speed projectile. *Shock Waves*, 18:205 – 212, 2008.

[96] Z. Jiang, K. Takayama, and B. W. Skews. Numerical study on blast flowfields induced by supersonic projectiles discharged from shock tubes. *Physics of Fluids*, 10(1):277–288, 1998.

[97] Zonglin Jiang, Yonghui Huang, and Kazuyoshi Takayama. Shocked flows induced by supersonic projectiles moving in tubes. *Computers & Fluids*, 33(7):953 – 966, 2004.

[98] E. Johnsen and T. Colonius. Implementation of WENO schemes in compressible multicomponent flow problems. *Journal of Computational Physics*, 219:715–732, 2006.

[99] G. R. Johnson and W. H. Cook. Fracture characteristics of three metals subjected

to various strains, strain rates, temperatures and pressures. *Engineering Fracture Mechanics*, 21(1):31 – 48, 1985.

[100] J. Kaca. An interferometric investigation of the diffraction of a planar shock wave over a semicircular cylinder. Technical Report 269, University of Toronto, Institute for Aerospace Studies (UTIAS), 1988.

[101] M. Kang, R.P. Fedkiw, and X.D. Liu. Boundary condition capturing method for multiphase incompressible flow. *Journal of Scientific Computing*, 15(3):323 – 360, 2000.

[102] S. Karni. Hybrid multi-fluid algorithms. *SIAM Journal of Scientific Computing*, 17:1019–1039, 1996.

[103] Smadar Karni, Alexander Kurganov, and Guergana Petrova. A smoothness indicator for adaptive algorithms for hyperbolic systems. *J. Comput. Phys.*, 178(2):323–341, 2002.

[104] R. Keppens, Nool. M., G. Tóth, and J.P. Goedbloed. Adaptive mesh refinement for conservative systems: multi-dimensional efficiency evaluation. *Computer Physics Communications*, 153(3):317 – 339, 2003.

[105] Akhtar S. Khan and Sujian Huang. *Continuum Theory of Plasticity*. Wiley-Interscience, 1995.

[106] B.A. Khasainov, A.A. Borisov, B.S. Ermolaev, and A.I. Korotkov. Two phase visco-plastic model of shock initiation of detonation in high density pressed explosives. In *Seventh Symposium (International) on Detonation, Naval Surface Weapons Center*.

[107] J.W. Kim and D.J. Lee. Generalized characteristic boundary conditions for computational aeroacoustics. *AIAA Journal*, 38:2040–2049, 2000.

[108] S. Krishnan. *An Adaptively Refined Cartesian Grid Method for Moving Boundary Problems Applied to Biomedical Systems*. PhD thesis, The University of Iowa, 2006.

[109] L. Krivodonova and M. J. Berger. High-order accurate implementation of solid wall boundary conditions in curved geometries. *Journal Of Computational Physics*, 211:492–512, 2006.

[110] Alexander Kurganov and Eitan Tadmor. Solution of two-dimensional Riemann problems for gas dynamics without Riemann problem solvers. *Numerical Methods for Partial Differential Equations*, 18:584 – 608, 2002.

[111] J.O. Langseth and R.J. Leveque. A wave propagation method for three dimensional hyperbolic conservation laws. *Journal of Computational Physics*, 165:125 – 166, 2000.

[112] V. S. Lanovets, V. A. Levich, N. K. Rogov, Yu. V. Tunik, and K. N. Shamshev. Dispersion of the detonation products of a condensed explosive with solid inclusions. *Shock Wave*, 29(5):638–641, 1993.

[113] Guillaume Layes, Georges Jourdan, and Lazhar Houas. Distortion of a spherical gaseous interface accelerated by a plane shockwave. *Physical Review Letter*, 91, 2003.

[114] Y. Ling, A. Haselbacher, and S. Balachandar. Modeling and simulation of explosive dispersal of particles in a multiphase explosion.

[115] T. G. Liu, W. F. Xie, and B. C. Khoo. The modified ghost fluid method for coupling of fluid and structure constituted with hydro-elasto-plastic equation of state. *SIAM J. Sci. Comput.*, 30(3):1105–1130, 2008.

[116] T.G. Liu, B.C. Khoo, and C.W. Wang. Ghost Fluid Method for compressible gas-water simulation. *Journal of Computational Physics*, 204:193–221, 2005.

[117] T.G. Liu, B.C. Khoo, and K.S. Yeo. The simulation of compressible multi-medium flow II. Application to 2D underwater shock refraction. *Computers and Fluids*, 30:315 – 337, 2001.

[118] T.G. Liu, B.C. Khoo, and K.S. Yeo. Ghost Fluid Method for strong shock impacting on material interface. *Journal of Computational Physics*, 190:651–681, 2003.

[119] T.G. Liu, B.C. Khoo, K.S. Yeo, and C. Wang. Underwater shock-free surface-structure interaction. *International Journal for Numerical Methods in Engineering*, 58:609–630, 2003.

[120] X.D. Liu and S. Osher. Convex ENO high order multi-dimensional schemes without field by filed decomposition or staggered grids. *Journal Of Computational Physics*, 142:304–330, 1998.

[121] Frank Losasso, Ronald Fedkiw, and Stanley Osher. Spatially adaptive techniques for level set methods and incompressible flow. *Computers and Fluids*, 35:2006, 2005.

[122] Frank Losasso, Frédéric Gibou, and Ron Fedkiw. Simulating water and smoke with an octree data structure. In *SIGGRAPH '04: ACM SIGGRAPH 2004 Papers*, pages 457–462, New York, NY, USA, 2004. ACM.

[123] V.L. Mali. *Combustion, Explosion, and Shock Waves.*, 214, 1975.

[124] S. Marella, S. Krishnan, H. Liu, and H.S. UdayKumar. Sharp interface Cartesian grid method I : An easily implemented technique for 3D moving boundary computations. *Journal Of Computational Physics*, 210:1–31, 2005.

[125] A. Marquina and P. Mulet. A flux-split algorithm applied to conservative models for multicomponent compressible flows. *Journal of Computational Physics*, 185:120 – 138, 2003.

[126] Daniel F. Martin, Phillip Colella, and Daniel Graves. A cell-centered adaptive projection method for the incompressible navier-stokes equations in three dimensions. *J. Comput. Phys.*, 227(3):1863–1886, 2008.

[127] R. Menikoff. Errors when shock waves interact due to numerical shock width. *SIAM Journal on Scientific Computing*, 15:1227–1242, 1994.

[128] Chohong Min and Frédéric Gibou. A second order accurate level set method on non-graded adaptive cartesian grids. *J. Comput. Phys.*, 225(1):300–321, 2007.

[129] J. F. Molinari. Finite element simulation of shaped charges. *Finite Elements in Analysis and Design*, 38(10):921 – 936, 2002.

[130] F.J. Mont'ans and R.I. Borja. Implicit j2-bounding surface plasticity using pragers translation rule. *International Journal for Numerical Methods in Engineering*, 55(10):1129 – 1166, 2000.

[131] Marc André Myers. *Dynamics Behaviour of Materials*. John Wiley and Sons, Inc., 1994.

[132] W.F. Noh. Errors for calculations of strong shocks using an artificial viscosity and an artificial heat flux. *Journal Of Computational Physics*, 72:78–120, 1987.

[133] R.R. Nourgaliev, T.N. Dinh, and T.G. Theofanous. The Characteristic Based Matching (CBM) method for compressible flow in complex geometries. In *Presented at the 41st AIAA Aerospace Sciences Meeting and Exhibit*, Reno, NV,USA, January 6-9 2003. AIAA 2003-0247.

[134] R.R. Nourgaliev, T.N. Dinh, and T.G. Theofanous. The direct numerical simulation of disperse multiphase high-speed flows. In *Presented at the 42nd AIAA Aerospace Sciences Meeting and Exhibit*, Reno, NV, USA, January 5-8 2004. AIAA 2004-1204.

[135] R.R. Nourgaliev, Dinh T.N., and T.G. Theofanous. The Characteristic Based Match-

ing (CBM) method for compressible flow with moving boundaries and interfaces. *ASME Journal of Fluids Engineering*, 126:586–604, 2004.

[136] R.R. Nourgaliev, Dinh T.N., and T.G. Theofanous. Adaptive Characteristics-Based Matching for compressible multi-fluid dynamics. *Journal of Computational Physics*, 213:500 – 529, 2006.

[137] S. Osher and J.A. Sethian. Fronts propagating with curvature dependent speed algorithms based on Hamilton - Jacobi. *Journal Of Computational Physics*, 79:12–49, 1988.

[138] Richard B. Pember, John B. Bell, Phillip Colella, William Y. Crutchfield, and Michael L. Welcome. An adaptive cartesian grid method for unsteady compressible flow in irregular regions. *J. Comput. Phys.*, 120(2):278–304, 1995.

[139] G. Perigaud and R. Saurel. A compressible flow model with capillary effects. *Journal of Computational Physics*, 209:139–178, 2005.

[140] J. M. Pittard, T. W. Hartquist, and J. E. Dyson. Self-similar evolution of wind-blown bubbles with mass loading by hydrodynamic ablation. *Astronomy and Astrophysics*, 373:1043–1055, 2001.

[141] T.J. Poinsot and S. K. Lele. Boundary conditions for direct simulations of compressible viscous flows. *Journal of Computational Physics*, 101:104–129, 1992.

[142] Jean-Philippe Ponthot. An extension of the radial return algorithm to account for rate-dependent effects in frictional contact and visco-plasticity. *Journal of Materials Processing Technology*, 80-81:628 – 634, 1998.

[143] Jean-Philippe Ponthot. Unified stress update algorithms for the numerical simulation of large deformation elasto-plastic and elasto-viscoplastic processes. *International Journal of Plasticity*, 18(1):91 – 126, 2002.

[144] Stéphane Popinet. GERRIS: a tree-based adaptive solver for the incompressible Euler equations in complex geometries. *Journal of Computational Physics*, 190(2):572 – 600, 2003.

[145] James J. Quirk. A parallel adaptive grid algorithm for computational shock hydrodynamics. *Appl. Numer. Math.*, 20(4):427–453, 1996.

[146] J.J. Quirk. *An Adaptive Grid Algorithm For Computational Shock Hydrodynamics*. PhD thesis, Cranfield Institute of Technology, 1991.

[147] J.J. Quirk and S. Karni. On the dynamics of shock bubble interaction. *Journal of Fluid Mechanics*, 318:129–163, 1996.

[148] Mittal R. Immersed Boundary Methods. *Annual Review of Fluid Mechanics*, 37:239 – 261, 2005.

[149] R.C. Ripley, F.S. Lien, and M.M. Yovanovich. Numerical simulation of shock diffraction on unstructured meshes. *Computers and Fluids*, 35:1420–1431, 2006.

[150] David J. Roddy, Sheldon H. Schuster, Martin Rosenblatt, Lisa B. Grand, Paul J. Hassig, and Kenneth N. Kreyenhagen. Computer simulations of large asteroid impacts into oceanic and continental sites - preliminary results on atmospheric, cratering and ejecta dynamics. *International Journal of Impact Engineering*, 5:525 – 541, 1987.

[151] Alexandre M. Roma, Charles S. Peskin, and Marsha J. Berger. An adaptive version of the immersed boundary method. *J. Comput. Phys.*, 153(2):509–534, 1999.

[152] T. Saito, M. Mauramoto, and K. Takayama. Numerical investigation of shock waves through gas-particle mixtures. *Shock Waves*, 13:299–322, 2003.

[153] T. Saito, M. Saba, M. Sun, and K. Takayama. The effect of an unsteady drag force on the structure of a non-equilibrium region behind a shock wave in a gas-particle mixture. *Shock Waves*, 17:255–262, 2007.

[154] S. Sambasivan and H.S. UdayKumar. Ghost Fluid Method for strong shock interactions part 2: Immersed solid boundaries. *AIAA Journal*, 47(12):2923–2937, December 2009.

[155] R. Saurel, P. Cocchi, and P. B. Butler. Numerical study of cavitation in the wake of a hypervelocity underwater projectile. *Journal of Propulsion and Power*, 15:513–522, 1999.

[156] H Schardin. *Stossrohre [Shock Tubes]*. Springer Verlag, New York, 1966.

[157] H Schardin. *Optische StromungsmeβTechnik*. Braun Verlag, Karlrushe, 1988.

[158] D. Scott Stewart and S.L. Yoo. High resolution numerical simulation of ideal and non-ideal compressible reacting flows with embedded internal boundaries. *Combustion Theory and Modeling*, 1:113–142, 1997.

[159] Kurt Sebastian and Chi-Wang Shu. Multidomain weno finite difference method with interpolation at subdomain interfaces. *J. Sci. Comput.*, 19(1-3):405–438, 2003.

[160] J. A. Sethian. *Level Set Methods and Fast Marching Methods: Evolving Interfaces in Computational Geometry, Fluid Mechanics, Computer Vision, and Materials Science*. Cambridge University Press, 2 edition edition, 1999.

[161] J.A. Sethian. Evolution, implementation, application of levelsets and fast marching methods for advancing fronts. *Journal Of Computational Physics*, 169:503–555, 2001.

[162] J.A. Sethian and P. Smereka. Levelset methods for fluid interfaces. *Annual Review of Fluid Mechanics*, 35:341–372, 2003.

[163] C.W. Shu and S. Osher. Efficient implementation of Essentially Non-Oscillatory shock capturing schemes II. *Journal Of Computational Physics*, 83:32–78, 1989.

[164] J.C. Simo and T. J. R. Hughes. General return mapping algorithms for rate independent plasticity. In C. S. Desai, E. Krempl, P. D. Kiousis, and T. Kundu, editors, *Constitutive Laws for Engineering Materials: Theory and Applications*. Elsevier Science Publishing Co.

[165] J.C. Simo and T.J.R. Hughes. *Computational Inelasticity*. Springer; Corrected edition, 2000.

[166] S. Sivier, E. Loth, J. Baum, and R. Lohner. Vorticity produced by shock wave diffraction. *Shock Waves*, 2:31–41, 1992.

[167] Vassili Sochinikov and Shlomo Efrima. Level set calculations of the evolution of boundaries on a dynamically adaptive grid. *International Journal for Numerical Methods in Engineering*, 56(13):1913 – 1929, 2003.

[168] M. Sommerfield. Unsteadiness of shock waves propagating through gas-particle mixtures. *Experiments in Fluids*, 3:197–206, 1985.

[169] John Strain. Fast tree-based redistancing for level set computations. *J. Comput. Phys.*, 152(2):664–686, 1999.

[170] John Strain. Semi-Lagrangian methods for level set equations. *J. Comput. Phys.*, 151(2):498–533, 1999.

[171] John Strain. Tree methods for moving interfaces. *J. Comput. Phys.*, 151(2):616–648, 1999.

[172] John Strain. A fast modular semi-Lagrangian method for moving interfaces. *J. Comput. Phys.*, 161(2):512–536, 2000.

[173] N. Sukumar, Brian Moran, and Ted B. Belytschko. The natural element method in solid mechanics. *International Journal Numerical Methods in Engineering*, 43(5):839, Nov 1998.

[174] M. Sun, T. Saito, K. Takayama, and H. Tanno. Unsteady drag on a sphere by shock wave loading. *Shock Waves*, 14:3–9, 2003.

[175] M. Sun and K. Takayama. Vorticity production in shock diffraction. *Journal of Fluid Mechanics*, 478(1):237–256, 2003.

[176] Mingyu Sun. *Numerical and Experimental Investigation of Shock Wave Interactions with Bodies*. PhD thesis, Tohoku University, 1998.

[177] M. Sussman, K.M. Smith, Ohta M. Hussaini, M.Y., and R. Zhi-Wei. A sharp interface method for incompressible two-phase flows. *Journal of Computational Physics*, 221(2):469 – 505, 2007.

[178] Mark Sussman and Emad Fatemi. An efficient, interface-preserving level set redistancing algorithm and its application to interfacial incompressible fluid flow. *SIAM Journal on Scientific Computing*, 20(4):1165–1191, 1999.

[179] Mark Sussman, Emad Fatemi, Peter Smereka, and Stanley Osher. An improved level set method for incompressible two-phase flows. *Computers & Fluids*, 27(5-6):663 – 680, 1998.

[180] Camacho. G. T. and M. Ortiz. Adaptive lagrangian modelling of ballistic penetration of metallic targets. *Computer Methods in Applied Mechanics and Engineering*, 142(3-4):269 – 301, 1997.

[181] H. Takahira and S. Yuasa. Numerical simulations of shock bubble interactions using an improved Ghost Fluid Method. In *2005 ASME Fluids Engineering Division Summer Meeting and Exhibition*, Houston, TX, USA, January 19-23 2005. ASME, FEDSM2005-77119.

[182] K. Takayama and K. Itoh. Unsteady drag over cylinders and aerofoils in transonic shock tube ows. In *Proceedings of the 15th International Symposium on Shock Waves and Shock Tubes*.

[183] H. S. Tang and F. Sotiropoulos. A second-order godunov method for wave problems in coupled solid-water-gas systems. *Journal of Computational Physics*, 151(2):790–815, 1999.

[184] H.S. Tang and D. Huang. A second order accurate capturing scheme for 1D invis-

cid flows of gas and water with vacuum zones. *Journal of Computational Physics*, 128(2):301 – 318, 1996.

[185] Geoffrey I. Taylor. The use of flat-ended projectiles for determining dynamic yield stress. i. theoretical considerations. *Proceedings of the Royal Society of London. Series A. Mathematical and Physical Sciences*, 194(1038):289–299, 1948.

[186] Geoffrey I. Taylor and H. Quinney. The latent energy remaining in a metal after cold working. *Proceedings of Royal Society, Series A*, 143:307–326, 1934.

[187] Hiroshi Terashima and Grtar Tryggvason. A front-tracking/ghost-gluid method for fluid interfaces in compressible flows. *Journal of Computational Physics*, 228(11):4012 – 4037, 2009.

[188] K.W. Thomson. Time dependent boundary conditions for hyperbolic systems II. *Journal of Computational Physics*, 89:439–461, 1990.

[189] E.F. Toro. *Riemann Solvers and Numerical Method for Fluid Dynamics - A Practical Introduction*. Springer, 2 edition, 1997.

[190] L. B. Tran and H.S. UdayKumar. A particle levelset based sharp interface Cartesian grid method for impact, penetration, and void collapse. *Journal Of Computational Physics*, 193:469–510, 2004.

[191] H.S. UdayKumar, S. Krishnan, and S. Marella. Adaptively refined, parallelised sharp interface cartesian grid method for three-dimensional moving boundary problems. *International Journal of Computational Fluid Dynamics*, 23:1061–8562, 2009.

[192] H.S. UdayKumar, L. Tran, D.M. Belk, and K.L. Vanden. An Eulerian method for computation of multi-material impact with ENO shock-capturing and sharp interfaces. *Journal Of Computational Physics*, 186:136–177, 2003.

[193] B van Leer. Towards the ultimate conservative difference scheme, V. A second order sequel to Godunov's method. *Journal of Computational Physics*, 32:101136, 1979.

[194] K. J. Vanden. Characteristic analysis of the uniaxial stress and strain governing equations with thermal-elastic and mie-grüneison equation of state. *Technical Memorandum, AFRL, Eglin AFB, FL*, 1998.

[195] W. P. Walters and Jonas A. Zukas. *Fundamentals of Shaped Charges*. Wiley-Interscience, 1989.

[196] C. Wang, H. Tang, and T .G. Liu. An adaptive ghost fluid finite volume method for compressible gas-water simulations. *J. Comput. Phys.*, 227(12):6385–6409, 2008.

[197] C.W. Wang, T.G. Liu, and B.C. Khoo. A real Ghost Fluid Method for the simulation of multi-medium compressible flow. *SIAM Journal of Scientific Computing*, 28(1):278–302, 2006.

[198] Z. J. Wang. A quadtree-based adaptive Cartesian/quad grid flow solver for Navier-Stokes equations. *Computers & Fluids*, 27(4):529 – 549, 1998.

[199] Alex B. Wenzel. A review of explosive accelerators for hypervelocity impact. *International Journal of Impact Engineering*, 5:681 – 692, 1987.

[200] P. Woodward and P. Colella. The numerical simulation of two dimensional fluid flow with strong shocks. *Journal of Computational Physics*, 54:115–173, 1984.

[201] Han-Chin Wu. *Continuum Mechanics and Plasticity*. Chapman & Hall, CRC Press, 2004.

[202] W. F. Xie, Y. L. Young, and T. G. Liu. Multiphase modeling of dynamic fluid-structure interaction during close-in explosion. *International Journal for Numerical Methods in Engineering*, 74(6):1019 – 1043, Oct 2006.

[203] Wenfeng Xie, Zhanke Liu, and Yin Lu Young. Application of a coupled eulerian-lagrangian method to simulate interactions between deformable composite structures and compressible multiphase flow. *International Journal for Numerical Methods in Engineering*, 9999(9999):609–630, July 2009.

[204] S. Xu, T.D. Aslam, and D. Scott Stewart. High resolution numerical simulation of ideal and non-ideal compressible reacting flows with embedded internal boundaries. *Combustion Theory and Modeling*, 1:113–142, 1997.

[205] Darren De Zeeuw and Kenneth G. Powell. An adaptively refined Cartesian mesh solver for the euler equations. *J. Comput. Phys.*, 104(1):56–68, 1993.

[206] Darren De Zeeuw and Kenneth G. Powell. An adaptively refined Cartesian mesh solver for the Euler equations. *Journal of Computational Physics*, 104(1):56–68, 1993.

[207] Darren L. De Zeeuw. *A quadtree-based adaptively-refined Cartesian-grid algorithm for solution of the Euler equations*. PhD thesis, Ann Arbor, MI, USA, 1993.

[208] F. Zhang, D.L. Frost, P.A. Thibault, and S.B. Murray. Explosive dispersal of solid particles. *Shock Waves*, 10(2):431 – 443, 2001.

[209] Fan Zhang, Paul A. Thibault, and Rick Link. Shock interaction with solid particles

in condensed matter and related momentum transfer. *Proceedings: Mathematical, Physical and Engineering Sciences*, 459(2031):705–726, March 8 2003.

[210] Y. Y. Zhu and S. Cescotto. Unified and mixed formulation of the 4-node quadrilateral elements by assumed strain method: Application to thermomechanical problems. *International Journal for Numerical Methods in Engineering*, 38(4):685–716, 1995.

[211] Udo Ziegle. A three-dimensional cartesian adaptive mesh code for compressible magnetohydrodynamics. *Computer Physics Communications*, 116(1):65 – 77, 1999.

[212] J. A. Zukas, T. Nicholas, H. F. Swift, L. B. Greszczuk, and D. R. Curran. *Impact Dynamics*. Krieger Publishing Company, 1992.

[213] J. A. Zukas and S. B. Segletes. Numerical modeling of hypervelocity impact phenomena with desktop computers. *Adv. Eng. Softw.*, 14(1):77–84, 1992.

[214] Jonas A. Zukas. *Introduction to Hydrocodes*. Elsevier Science, 2004.